

## CFD Modelling of Hlsarna Off-gas System

Hosseini, A.

**DOI**

[10.4233/uuid:b3121ed4-0554-4823-8ffe-1b88309f09ff](https://doi.org/10.4233/uuid:b3121ed4-0554-4823-8ffe-1b88309f09ff)

**Publication date**

2023

**Document Version**

Final published version

**Citation (APA)**

Hosseini, A. (2023). *CFD Modelling of Hlsarna Off-gas System*. [Dissertation (TU Delft), Delft University of Technology]. <https://doi.org/10.4233/uuid:b3121ed4-0554-4823-8ffe-1b88309f09ff>

**Important note**

To cite this publication, please use the final published version (if applicable).  
Please check the document version above.

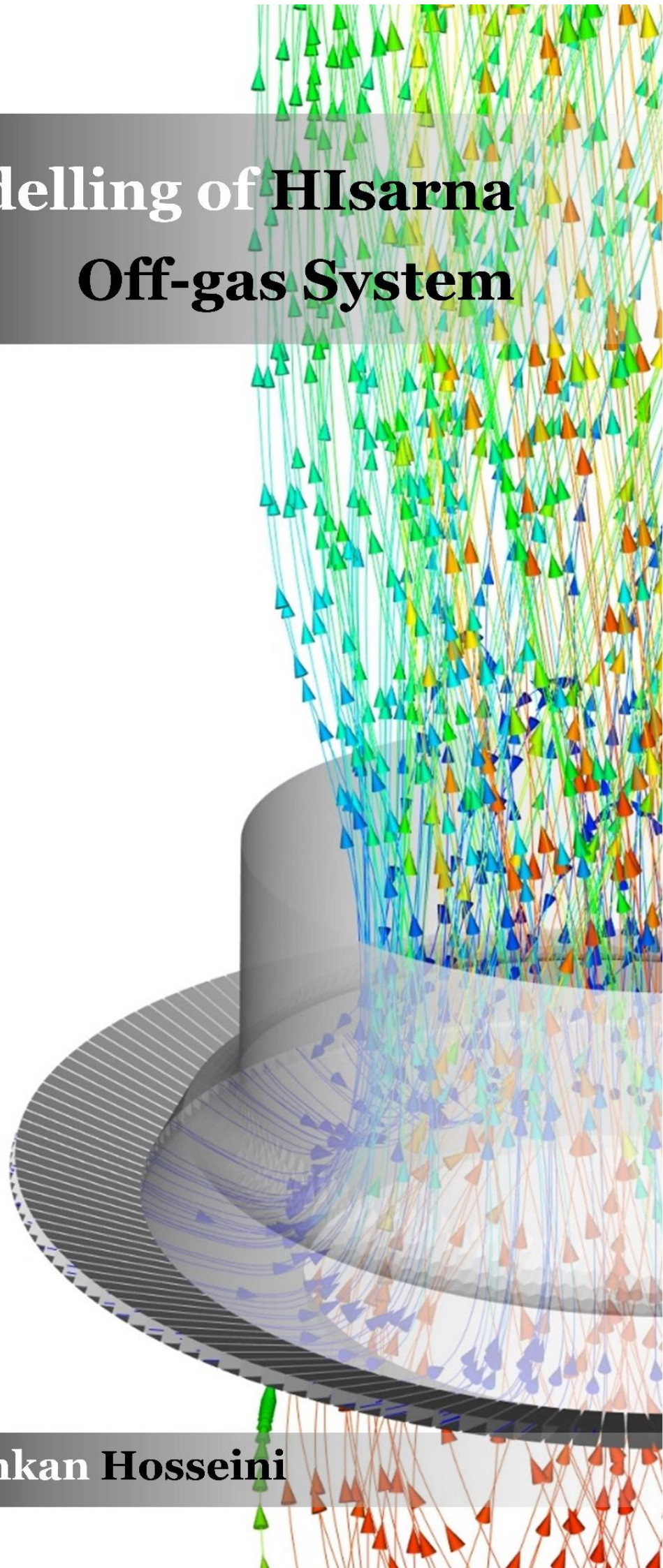
**Copyright**

Other than for strictly personal use, it is not permitted to download, forward or distribute the text or part of it, without the consent of the author(s) and/or copyright holder(s), unless the work is under an open content license such as Creative Commons.

**Takedown policy**

Please contact us and provide details if you believe this document breaches copyrights.  
We will remove access to the work immediately and investigate your claim.

# CFD Modelling of HIsarna Off-gas System



Ashkan Hosseini

# **CFD Modelling of Hisarna Off-gas System**

Dissertation

for the purpose of obtaining the degree of doctor

at Delft University of Technology

by the authority of the Rector Magnificus prof.dr.ir. T.H.J.J. van der Hagen,

Chair of the Board for Doctorates

to be defended publicly on

Wednesday 20 December 2023 at 12:30 o'clock

by

**Ashkan HOSSEINI**

Master of Science in Energy Engineering, Politecnico di Milano,  
born in Bukan, Iran

This dissertation has been approved by the promotor.

Composition of the doctoral committee:

Rector Magnificus	chairperson
Dr. Y. Yang	Delft University of Technology, promotor
Dr.ir. S.E. Offerman	Delft University of Technology, promotor

Independent members:

Prof.dr. M.J. Santofimia Navarro	Delft University of Technology
Prof.dr. H. Saxén	Åbo Akademi University, Finland
Prof.dr.ir. N.G. Deen	Eindhoven University of Technology, the Netherlands
Prof.dr. A. Jokilaakso	Aalto University, Finland
Prof.dr.ir. J.A.M. Kuipers	Eindhoven University of Technology, the Netherlands
Prof.dr. J. Dik	Delft University of Technology, reserve member



**Keywords:** Computational fluid dynamics, Discrete element method, Finite element method, Discrete phase model, HIsarna iron making, Combustion, Fluidic oscillator, Post combustion chamber, Thermodynamic analysis, Zinc ferrite formation, CFD-assisted scale up, Particle flow modelling

This research is part of the Reclamet Project (Nr 17209) funded by EIT RawMaterials (<https://eitrawmaterials.eu/project/reclamet>).

**Cover:** By Ashkan Hosseini

**Print:** ProefschriftMaken || [www.proefschriftmaken.nl](http://www.proefschriftmaken.nl)

Copyright © 2023 by Ashkan Hosseini

ISBN: 978-94-6384-517-5

An electronic version of this dissertation is available at <http://repository.tudelft.nl>



# Table of contents

<b>Chapter 1: Introduction</b>	<b>1</b>
1.1. Ironmaking history: from a clay pit to modern engineering marvels	2
1.2. Bloomery	3
1.3. Blast furnace	5
1.4. Global warming and developments in novel ironmaking technologies	8
1.5. Blast furnace vs Hisarna	10
1.6. Hisarna process component	12
1.6.1. Cyclone converter furnace (CCF)	14
1.6.2. Smelting reduction vessel (SRV) and bath	17
1.6.3. Off-gas system and its evolution	18
1.6.4. Air Quench	22
1.6.5. Water quench	23
1.6.6. Off-gas system walls	24
1.7. ReclaMet Project Description – Zinc Recovery Concept	25
1.8. Outline of the thesis	29
References	32
<b>Chapter 2: CFD model Development</b>	<b>34</b>
2.1. Introduction	35
2.2. Governing equation for CFD model	41
2.3. Model development	51
2.3.1. Description of the off-gas system	51
2.3.2. Computational grid (Mesh) generation	53
2.3.3. Inlet boundary condition	54
2.3.4. Wall boundary condition and wall modelling in CFD	56
2.3.5. Reactions and reaction kinetics	60
2.3.6. Model summary and solution procedure	61
2.3.7. Simulation results of the initial-model	62
2.4. Tuned-model	64
2.4.1. Wall thermal properties calculation using EMA correlations	64
2.4.2. CFD results of the tuned-model	68
2.5. Final-model development	72
2.5.1. Wall properties using Finite Element Method (FEM)	72
2.5.2. Methodology	73
2.5.3. FEM analysis	75
2.5.4. Effective thermal conductivity of equivalent wall (Step 0)	78
2.5.5. Sensitivity analysis using the final CFD model (Steps 1, 2, and 3)	81
2.6. Conclusion	87
References	90
<b>Chapter 3: Sensitivity analysis and model selection</b>	<b>101</b>
3.1. Introduction	103
3.2. Effect of mesh cell type	105

3.3. Effect of mesh cell count (mesh sensitivity analysis)	112
3.4. Selection of turbulence model	113
3.5. Effect of turbulent-chemistry interaction models	115
3.6. Effect of gas-solid (carbon particles) reaction	129
3.7. Effect of carbon particle dispersion	130
3.8. Effect of the radiation model	132
3.9. Conclusion	140
Reference	143

## **Chapter 4: Off-gas system flow analysis 151**

4.1. CFD model summary and review	154
4.2. Flow and wall temperature	154
4.3. Carbon track and conversion	157
4.4. Effect of water injection	158
4.5. Effect of oxygen injection	162
4.6. Effect of inlet CO content	165
4.7. Effect of inlet O <sub>2</sub> content	166
4.8. Conclusion	167

## **Chapter 5: Behaviour of pre-reduced molten ore particles 169**

5.1. Introduction	170
5.2. Governing equation	173
5.3. Phenomena description	173
5.4. Geometry, mesh, and boundary conditions	176
5.5. Base model: dog-leg geometry	177
5.6. Reflux chamber geometry modification	178
5.7. Further modifications	181
5.8. Conclusion and future improvement	183
References	185

## **Chapter 6: Flow analysis of the modified reflux chamber 187**

6.1. Introduction	188
6.2. Temperature and composition profiles	190
6.3. Carbon and CO conversion	193
6.4. Further modification of frog-leg geometry	197
6.5. Conclusion	200

## **Chapter 7: Zinc ferrite formation in off-gas system 201**

7.1. Introduction	202
7.2. Zinc recovery through the HIsarna process	205
7.3. Tools and Methods	207
7.3.1. CFD results	207
7.3.2. FactSage calculation	208
7.4. Results and discussion	211
7.4.1. Current pilot scale – Dog-leg geometry	211
7.4.2. Modified reflux chamber – Frog-leg geometry	213

7.4.3. Reflux chamber wall modification	217
7.4.4. Increasing CO content inside the reflux chamber	219
<b>7.5. Conclusions</b>	<b>220</b>
<b>References</b>	<b>223</b>

## **Chapter 8: Fluidic Oscillator for post-combustion** **225**

<b>8.1. Introduction</b>	<b>226</b>
<b>8.2. Transient simulation of fluidic oscillator</b>	<b>231</b>
8.2.1. Governing equation	231
8.2.2. Geometry, mesh, and boundary conditions	231
8.2.3. CFD results	232
<b>8.3. Fluidic oscillator for post-combustion</b>	<b>234</b>
8.3.1. Geometry, mesh, and boundary conditions	234
8.3.2. CFD results	234
<b>8.4. Conclusion</b>	<b>236</b>
<b>References</b>	<b>238</b>

## **Chapter 9: Scale up from pilot to industrial scale** **240**

<b>9.1. Introduction</b>	<b>241</b>
<b>9.2. Scale-up procedure</b>	<b>243</b>
<b>9.3. Industrial scale modelling</b>	<b>245</b>
9.3.1. Inlet boundary conditions	245
9.3.2. Oxygen injection calculations	246
9.3.3. Wall design	246
9.3.4. Industrial scale model summary	250
<b>9.4. Results and discussion</b>	<b>251</b>
9.4.1. Geometry and oxygen injectors	251
9.4.2. Base model	252
9.4.3. Effect of oxygen injection and optimization of post-combustion	254
9.4.4. Effect of wall thickness	257
9.4.5. Effect of CO at the inlet	258
<b>9.5. Conclusions</b>	<b>259</b>
<b>References</b>	<b>262</b>

## **Chapter 10: Conclusions and recommendations** **264**

<b>10.1. Conclusions</b>	<b>265</b>
10.1.1. CFD modelling of the HIsarna off-gas system	265
10.1.2. Thermodynamic analysis of zinc ferrite formation	266
10.1.3. Fluidic oscillator application	267
<b>10.2. Recommendations</b>	<b>267</b>
10.2.1. CFD modelling	267
10.2.2. Thermodynamic modelling	268
10.2.3. Plant measurements	268
10.2.4. Experimental studies	269

## **Nomenclature** **271**

<b>Summary</b>	<b>273</b>
<b>Samenvatting</b>	<b>276</b>
<b>Publications</b>	<b>279</b>
<b>Acknowledgments</b>	<b>280</b>
<b>Curriculum vitae</b>	<b>281</b>

# Chapter 1

## Introduction



**This chapter describes a brief history of ironmaking, and the story is gradually progressing to the current dominant technologies. The pros and cons of these common technologies are discussed, and the scientific efforts to overcome the disadvantages are reviewed. Ultimately, modern technologies are discussed, and special attention is paid to the HIsarna process as one of the alternative routes to the conventional ironmaking processes. The HIsarna process is described, and important process units are discussed, focusing on the off-gas system, which is the main zone of interest for the current Ph.D. study. Finally, the scope, aims, and the Ph.D. thesis outline are presented.**



## 1.1. Ironmaking history: from a clay pit to modern engineering marvels

Steel is a basic material supporting economic development with unique properties of strength, formability, and many other functions. One cannot find any country that has achieved high per capita incomes without substantially increasing its steel consumption. Iron metallurgy is a "sustaining technology" fundamental to the subsistence of the members of the societies that possess it [1].

However, steel is essentially a derivative of a simpler material called pig iron. Let us go back in time a bit to have a quick look at the history of iron to shed light on why this material is so important.

Iron as a commodity dates back to 3300 B.C. when there is evidence of using metal iron from meteorites in weapons and luxury articles during the reign of Tutankhamun in Egypt (example shown in Figure 1-1).



Figure 1-1. Fallen star sword. Daniella Comelli/University of Pisa [2].

Around 1500 B.C., advanced civilizations in the east Mediterranean region began to use iron more extensively. But it did not become the cheapest and most important of their metals until the 13th or even the 10th century B.C.

Driven by the increasing demand for metals and serving as a substitute for bronze, the Iron Age kicked off upon which the civilizations of the preceding centuries were built. The Iron Age began at various points worldwide at different times when

humankind started extracting iron from its ore. For example, in Britain and the south-eastern Alps in Austria, it commenced around 800 B.C. [3], and it was not until 300 B.C. that iron replaced bronze in China [4]. In Egypt, although iron existed from the 26th Dynasty (ca. 665–525 B.C.), it did not become common until the Ptolemaic period (305 B.C.–30 B.C.) [5].



Figure 1-2. a) Large heap of slag found in 2005 and b) porcelain kiln excavated in 2005 in HF, possibly active during the late Ming Dynasty; c) and d) excavation of furnaces in LD in progress; note the small size of the structures [6].

Archaeological evidence for iron production comes in four forms: by-products (slag and unused ore), production sites (furnaces and forges), tools, and finished objects. For example, Figure 1-2 shows an archaeological discovery of a production site with residual slag from the middle Qing Dynasty (1636 to 1912 A. C.).

## 1.2. Bloomery

Based on historical evidence, the most prevalent ironmaking method has been through a simple structure called "Bloomery". In bloomery, sponge iron or iron bloom is produced from the direct reduction of the iron ore with charcoal. It has a long historical application from the early second millennium B.C. and was practiced on all the inhabited continents [1].

Bloomeries are simple structure furnaces with conical shapes, usually made of clay or stone.

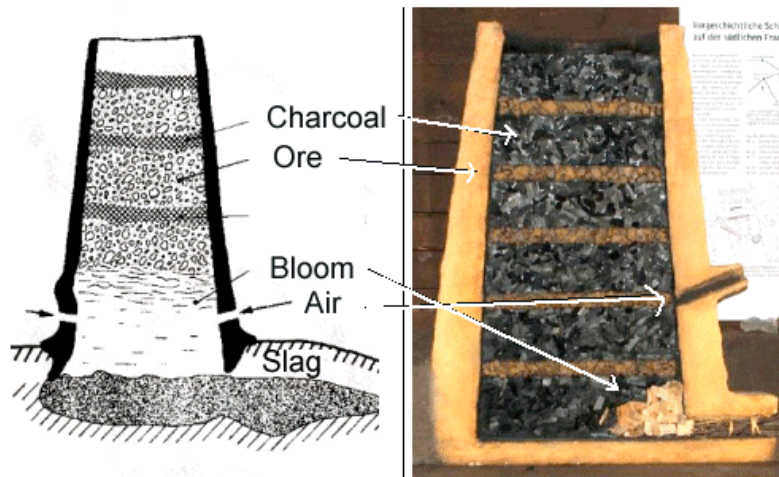


Figure 1-3. A schematic representation of an early bloomery with ore and charcoal feed [7].

Beneath the structure, tuyeres were inserted into the tuyere-holes, through which air is blown (manually in ancient times and mechanically in modern times). The charcoal and iron are fed in alternating layers. The generated heat and carbon monoxide from charcoal reduces the iron oxides in the ore to metallic iron without melting the ore. The mixture of slag and iron in the resulting bloom, known as sponge iron, is typically consolidated and further forged into wrought iron, which is low-carbon iron and easily malleable.

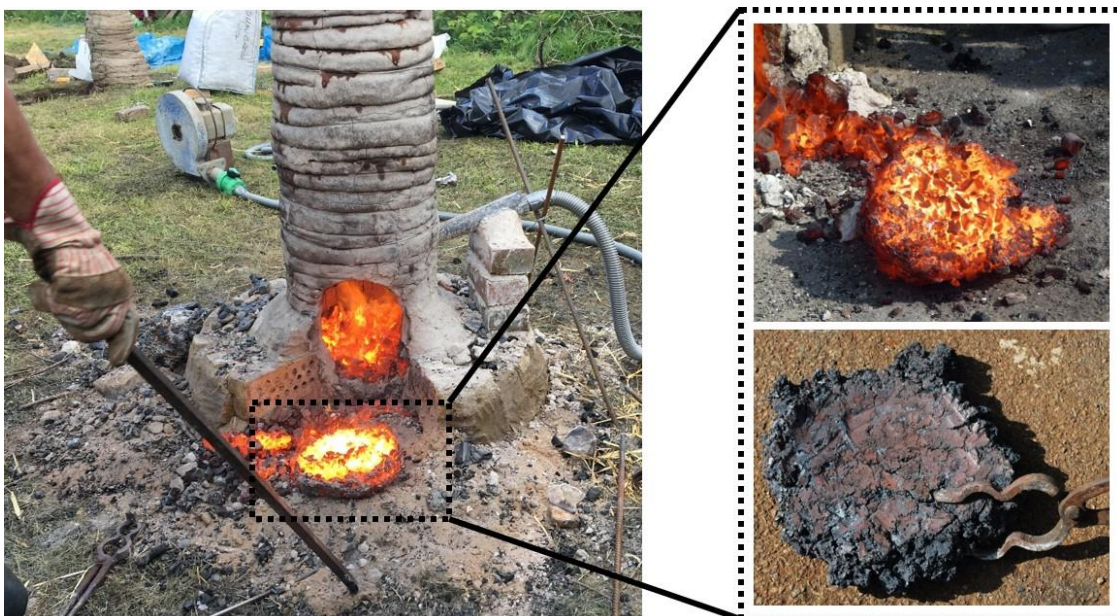


Figure 1-4. Sponge iron production from an experimental bloomery

Bloomeries remained in use until the mid-20<sup>th</sup> century. Figure 1-5 displays 6 out of 32 modern bloomeries that were operational in the Adirondack region of New York in 1888.



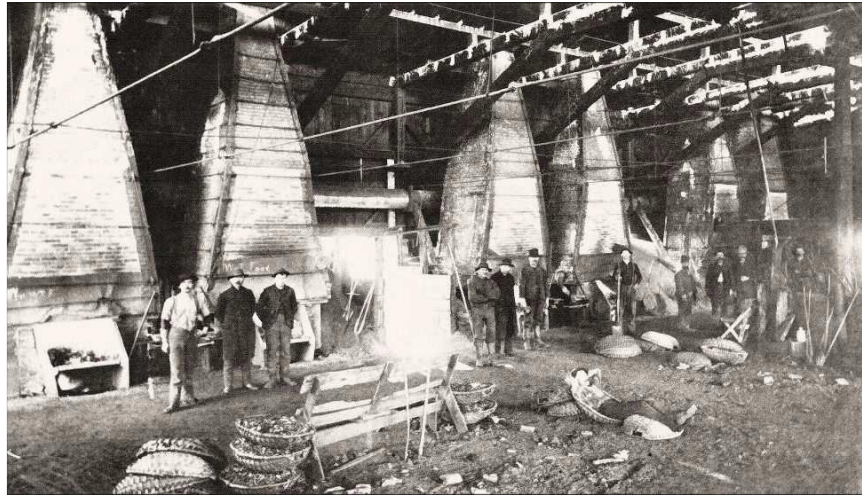


Figure 1-5. Interior of a nineteenth century Adirondack bloomery forge (Adirondack region of New York State 1888) [8,9].

The bloomery in everyday use in the Adirondack consisted of a hearth made of water-cooled cast-iron plates set within a brick stack. A heat exchanger for preheating the air blast was integrated into the stack above the hearth. The operation of the hearth was the responsibility of a single individual known as the bloomer. The bloomer placed iron ore in the hearth, where it was reduced by carbon monoxide generated from a charcoal fire. Periodically, slag was tapped through holes at the front of the hearth. When the iron bloom had grown to occupy most of the hearth space, it was levered onto the floor and then taken to a helve hammer to remove the contained slag and shape it into a billet [1,9].

### 1.3. Blast furnace

The surge in iron consumption and the increasing demands of rapidly growing industries, such as civil engineering structures, machinery, and engine sectors, paved the road for technological advancements in iron metallurgy to meet the growing demand.

The need arose for higher-quality iron in larger quantities and within shorter timeframes. While Blast Furnaces share some structural similarities with bloomeries, they are significantly more efficient in terms of energy and productivity.

A key distinction between the blast furnace and the bloomery lies in their objectives. The blast furnace is designed to produce molten metal that can be tapped from the

furnace, whereas the bloomery aims to prevent melting to avoid the carbon becoming dissolved in the iron [10].

In essence, a blast furnace (the schematic shown in Figure 1-6) is a giant shaft furnace that is fed from the top with alternating layers of sinter ore (produced from iron ore), coke (produced from coal), and limestone, forming a porous bed. From the beneath of the furnace and through tuyeres, hot air (blast air) is injected at the bottom of the furnace. While the hot air passes through the bed, the coke is oxidized, generating heat and carbon monoxide gas, which reduce and melt the ore bed, resulting in the formation of pig iron. Pig iron from a blast furnace typically has a high carbon content, around 4%. The molten iron descends to the bottom of the furnace and is periodically “tapped” from the furnace along with the accompanying slag [11,12].

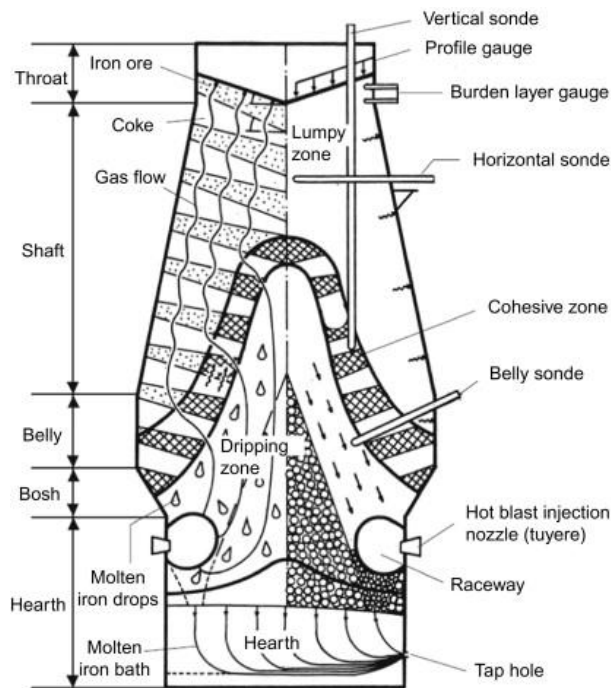


Figure 1-6. Modern blast furnace schematic view [12].

The blast furnace application dates back to the 14<sup>th</sup> and 15<sup>th</sup> centuries, originating from the Namur region in Belgium. From there, it spread to the eastern boundary of Normandy (North-West of France) and then to Weald of Sussex (Southeast England) in about 1491 A.D. Till 1530 A.D., the application of blast furnace remained limited and did not grow until about 1530 A.D., reaching the peak about 1590 A.D. [13]. Similar to bloomeries, charcoal was the primary fuel used in the early blast furnaces. However, the consumption of charcoal for large-scale blast furnaces was relatively high due



to its lower heating value and limited availability compared to coal. The successful substitution of coke for charcoal is widely credited to Abraham Darby in 1709 [12]. The very first blast furnace structure used by Darby is shown in Figure 1-7.



Figure 1-7. Remains of Abraham Darby's blast furnaces (obtained from ALAMY photo gallery [www.alamy.com](http://www.alamy.com))

The efficiency of the process was further enhanced by preheating the injected air, known as blast air, a method patented by James Beaumont Neilson in 1828. In modern-day blast furnaces, the blast air is supplied through a dedicated stove that burns the waste gas from a blast furnace containing combustible  $\text{CO-H}_2$  compounds, using air as an oxidant. The heat generated during combustion is utilized to preheat the cold blast air [14].

There are many examples of early modern blast furnaces, among which the Lithgow Iron and Steel Industry (Australia) is worth mentioning. It was founded in October 1875 with a small-capacity blast furnace (Figure 1-8). In 1907, a blast furnace with a capacity of 1,000 tons per week was inaugurated, which could treat 51,000 tons of ore and employed 632 people during the first year. By 1926, the company had turned out 178,000 tons of ore, resulting in 105,000 tons of pig iron [15].

During the twentieth century, there were considerable improvement and development in the blast furnace process scale-up and sizing. For example, the hearth of a blast furnace had a maximum diameter of 4 to 5 meters (100,000 tonnes of hot metal per year) at the beginning of the century, which was scaled up to 14 to 15 meters (3–4 million tons of hot metal per year) by the end of the century. To this date, the blast furnace route is still efficient in terms of production capacity and costs; however, using this route has made the iron and steel production industry one of the sectors with the most significant  $\text{CO}_2$  footprint. Via blast furnace technology, every ton of produced steel emitted, on average, 1.85 tons of carbon dioxide from

2018 to 2020. In 2020, with total production of 1,860 million tonnes of steel, total direct emissions from this sector were 2.6 billion tonnes, representing between 7% and 9% of global anthropogenic CO<sub>2</sub> emissions [16–19].

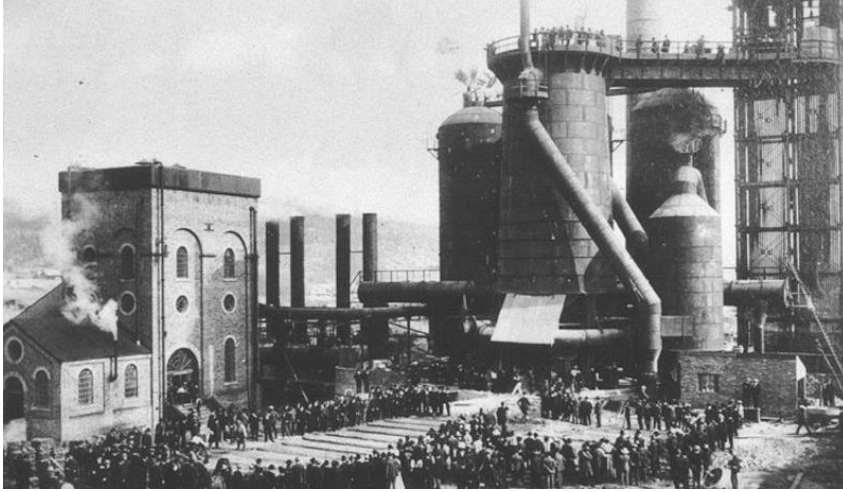


Figure 1-8. Lithgow Iron and Steel Industry - Opening of the Blast Furnace May 1907 [15]

If we count the emissions of the steel industry as if it were a nation, it would rank as the fifth largest CO<sub>2</sub>-producing nation in the world [16–19]. That figure makes the blast furnace route one of the main obstacles to achieving a carbon-free steel industry, which must be mitigated by modifications or alternative routes.

## 1.4. Global warming and developments in novel ironmaking technologies

Many attempts and research have been made to develop strategies to mitigate emissions and energy consumption in current blast furnace technologies.

These mitigation approaches have been practiced from various perspectives, such as supply-side mitigation, supplied energy optimization, and CO<sub>2</sub> recycling from steelmaking systems. Many researches focused on demand-side mitigation to develop strategies, namely recycling and reusing scrap steel or hydrogen-based steelmaking technology. However, given the fact that the coke from coal is used as the main reduction agent in the ironmaking process, coal has been the dominant energy input for the iron and steelmaking processes, accounting for almost three-quarters of the total energy inputs, making CO<sub>2</sub> emissions hard to abate [19]. There is a growing interest in developing innovative ways of steel production to meet CO<sub>2</sub> and other pollutant emission requirements. An alternative ironmaking process is

needed to meet criteria such as simplified material preparation, metal production with fewer impurities, independent process steps, efficient pollution control, and minimal waste generation. Ultimately, an alternative process should reach a level of maturity with higher productivity per unit volume than the blast furnace and lower capital costs [20]. The novel ironmaking processes can be categorized into two classes: direct reduction and smelting reduction.

In the direct reduction process, the iron ore is reduced by CO and H<sub>2</sub> gases mainly derived from natural gas reforming and, in limited cases, coal gasification. The reduction is performed at lower temperatures without melting the ore, during which large micro-pores are left from the removal of oxygen, forming so-called sponge iron. Direct reduction generally has a higher purity than the pig iron from the blast furnace process [11]. The best-known technologies for direct reduction are MIDREX and HYL, and MIDREX processes account for more than 78% of the direct reduced iron production [10].

Smelting reduction is another alternative path to the blast furnace. It is developed to use coal directly to reduce the molten ore, ultimately eliminating the consumption of the energy-intensive coke-making and sintering processes [22, 11]. The coal is injected into a molten pre-reduced iron ore bath, which is gasified inside the bath to produce CO that reduces the molten ore. Several smelting reduction processes have been commercially proven, such as HIsarna, COREX, FINEX, HIs melt, and the ITmk3 project [10]. Hasanbeigi et al. [11], de Beer et al. [22], and Greene [21] have consolidated available information on alternative emerging ironmaking technologies, which the summary is depicted in Figure 1-9 and Table 1-1.

Table 1-1. A comparison of novel ironmaking technologies [11]

Technology	Reducing agent and energy source				Form of iron ore				Oxygen	Coal gasification	Status
	Coal	Coke	NG	Other	Sinter	Pellet	lump	Fine			
<b>Blast furnace</b>		X			X	X					Commercial
<b>COREX®</b>	X				X	X	X		X		Commercial
<b>FINEX®</b>	X							X	X		Commercial
<b>Tecnored</b>	X					X		X			Pilot
<b>ITmk3</b>	X					X		X			Demonstration
<b>PSH</b>	X					X		X			Development
<b>HYL</b>	X					X	X			X	Commercial
<b>MIDREX</b>	X					X	X		X	X	Demonstration
<b>Circored®</b>	X			X				X			Demonstration
<b>Circofer®</b>	X			X				X			Demonstration
<b>CCF</b>	X					X	X		X		Pilot
<b>MOE</b>				X		X	X				Research
<b>HIsarna</b>	X							X	X	X	Pilot/demo

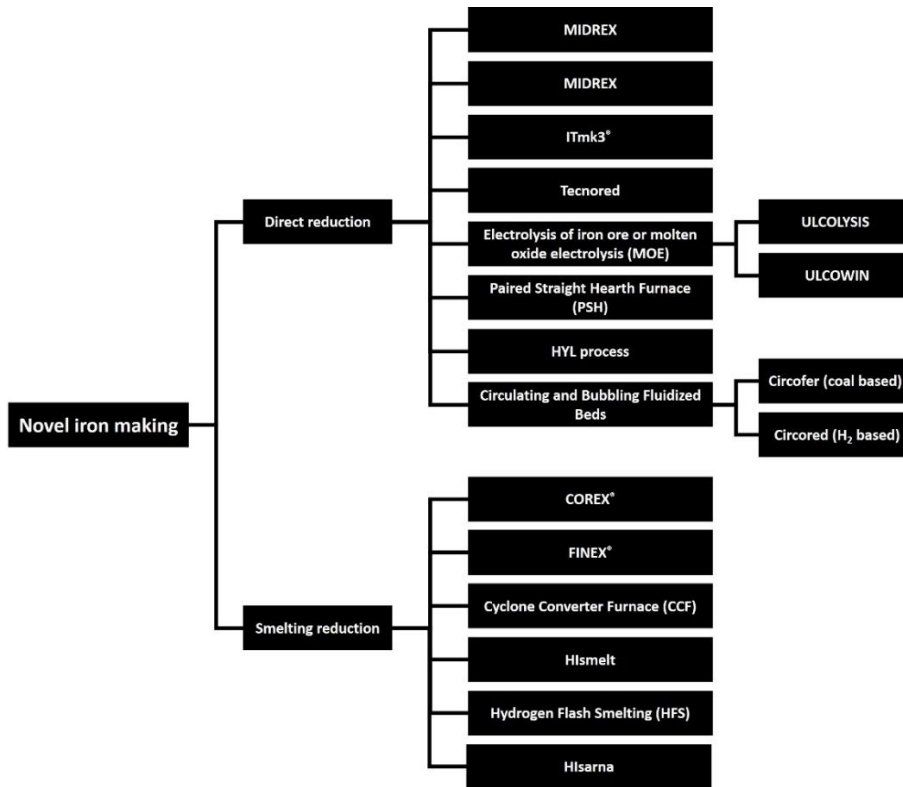


Figure 1-9. Summary of available alternative ironmaking processes (drawn based on data from references [11,21,22])

### 1.5. Blast furnace vs HIsarna

Among the mentioned alternative routes, the HIsarna process has drawn researchers' and investors' attention and shown promising results to be fully scaled up to the commercial scale. HIsarna is a new and breakthrough smelting reduction technology to produce liquid hot metal from iron ore. Compared to the blast furnace route, HIsarna offers a 20% reduction of CO<sub>2</sub> emission by eliminating coking and iron ore agglomeration (sintering and pelletizing), and the coal and fine iron ore are directly fed into the reactor. According to the plant analysis, up to 50 % of the material added to the process can be made of scrap steel, reducing the requirement for raw materials compared to the blast furnace process. In addition, more than 40% of the granular coal was replaced by sustainable biomass, leading to higher neutral CO<sub>2</sub> emissions. Since the HIsarna installation produces highly concentrated CO<sub>2</sub>, it is ideally suited for CCS without needing a costly gas separation stage. Combining the HIsarna with CCS solutions could lead to a total CO<sub>2</sub> saving of at least 80 % from the iron and steel production. As mentioned before and depicted in Figure 1-10, the process is a combination of the Cyclone Converter Furnace (CCF) technology

(developed by Hoogovens, now Tata Steel Nederland) and the smelting reduction vessel of HIs melt technology (developed by Rio Tinto) built-in pilot scale.

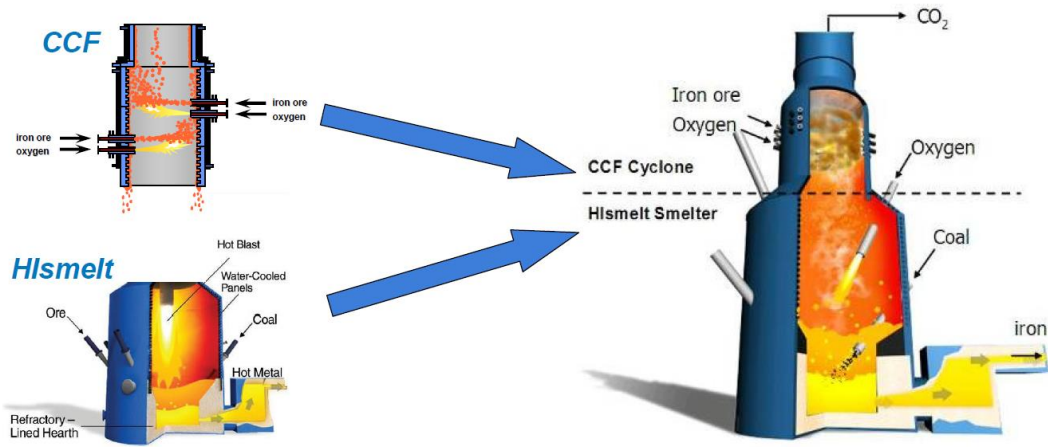


Figure 1-10. Combination of HIs melt and CCF technology to construct HIsarna

The HIsarna pilot plant started producing 8 tons/h of hot metal in the IJmuiden Works of Tata Steel Nederland in 2010. Since then, it has been under further development towards industrial demonstration. Figure 1-11 shows a comparison between HIsarna technology and blast furnace, and as it can be seen, the overall compound balance is quite similar. The main difference (besides physical and geometrical differences and elimination of sintering and coking in HIsarna) would be the raw material transition to products.

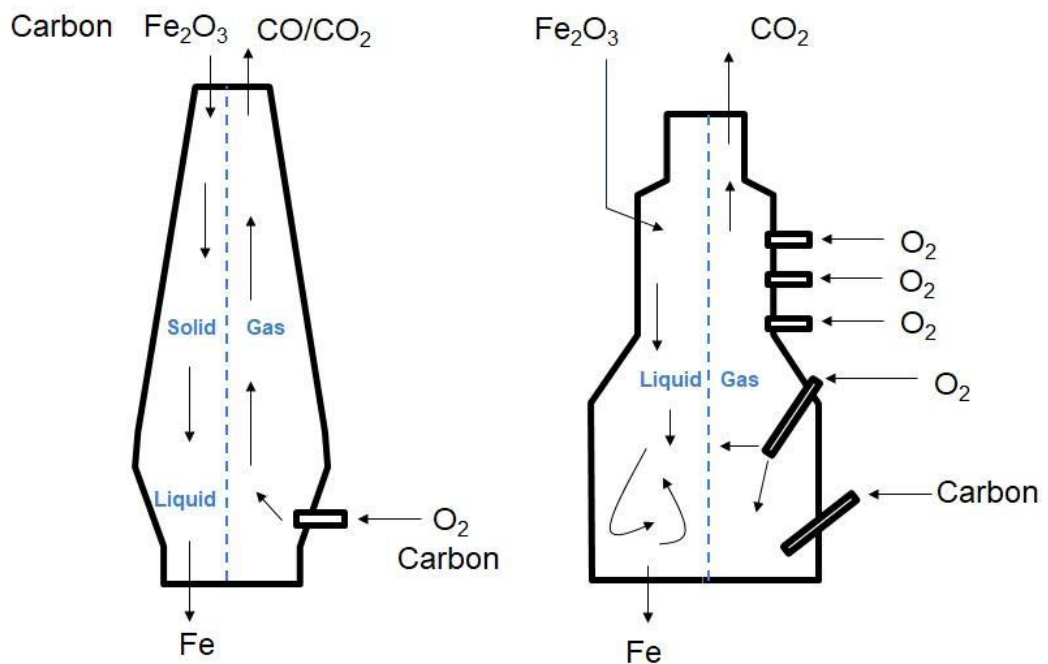


Figure 1-11. Schematic view of Blast furnace and HIsarna reactor



Figure 1-12 shows the raw material path from solid ore to pre-reduced and molten iron. In HIsarna technology, the transition from the solid-state of the raw material to the liquid or gaseous-state is almost instantaneous once raw material is injected into the CCF. In contrast, the phase transition from solid to liquid-state in the blast furnace is gradual, with an average residence time typically lasting 8 hours.

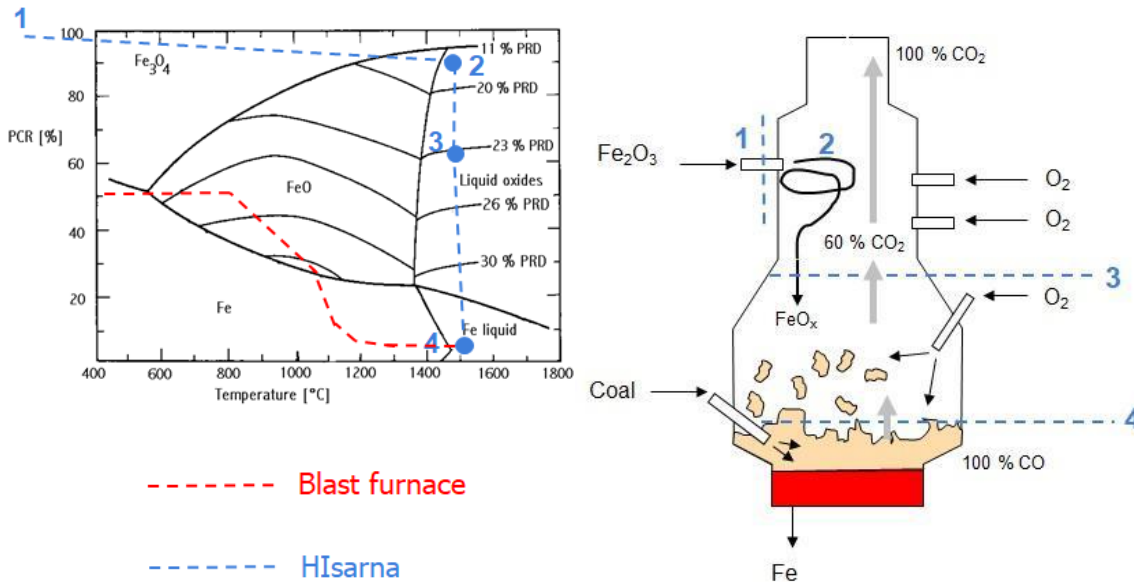


Figure 1-12. Iron ore path from the point of injection into the HIsarna reactor (obtained from TATA Steel Ijmuiden R&D)

In one research project (EU project in CORDIS, LoCO<sub>2</sub>Fe), the HIsarna process was compared to other alternative routes, including two cases with blast furnaces combined with carbon capture and storage (CCS) [23]. According to the analysis, in the blast furnace route, the CO<sub>2</sub> is distributed over more stacks, and capturing the CO<sub>2</sub> requires multiple installations, making it costly. On the other hand, the HIsarna can achieve the 2030 emission targets when scrap and biomass are used to partially replace iron ore and coal (part of the current ReclaMet research program), and HIsarna with CCS can achieve the emission targets for 2050 as depicted in Figure 1-13 [23].

## 1.6. HIsarna process component

Figure 1-14 shows the overall scheme of the process at the pilot scale. Figure 1-15 shows the configuration of the main reactor composed of CCF, SRV, and bath. Fine iron ore is injected into the CCF along with pure oxygen. The oxygen is needed to

combust the CO-H<sub>2</sub> mixture in the off-gasses from the Smelting Reduction Vessel (SRV). The combustion process provides heat to pre-reduce and melt the iron ore during the flight time, which is ultimately deposited against the wall of the furnace. The accumulation of the particles on the wall creates a liquid film, which is then dripped along the wall and falls into the molten iron bath of the SRV.

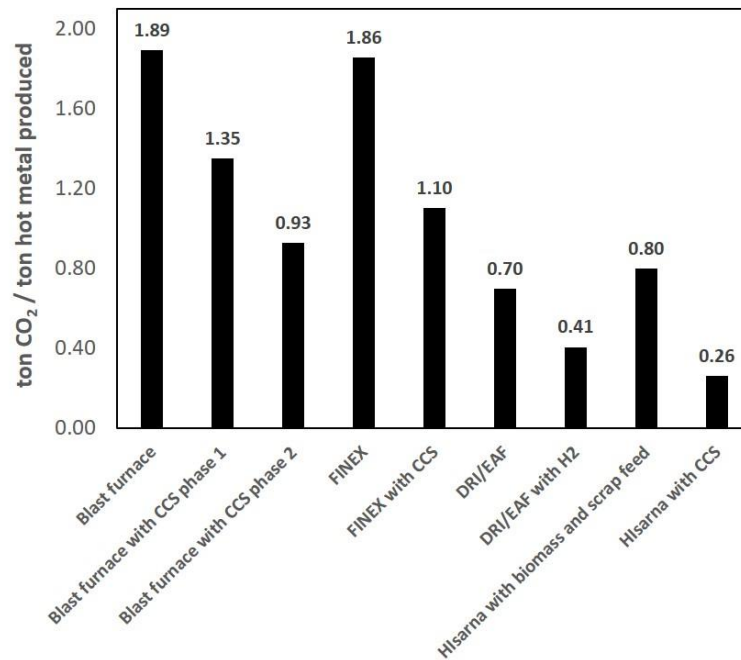


Figure 1-13. Calculated CO<sub>2</sub> emissions for different steel production routes with and without CCS [23].

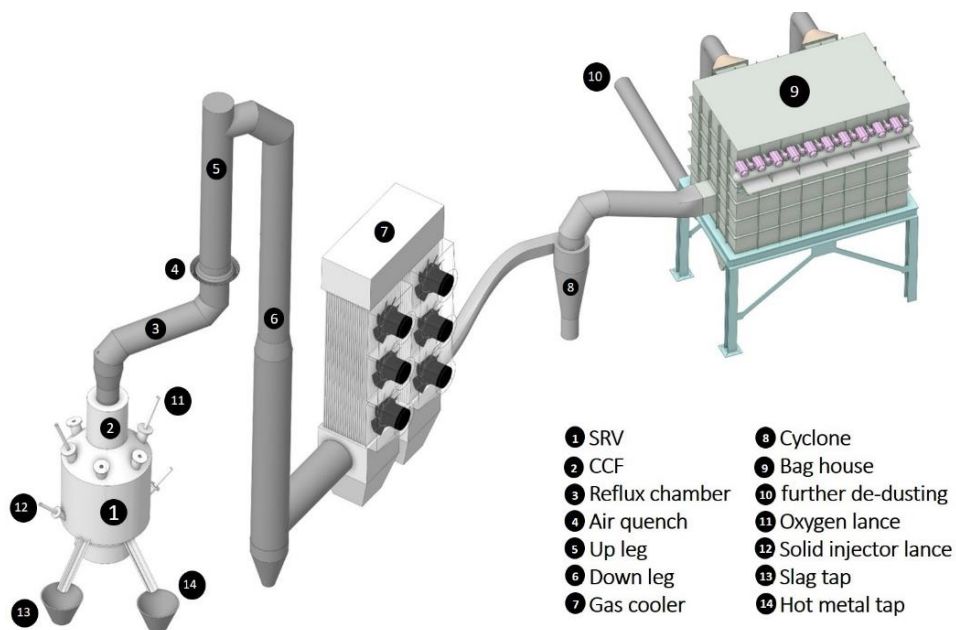


Figure 1-14. Schematic representation of the Hisarna main components

Coal is injected into the slag layer using a carrier gas to reduce the pre-reduced iron oxide ( $\text{FeO}_x$ ) droplets dripping into the bath from the CCF. CO gas is generated in the form of bubbles and will reach the top space of the SRV to combust partially with oxygen injected through oxygen lances (OL), providing the necessary heat in the SRV.

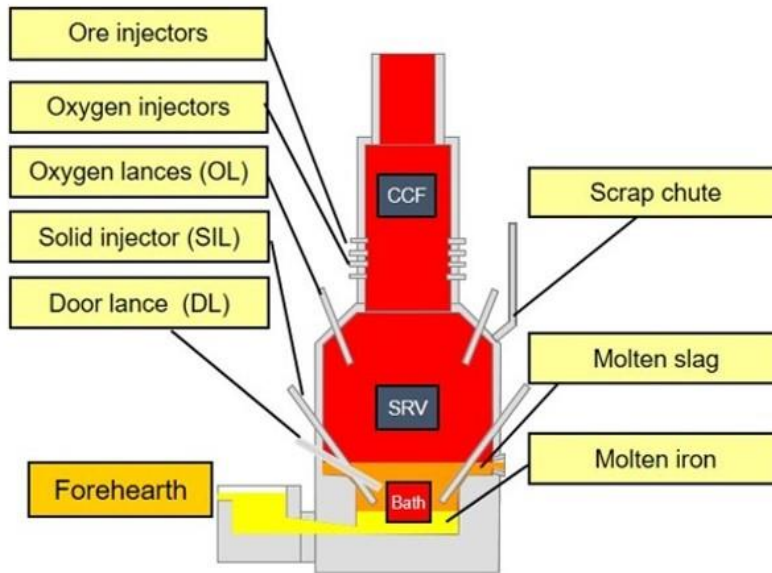


Figure 1-15. HI-sarna reactor main sections

After the main reactor, there is a horizontal pipe called the Reflux Chamber. The flue gas will be air-quenched via air inlet ports above the reflux chamber. The air injection is also responsible for keeping the pipe wall clean from the deposition of molten particles (will be discussed later). Flue gas is then further cooled and passed through dust-capturing units.

### 1.6.1. Cyclone converter furnace (CCF)

Fine ore and flux (limestone) are fed into the smelting cyclone with oxygen. The injectors are configured with an angle to create a swirl motion. This configuration increases the residence time, allowing them to react with the reducing gases ( $\text{CO}/\text{H}_2$ ) coming from the SRV.

High-purity oxygen is used to combust the flue gas from the SRV, which enters from the bottom of the cyclone and mainly consists of  $\text{CO}$  and  $\text{H}_2$ . The heat from this combustion is used to melt the ore and heat it to the SRV temperature, which is around  $1450\text{-}1500\text{ }^\circ\text{C}$ . The temperature inside the CCF is much higher, and the

highest gas temperature could reach 1700-2000 °C, which is sufficient to decompose the iron ore. In CCF, the iron ore is reduced through two different mechanisms: reduction via reducing agents (CO/H<sub>2</sub>) and reduction via thermal decomposition. A pre-reduction degree of around 20% is achieved through both mechanisms. The process happens in a fraction of a second before the molten particles hit the wall, creating a molten layer of material that drips into the SRV bath. A schematic view of CCF with a graphical representation of film formation is depicted in Figure 1-16.

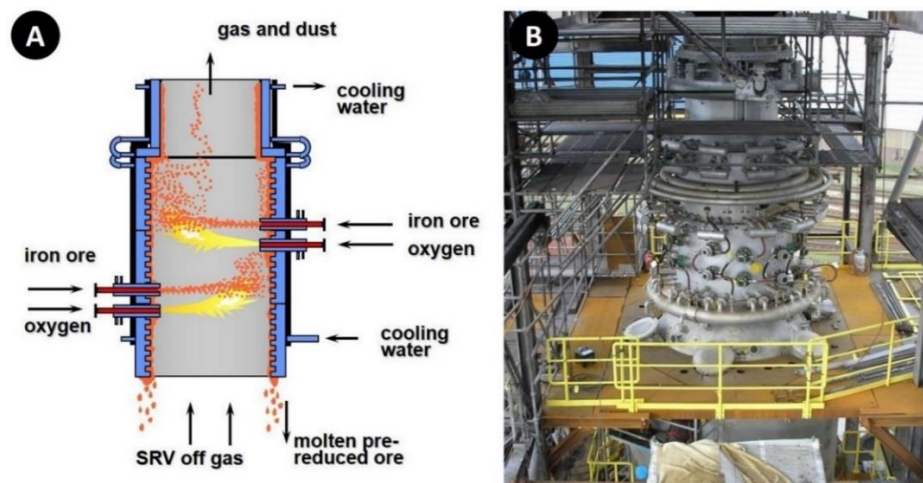


Figure 1-16. Cyclone Converter Furnace schematic view (A) and during installation (B) (Obtained from TATA Steel Ijmuiden R&D)

Iron oxide injected into the CCF may exist in three forms since the pre-reduction reactions are not complete:

- hematite, Fe<sub>2</sub>O<sub>3</sub>, melting point = 1565 °C,
- magnetite, Fe<sub>3</sub>O<sub>4</sub>, melting point = 1597 °C,
- wüstite, FeO, melting point = 1377 °C.

The coexistence and their ratio depend on the temperature and gaseous partial pressure.

The following reactions may occur in CCF:

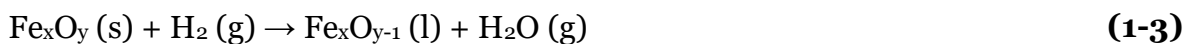
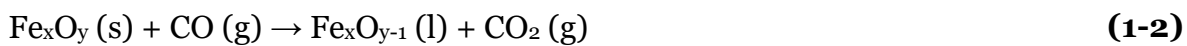
***Thermal decomposition + melting***



The thermal decomposition degree of iron ore in the smelting cyclone is determined by the gas atmosphere, temperature profile, particle trajectory, particle size, and residence time.

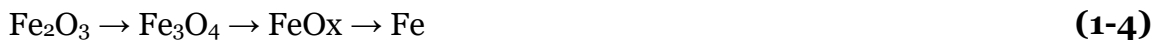
The temperature at which thermal decomposition occurs depends on the partial pressure of oxygen. Lower  $P_{O_2}$  results in a higher degree of decomposition. Keeping  $P_{O_2}$  as low as zero would allow the reaction (mainly the decomposition of hematite to magnetite) to proceed completely at lower temperatures. However, the temperature in CCF is significantly higher than the starting decomposition temperature of hematite and partially magnetite (around 1200 °C).

### ***Reduction with CO or H<sub>2</sub> + melting***



Reduction of hematite via reducing agent is always stepwise. Depending on temperature, it can be done in two or three steps.

When  $T > 570$  °C:



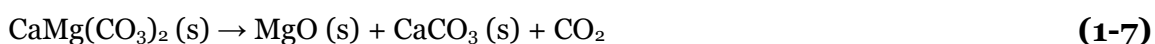
If  $T < 570$  °C, the magnetite is directly converted into Fe since at this temperature range, wüstite is thermodynamically unstable.



HIsarna reactor operates at a temperature much higher than 570 °C; therefore, the reduction from ore to iron is always in 3 steps along the reactor.

### ***Calcination*** (thermal decomposition between 720 to 780°C)

Calcite and dolomite are added to CCF and SRV into the slag phase as a flux to participate in the following reactions:



### ***CO/H<sub>2</sub> combustion***

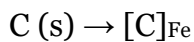
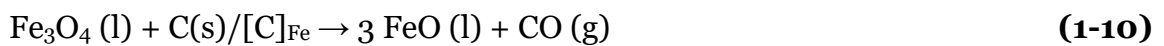


The gaseous phase combustion occurs throughout the entire process, from the SRV to the CCF and reflux chamber. The generated flue gas from the reduction reactions is mostly composed of CO and H<sub>2</sub> compounds. Gaseous reactions provide the necessary heat in SRV and CCF to sustain the reduction reactions in the following reactions:



### 1.6.2. Smelting reduction vessel (SRV) and bath

A schematic view of SRV is shown in Figure 1-17. Inside the molten bath, coal is injected into the slag layer. This will cause bath carburisation. Partially reduced molten ore droplets path through the slag layer, and the following reactions could occur (part of saturated iron droplets will be in the slag phase, too):



The generated gas at the upper part of the SRV is at 1400-1500 °C and has a post-combustion ratio (PCR) of around 50 %.

FeO will be reduced to Fe, with typically around 5-6% of FeO remaining in the slag. Coal injection is also responsible for mixing metal and slag, indirectly transferring heat from gas to slag.

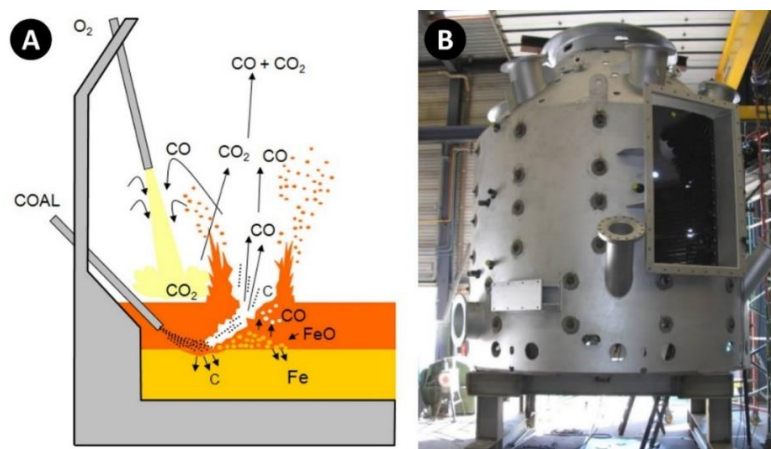


Figure 1-17. SRV schematic view (A) and real SRV facility during the installation (B) (obtained from TATA Steel Ijmuiden R&D)

Above the bath, there is the gaseous zone of SRV. High-temperature oxygen is injected into the surface of the slag. The oxygen will combust the CO from the bath in the space above the melt phase (due to the above reactions), which is the primary heat source for the process. Here, the slag layer plays an important role. It shields the reduction zone (inside the slag) from oxidation, which could otherwise happen by oxygen injection. This shielding also minimizes direct combustion of the carbon, which is injected into the bath (the slag layer).

### 1.6.3. Off-gas system and its evolution

In the old pilot scale installation, there was a straight pipe to carry off-gases from CCF, as shown in Figure 1-18.

The flue gas from CCF contains CO, CO<sub>2</sub>, unburnt carbon, and droplets of pre-reduced iron ore (mainly Fe<sub>2</sub>O<sub>3</sub> and Fe<sub>3</sub>O<sub>4</sub>). The flue gas was combusted in an incinerator downstream to achieve a 100% post-combustion ratio (PCR).

The pipe was water-cooled, and the temperature along the pipe was quenched to 800-1000 °C (from a flue gas temperature of 2000 to 2273 °C in CCF).

Using this configuration, several problems were raised:

- As mentioned before, an incinerator was installed downstream after the vertical pipe to combust CO and unburnt carbon particles, preventing CO emission. The inlet temperature of the flue gas at the incinerator was between 800-1100 °C. However, this temperature was not sufficient to fully combust CO. Moreover, depending on the post-combustion degree (PCD) of the off-gases in the cyclone, its composition and hence its temperature varied widely. It is required that the temperature in the incinerator remains within an acceptable operational window to ensure its stable operation and also the complete combustion of the unwanted species. During one of the HIsarna campaigns, a significant drop in temperature was observed in the incinerator within a short production period. Detailed data analysis revealed that high post-combustion in the cyclone resulted in the incinerator receiving less fuel gas from the smelter than expected, leading to lower flue gas temperatures. Low temperatures in the incinerator could give rise to two scenarios: (i) incomplete combustion of fuel components (CO), resulting in unwanted

emissions; (ii) in the case of an extremely high solid carbon load in the off-gas, explosive mixtures could form, potentially igniting at a later stage, thereby causing process instability and possible damage to the plant. Hence, an additional control strategy was required to oversee the entire operation.

- Another issue was the solid layer of molten iron ore accumulating along the pipe walls as the temperature dropped, causing thickness to increase along the flue gas path.

The ore deposit layer caused two problems:

- The heat transfer from the flue gas to the wall and subsequently to the cooling water would diminish as a result of the insulating solidified layer. This reduction could lower the overall heat transfer coefficient and, under constant heat flux, disrupt the pipe's temperature profile. This, in turn, posed challenges in process control and had the potential to disrupt downstream units, such as the incinerator (not shown in the figures).
- The thickened layer would get heavier at the top, and ultimately, due to vibration in the pipe, it would crack and fall to the CCF as a big chunk, as shown in Figure 1-19. Additionally, certain sections of the layer might extend into downstream equipment.

Major changes have been implemented in the new installation to resolve these issues (solid layer, incinerator instabilities, etc.). The straight pipe is replaced with a bent horizontal pipe (reflux chamber), and the incinerator is removed. Post-combustion is now performed in the off-gas system by injecting  $O_2$  at a high temperature. The modified configuration is shown in Figure 1-20, and detailed reflux chamber geometry is illustrated in Figure 1-21.

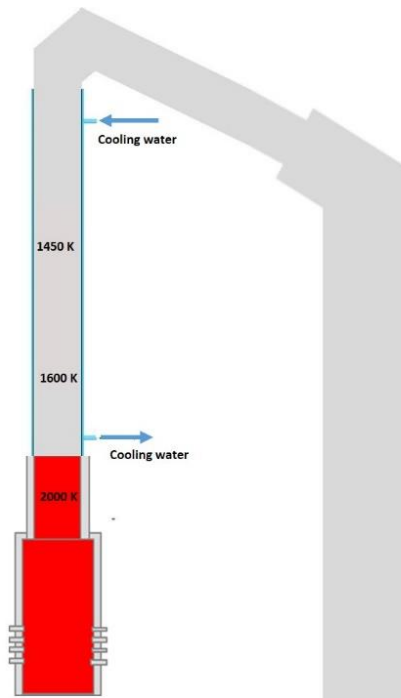


Figure 1-18. Scheme of the flue gas duct – old design

A more detailed representation of the modified off-gas system is shown in Figure 1-22. As pre-reduced ore droplets are carried with the flue gas, they hit the bend and gather at the lower part of the horizontal pipe, forming a pool of molten material. This layer remains molten because the temperature in the reflux chamber stays elevated and above the melting point of pre-reduced ore ( $T_{\text{melting}} = 1050\text{-}1157\text{ }^{\circ}\text{C}$ ).

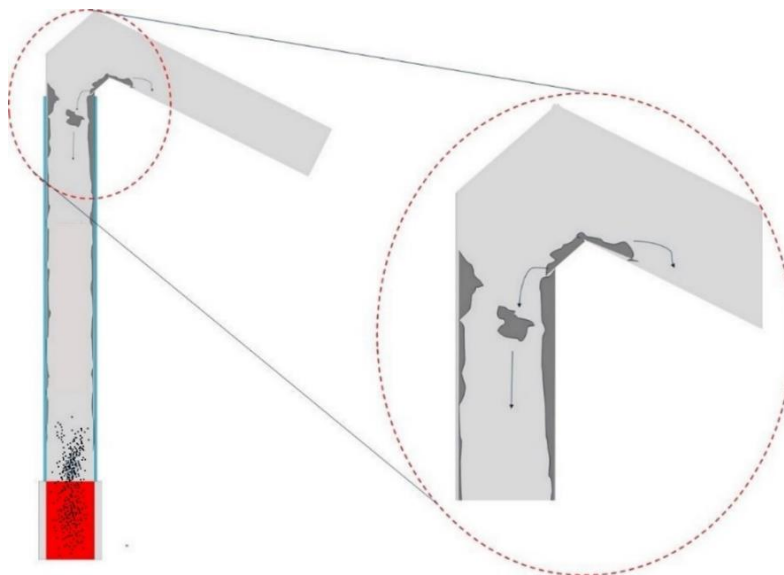


Figure 1-19. The old design of flue gas duct – solid layer build-up issue

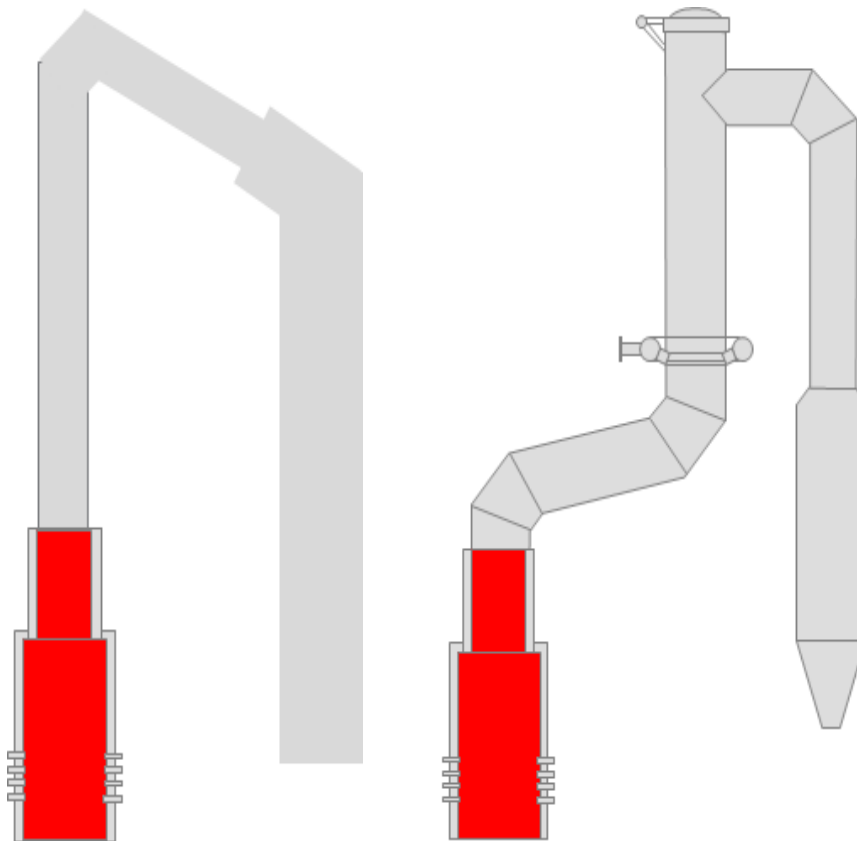


Figure 1-20. Old (left) and new (right) design of the flue gas duct

Even though extensive operational improvements have been achieved using the modified system, other problems persist. The dust carryover remains high. It was 10% in the pilot-scale plant, and in the demo-scale facility, it is estimated to be at 1% concerning the ore injection in CCF.

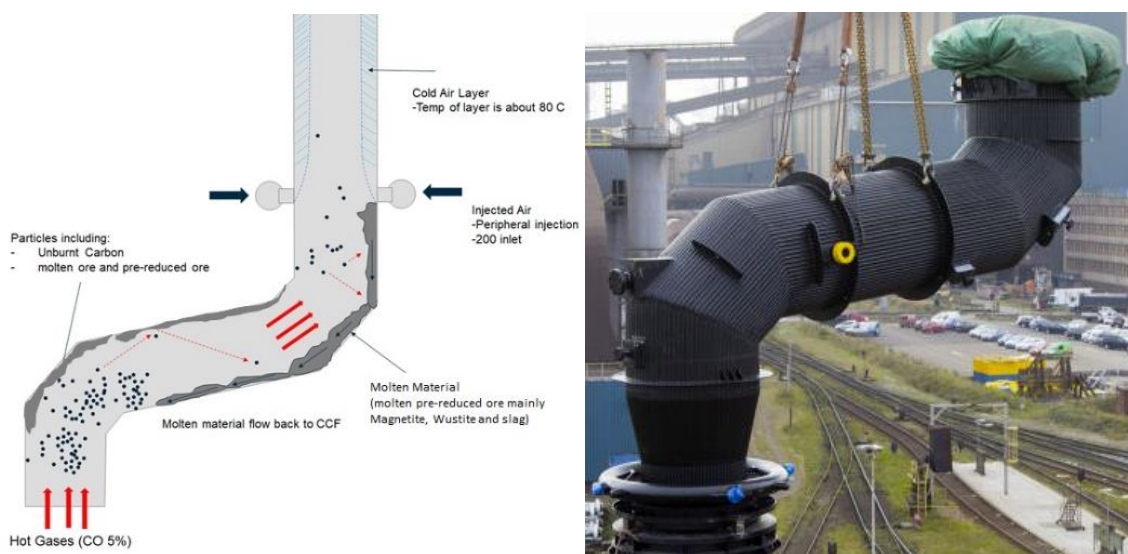


Figure 1-21. Illustration of the current reflux chamber installation (obtained from TATA Steel Ijmuiden R&D)

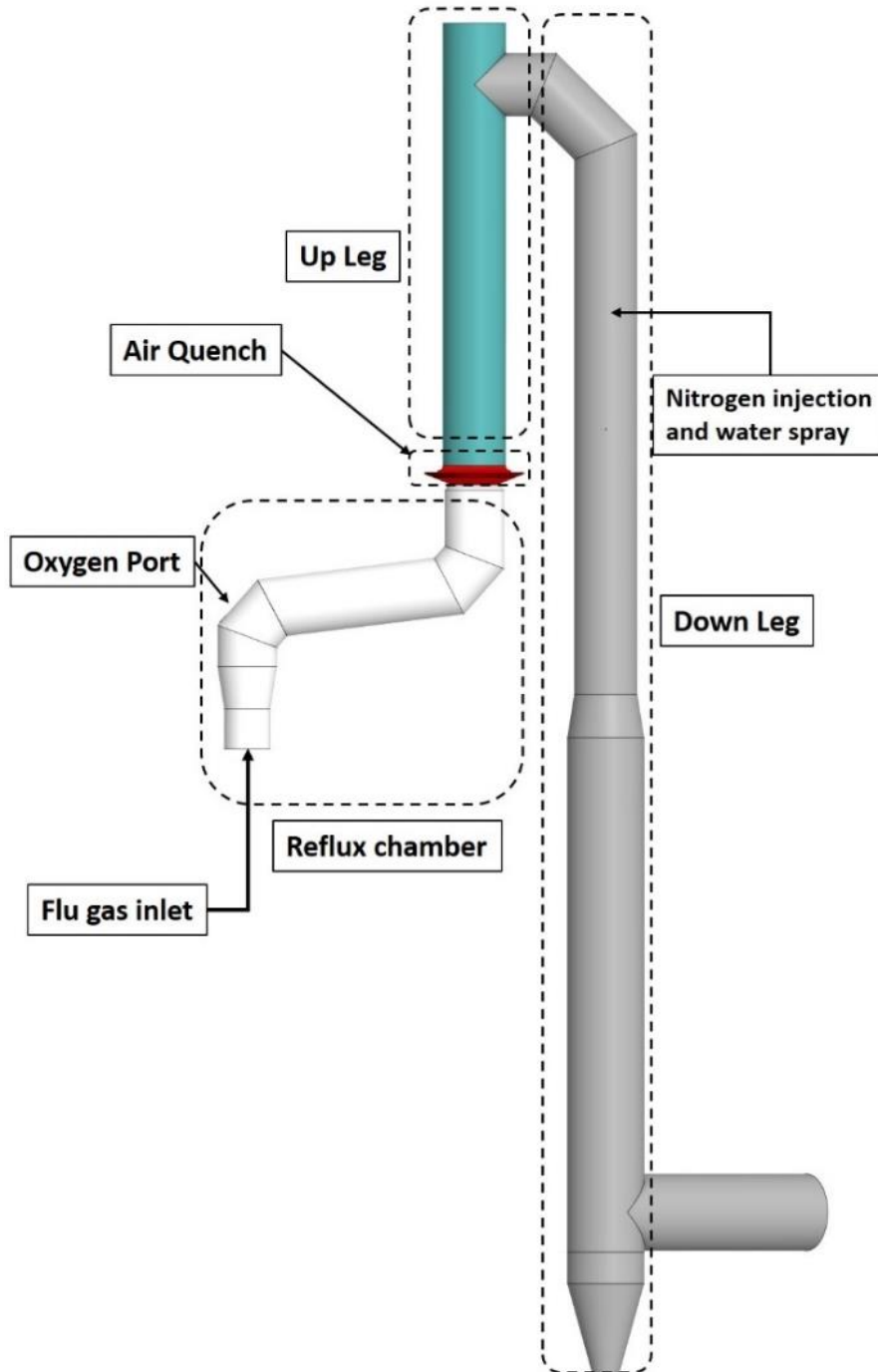


Figure 1-22. Current off-gas system installation with main components

### 1.6.4. Air Quench

Above the reflux chamber, air is injected through multiple ports, creating a layer of cold air in the up-leg section. The immediate purpose of this section is to rapidly quench the flue gas, which is still at a high temperature, as shown in Figure 1-23.

From the figure, the formation of the cold layer near the wall is clearly visible.

This will serve two main purposes:

1. Cooling the flue gas to reach an appropriate temperature for the cleaning process
2. Preventing the accumulation of molten pre-reduced iron ore particles (escaped from CCF and then the Reflux chamber) by freezing them.

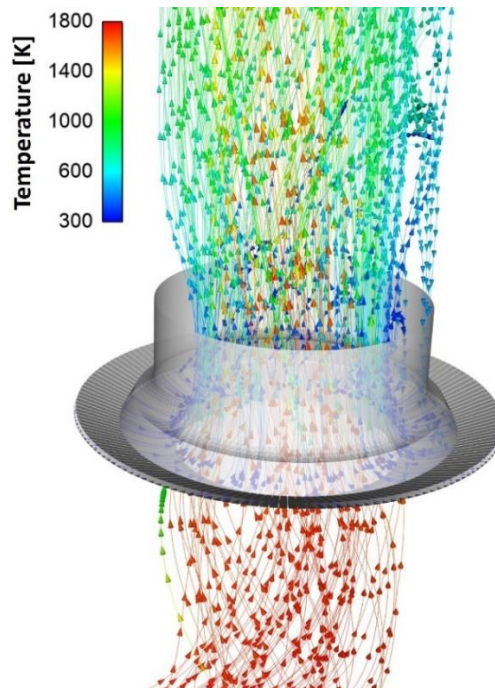


Figure 1-23. Flue gas streamlines colored by temperature (obtained from CFD calculations in this study)

### 1.6.5. Water quench

In the down-leg section, further temperature reduction is achieved by evaporative cooling. Three tilted atomizers are installed, spraying the cooling water via nitrogen as a carrier gas. In the current installation, it is possible to cool down the flue gas by at least 100 °C. Since the temperature of the flue gas fluctuates, the atomizers are active only in cases where a high post-combustion ratio in the CCF is achieved, leading to a significant increase in the flue gas temperature.

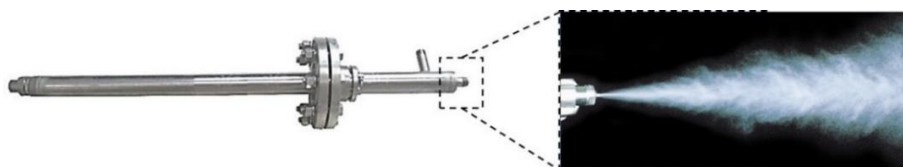


Figure 1-24. Air blast atomizer of water



### 1.6.6. Off-gas system walls

The walls of the off-gas system are made of welded steel pipes in circular patterns, forming a cooling jacket, as shown in Figure 1-25. Cooling water flows through the annular pipes to maintain proper wall temperature during the operation.

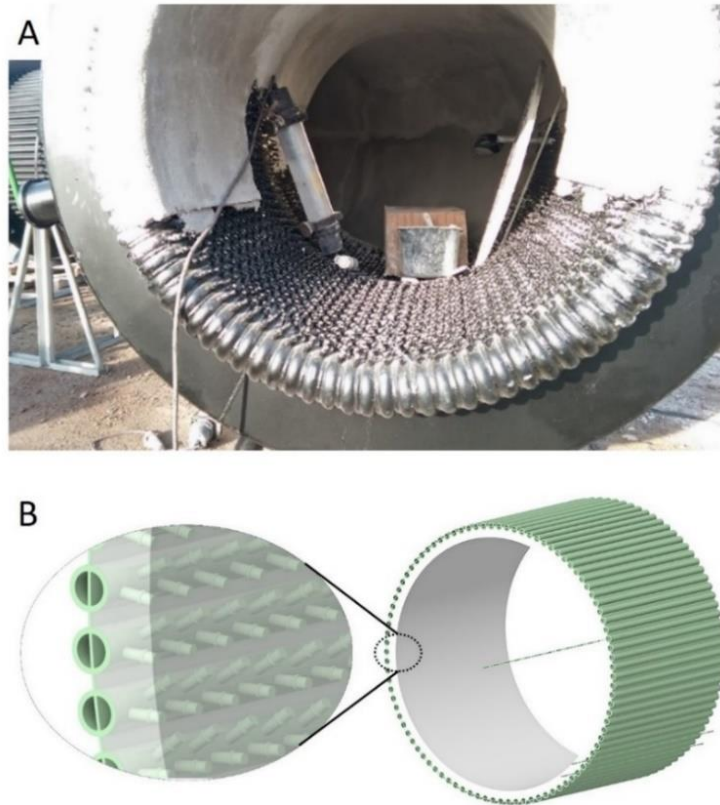


Figure 1-25. Reflux chamber cooling jacket and fresh refractory layer (obtained from TATA Steel Ijmuiden R&D)

This section of the off-gas system necessitates special wall treatment because of the extremely high temperatures at the inlet and inside the reflux chamber. A refractory layer with very low thermal conductivity is applied on top of the cooling pipes to serve as an insulator. Above the reflux chamber, the cooling pipes remain exposed without anchors or refractory coating.

To firmly hold refractory material on the cooling pipes, rows of anchors are placed on each pipe, as shown in Figure 1-26. The fresh refractory layer has an initial thickness of 1 cm above the anchor tips. Consequently, the wall of the reflux chamber can be considered a composite material consisting of refractory and aligned steel

rods. This combination can influence the thermal and physical properties of the wall, including thermal conductivity, specific heat capacity, and density.

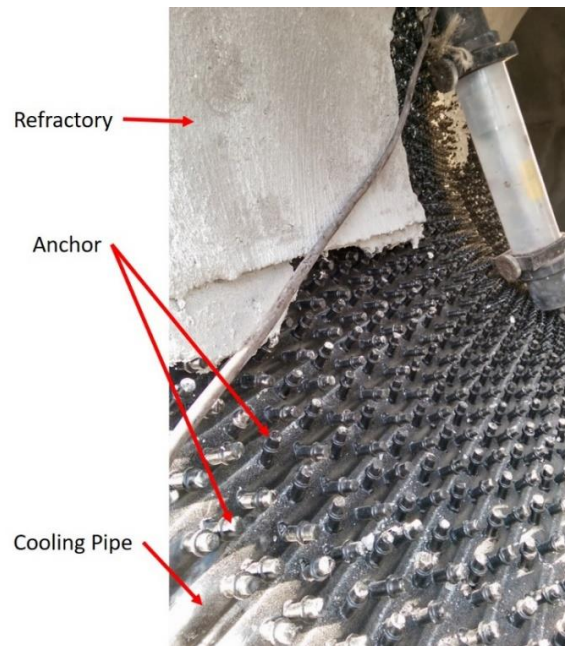


Figure 1-26. Reflux chamber cooling jacket and fresh refractory layer (obtained from TATA Steel Ijmuiden R&D)

The harsh conditions within the reflux chamber, characterized by complex chemical attacks, thermo-mechanical loads, and temperature fluctuations during operation, can result in the refractory's irreversible structural responses, including cracking, crushing, and gradual material loss.

Over the long term, the refractory thickness diminishes due to erosion and thermal stresses. Additionally, escaped molten iron ore particles from the Cyclone Converter Furnace (CCF) accumulate and adhere to certain parts of the refractory, complicating the performance of the reflux chamber wall in comparison to the rest of the off-gas system.

## 1.7. ReclaMet Project Description – Zinc Recovery Concept

Zinc has always posed challenges in blast furnace operations and can significantly disrupt the entire process. It can enter the blast furnace through various pathways. Zinc can enter blast furnace as a constituent of the raw material charge in the form

of oxides ( $\text{ZnO}$ ), ferrite ( $\text{ZnFe}_2\text{O}_4$ ), silicates ( $\text{Zn}_2\text{SiO}_4$ ), and sulfide ( $\text{ZnS}$ ) [24]. However, the primary source of zinc in the blast furnace comes from recycled materials introduced through the use of cold-bonded briquettes and the injection of blast furnace dust [35]. In the latter case, the recycling of briquettes and the injection of dust accounted for 61% and 14% of the total zinc load, respectively [25]. The zinc compounds that enter the blast furnace via the top-charged materials descend and react with the reducing gas at temperatures exceeding  $1000^\circ\text{C}$ , forming elemental zinc. As zinc has a boiling point of  $907^\circ\text{C}$ , the reduced zinc is vaporized and ascends with the gas to the colder parts of the blast furnace, where reoxidation and condensation on the ferrous burden and coke occur [24,25]. Part of the condensed oxidic zinc phases leaves the blast furnace via the top gas, whereas the remaining amount descends with the burden. This continuous process of reduction, vaporization, condensation, and oxidation creates a cyclical pattern, as illustrated in Figure 1-27.

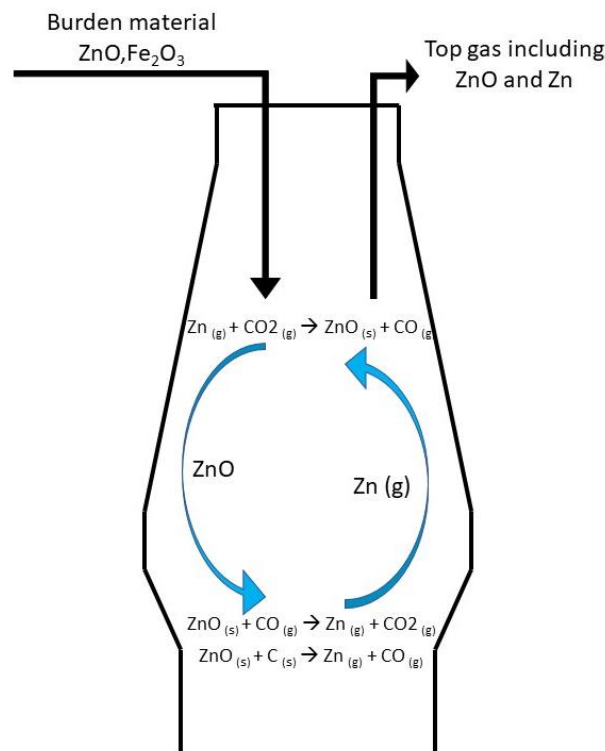


Figure 1-27. Simplified zinc circulation inside blast furnace

The formation of the zinc cycle prevents the uniform distribution of gases and adversely affects the performance of the blast furnace process [24]. It can cause the deposition of extremely fine particles on large surfaces, reducing the life of the blast furnace and weakening the quality of the pig iron product. The accumulation of fine

particles could also block the gas pipelines. It may also diminish the quality of coke after the reaction. More importantly, zinc vapor penetrates the lining of the furnace and causes severe damage to the refractories and linings [26].

Based on the HIsarna plant data, except for minor depositions on the wall surfaces, zinc cycling is not an issue in the HIsarna main reactor, making it an interesting process to recover zinc from the injected zinc-bearing material.

During the fourth HIsarna campaign in 2014, fully funded by the industrial project partners, a test was done where dust containing zinc was injected into the HIsarna process together with iron ore (into CCF). This dust is mainly made up of iron oxides but also contains up to 5 wt% of zinc. During these tests, it was demonstrated that it was possible to concentrate Zn into the HIsarna process dust up to 16%, as shown in Figure 1-28.

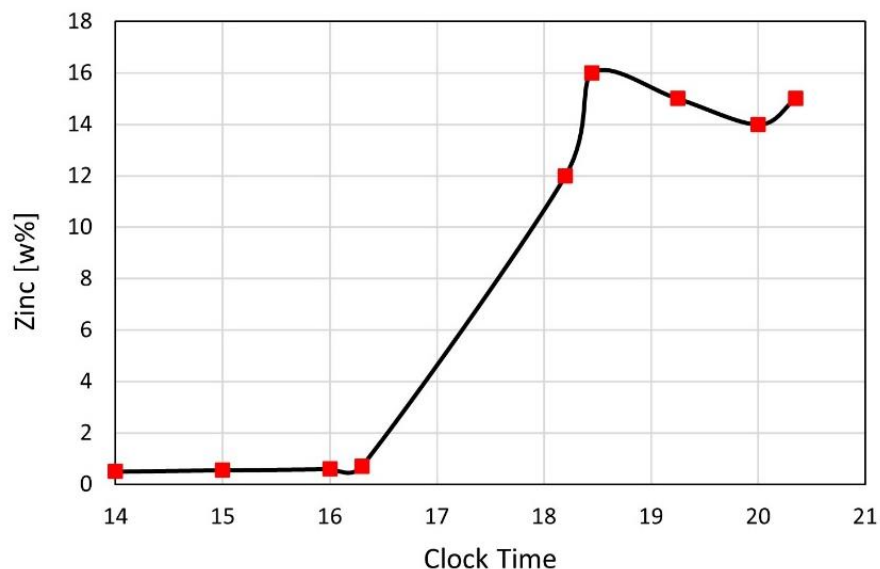


Figure 1-28. Result of Zn enrichment of the HIsarna flue dust after zinc-containing dust into CCF (obtained from TATA Steel Ijmuiden R&D)

However, during this test, injecting a small amount of this dust for a short period was possible. This means that the achieved zinc enrichment was limited, but it offered the prospect of achieving much higher levels of Zn in the dust.

This experience triggered an idea within Tata Steel R&D. “*What if we could inject other forms of zinc-bearing material, such as galvanized steel scrap?*”.

The idea is to inject steel scrap into the SRV bath (pouring on top of the slag), as shown in Figure 1-29. The scrap particles will hit the slag surface, increasing their

temperature. The zinc content of the particles, which is applied as a coating, immediately evaporates and is carried away by the flue gas from the surface of the slag. In the meantime, the scrap particles fall into the slag and are warmed up, and ultimately melt down in a carburized molten iron. After oxidation, the evaporated zinc will travel upward and eventually be concentrated in the off-gas dust.

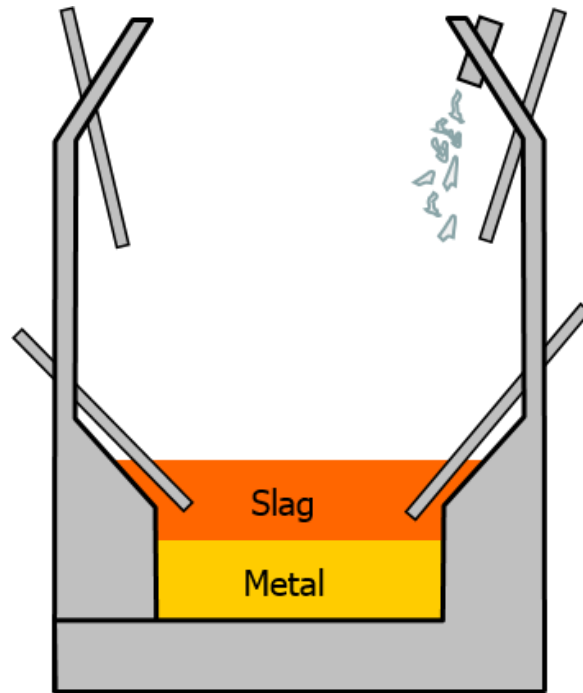


Figure 1-29. Scrap injection into SRV slag

Therefore, the HIsarna process can technically separate zinc from the steel and concentrate the zinc in the process dust. The zinc-containing dust can serve as an alternative raw material for zinc smelters, while iron is used as liquid hot metal. Consequently, the processing costs will not only pertain to the recovered dust but also to the hot metal product, rendering the processing economically attractive.

In theory, the HIsarna process has the capacity to utilize steel scrap for up to 50% of its input, effectively doubling the maximum usage seen in current integrated steel facilities. This implies that on a steelmaking site similar in size to Tata Steel IJmuiden, approximately 650 kton/year of galvanized scrap could be processed. Additionally, this estimate does not take into account other zinc-bearing materials, such as DRI briquets, briquettes from zinc-bearing residues, direct injection of zinc-bearing dust, zinc-bearing sludge, and goethite, all of which have demonstrated significant potential for recovering their zinc content through the HIsarna route.

The current Ph.D. research is part of a more comprehensive project called "Reclamet". The primary objective of the Reclamet project is to explore the feasibility of recycling materials containing zinc by introducing various secondary zinc-bearing feeds (residues and solid waste) into the HIsarna process. The ultimate goal is to concentrate the evaporated zinc from the injected material into the process dust, which can then serve as raw materials for zinc recovery in zinc smelters.

This Ph.D. research project encompasses work packages 4 and 5, focusing primarily on the development of reliable computational fluid dynamics (CFD) and thermodynamic models. The primary objective is to predict the behaviour of the off-gas system and investigate the feasibility and efficiency of zinc recovery. The main emphasis is on recovering evaporated zinc in the form of free zinc oxide (ZnO), the preferred zinc-containing compound that can be directly utilized in zinc smelting facilities. However, a challenge in zinc recovery within the HIsarna process lies in the off-gas system, where local temperatures are low and oxidants and iron oxide are abundant. These conditions create a favourable environment for the formation of zinc vapor into zinc ferrite ( $\text{ZnFe}_2\text{O}_4$ ) rather than free ZnO. The formation of ferrite necessitates an additional pre-processing step (acid leaching) before being introduced into the zinc smelting unit, resulting in additional costs and making ferrite formation less desirable.

Hence, the development of CFD models is imperative for accurately predicting the gas and dust behaviour within the off-gas system. Using a validated model, it becomes feasible to conduct a parametric study aimed at proposing optimized operational and geometrical modifications to minimize the formation of zinc ferrite.

Another important aim of the project is to reduce the dust carryover from the ore injection in CCF. This reduction will have a direct impact on decreasing ferrite formation and potential economic losses due to the loss of ore particles as raw materials during the main smelting process.

## **1.8. Outline of the thesis**

The research activities of the thesis could be divided into three parts (excluding the introduction and conclusion), as shown in the sketch of Figure 1-30. After a brief discussion and introduction on the HIsarna process in the current chapter (Chapter 1), Part 1 of the thesis begins with Chapter 2.



A comprehensive CFD model is developed for the whole off-gas system in **Chapter 2**, using the detailed reaction mechanism and kinetic data for post-combustion of a CO-H<sub>2</sub> mixture and carbon particles. The wall modelling approach plays a vital role in developing a reliable CFD model that can be later used for scaling-up purposes and redesigning the cooling walls and refractories. Therefore, the FEM analysis is performed to obtain the thermal conductivity of the composite wall of the refractory and embedded anchors. The final model is set up using the calculated thermal conductivity for the average measured thickness of the reflux chamber refractory.

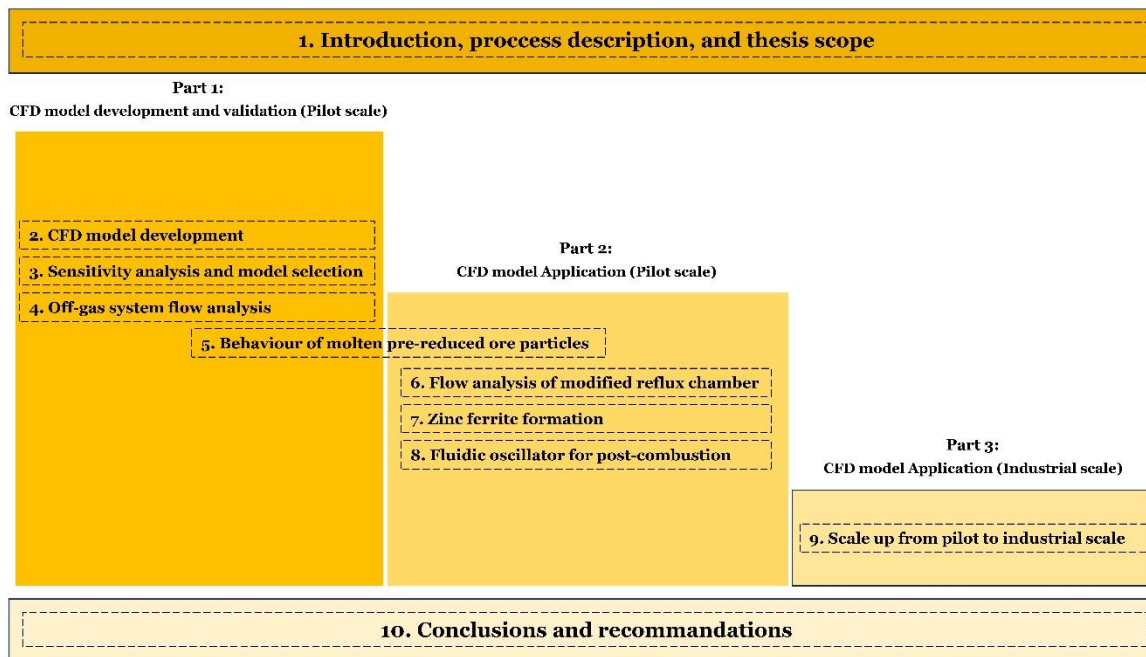


Figure 1-30. Thesis scope and division – different colors represent different parts of the thesis

A detailed discussion and a guideline regarding sub-model selection for high-temperature reactive systems are discussed in **Chapter 3**, and the effects of turbulence, particle dispersion, turbulence-chemistry interaction, chemical kinetic mechanism, etc., are investigated. Based on the analysis, the eddy dissipation concept with a detailed kinetic mechanism and discrete ordinate radiation model leads to accurate predictions that agree with measured data.

In **Chapter 4**, using the developed and validated final model, a detailed parametric study is performed to see the effect of carbon particle reaction and water injection on the temperature, composition profile, and heat losses in the off-gas cooling system. Ultimately, the possibility of oxygen supply reduction for post-combustion is investigated. It is concluded that it is possible to reduce the oxygen injection up to

50% as the temperature remains high to burn the unwanted species above the reflux chamber.

Part 2 of the thesis shifts the thesis focus to the practical application of the developed CFD model for process optimization and modifications. The behavior of molten pre-reduced ore particles is investigated in **Chapter 5**. The walls of the reflux chamber act as a capturing surface on which partially molten ore particles are trapped. This will reduce the out-flow particles and lower the off-gas system's ore loss. In the same chapter, a geometrical modification of the reflux chamber is proposed to increase the particle-capturing efficiency. This modification could lead to a 20% lower particle loss in the off-gas system. In **Chapter 6**, the same flow analysis using the validated CFD model is performed for the modified geometry to see the proposed modification's effect on the off-gas system's flow behavior. It is concluded that the modified geometry can also lead to a higher conversion of unwanted species inside the reflux chamber.

In **Chapter 7**, the formation of zinc ferrite for both original and modified geometries of the reflux chamber is investigated using thermodynamic and CFD tools. According to thermodynamic analysis, the formation of zinc ferrite could be limited by increasing the temperature and reducing oxygen content in the flow. The modified geometry provides a larger space (therefore higher residence time) with an ideal operating condition for converting zinc vapor into zinc oxide (the desired product).

**Chapter 8** investigates the possibility of utilizing the fluidic oscillator to replace the static oxygen injector. A detailed CFD model is set up, and according to the predictions, the designed fluidic oscillator can increase the spread of oxygen and turbulent intensity of fuel-oxidant, thus, the mixing rate within the reflux chamber. Ultimately, it is possible to increase the combustion efficiency and remove the CO-H<sub>2</sub> mixture in a shorter length of the reflux chamber.

In **Chapter 9** (Part 3), a CFD-assisted scale-up from pilot to industrial scale is performed, and a better design for the reflux chamber and detailed refractory wall design is proposed. Ultimately, a brief conclusion and outlook of this thesis are presented in **Chapter 10**.

## References

- [1] R.B. Gordon, D.J. Killick, *Adaptation of Technology to Culture and Environment: Bloomery Iron Smelting in America and Africa*, *Technology and Culture*. 34 (1993) 243–270. <https://doi.org/10.2307/3106536>.
- [2] J. Adetunji, *Why did Tutankhamun have a dagger made from a meteorite?*, *The Conversation*. (2016). <https://theconversation.com/why-did-tutankhamun-have-a-dagger-made-from-a-meteorite-60408> (accessed April 13, 2022).
- [3] B. Boëthius, *A history of iron-making*, *Scandinavian Economic History Review*. 4 (1956) 82–94. <https://doi.org/10.1080/03585522.1956.10411484>.
- [4] *Shang and Zhou Dynasties: The Bronze Age of China.*, Department of Asian Art. n Heilbrunn Timeline of Art History. New York: The Metropolitan Museum of Art. (2004). [https://www.metmuseum.org/toah/hd/shzh/hd\\_shzh.htm](https://www.metmuseum.org/toah/hd/shzh/hd_shzh.htm).
- [5] G. De Young, *Metallurgy in Egypt BT - Encyclopaedia of the History of Science, Technology, and Medicine in Non-Western Cultures*, in: H. Selin (Ed.), Springer Netherlands, Dordrecht, 2008: pp. 1634–1636. [https://doi.org/10.1007/978-1-4020-4425-0\\_9274](https://doi.org/10.1007/978-1-4020-4425-0_9274).
- [6] D. Larreina-Garcia, Y. Li, Y. Liu, M. Martínón-Torres, *Bloomery iron smelting in the Daye County (Hubei): Technological traditions in Qing China*, *Archaeological Research in Asia*. 16 (2018) 148–165. <https://doi.org/https://doi.org/10.1016/j.ara.2018.10.001>.
- [7] Bloom and bloomeries, (n.d.). [https://www.tf.uni-kiel.de/matwis/amat/iss/kap\\_a/illustr/ia\\_2\\_4.html](https://www.tf.uni-kiel.de/matwis/amat/iss/kap_a/illustr/ia_2_4.html) (accessed April 16, 2022).
- [8] D. Staley, *Iron in New York*, The University of the State of New York, 2018.
- [9] R.F. Allen, J.C. Dawson, M.F. Glenn, R.B. Gordon, D.J. Killick, R.W. Ward, *An Archeological Survey of Bloomery Forges in the Adirondacks*, *IA. The Journal of the Society for Industrial Archeology*. 16 (1990) 3–20.
- [10] H.Y. Sohn, *Energy Consumption and CO<sub>2</sub> Emissions in Iron-making and Development of a Novel Flash Technology*, *Metals*. 10 (2020). <https://doi.org/10.3390/met10010054>.
- [11] A. Hasanbeigi, M. Arens, L. Price, *Alternative emerging iron-making technologies for energy-efficiency and carbon dioxide emissions reduction: A technical review*, *Renewable and Sustainable Energy Reviews*. 33 (2014) 645–658. <https://doi.org/https://doi.org/10.1016/j.rser.2014.02.031>.
- [12] Y. Yang, K. Raipala, L. Holappa, *Chapter 1.1 - Iron-making*, in: S.B.T.-T. on P.M. Seetharaman (Ed.), Elsevier, Boston, 2014: pp. 2–88. <https://doi.org/https://doi.org/10.1016/B978-0-08-096988-6.00017-1>.
- [13] B.G. Awty, C. Whittick, *The lordship of Canterbury, iron-founding at Buxted, and the continental antecedents of cannon-founding in the Weald.*, *Archaeology Data Service*, 2004. <https://doi.org/10.5284/1085896>.
- [14] S. Freund, M. Abarr, J.D. McTigue, K.L. Frick, A. Mathur, D. Reindl, A. Van Asselt, G. Casubolo, *Chapter 3 - Thermal energy storage*, in: K. Brun, T. Allison, R.B.T.-T. Dennis Mechanical, and Hybrid Chemical Energy Storage Systems (Eds.), Academic Press, 2021: pp. 65–137. <https://doi.org/https://doi.org/10.1016/B978-0-12-819892-6.00003-4>.
- [15] No Title, (n.d.). <https://lithgow-tourism.com/blasthist.htm> (accessed April 16, 2022).
- [16] IEA, *Iron and Steel Technology Roadmap*, (n.d.). <https://www.iea.org/reports/iron-and-steel-technologyroadmap> (accessed October 19, 2021).
- [17] worldsteel, *press release*, (n.d.). <https://www.worldsteel.org/media-centre/press-releases/2021/Global-crude-steeloutput-decreases-by-0.9--in-2020.html> (accessed October 19, 2021).

- [18] climate policy, (n.d.). <https://www.worldsteel.org/publications/position-papers/climate-change-policy-paper.html> (accessed October 19, 2021).
- [19] Y. Lin, H. Yang, L. Ma, Z. Li, W. Ni, Low-Carbon Development for the Iron and Steel Industry in China and the World: Status Quo, Future Vision, and Key Actions, *Sustainability* . 13 (2021). <https://doi.org/10.3390/su132212548>.
- [20] C. Stănășilă, C. Nicolae, O. Stănășilă, R. Petrache, Alternative iron making technologies, *Metalurgia International*. 14 (2009).
- [21] L. Greene, Iron-making Process Alternative Screening Study, Volume 1, (2005). <https://doi.org/10.2172/885549>.
- [22] J. de Beer, E. Worrell, K. Blok, Future Technologies For Energy-Efficient Iron And Steel Making, *Annual Review of Energy and the Environment*. 23 (1998) 123–205. <https://doi.org/10.1146/annurev.energy.23.1.123>.
- [23] Development of a Low CO<sub>2</sub> Iron and Steel-making Integrated Process Route for a Sustainable European Steel Industry, <https://cordis.europa.eu/project/id/654013> (access: May 2020).
- [24] D.E. Esezobor, S.A. Balogun, Zinc accumulation during recycling of iron oxide wastes in the blast furnace, *Ironmaking & Steelmaking*. 33 (2006) 419–425. <https://doi.org/10.1179/174328106X114020>.
- [25] A. Andersson, Recycling of Blast Furnace Sludge within the Integrated Steel Plant : Potential for Complete Recycling and Influence on Operation, Luleå University of Technology, Minerals and Metallurgical Engineering, 2019.
- [26] S. Mustafa, L. Luo, B.-T. Zheng, C.-X. Wei, N. Christophe, Effect of Lead and Zinc Impurities in Iron-making and the Corresponding Removal Methods: A Review, *Metals (Basel)*. 11 (2021). <https://doi.org/10.3390/met11030407>.

# Chapter 2

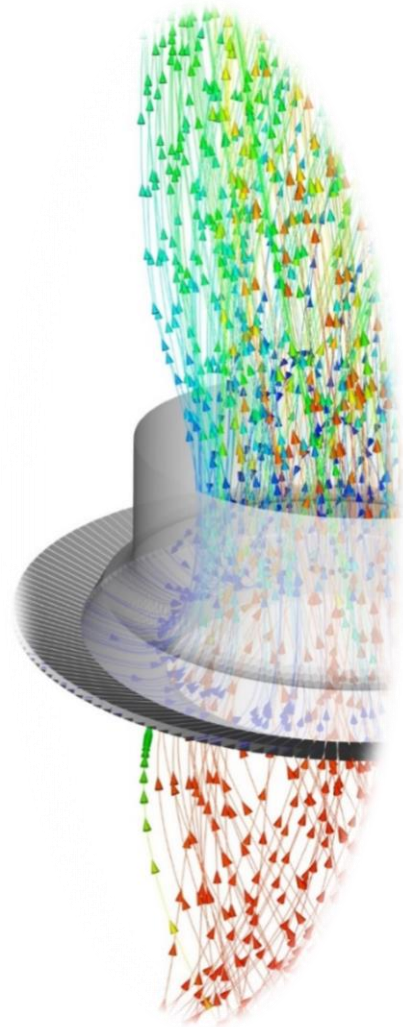
## CFD MODEL DEVELOPMENT

**This chapter is based on the following papers:**

Ashkan Hosseini, Vinod Dhiman, Koen Meijer, Christiaan Zeilstra, Johannes Hage, Tim Peeters, Erik Offerman & Yongxiang Yang, CFD modelling of the off-gas system of HIsarna ironmaking process. Part 1: model development using detailed reaction mechanism for post-combustion of CO-H<sub>2</sub> mixture and carbon particles, *Ironmaking & Steelmaking* (2022), 49:8, 828-844, DOI: <https://doi.org/10.1080/03019233.2022.2062929>.

A. Hosseini, R. Calis, D. van der Plas, P. Put, J. Agema, K. Meijer, J.L.T. Hage, E. Offerman, Y. Yang, *Computational Fluid Dynamics Modelling of HIsarna Off-Gas System—Wall Modelling and Heat Loss Prediction*. *Processes* (2023), 11, 3082, DOI: <https://doi.org/10.3390/pr11113082>.

**In this chapter, a base CFD model for the HIsarna off-gas system is developed, tuned, and validated with measured plant data. All boundary conditions are taken from real operating data. However, during the initial modeling phase, it was evident that the calculated temperature and composition profiles did not align with the measured values. The discrepancy was traced back to the thermo-physical properties assigned to the wall boundary conditions. The walls are modelled using the shell conduction approach. The reflux chamber walls are made of two layers of refractory and steel layer (cooling pipe thickness). During initial analysis, the refractory layer properties were assigned as pure refractory material with very low thermal conductivity. However, the refractory layer contains embedded steel anchors, which increase the thermal conductivity of the refractory layer. To assess the effective thermal conductivity of the refractory layer, the wall is treated as a composite material, and both the Effective Medium Approximation (EMA) and Finite Element Method (FEM) approaches are employed to calculate this value. By incorporating the newly determined thermal conductivity, a significant improvement is realized, resulting in calculated profiles and heat loss that closely match their measured counterparts with minimal error.**



## 2.1. Introduction

Computational Fluid Dynamics (CFD) is becoming an important tool for understanding fluid flow-related phenomena in iron and steelmaking processes. Using CFD tools, it is possible to simulate three-dimensional, transient/steady state, single/multiphase flows, including particle or bubble interaction, phase changes, electromagnetic forces in fluid flows, and chemical reactions such as reduction and oxidation.

In the past, practical experience with operations and simplified yet fundamental knowledge of chemistry and materials were the primary sources of insight into processes. However, today, the use of CFD modeling allows us to gain valuable insights into flow phenomena that are either challenging or impossible to measure and experimentally investigate. These insights enhance the transparency of the processes and aid in the development of new products. Currently, CFD techniques find wide application across all scales, from laboratory to industrial settings, supporting new developments and troubleshooting operational issues.

Despite the extensive use of these techniques, certain limitations still require further improvement. One significant concern is the computational costs associated with CFD calculations, which often demand extended computational time to reach a stable final solution, especially in the context of transient large-scale applications. In recent years, efforts have been made to mitigate this issue by developing high-performance computing capabilities; however, it is still an ongoing challenge.

Another issue, which is less dependent on computer power, pertains to the available knowledge and the ability to describe the physics of the relevant phenomena. Notably, the predictive capacity of the models is intrinsically tied to the depth of physical understanding upon which these models are constructed. As we move towards addressing more complex industrial challenges, the development of robust and predictive models is expected to pose a significant challenge in the years to come.

Metallurgical applications of CFD are widespread and have been used to describe processes such as direct reduction and electric arc furnaces [1–5], blast furnaces [6–11], other novel ironmaking reactors, converters [12–16], dust collecting facilities and continuous casting [17–23].



One important metallurgical application of CFD tools is to design and improve off-gas systems [24,25] and post-combustion chambers [26–29].

In the steelmaking processes, CO and H<sub>2</sub> are emitted through iron oxide reduction (partial or full) and incomplete carbon oxidation reactions. The emitted gases are carried away with the flue gas into the off-gas system [30].

In general, CO in the flue gas is regarded as a pollutant, and H<sub>2</sub> is considered an explosive and hazardous compound. For the following reasons, it is essential to remove both of these species from the flue gas before releasing it into the environment:

- CO is a poisonous gas whose emission might not comply with environmental regulations.
- CO-H<sub>2</sub> mixture usually has a high heating value and is considered a fuel that can be utilized for energy recovery. Therefore, releasing it into the environment is an energy loss.

The most efficient way to remove and recover the energy of the CO-H<sub>2</sub> mixture at high temperatures is through the so-called post-combustion process. Indeed, post-combustion is a process that allows the harnessing of the chemical energy from gaseous mixtures through oxygen injection [30].

One important iron and steelmaking process in which post-combustion plays a vital role is the electric arc furnace (EAF). CO generation rate is approximately 44 kg per ton of produced steel, corresponding to an energy release of 425 MJ through a complete combustion [31].

In the EAF process, the post-combustion is performed at two stages, as shown in Figure 2-1. One is inside the main reactor to combust the CO-H<sub>2</sub> mixture via oxygen injection through injectors and during the scrap melting. This way, the post-combustion can transfer significant potential chemical energy into the steel scrap and liquid metal.

Another stage is to combust the escaped gas mixture from the main reactor inside the off-gas duct to avoid unwanted emissions. Air is sucked into the duct through a so-called “gap” since EAF operates slightly under atmospheric pressure. The post-

combustion is then performed with oxygen after the gap. Several CFD studies on CO-H<sub>2</sub> post-combustion in the EAF process have been conducted [24,27–39].

Tang et al. [31] have performed CFD analysis of the CO post-combustion above the molten pool of the EAF using detailed kinetic data. The study investigated the impact of CO post-combustion and oxygen mass flow rates on the heat transfer efficiency within the EAF furnace.

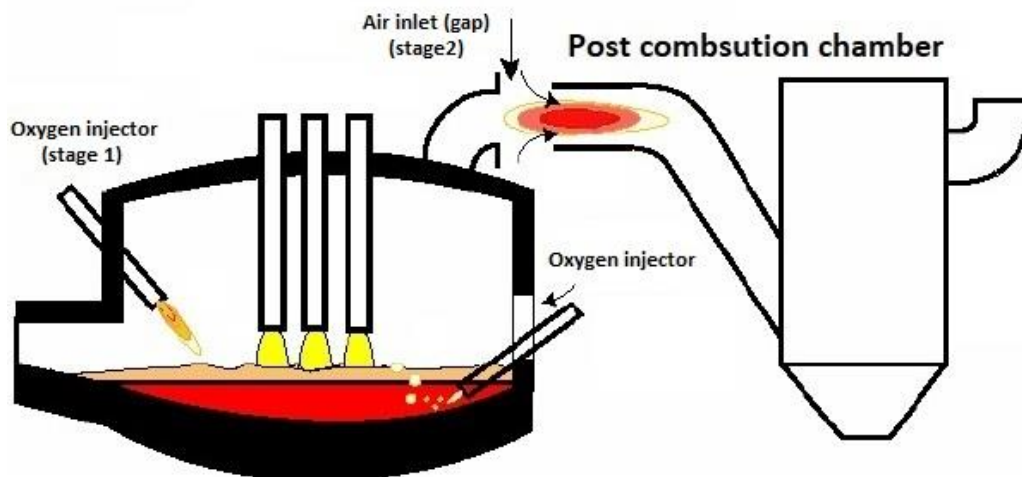


Figure 2-1. EAF main reactor and post-combustion chamber [40]

The results indicate that the CO post-combustion improves the energy efficiency in the EAF. Additionally, the average gas temperature in the EAF has an optimal point when increasing the oxygen mass flow rate. The heat transfer efficiency from gas to the molten bath is also increased with the oxygen mass flow rate.

Arzpeyma et al. [24] have developed a CFD model of the EAF flue gas to investigate the effect of oxygen flow rate on CO conversion, post-combustion ratio, and thermal capacity. They observed an elevated post-combustion ratio when introducing secondary oxygen (via an additional set of injectors inside the reactor) into the primary reactor, which can potentially increase the energy supplied to the molten bath.

Labiscsak et al. [28] have focused on developing a CFD model for an EAF post-combustion chamber to investigate the effect of air gap dimension on the final stage of CO-H<sub>2</sub> removal. According to their findings, when the gap size was set to 30 and 40 cm, a high hydrogen and carbon monoxide conversion rate, leading to complete oxidation, was achieved. Additionally, they noted that the thermal efficiency decreases when the gap size is larger, although the reduction is not substantial.

Consequently, a larger gap is preferred to prevent carbon monoxide and hydrogen from escaping into the environment.

Trivellato et al. [27] performed a similar study to optimize the air gap inlet area for a higher CO-H<sub>2</sub> removal while preserving the thermal efficiency of the post-combustion.

In another interesting study, Tang et al. [29] compared three different post-combustion units for CO-H<sub>2</sub> removal experimentally and numerically. The three units were post-combustion in a horizontal off-gas duct, a water-cooled chamber without an additional energy supply (no gas or air/oxygen injectors), and a chamber with additional energy input. They have performed a parametric study to optimize all investigated designs.

Hot Blast Stove (HBS) is another post-combustion equipment during which the CO-H<sub>2</sub> content of the blast furnace top off-gas is utilized for thermal recovery to pre-heat the blast air (Figure 2-2).

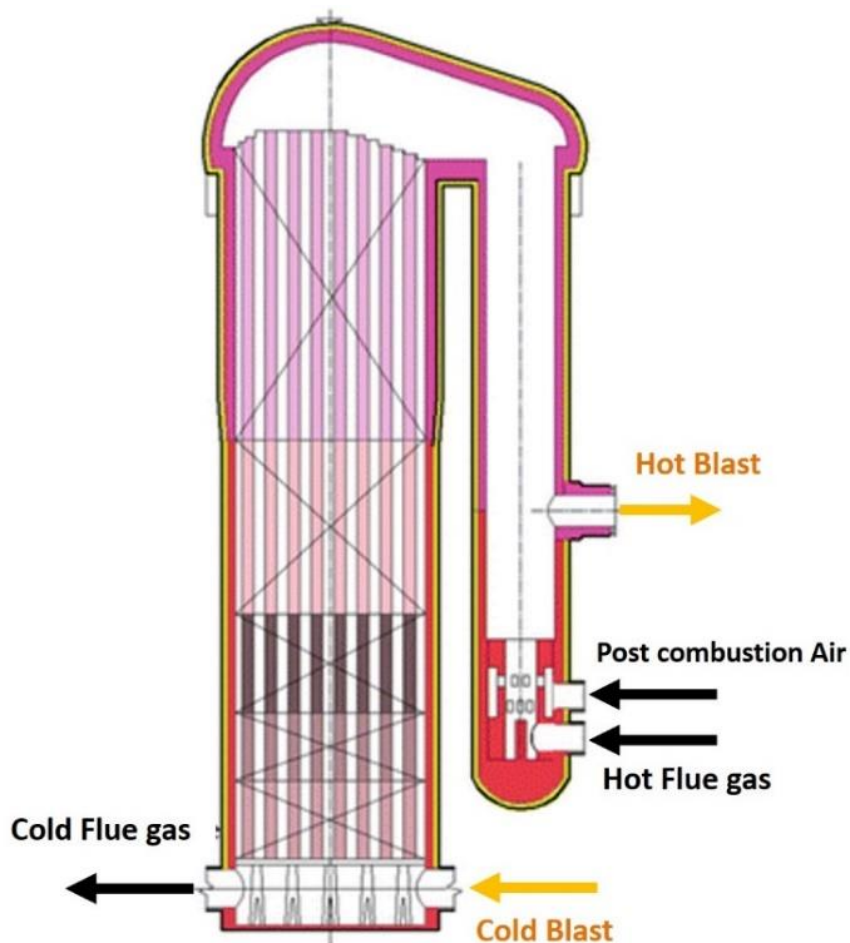


Figure 2-2. Hot Blast Stove design [41]

In fact, HBS is a counter-current regenerative heat exchanger. On one side, the CO-H<sub>2</sub> mixture is burnt with the injected air to provide heat and to increase the air temperature on the cold side of the heat exchanger [41]. The pre-heated air is then fed into the blast furnaces. Utilizing HBS is of utmost importance since it increases the output and quality of the blast furnace, reduces the coke ratio in ironmaking, reduces energy consumption, and enhances production efficiency [37].

Zhang et al. [37] developed a comprehensive CFD model to study the combustion and air supply characteristics of an HBS. Based on their validated model, they proposed geometrical modifications to the traditional design. The simulation results indicated that the improved hot blast stove would perform better than the conventional stove regardless of the maximum temperature of the combustion chamber.

Cuervo-Pinera et al. [39] investigated the removal efficiency of CO and NO formation inside the HBS during the heating period using a validated CFD model. According to their findings, NO formation occurs in the high-temperature zones in the top section of the heat exchanger during the heating period, primarily due to CO combustion.

As mentioned before, in the HIsarna process, the off-gas from the main reactor contains CO, H<sub>2</sub>, and carbon particles, which must be removed for environmental and energy efficiency purposes. This process is quite similar to the EAF post-combustion, for which some studies are mentioned above. In HIsarna's old installation, the geometry and operation of the post-combustion chamber were similar to the EAF post-combustion chamber studied by Zhang et al. [37].

In the old configuration of HIsarna, the flue gas was passed through an incinerator that burns CH<sub>4</sub> to provide enough heat for unwanted species removal. The incinerator needed to be operated within a temperature window to guarantee complete combustion of the off-gases.

Sripriya et al. [25] developed a CFD model to investigate the performance of the old design of the HIsarna off-gas system incinerator to remove unwanted species for different compositions and flow rates of the off-gases from the main reactor. The combustion model predicts a complete burnout of CO, CH<sub>4</sub>, and H<sub>2</sub> when sufficient air/O<sub>2</sub> is injected.

They reported from plant data analysis that achieving high post-combustion in the main reactor results in lower CO (fuel) reaching the incinerator, decreasing upstream temperature. In such cases, the flue gas temperature could potentially drop below the auto-ignition temperature of the gaseous mixture, causing undesirable emissions. They used their model to propose a safer incinerator operation to minimize and mitigate any potential unwanted emissions. After considering various options, they concluded that the safest operational mode involved mixing natural gas with the off-gases from the HIsarna cyclone and injecting pure oxygen through two smaller ports alongside combustion air from other ports. With this configuration, a higher incinerator temperature is ensured.

It is worth noting that the design for post-combustion mentioned above is now considered outdated, as a superior design has been proposed and implemented to address temperature-related issues.

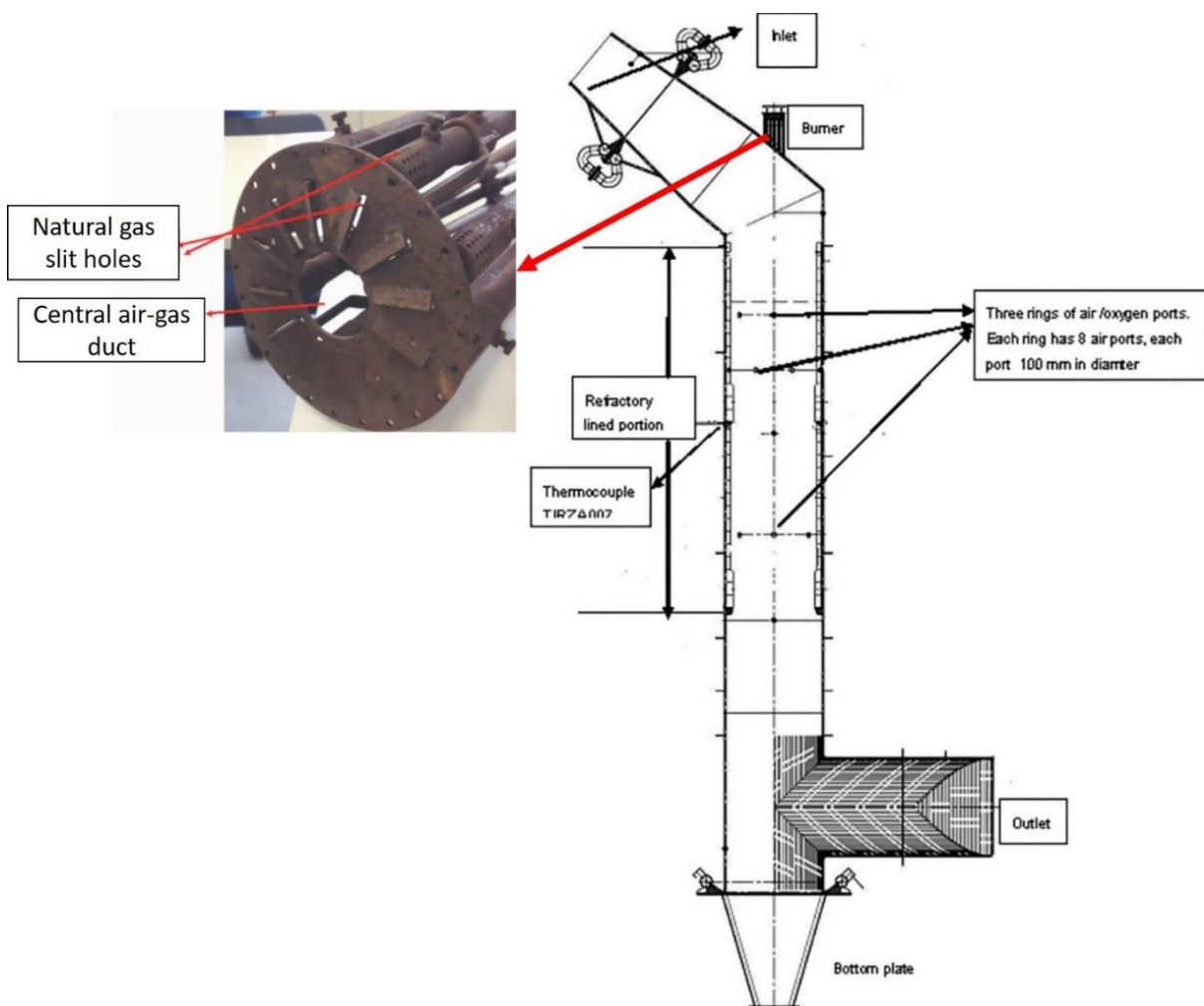


Figure 2-3. HIsarna post-combustion system (old installation) [17]

In the new design, the CO-H<sub>2</sub> and carbon mixture is combusted by oxygen injection immediately after the CCF outlet, where the temperature is high enough to auto-ignite the CO-H<sub>2</sub> mixture (similar to the EAF post-combustion chamber). This way, the gas combustor is eliminated to reduce fuel consumption, and post-combustion is achieved without external fuel consumption. A detailed process description of the off-gas system is already discussed in Chapter 1. The following parts discuss a detailed step-by-step CFD model development and improvement for the current HIsarna off-gas system.

## 2.2. Governing equation for CFD model

In developing the current CFD model, all possible phenomena such as turbulence, radiation, species transport, volumetric reactions with detailed kinetic data, particle flow, gas-solid reactions, and detailed wall modelling are considered.

In the context of CFD modeling, a set of conservation and transport equations is solved to depict various phenomena within the modeled system. The solution of continuity and momentum equations is essential for deriving pressure, velocity, and density fields. Depending on the specific application, additional equations and models may be incorporated.

The equation for conservation of mass, or continuity equation, can be written as follows (all of the parameters' definitions and units can be found in nomenclature):

$$\frac{\partial}{\partial t}(\rho) + \frac{\partial}{\partial x_i}(\rho \bar{u}_i) = 0 \quad (2-1)$$

Conservation of momentum is described by

$$\frac{\partial}{\partial t}(\rho \bar{u}_i) + \frac{\partial}{\partial x_j}(\rho \bar{u}_i \bar{u}_j) = -\frac{\partial p}{\partial x_i} + \frac{\partial}{\partial x_j} \left[ \mu \left( \frac{\partial \bar{u}_i}{\partial x_j} + \frac{\partial \bar{u}_j}{\partial x_i} - \frac{2}{3} \delta_{ij} \frac{\partial \bar{u}_l}{\partial x_l} \right) \right] + \frac{\partial}{\partial x_j}(-\rho \overline{u'_i u'_j}) \quad (2-2)$$

where,  $\frac{\partial \bar{u}_i}{\partial x_i} = \nabla \cdot \bar{u}$ . IM,  $\bar{u} = u - u'$

$$\text{and Reynolds stress } -\rho \overline{u'_i u'_j} = -\rho \begin{bmatrix} \overline{u'_x u'_x} & \overline{u'_x u'_y} & \overline{u'_x u'_z} \\ \overline{u'_y u'_x} & \overline{u'_y u'_y} & \overline{u'_y u'_z} \\ \overline{u'_z u'_x} & \overline{u'_z u'_y} & \overline{u'_z u'_z} \end{bmatrix} \quad (2-3)$$

Reynolds stresses are related to the mean velocity gradients through the Boussinesq hypothesis as follows:



$$-\rho \overline{u'_i u'_j} = \mu_t \left( \frac{\partial \bar{u}_i}{\partial x_j} + \frac{\partial \bar{u}_j}{\partial x_i} \right) - \frac{2}{3} \left( \rho k + \mu_t \frac{\partial \bar{u}_i}{\partial x_i} \right) \delta_{ij} \quad (2-4)$$

### **Turbulence models**

The flow inside the current off-gas system is turbulent, with a high Reynolds number of about 51000. To account for the effect of turbulence, two different models, namely k- $\epsilon$  and SST k- $\omega$  (shear stress transport) model, are widely used for large-scale applications. In this study, the realizable k- $\epsilon$  model is used to formulate turbulent viscosity  $\mu_t$  relation by solving the transport equations for k and  $\epsilon$  variables as below.

$$\frac{\partial}{\partial t} (\rho k) + \frac{\partial}{\partial x_i} (\rho k \bar{u}_i) = \frac{\partial}{\partial x_j} \left[ \left( \mu + \frac{\mu_t}{\sigma_k} \right) \frac{\partial k}{\partial x_j} \right] + G_k + G_b - \rho \epsilon - Y_M + S_k \quad (2-5)$$

$$\frac{\partial}{\partial t} (\rho \epsilon) + \frac{\partial}{\partial x_j} (\rho \epsilon \bar{u}_j) = \frac{\partial}{\partial x_j} \left[ \left( \mu + \frac{\mu_t}{\sigma_\epsilon} \right) \frac{\partial \epsilon}{\partial x_j} \right] + \rho C_1 S \epsilon - \rho C_2 \frac{\epsilon^2}{k + \sqrt{\theta \epsilon}} + C_{1\epsilon} \frac{\epsilon}{k} C_{3\epsilon} G_b + S_\epsilon \quad (2-6)$$

The SST k- $\omega$  model [42,43] is used to formulate  $\mu_t$  relation by solving the conservation equation for k and  $\omega$  variables as below.

$$\frac{\partial}{\partial t} (\rho k) + \frac{\partial}{\partial x_i} (\rho k \bar{u}_i) = \frac{\partial}{\partial x_j} \left[ \Gamma_k \frac{\partial k}{\partial x_j} \right] + G_k - Y_k + S_k \quad (2-7)$$

$$\frac{\partial}{\partial t} (\rho \omega) + \frac{\partial}{\partial x_j} (\rho \omega \bar{u}_j) = \frac{\partial}{\partial x_j} \left[ \Gamma_\omega \frac{\partial \omega}{\partial x_j} \right] + G_\omega - Y_\omega + D_\omega + S_\omega \quad (2-8)$$

$\Gamma$  is effective diffusivities and given as:

$$\Gamma_k = \mu + \frac{\mu_t}{\sigma_k} \quad (2-9)$$

$$\Gamma_\omega = \mu + \frac{\mu_t}{\sigma_\omega} \quad (2-10)$$

$\sigma_k$  and  $\sigma_\omega$  are turbulent Prandtl numbers and, along with  $\mu_t$  are calculated as below:

$$\mu_t = \frac{\rho k}{\omega} \frac{1}{\max \left[ \frac{1}{\alpha^*}, \frac{S_r F_2}{a_1 \omega} \right]} \quad (2-11)$$

$$\sigma_k = \frac{1}{F_1/\sigma_{k,1} + (1-F_1)/\sigma_{k,2}} \quad \sigma_\omega = \frac{1}{F_1/\sigma_{\omega,1} + (1-F_1)/\sigma_{\omega,2}} \quad (2-12)$$

$$F_1 = \tanh(\phi_1^4) \quad F_2 = \tanh(\phi_2^2) \quad (2-13)$$

$$\phi_2 = \max \left[ \frac{\sqrt{k}}{0.09\omega y_{\text{dis}}}, \frac{500\mu}{\omega y_{\text{dis}}^2 \rho} \right] \quad (2-14)$$

$$\phi_1 = \min \left[ \max \left( \frac{\sqrt{k}}{0.09\omega y_{\text{dis}}}, \frac{500\mu}{\omega y_{\text{dis}}^2 \rho} \right), \frac{4\rho k}{\sigma_{\omega,2} D_{\omega}^+ y_{\text{dis}}^2} \right]$$

$$D_{\omega}^+ = \max \left[ 2\rho \frac{1}{\sigma_{\omega,2}\omega} \frac{\partial k}{\partial x_j} \frac{\partial \omega}{\partial x_j}, 10^{-10} \right] \quad (2-15)$$

### ***Energy and radiation models***

The energy equation has the following form:

$$\frac{\partial}{\partial t}(\rho E) + \nabla \cdot (\bar{u}(\rho E + p)) = \nabla \cdot (k_{\text{eff}} \nabla T - \sum_j h_j \vec{J}_j + (\tau_{\text{eff}} \cdot \bar{u})) + S_h \quad (2-16)$$

Given the elevated temperature of the flue gas and the substantial difference between the water-cooled walls and the flue gas, it is imperative to consider the impact of thermal radiation. This consideration necessitates its inclusion in the source term of the energy equation ( $S_h$ ) to ensure accurate heat flux and temperature profile prediction across the off-gas system.

Three different radiation models, Rosseland, P1, and discrete ordinate model (DOM), are mainly used in literature. Among them, the DOM is a comprehensive model which considers the directional nature of the radiation. The DOM considers the Radiative Transport Equation (RTE) in the direction of  $\vec{s}$  as a field equation. Hence, the RTE equation can be rewritten as:

$$\nabla \cdot (I(\vec{r}, \vec{s}) \vec{s}) + (a + \sigma_s) I(\vec{r}, \vec{s}) = a n^2 \frac{\sigma T^4}{\pi} + \frac{\sigma_s}{4\pi} \int_0^{4\pi} I(\vec{r}, \vec{s}') \phi(\vec{s}, \vec{s}') d\Omega' \quad (2-17)$$

The P1 model is a relatively simpler approach for modelling radiative heat transfer in which the radiation flux ( $q_r$ ) is written based on the incident radiation ( $G$ ) as:

$$q_r = -\Gamma_r \nabla G \quad (2-18)$$

$$\Gamma_r = \frac{1}{3(a + \sigma_s) - C\sigma_s} \quad (2-19)$$

the above equation for  $q_r$  is combined with the transport equation for incident radiation to obtain the below equation:

$$\nabla \cdot (\Gamma_r \nabla G) - \alpha G + 4an^2 \sigma T^4 = 0 \quad (2-20)$$

$$-\nabla \cdot \mathbf{q}_r = aG - 4a\sigma T^4 \quad (2-21)$$

Equation (2-21) is basically an expression for radiation flux gradient ( $\nabla \cdot \mathbf{q}_r$ ), which will be included in the energy equation to account for heat sources or sinks due to radiation.

The Rosseland model can be obtained from the same radiation flux equation by assuming incident radiation constant and equal to black body radiation without solving the transport equation:

$$G = 4\sigma n^2 T^4 \quad (2-22)$$

By substituting this equation in (2-20), the equation for radiation flux is obtained and can be included in the energy equation source term:

$$\mathbf{q}_r = -16\sigma \Gamma_r n^2 T^3 \nabla G$$

A composition-dependent absorption coefficient model, known as the weighted-sum-of-gray-gases model (WSGGM), is used instead of constant absorption coefficients for all radiation models. See references [44–47] for more details.

### ***Species transport model and turbulent-chemistry interaction***

The flue gas within the off-gas system consists of various gaseous species, making it a multi-component system. To obtain the local mass fraction for each species ( $Y_i$ ) a convection-diffusion equation known as the species transport equation needs to be solved:

$$\frac{\partial}{\partial t} (\rho Y_i) + \frac{\partial}{\partial x_j} (\rho \bar{U}_j Y_i) = -\nabla \cdot \vec{J}_i + R_i + S_i \quad (2-23)$$

$$\vec{J}_i = -\left(\rho D_{i,m} + \frac{\mu_t}{Sc_t}\right) \nabla Y_i - D_{T,i} \frac{\nabla T}{T} \quad (2-24)$$

In a non-reactive flow, the term  $R_i$  (net source of chemical species due to reaction) and  $S_i$  (net rate of creation by addition from the dispersed phase, such as particles) in the equation are zero, but for reactive flow cases, it will be calculated through turbulent-chemistry interaction models (a.k.a combustion models).

The most basic model is based on the finite rate approach [48], where  $R_i$  is calculated as the sum of the Arrhenius reaction sources over the limited number of reactions that the species participate in:

$$R_i = M_{w,i} \sum_{r=1}^{N_R} \widehat{R}_{i,r} \quad (2-25)$$

For a reversible reaction,  $\widehat{R}_{i,r}$  (the molar rate of creation/destruction of species  $i$  in reaction  $r$ ) is given by:

$$\widehat{R}_{i,r} = \theta (v_{i,r}'' - v_{i,r}') \left( k_{f,r} \prod_{j=1}^N [C_{j,r}]^{\eta_{j,r}'} - k_{b,r} \prod_{j=1}^N [C_{j,r}]^{\eta_{j,r}''} \right) \quad (2-26)$$

$\theta$  represents the net effect of third bodies on the reaction rate. This term is given by

$$\theta = \sum_j^N \gamma_{j,r} C_j \quad (2-27)$$

$k_{f,r}$  is the forward rate constant for  $r^{\text{th}}$  reaction as:

$$k_{f,r} = A_r T^{\beta_r} e^{-E_r/RT} \quad (2-28)$$

$k_{b,r}$  is backward rate constant given as:  $k_{b,r} = \frac{k_{f,r}}{K_r}$

$K_r$  is the equilibrium constant for the  $r^{\text{th}}$  reaction, computed from

$$K_r = \exp \left( \frac{\Delta S_r}{R} - \frac{\Delta H_r}{RT} \right) \left( \frac{P_{atm}}{RT} \right)^{\sum_{i=1}^N (v_{i,r}'' - v_{i,r}')} \quad (2-29)$$

Where  $P_{atm}$  denotes atmospheric pressure (101325 Pa). The term within the exponential function represents the change in Gibbs free energy, and its components are computed as follows:

$$\frac{\Delta S_r}{R} = \sum_{i=1}^N (v_{i,r}'' - v_{i,r}') \frac{S_i}{R} \quad (2-30)$$

$$\frac{\Delta H_r}{R} = \sum_{i=1}^N (v_{i,r}'' - v_{i,r}') \frac{h_i}{RT} \quad (2-31)$$

With the finite rate approach, the  $R_i$  is calculated solely based on the kinetic data, and the effect of turbulence is not taken into account.

There are some approaches to model the behaviour of turbulent reactive flow, namely, eddy dissipation (EDM), finite rate eddy dissipation (FR-EDM), and eddy dissipation concept (EDC) model.

The EDM [49] assumes the chemical reaction is faster than the transport processes. The products are instantaneously formed once the reactants are mixed, and the overall reaction rate is controlled by turbulent mixing. This way, the rate of the reaction can be calculated without considering kinetic data and is solely defined by the turbulent kinetic energy  $k$  and its dissipation rate  $\epsilon$ .

The model assumes that the reaction rate may be related directly to the time required to mix the reactants at the molecular level. In turbulent flows, this mixing time is dominated by the eddy properties. Therefore, the rate is proportional to a mixing time defined by the turbulent kinetic energy ( $k$ ) and the eddy dissipation ( $\epsilon$ ).

$$R_i = \frac{A\epsilon}{k} \min(f_i, v_i) \quad (2-32)$$

Using this model, the properties may be poorly predicted if the ignition is important or when chemical kinetics control the reaction rate. This is indeed the main drawback of this approach.

The EDM can be combined with the FR approach to redeem the drawbacks and consider the effect of kinetics. This combination is usually referred to as the finite rate/eddy dissipation model (FR-EDM). In this approach, two values for  $R_i$  are obtained, one from the FR approach and the other by the EDM, and the slowest reaction rate is employed. The Arrhenius rate acts as a kinetic switch, preventing reaction before ignition. Once the reaction is ignited, the eddy-dissipation rate is generally smaller than the Arrhenius rate, and reactions are mixing limited.

There are still some problems with this approach. For example, the reactions are not initiated in some cases, and artificial heat sources are required for persistent reactions and flame formation. One solution to this issue would be driving the species compositions to their equilibrium state and calculating  $R_i$  as:

$$R_i = \rho \frac{Y_i^{\text{eq}} - Y_i}{\tau_{\text{char}}} \quad (2-33)$$

Superscript *eq* denotes chemical equilibrium, and  $\tau_{char}$  is the characteristic time scale, which implies that species react toward their chemical equilibrium state over the characteristic time,  $\tau_{char}$ .

Another approach is the application of the eddy-dissipation-concept model [50], which is an extension of the eddy-dissipation model to include detailed chemical mechanisms in turbulent flows. It assumes that the reaction occurs in small turbulent structures, called fine structures, where the dissipation of turbulent kinetic energy takes place. The length fraction of the fine scales is modelled as follows:

$$\zeta^* = C_\zeta \left( \frac{v\varepsilon}{k^2} \right)^{0.25} \quad (2-34)$$

$C_\zeta = 2.1377$ , is volume fraction constant, and  $v$  is kinematic viscosity. The volume fraction of the fine scales is calculated as  $\zeta^{*3}$ .

Species are assumed to react in the fine structures over a time scale, defined as follows:

$$\tau^* = C_\tau \left( \frac{v}{\varepsilon} \right)^{0.5} \quad (2-35)$$

where  $C_\tau$  is a time scale constant equal to 0.4082.

The finite-rate chemical kinetics are considered by treating the fine structures as constant pressure and adiabatic homogeneous reactors with initial conditions taken as the current species and temperature in the cell. The mass fraction values of the fine structures can be calculated by solving a system of ordinary differential equations (ODE) [51].

Reactions proceed over the time scale  $\tau^*$  governed by the Arrhenius rates and are integrated numerically. Ultimately  $R_i$  is modelled as:

$$R_i = \frac{\rho(\zeta^*)^2}{\tau^*[(1 - (\zeta^*)^3)]} (Y_i^* - Y_i) \quad (2-36)$$

where  $Y_i^*$  is the mass fraction of fine scale species after reacting over time  $\tau^*$ .

### ***Discrete phase method and particle modelling***

Particle behaviour is modelled using the Lagrangian discrete phase method (DPM). The force balance equation can be written in the Lagrangian reference frame as follows:

$$m_p \frac{d\vec{u}_p}{dt} = m_p \frac{\vec{u} - \vec{u}_p}{\tau_r} + m_p \frac{\vec{g}(\rho_p - \rho)}{\rho_p} + \vec{F} \quad (2-37)$$

By integrating the force balance on each particle, individual trajectories are calculated. The spherical drag force proposed by Morsi et al. [21] is used in this study, where particles are considered smooth and spherical. The explained approach (DPM) is used for carbon particle and water droplet trajectory calculations.

The dispersion of particles due to turbulence in the fluid phase can be predicted using the discrete random walk (DRW) model. With this approach, individual trajectories are calculated by instantaneous fluid velocity. The details and equations for the DRW model are not mentioned in this study; however, readers can refer to the study of Mofakham et al. [52] for more details.

### ***Particle evaporation and combustion***

Water droplets evaporation is modelled using a Convection/Diffusion Controlled sub-model [25]. The following expression for the mass balance is used when the droplet temperature is lower than the boiling point:

$$\frac{dm_p}{dt} = k_c A_p \rho \cdot \ln\left(1 + \frac{Y_{i,s} - Y_{i,\infty}}{1 - Y_{i,s}}\right) \quad (2-38)$$

When the droplet temperature reaches the boiling point while containing mass that can evaporate, convective boiling of a discrete phase droplet is used, for which the details and related equations can be found here [14].

For carbon particle combustion, the Field Char Oxidation (FCO) model is used, which is a simplification of the unreacted shrinking core model (USCM). In this model, the gas-solid reaction proceeds in a couple of steps as follows:

1. The oxidant from the gas phase diffuses into the surface and reacts with the solid at the surface.
2. A layer of products (in the case of coal and carbon, the ash) is formed on the surface. This layer of products increases the resistance to gas diffusion into the unreacted core of the particle.



3. The gas penetrates the product layer at the surface and reacts with available solids in the unreacted core (also known as the reaction site).
4. The gases produced from the gas-solid reactions diffuse from the reaction site to the particle surface.
5. Ultimately, from the particle surface to the surrounding bulk.

The combustion rate of solid carbon is modelled using DPM multiple surface reaction model, and the rate is calculated from the below expression [22]:

$$\overline{R_{char}} = \frac{dm_c}{dt} = -A_p y_j R_{char,i} \quad (2-39)$$

where  $y_j$  is the mass fraction of reactive surface species,  $A_p$  is the particle surface area ( $m^2$ ),  $\frac{dm_c}{dt}$  =rate of char depletion (kg/s) and  $R_{char,i}$  is the overall rate of solid reaction per unit particle surface area (kg/ $m^2 \cdot s$ ) defined as:

$$R_{char,i} = \frac{1}{\frac{1}{k_{diff,i}} + \frac{1}{k_{s,i} Y^2} + \frac{1}{k_{dash,i} \left(\frac{1}{Y} - 1\right)}} (P_i - P_i^*) \quad (2-40)$$

where  $Y$  is a parameter to consider diffusion resistance due to the thickness of ash on the outer surface. To simplify the model,  $Y = 1$  is considered, which ignores the resistance effect of the ash layer formation.

A summary of described governing equations and sub-models is listed in Table 2-1.

Table 2-1. Governing equations and sub-models for CFD modelling of the HISarna off-gas system

Phenomena/models	Main equation
<b>Continuity equation</b>	$\frac{\partial}{\partial t} (\rho) + \frac{\partial}{\partial x_i} (\rho \bar{u}_i) = 0$
<b>Momentum equation</b>	$\frac{\partial}{\partial t} (\rho \bar{u}_i) + \frac{\partial}{\partial x_j} (\rho \bar{u}_i \bar{u}_j) = -\frac{\partial p}{\partial x_i} + \frac{\partial}{\partial x_j} \left[ \mu \left( \frac{\partial \bar{u}_i}{\partial x_j} + \frac{\partial \bar{u}_j}{\partial x_i} - \frac{2}{3} \delta_{ij} \frac{\partial \bar{u}_l}{\partial x_l} \right) \right] + \frac{\partial}{\partial x_j} (-\rho \overline{u'_i u'_j})$
<b>Turbulence models</b>	<b>Realizable k-ε Model</b>
	<b>Equation for turbulent kinetic energy (k)</b>
	$\frac{\partial}{\partial t} (\rho k) + \frac{\partial}{\partial x_i} (\rho k \bar{u}_i) = \frac{\partial}{\partial x_j} \left[ \left( \mu + \frac{\mu_t}{\sigma_k} \right) \frac{\partial k}{\partial x_j} \right] + G_k + G_b - \rho \varepsilon - Y_M + S_k$
	<b>Equation for dissipation of turbulent kinetic energy (ε):</b>
	$\frac{\partial}{\partial t} (\rho \varepsilon) + \frac{\partial}{\partial x_j} (\rho \varepsilon \bar{u}_j) = \frac{\partial}{\partial x_j} \left[ \left( \mu + \frac{\mu_t}{\sigma_\varepsilon} \right) \frac{\partial \varepsilon}{\partial x_j} \right] + \rho C_1 S \varepsilon - \rho C_2 \frac{\varepsilon^2}{k + \sqrt{\vartheta \varepsilon}} + C_{1\varepsilon} \frac{\varepsilon}{k} C_{3\varepsilon} G_b + S_\varepsilon$
	<b>SST k-ω model</b>
	<b>Equation for turbulent kinetic energy (k)</b>
	$\frac{\partial}{\partial t} (\rho k) + \frac{\partial}{\partial x_i} (\rho k \bar{u}_i) = \frac{\partial}{\partial x_j} \left[ \left( \mu + \frac{\mu_t}{\sigma_k} \right) \frac{\partial k}{\partial x_j} \right] + G_k - Y_k + S_k$
	<b>Equation for turbulent kinetic energy dissipation rate (ω):</b>

	$\frac{\partial}{\partial t}(\rho\omega) + \frac{\partial}{\partial x_j}(\rho\omega\bar{u}_j) = \frac{\partial}{\partial x_j}\left[\left(\mu + \frac{\mu_t}{\sigma_\omega}\right)\frac{\partial\omega}{\partial x_j}\right] + G_\omega - Y_\omega + D_\omega + S_\omega$
<b>Energy equation</b>	$\frac{\partial}{\partial t}(\rho E) + \nabla \cdot (\bar{u}(\rho E + p)) = \nabla \cdot (k_{eff}\nabla T - \sum_j h_j\vec{J}_j + (\tau_{eff} \cdot \bar{u})) + S_h$
<b>Radiation models</b>	<b>Discrete ordinate model (DOM)</b>
	$\nabla \cdot (I(\vec{r}, \vec{s})\vec{s}) + (a + \sigma_s)I(\vec{r}, \vec{s}) = an^2\frac{\sigma T^4}{\pi} + \frac{\sigma_s}{4\pi}\int_0^{4\pi} I(\vec{r}, \vec{s}')\phi(\vec{s}, \vec{s}')d\Omega'$
	<b>P1 model</b>
	$q_r = -\Gamma_r\nabla G$
	$\Gamma_r = \frac{1}{3(a + \sigma_s) - C\sigma_s}$
	$\nabla \cdot (\Gamma_r\nabla G) - \alpha G + 4an^2\sigma T^4 = 0$
	$-\nabla \cdot q_r = \alpha G - 4a\sigma T^4$
	<b>Rosseland model</b>
	$\vec{q}_r = -\Gamma_r\nabla G$
	$G = 4\sigma n^2 T^4$
	$q_r = -16\sigma\Gamma_r n^2 T^3 \nabla G$
<b>Species transport equation</b>	$\frac{\partial}{\partial t}(\rho Y_i) + \frac{\partial}{\partial x_i}(\rho\bar{U}Y_i) = -\nabla \cdot \vec{J}_i + R_i + S_i$
<b>Turbulence-chemistry interaction models</b>	<b>Finite rate model (FR)</b>
	$R_{i-FR} = M_{w,i} \sum_{r=1}^{N_R} \hat{R}_{i,r}$
	$\hat{R}_{i,r} = \theta(v_{i,r}^* - v_{i,r}') \left( k_{f,r} \prod_{j=1}^N [C_{j,r}]^{n_{j,r}'} - k_{b,r} \prod_{j=1}^N [C_{j,r}]^{n_{j,r}''} \right)$
	<b>Eddy dissipation model (EDM)</b>
	$R_{i-EDM} = \frac{A\varepsilon}{k} \min(f_i, v_i)$
	<b>Finite rate eddy dissipation model (FR-EDM)</b>
	$R_{i-FR-EDM} = \min(R_{i-EDM}, R_{i-FR})$
	<b>Finite rate eddy dissipation model – relaxed to equilibrium (FR-EDM-rem)</b>
	$R_i = \rho \frac{Y_i^{eq} - Y_i}{\tau_{char}}$
	<b>Eddy dissipation concept (EDC)</b>
	$R_i = \frac{\rho(\zeta^*)^2}{\tau^*[(1 - (\zeta^*)^3)]} (Y_i^* - Y_i)$
	$\zeta^* = C_\zeta \left(\frac{\nu\varepsilon}{k\bar{z}}\right)^{0.25}$
	$\tau^* = C_\tau \left(\frac{\nu}{\varepsilon}\right)^{0.5}$
<b>Particle force balance equation - Discrete phase model</b>	$m_p \frac{d\bar{u}_p}{dt} = m_p \frac{\bar{u} - \bar{u}_p}{\tau_r} + m_p \frac{\bar{g}(\rho_p - \rho)}{\rho_p} + \bar{F}$
<b>Particle evaporation model</b>	$\frac{dm_p}{dt} = k_c A_p \rho \cdot \ln\left(1 + \frac{Y_{i,s} - Y_{i,\infty}}{1 - Y_{i,s}}\right)$
<b>carbon particle reaction rate</b>	$\bar{R}_{char} = \frac{dm_c}{dt} = -A_p y_j R_{char,i}$
	$R_{char,i} = \frac{1}{\frac{1}{k_{diff,i}} + \frac{1}{k_{s,i} Y^2} + \frac{1}{k_{dash,i}} \left(\frac{1}{Y} - 1\right)} (P_i - P_i^*)$

## 2.3. Model development

### 2.3.1. Description of the off-gas system

The details of different off-gas system sections are discussed in chapter 1. Figure 2-4. shows a more detailed description of the off-gas system with the indication of the cooling stacks. Cooling stacks denote the cooling circuit responsible for maintaining the appropriate temperature of the off-gas system walls, accomplished by employing water as a cooling agent, which subsequently enters the heat exchanger network. Furthermore, four different points are highlighted, which refer to the gas temperature and composition measurement points. In the current operation, the temperature is measured at points A, B, and D; however, the gas compositions are available only at points A and D. These measurements are used for model validation and are reported in Table 2-2.

Table 2-2. Measured temperature and composition for model validation

<b>Composition (dry basis mole fraction)</b>	<b>Point A</b>	<b>Point B</b>	<b>Point D</b>
<b>CO</b>	0	-	0
<b>CO<sub>2</sub></b>	0.749	-	0.327
<b>H<sub>2</sub></b>	0	-	0
<b>O<sub>2</sub></b>	0.0542	-	0.134
<b>N<sub>2</sub></b>	0.197	-	0.539
<b>Temperature [K]</b>	1710*	1023*	713*
<b>* The values are measured with ±10% error</b>			

The measured heat losses through the off-gas walls are reported in Table 2-3. The measured values for heat losses do not represent the actual heat loss to the cooling water since some of the heat is lost into the surroundings. According to finite element analysis, which will be discussed in detail later, the ratio of total heat loss to the heat loss into the surroundings is 7.5% and 35% for the reflux chamber (stack 1) and the rest of the wall (stack 2, 3 and 4) respectively. The heat loss to the environment above the reflux chamber is relatively high due to the high thermal conductivity of pipes with no refractory coating applied. The total heat loss reported in Table 2-3 should be used to validate the model predictions.

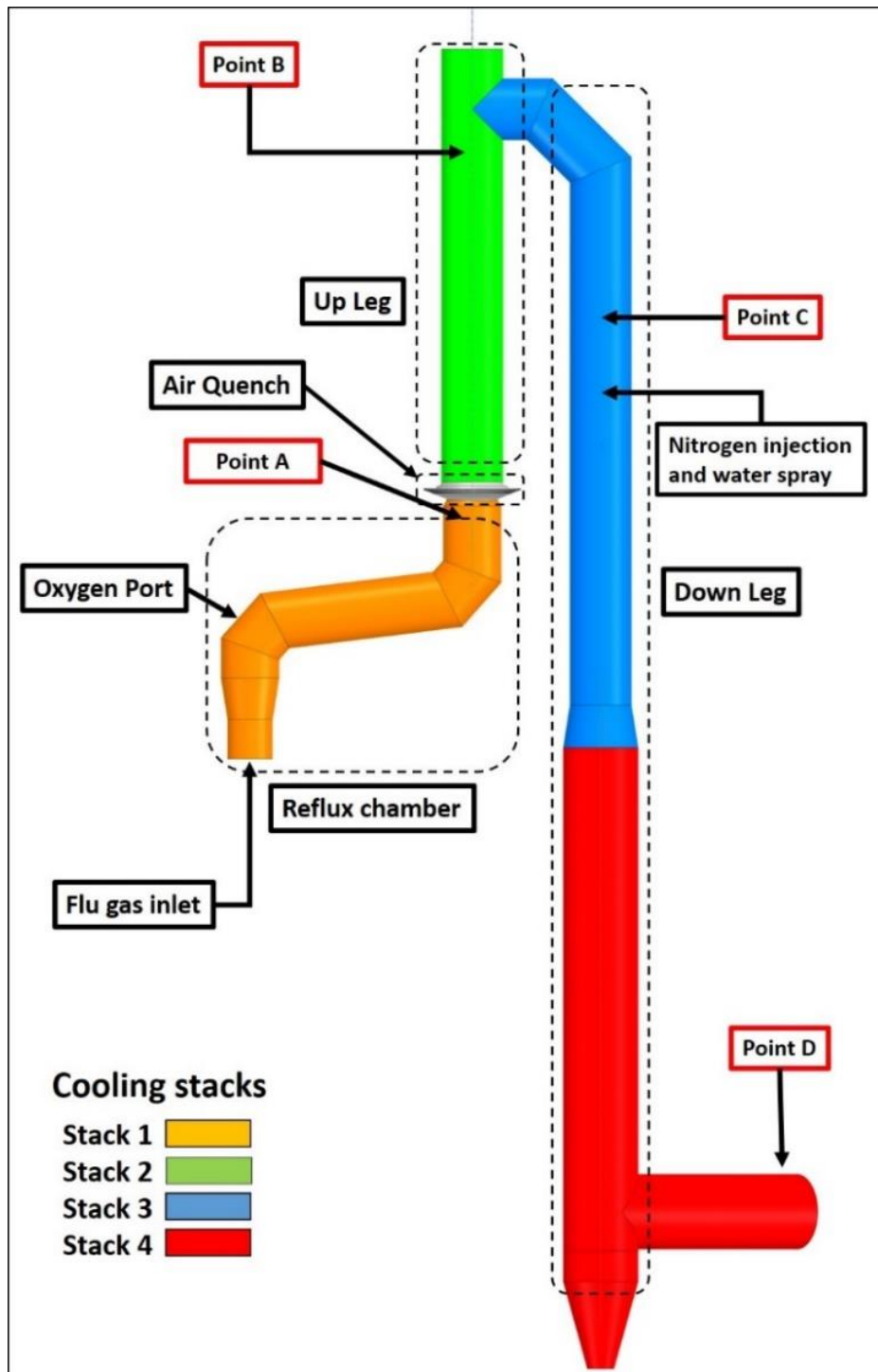


Figure 2-4. Off-gas system components and data acquisition points (point A: reflux chamber outlet, Point B: end of up leg, Point C: 3 meters above water quench atomizers, Point D: exit to gas cooler)

The carbon conversion at the outlet of the reflux chamber is indirectly measured using the data from the gas analyzer that measures the gas composition in the reflux chamber. It is determined to be 50% from the pilot plant data, which will also be used for model validation.

Table 2-3. Measured heat loss in the off-gas system (in MW)

	Measured loss to cooling water	Loss to the surrounding	Total loss
<b>Reflux chamber (stack 1)</b>	3.6	0.30	3.9
<b>Rest (stack 2, 3, 4)</b>	3.5	1.9	5.4
<b>Sum</b>	7.1	2.2	9.3

### 2.3.2. Computational grid (Mesh) generation

Various cell types can be utilized to discretize the computational domain. The most common basic cell types for generating the computational domain include tetrahedral, hexahedral, and polyhedral cells, as illustrated in Figure 2-5.

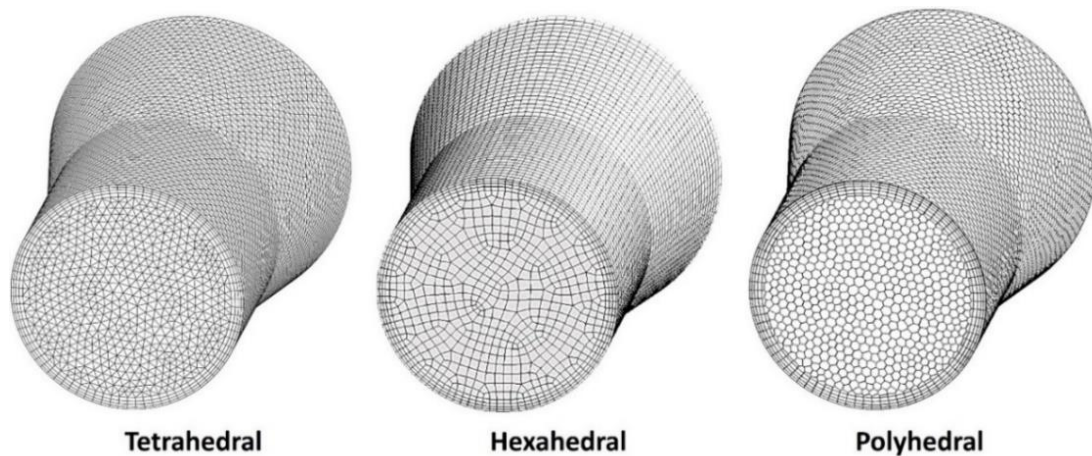


Figure 2-5. Basic cell types for constructing computational grid (mesh)

Further discussion on the impact of cell types and grid independence is provided in Chapter 3. For all calculations, a medium-sized polyhedral grid is selected based on the results of mesh sensitivity analysis. In all cases within this thesis, prism layers with a first layer thickness of 10 mm are employed, along with four layers, to generate inflation on the walls and to maintain  $y^+ > 30$ , as stipulated by the k- $\epsilon$  model. A representation of the computational grid is shown in Figure 2-6. The primary advantage of employing polyhedral cells is their ability to achieve accurate predictions while requiring fewer cells than tetrahedral and hexahedral elements. The equivalent tetrahedral cell type is also reported in Table 2-4. As can be seen, using the polyhedral mesh can reduce the cell count by a factor of 4.3, leading to a considerable reduction in computational costs.

Table 2-4. Computational grid for simulations and grid independence study

	Zone - Cell Size [mm]			Cell Type and count (million)		
	Reflux chamber	Air quench	Up/down leg	Tetrahedral	Hexahedral	Polyhedral
<b>Coarse</b>	55	45	65	5.3	1.8	1.2
<b>Medium</b>	40	30	50	11	4.2	2.6
<b>Fine</b>	30	25	40	18	7.1	4.2

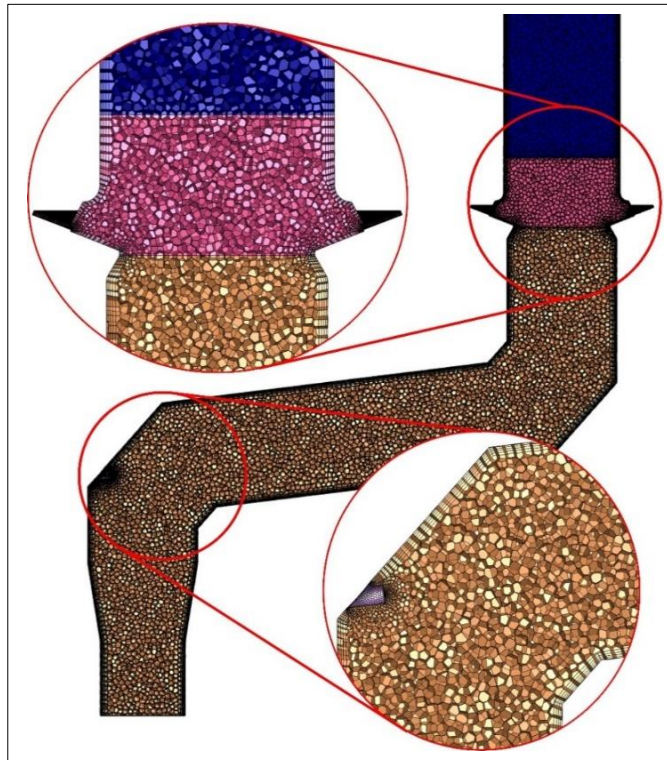


Figure 2-6. Final generated computational grid for CFD modelling using polyhedral cells

### 2.3.3. Inlet boundary condition

The data for boundary conditions are obtained from the HIsarna pilot plant by averaging over a fixed operating period. The obtained data are listed in Table 2-5.

Table 2-5. Inlet boundary conditions for CFD model setup

	Reflux chamber	Air quench	Oxygen port	Nitrogen ports	Water Spray
<b>Inlet temperature [K]</b>	2086	293	293	293	293
<b>Actual volumetric flowrate [m<sup>3</sup>/s]</b>	20.8	3.10	0.206		-
<b>Average density [kg/m<sup>3</sup>]</b>	0.208	1.19	1.31	1.25	998
<b>Inlet mass flowrate [kg/s]</b>	4.33	3.69	0.27	0.205	0.45
<b>Carbon particles flowrate [kg/s] diameter = <math>12 \times 10^{-5}</math> m</b>	0.0282				
<b>Composition – average mole fraction at inlet</b>					
<b>CO</b>	0.0261	0	0	0	0
<b>CO<sub>2</sub></b>	0.61	0.0003	0	0	0
<b>H<sub>2</sub></b>	0.002	0	0	0	0
<b>O<sub>2</sub></b>	0	0.21	0.995	0	0
<b>N<sub>2</sub></b>	0.166	0.78	0.005	1	0
<b>H<sub>2</sub>O</b>	0.2	0.012	0	0	1
<b>Post combustion ratio [%]</b>	96.63	-	-	-	-

Another important consideration is the nonuniform species and temperature inlet profiles. Oxygen is injected from the sides of the CCF, while the majority of remaining CO and H<sub>2</sub> tend to concentrate in the central flow region at the CCF outlet. Similar non-uniform profiles are expected for other species, as depicted in Figure 2-7. These profiles are acquired from another CFD model specifically developed for CCF at Tata Steel, R&D. Furthermore, the injection of iron ore and oxygen into the CCF is characterized by a non-radial configuration, with injection ports tilted to include a tangential velocity component. This arrangement induces a swirl motion that is conveyed upward to the reflux chamber. Consequently, the flow at the inlet of the off-gas system is not strictly axial but exhibits a pronounced swirl motion.

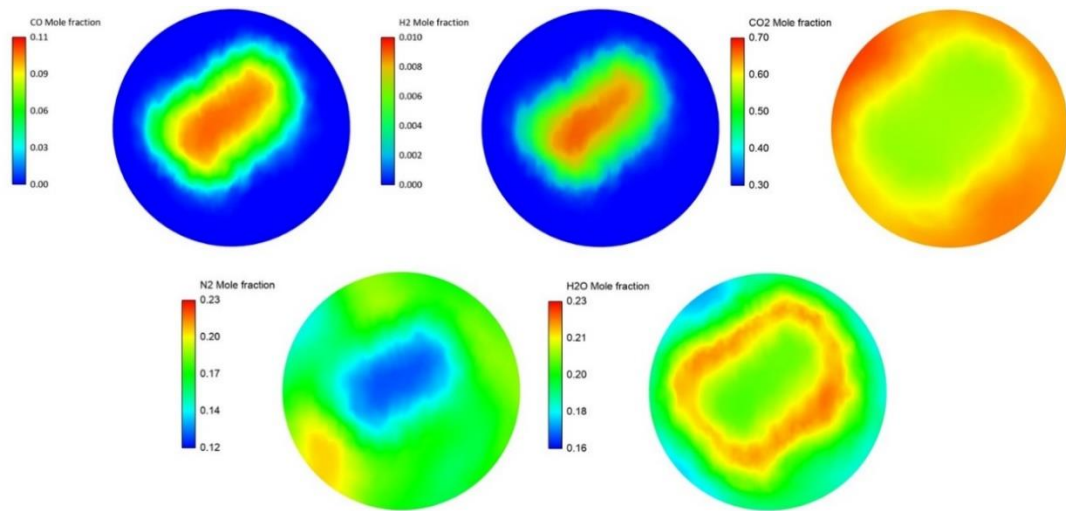


Figure 2-7. Species profile at the inlet of reflux chamber (average values are reported in Table 2-5)

The intensity of a swirl motion is characterized by the swirl number ( $S_w$ ). It is defined as the ratio of the tangential ( $G_t$ ) to the axial momentum flux ( $G_a$ ) and is calculated as:

$$S_w = \frac{G_t}{R \cdot G_a} = \frac{\int \rho U_a \cdot U_t \cdot r \cdot dA}{R \int \rho U_a^2 \cdot dA} \quad (2-41)$$

where  $U_a, U_t, r, A$  are axial velocity, tangential velocity, radial coordinate, and surface area, respectively (all in SI units). According to the CFD model prediction for CCF, the swirl number inside the CCF can reach 0.6, and this value is also applied at the inlet of the reflux chamber to consider the impact of the swirl motion. The carbon particle flow rate is 0.0282 kg/s with a uniform particle size of  $12 \times 10^{-5}$  meter.



### 2.3.4. Wall boundary condition and wall modelling in CFD

The walls of the off-gas system are constructed from steel pipes (outer diameter: 38 mm, thickness: 5 mm). Counter-current cooling water flows through these pipes to cool the walls. To safeguard the cooling pipes from melting and thermal stresses within the reflux chamber, a 40 mm thick layer of refractory material (commercial name: Calde Stix 151) is applied on top of the cooling pipes. This refractory layer is situated at the outer surface of the cooling pipes, which corresponds to the inner surface of the reflux chamber. Rows of anchors, made from the same material as the pipes, are strategically placed around the circumference of the pipes to securely support the applied refractory layer, as depicted in Figure 2-8.

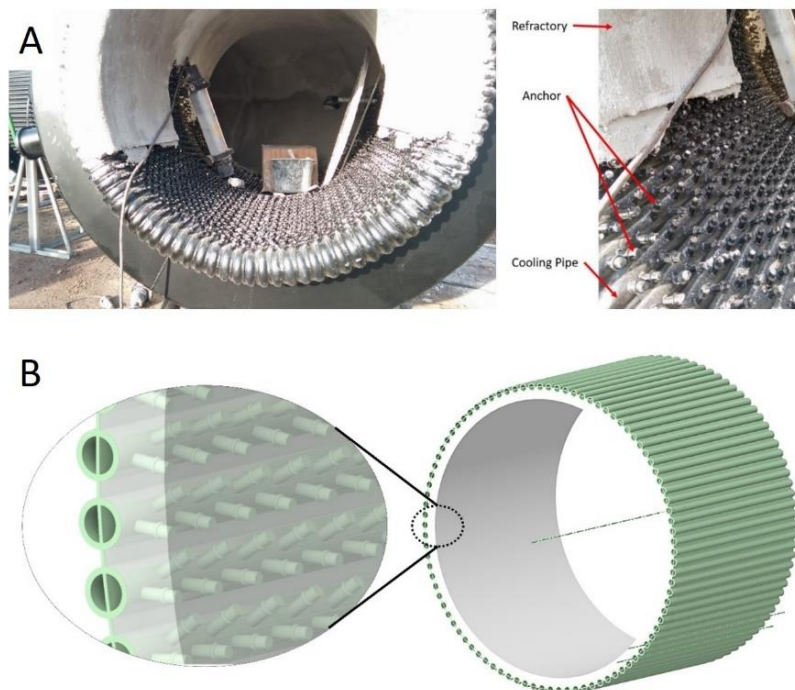


Figure 2-8. Reflux chamber fresh refractory layer (A) and cooling jacket (B)

Three methods can be used to model a wall in CFD. The first option would be directly resolving the wall by considering the wall details and its thickness in the geometry, meshing it, and assigning it as a solid zone in the CFD solver. While this method provides the most comprehensive representation and accounts for heat transfer in all directions, it results in an extremely fine computational grid within the wall region. Consequently, it can become computationally demanding. For example, for the current case, considering a refractory thickness, anchors detail, cooling pipe, and a reasonable cell size would lead to a grid with  $2.5 \times 10^9$  cells, which is practically

impossible to solve with available computational resources. The wall layers are often not resolved directly and are instead modelled using the thin wall approach to alleviate computational demands.

This leads to considering the second option, in which only the fluid region is meshed, and the wall is represented by specifying a wall thickness and assigning a specific material to it. Thermal resistance across the wall thickness is appropriately imposed, and wall conduction is accounted for without including the wall thickness in the geometry. However, this approach considers conduction in the wall only in the normal direction, and it does not allow for the consideration of different wall layers.

If the wall is composed of different material layers and conduction in the planar direction of the wall is important, the third option, known as the “shell conduction” approach, can be used. In this approach, the solver automatically generates a layer of prism or hex cells (virtual cells) on the specified wall boundaries, and the conduction heat transfer equation is solved in all directions for these virtual cells. A visual summary of the three wall modeling approaches mentioned above is presented in Figure 2-9.

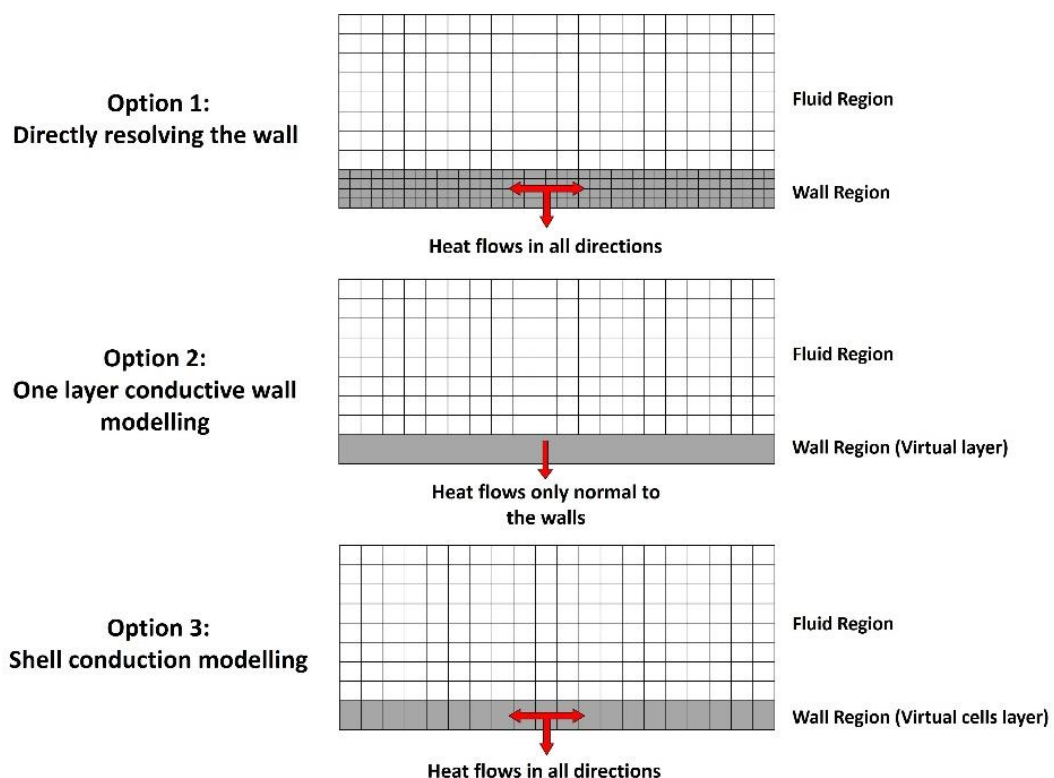


Figure 2-9. Wall modelling approaches in CFD

Numerous studies have used the shell conduction approach to model the conductive heat transfer through the walls. Mahmoodi et al. [51] have used this approach to model the heat transfer through an industrial H<sub>2</sub>S removal unit and reported well-predicted heat loss and temperature profiles. Ghosh et al. [53] have used the shell conduction model to investigate thermal convection inside a space flight sensor. Al-Abbas [54] has studied heat transfer in a solar heating system and has used the same approach to consider different wall layers for conductive heat transfer through the wall. Jayakumar et al. [55] have modelled the walls of a coiled heat exchanger, and Popescu et al. [56] have modelled the walls of a swirl combustor using the same technique.

In the first attempt to build a CFD model (which will be called initial-model hereafter), the walls are modelled using the shell conduction approach with two layers. The first layer will be the refractory wall; the second layer is the cooling pipe wall made of steel (Figure 2-10).

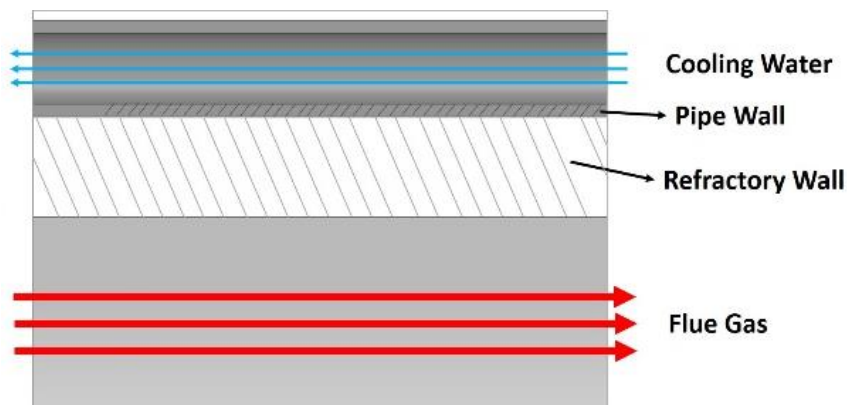


Figure 2-10. A schematic representation of the reflux chamber wall

For the walls, specific heat, density, and thermal conductivity of the materials are important properties to predict the heat transfer in the CFD model correctly. For the initial-model, these properties are described in Table 2-6. The influence of anchors embedded within the walls is currently disregarded but will be incorporated and discussed in section 2.4.

Table 2-6. Material properties for the initial-model (obtained from TATA Steel Ijmuiden R&D)

Material	$\rho$ [kg/m <sup>3</sup> ]	$k$ [W/m. K]	$c_p$ [j/kg. K]	Thickness [mm]
Refractory (Calde Stix 151)	2200	1.15	900	40
Steel (P235GH-TC1)	7850	45	461	5

The heat transfer properties of the cooling water, such as the average temperature and heat transfer coefficient, are imposed at the outer surface of the second layer as a boundary condition.

The cooling system is divided into four different cooling stacks. The flow rate and average temperature of the cooling water are shown in Figure 2-11.

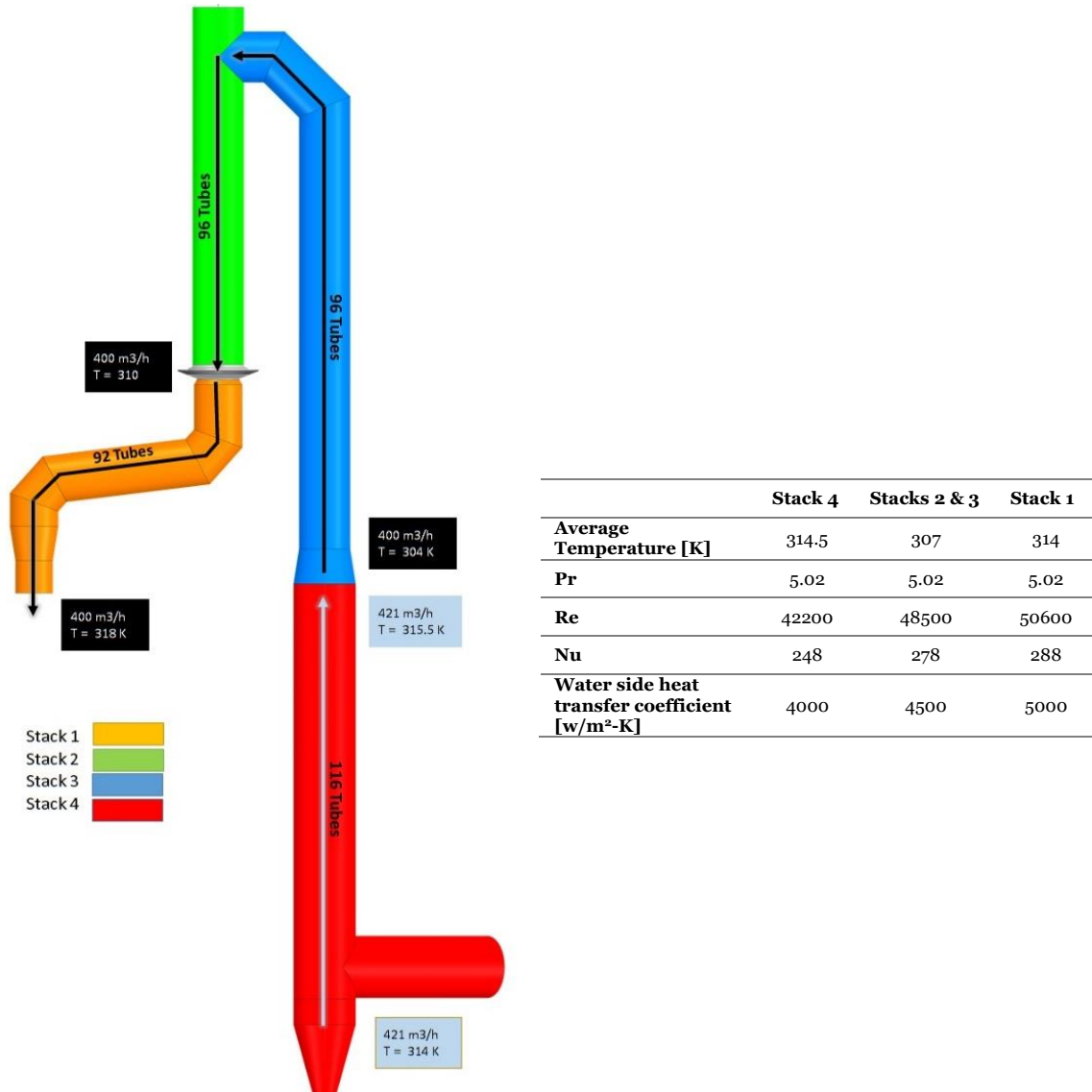


Figure 2-11. The off-gas cooling water circuit

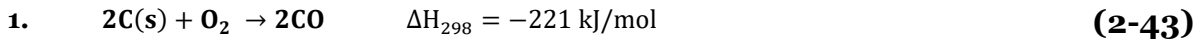
The heat transfer coefficient for the cooling water side is calculated for each cooling stack according to the Pak and Cho relation [24]:

$$Nu = \frac{hL}{k} = 0.016Pr^{0.5}Re^{0.83} \quad (2-42)$$

where  $h$  is the convective heat transfer coefficient of the cooling water flow,  $L$  is the characteristic length,  $k$  is the thermal conductivity of the water,  $Re$  and  $Pr$  are Reynolds and Prandtl numbers.

### 2.3.5. Reactions and reaction kinetics

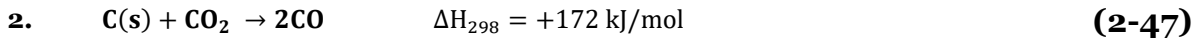
A detailed kinetic mechanism proposed by Frassoldati et al. [57] is used for the CO-H<sub>2</sub> mixture combustion. The mechanism contains 14 species and 33 reactions, and it is validated using experimental data by the same researchers. Three different reactions are considered for carbon combustion. The kinetic expressions are taken from the study of Wen et al. [22] in the form of Equation 2-40. The reactions and the kinetic data are as follows:



$$\bullet \quad k_s = 8710 \exp\left(-\frac{17967}{T_s}\right) \quad (2-44)$$

$$\bullet \quad k_{diff} = 1.383 \times 10^{-3} \left(\frac{T}{1800}\right)^{0.75} / (P_{op} \cdot d_p) \quad (2-45)$$

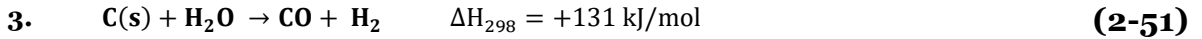
$$\bullet \quad P_i - P_i^* = P_{O_2} \quad (2-46)$$



$$\bullet \quad k_s = 247 \exp\left(-\frac{21060}{T_s}\right) \quad (2-48)$$

$$\bullet \quad k_{diff} = 7.45 \times 10^{-4} \left(\frac{T}{2000}\right)^{0.75} / (P_{op} \cdot d_p) \quad (2-49)$$

$$\bullet \quad P_i - P_i^* = P_{CO_2} \quad (2-50)$$



$$\bullet \quad k_s = 247 \exp\left(-\frac{21060}{T_s}\right) \quad (2-52)$$

$$\bullet \quad k_{diff} = 1 \times 10^{-4} \left(\frac{T}{2000}\right)^{0.75} / (P_{op} \cdot d_p) \quad (2-53)$$

$$\bullet \quad P_i - P_i^* = P_{H_2O} \quad (2-54)$$

In the above equations,  $T = (T_g + T_p)/2$ , and  $T_p$  is the particle temperature and other parameter definitions and units can be found in the nomenclature. For the sake of simplification, the impact of the ash layer on combustion is omitted, and the combustible fraction is fixed at 99%. The above parameters lead to an overall rate with the unit of  $\frac{g}{cm^2 s atm}$ . Proper unit conversions can be performed, and expressions can be implemented through a user defined function (UDF). In this thesis, for simplicity of the setup, direct Fluent input parameters (by manipulating equations 2-43 to 2-54) are calculated and used for all cases according to Table 2-7.

In the HIsarna pilot plant, the water is sprayed through a two-fluid atomizer with nitrogen as carrier gas (blast atomizer). Unfortunately, there was limited available

information regarding the atomizer's specifications and geometry. The only available data were the nitrogen and water flow rates and the injection spray angle. Therefore, for water droplet injection, the data are set based on Poozesh et al. [23], who have studied the droplet size and velocity distribution of a two-fluid atomizer experimentally and numerically. The water droplet injection is modelled using the cone injection model with a uniform diameter of  $9 \times 10^{-5}$  m, injection velocity of 25 m/s, and spray angle of 30 degrees. As mentioned in section 2.2, the dispersion of carbon and water droplet particles due to turbulence in the fluid phase is considered by the DRW model.

To accurately compute the overall behavior of particles and represent the particle flow rate adequately, a sufficient number of particles must be included in the computational domain.

Table 2-7. Kinetic data for carbon gasification in Arrhenius equation form

Reaction	A	E (j/kmol)	Temperature exponent	Diffusion rate constant
$2\text{C(s)} + \text{O}_2 \rightarrow 2\text{CO}$	0.85961	$1.49378 \times 10^8$	1	$4.94 \times 10^{-12}$
$\text{C(s)} + \text{CO}_2 \rightarrow 2\text{CO}$	0.02438	$1.75093 \times 10^8$	0	$2.4584 \times 10^{-12}$
$\text{C(s)} + \text{H}_2\text{O} \rightarrow \text{CO} + \text{H}_2$	0.02438	$1.75093 \times 10^8$	0	$3.3 \times 10^{-13}$

In the DRW model, the number of particles can be controlled by a parameter called "number of tries". A higher number of tries means a higher number of injected particles, which leads to a better consideration of the random effects of turbulence on the particle dispersion. However, higher tries can substantially increase the calculation time of particle trajectory. In the initial-model, NTs = 20 tries is considered, leading to the injection of 16,000 particles.

Similar to the grid independence analysis, it is necessary to conduct a sensitivity analysis to determine the appropriate number of particles. The effect of this parameter will be discussed in more detail in Chapter 3.

### 2.3.6. Model summary and solution procedure

ANSYS FLUENT commercial software, a CFD code solver package based on the finite volume method, is used to solve and couple the governing equations. Table 2-8 summarizes the main models and sub-models used in this study. Numerical discretization of conservation equations is performed using the second-order upwind scheme. A convergence criterion of  $10^{-4}$  for the relative error between two

successive iterations is used. Mean temperature, composition, and heat loss through the walls are monitored at different cross sections, and iterative calculation is carried out until the variations of the monitored values become negligible and approximately constant, along with the satisfied convergence criterion of  $10^{-4}$ .

Table 2-8. Summary of sub-models used to set up the initial-model

Interaction/Phenomena	Model/algorithm
Pressure-velocity coupling and governing equation solving	Coupled algorithm
Turbulent flow	Realizable k- $\epsilon$ model with enhanced wall treatment
Turbulence-chemistry interaction	EDC model
Thermal radiation	DOM
Particle trajectory	DPM model with stochastic tracking
Gas solid reaction	DPM multiple surface reaction model Field char oxidation
Particle evaporation	Convective evaporation model

### 2.3.7. Simulation results of the initial-model

Figure 2-12 shows the calculated temperature profile of the flue gas across the off-gas system. The profile is calculated as the cross sectional average of the flue gas temperature across the reflux chamber. An apparent discrepancy exists between the measured and calculated profiles. This difference is also noticeable in the calculated and measured heat losses through the off-gas system walls, with the most significant disparity observed for the wall of the reflux chamber (see Table 2-9).

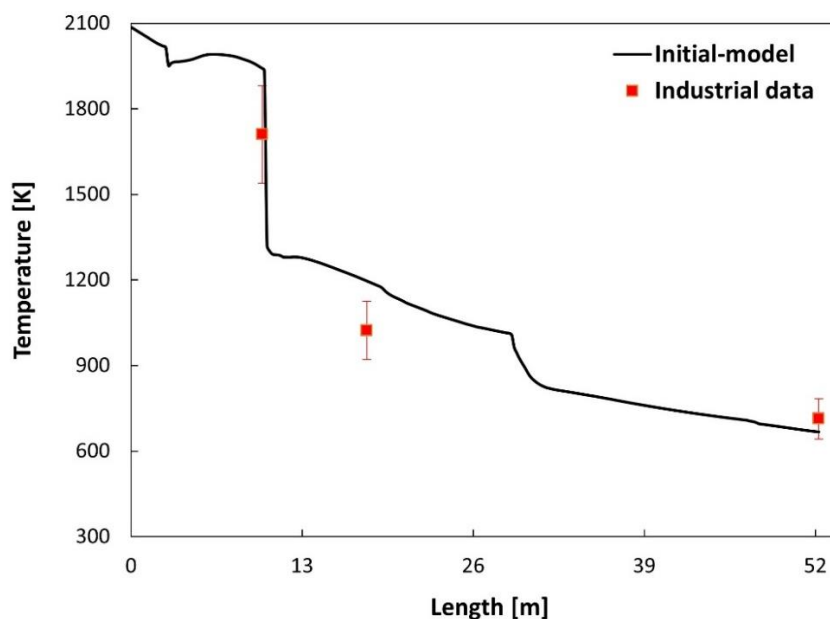


Figure 2-12. Predicated temperature profile along the off-gas system using the initial-model



The primary cause of these errors lies in the inaccurate thermal properties of the wall materials, particularly the refractory material. As mentioned before, the refractory wall is firmly held by rows of anchors attached to the cooling pipes. The anchors are made of steel (the same material as cooling pipes) with a high thermal conductivity and density compared to the refractory material. The refractory wall can be regarded as a composite material, with the refractory serving as the matrix and the embedded anchors acting as fillers. This embedding process augments the effective thermos-physical properties of the reflux chamber wall. From the study of several parameters and conditions, thermal conductivity considerably affects thermal exchanges [58], thus a critical parameter for the correct prediction of heat transfer and losses through a wall. It was noted that even a small change in thermal conductivity considerably affects the model predictions (heat loss and temperature profiles), whereas variations in the heat capacity and density do not have such a significant impact.

Table 2-9. Calculated and measured values for temperature and heat loss for the initial-model

<b>Temperature [K]</b>	<b>Calculated</b>	<b>Measured</b>	<b>Error</b>
Point A (length: 10 m)	1941	1710	16%
Point B (length: 18 m)	1193	1023	23%
Point D (length: 52 m)	667	713	10%
<b>Heat loss [MW]</b>			
Reflux chamber	1.71	3.9	56%
Rest	6.85	5.4	27%

Two methods are available for determining the thermos-physical properties of the composite wall. One approach involves employing numerical and experimental correlations, commonly known as effective medium approximations (EMA). The other method entails acquiring thermos-physical properties through finite element method (FEM) analysis, taking into account the detailed geometry and orientation of the matrix and fillers.

## 2.4. Tuned-model

### 2.4.1. Wall thermal properties calculation using EMA correlations

As mentioned before, the reflux chamber refractory wall can be considered a composite material made of the refractory material (matrix) and anchor (fillers). Nonetheless, only homogeneous layers can be accommodated for each distinct layer when employing the shell conduction approach for wall modeling. Therefore, the combination of the anchors and refractory material is regarded as a homogeneous layer, which will be referred to as the "refractory equivalent wall" or simply the "equivalent wall" throughout the thesis text (see Figure 2-13). Effective specific heat, density, and thermal conductivity are important properties for the equivalent wall to predict the heat transfer in the final CFD model correctly. Effective specific heat and density are calculated using mixing law by considering the mass fraction of matrix and filler as follows:

$$\rho_{eff} = m_f \rho_f + m_m \rho_m \quad (2-55)$$

$$Cp_{eff} = m_f Cp_f + m_m Cp_m \quad (2-56)$$

Using this formulation and considering the mass fraction of fillers and matrix,  $\rho_{eff} = 2970$  and  $Cp_{eff} = 840$  are calculated for the equivalent wall, slightly different from the considered values in the initial-model (see Table 2-6).

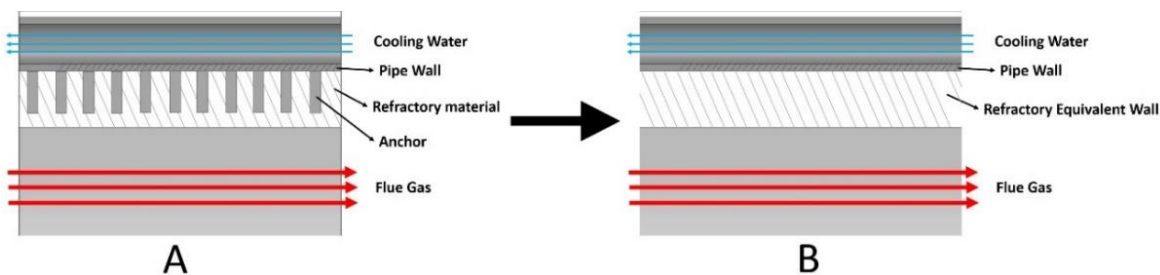


Figure 2-13. schematic representation of reflux chamber wall (A) and equivalent simplification (B). Calculating thermal conductivity is not as straightforward as determining density and heat capacity. It significantly depends on the geometry and orientation of the fillers within the material. Various effective medium approximation (EMA) correlations exist in the literature to predict the effective thermal conductivity of

such composite materials. The Maxwell model serves as a fundamental model for calculating the thermal conductivity of heterogeneous materials and has been used as the foundation for many other models and modifications [59]. Maxwell considered the problem of dilute dispersion of spherical particles of conductivity  $k_f$  embedded in a continuous matrix of conductivity  $k_m$ . Thermal interactions between filler particles were ignored. Maxwell's expression is as follows:

$$\frac{k_{eff}}{k_m} = 1 + \frac{3\varphi}{\left(\frac{k_f + 2k_m}{k_f - k_m}\right) - \varphi} \quad (2-57)$$

where  $\varphi$  is the volume fraction of the filler and  $k_{eff}$  is the effective thermal conductivity of the composite. Maxwell's formula was found to be valid only in the case of low  $\varphi$  (under about 25%).

The Lewis-Nielsen model (utilized in reference [60]) is another popular method for moderate filler volume fractions (up to 40%). The effective thermal conductivity of a composite according to the Lewis-Nielsen model is given as:

$$k_{eff} = \left(\frac{1+AB\varphi}{1-B\psi\varphi}\right), B = \left(\frac{\frac{k_f}{k_m} - 1}{\frac{k_f}{k_m} + A}\right), \psi = 1 + \left(\frac{1-\varphi_m}{\varphi_m^2}\right)\varphi \quad (2-58)$$

where  $\varphi_m$  is the maximum filler volume fraction (0.78 to 0.82), and  $A$  is the shape coefficient for the filler particles equal to 1.88.

Rayleigh model [61], which is an extension of the Maxwell model, includes analytical expressions for effective thermal conductivity of a continuous matrix reinforced with parallel cylindrical fibers arranged in a uniaxial simple cubic array (Figure 2-14). This arrangement closely resembles the structure of the reflux chamber wall. It's important to note that the thermal conductivity of such materials is direction-dependent. Assuming "z" represents the axis parallel to the fibers, Rayleigh's formulae are as follows:

$$\frac{k_{effz}}{k_m} = 1 + \left(\frac{k_f - k_m}{k_m}\right)\varphi \quad (2-59)$$

$$\frac{k_{eff\ x}}{k_m} = \frac{k_{eff\ y}}{k_m} = 1 + \left( \frac{2\varphi}{C_1 - \varphi - C_2(0.30584\varphi^4 - 0.013363\varphi^8)} \right) \quad (2-60)$$

$$C_1 = \frac{k_1 + k_m}{k_1 - k_m}, \quad C_2 = \frac{k_1 - k_m}{k_1 + k_m}$$

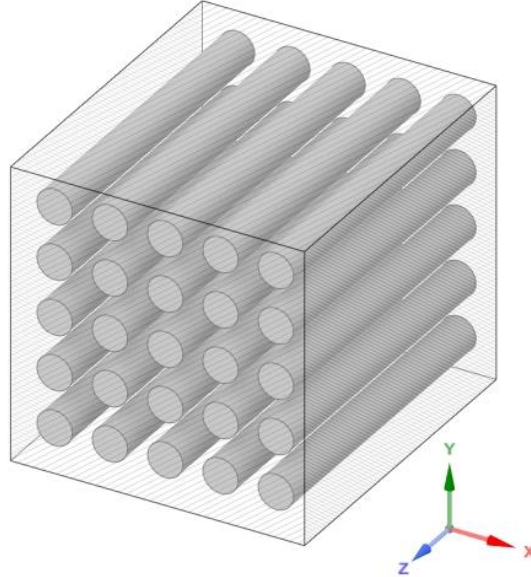


Figure 2-14. The schematic of matrix and fillers considered by Rayleigh consists of parallel cylinders embedded in a continuous matrix [59]

Bruggemann (whose model is utilized in [62]) has proposed a nonlinear correlation as follows:

$$(1 - \varphi) = \left( \frac{k_f - k_{eff}}{k_f - k_m} \right) \left( \frac{k_m}{k_{eff}} \right)^{\frac{1}{X}+1} \quad (2-61)$$

where  $X=2$  for spheres and  $X=1$  for cylinders oriented perpendicular to the heat flow.

Springer and Tsai (whose model is utilized in [63]) assume a square distribution of cylindrical fibers in the matrix material and propose the below expression:

$$k_{eff} = k_m \left[ 1 - 2\sqrt{\frac{\varphi}{\pi}} + \frac{1}{B} \left[ \pi - \frac{4}{\sqrt{1 - \left( B^2 \frac{\varphi}{\pi} \right)}} \cdot \tan^{-1} \left[ \frac{\sqrt{1 - \left( B^2 \frac{\varphi}{\pi} \right)}}{1 + B\sqrt{\frac{\varphi}{\pi}}} \right] \right] \right] \quad (2-62)$$

$$B = 2 \cdot \left[ \frac{k_m}{k_f} - 1 \right]$$

Hamilton and Crosser (whose model is utilized in [64,65]) defined the below expression for effective thermal conductivity:

$$k_{eff} = k_m \cdot \left[ \frac{k_f + 2k_m - 2\varphi(k_m - k_f)}{k_f + 2k_m + \varphi(k_m - k_f)} \right] \quad (2-63)$$

These models can be applied when the properties and volume fractions of the constituents are known. In the case of the reflux chamber wall, the volume fraction of anchors within the refractory material is 4.5% per square meter of the wall, considering a refractory thickness of 4 cm (with 1 cm above the anchor tips). Using the obtained volume fraction for fillers and thermal conductivity values listed in Table 2-6 for refractory material (matrix) and steel anchors (fillers), the thermal conductivity using each correlation is calculated and reported in Table 2-10.

Table 2-10. Calculated thermal conductivity using different EMA correlations for a refractory wall thickness of 40 mm

Correlation	Calculated k [W/m. K]
Rayleigh	3.2
Maxwell	1.31
Lewis-Nielsen	1.2
Bruggemann	1.2
Hamilton and Crosser	1.4
Springer	1.22

From the calculated values, only the Rayleigh correlation has predicted noticeably higher values for thermal conductivity, and the rest of the correlations have predicted a value pretty close to the thermal conductivity of pure refractory material. The material properties used for the tuned-model are reported in Table 2-11.

Table 2-11. Thermos-physical properties of different wall layers

Material	$\rho$ [kg/m <sup>3</sup> ]	k [W/m.K]	C <sub>p</sub> [j/kg K]	thickness [mm]
Refractory Equivalent wall	2970	3.2	840	40
Steel (P235GH-TC1)	7850	45	461	5

### 2.4.2. CFD results of the tuned-model

For the tuned-model, as can be seen from Figure 2-15, the temperature profile prediction is now much closer to the measured values and falls within the measurement errors. The calculated heat losses through the walls are also predicted with much lower error with respect to measured values, as reported in Table 2-12.

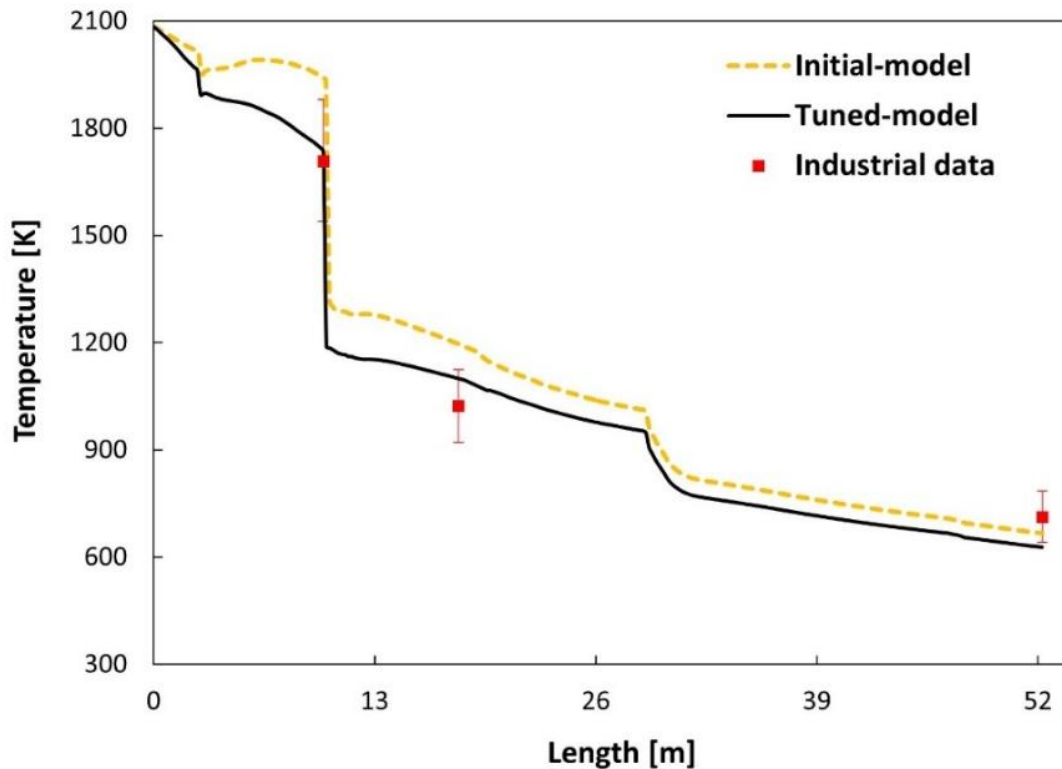


Figure 2-15. Predicted temperature profile for initial and tuned-model

The obtained results yield an interesting conclusion, highlighting the significance of wall modeling and its thermophysical properties, particularly thermal conductivity.

Table 2-12. Results from different developed models

Temperature [K]	Initial-model	Tuned-model	Measured	Error-Initial-model	Error-Tuned-model
Point A (length: 10 m)	1941	1740	1710	16%	2%
Point B (length: 18 m)	1193	1095	1023	23%	10%
Point D (length: 52 m)	667	630	713	10%	19%
<b>Heat loss [MW]</b>					
Reflux chamber	1.71	3.54	3.9	56%	9%
Rest	6.85	4.8	5.4	27%	11%

This result agrees with the finding of Joliff et al. [58], who have studied the effect of thermal conductivity on the heat-affected zone evolution for the homogenous material. They reported thermal conductivity as the driving physical parameter in the thermal exchange. Even though the tuned-model is in good agreement with measured values of the temperature and heat losses, there are limitations to using the model with confidence, and further improvement is required.

Following a recent inspection of the reflux chamber walls, the model underwent further improvements during a plant shutdown. The inspection revealed several insights. First, it was noted that the refractory layer thickness was no longer constant and uniform within the reflux chamber. The severe conditions inside the chamber, including complex chemical attacks, thermo-mechanical loading, and temperature fluctuations during various operations, had caused irreversible structural responses in the refractory material, including cracking, crushing, and gradual material loss. Second, the escaped molten iron ore from the CCF created accretion and build-up on some parts of the refractory, making the performance of the reflux chamber wall more complicated compared to the rest of the off-gas system (which do not have the refractory coatings on the wall).

Figure 2-16 shows the reflux chamber walls (used wall or non-fresh wall) near the oxygen lance during two different operational campaigns. According to the observations, erosion is most pronounced near the reflux chamber inlet, where the temperature is the highest. In these areas, the erosion has progressed to the point where the anchors' tips are visible. However, at certain points near the exit of the reflux chamber, the formation of slag layers has been observed. This phenomenon can be attributed to lower wall temperatures resulting from water cooling (not shown here).

The averaged refractory thickness is determined to be between 32 and 38 mm, with the data obtained from laser measurement at different cross sections. These measurements indicate a reduction in thickness compared to the original fresh wall thickness. It is essential to consider this phenomenon to develop a more reliable model that encompasses all possible phenomena and physics. As a result, new definitions were incorporated to establish a comprehensive methodology for wall modeling.



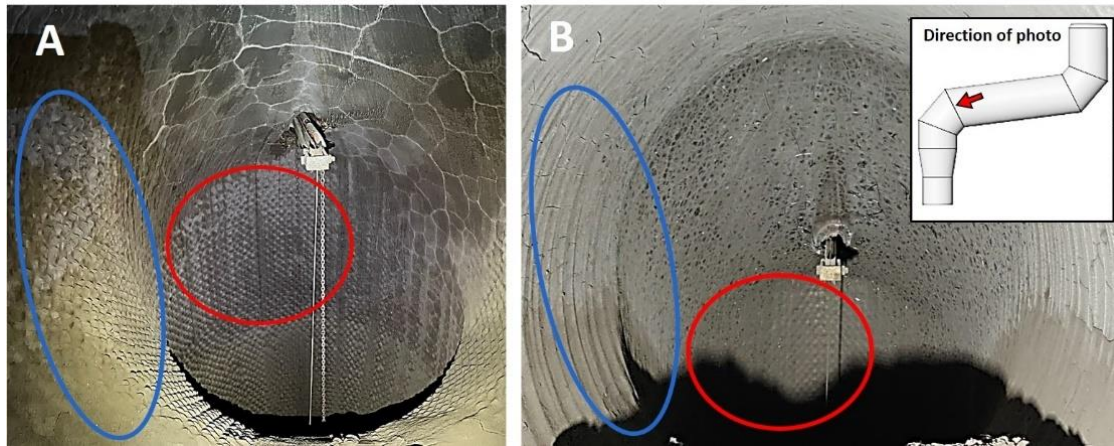


Figure 2-16. Reflux chamber wall inspection, inspection in 2021 (A) and inspection in 2019 (B)

In previous models, the fresh refractory wall thickness was considered 40 mm, which is a thickness from the base of the anchors, as shown with the letter “*d*” in Figure 2-17.

However, this thickness will not accurately represent the actual thickness of the equivalent wall in the model, as a substantial amount of refractory material is excluded from consideration. Therefore, it is more appropriate to define an effective thickness and utilize it as the equivalent wall thickness in the shell conduction approach.

The effective thickness ( $d_{eff}$ ) is defined as  $\frac{d+D}{2}$ . The “*d*” parameter represents tip thickness, which refers to the refractory thickness from the outer surface of the pipes. The “*D*” value is called “base thickness”, which indicates the refractory thickness starting from the middle of the cooling pipes where the refractory material begins.

In the shell conduction models, the value of  $d_{eff}$  will be used to assign equivalent wall thickness. For fresh refractory, the value of effective thickness is  $d_{eff} = 49.5$  mm ( $d_{eff} = d + pipe\ inner\ diameter\ (19\ mm) + pipe\ thickness\ (5\ mm)$ ).

The other parameters are the effective thermos-physical properties of the equivalent wall, which must be calculated by considering the effect of the embedded anchors. The EMA correlations presented before are unreliable and unable to accurately predict heterogenic material properties beyond a defined percolation threshold for the filler volume fraction.

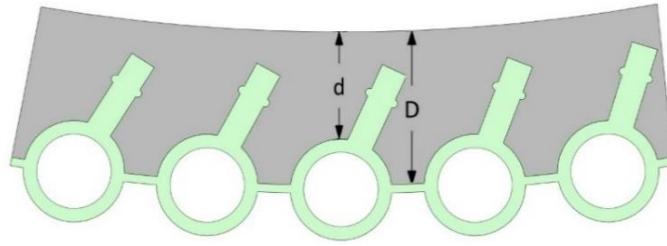


Figure 2-17. Schematic representation of refractory wall cross section with embedded anchors

Furthermore, for models that account for cylindrical fillers, such as the Rayleigh correlation, the alignment of fillers is typically regular and perpendicular to the heat transfer direction. This alignment differs from the situation in the reflux chamber wall. Additionally, in EMA correlations, the thermal interaction between fillers and the effects of filler orientation are either not included or are poorly defined for specific cases, which may not accurately represent the conditions in the present study. As mentioned earlier, in some regions of the reflux chamber wall, the refractory material loss is to a point where the tips of anchors become visible (see Figure 2-18).

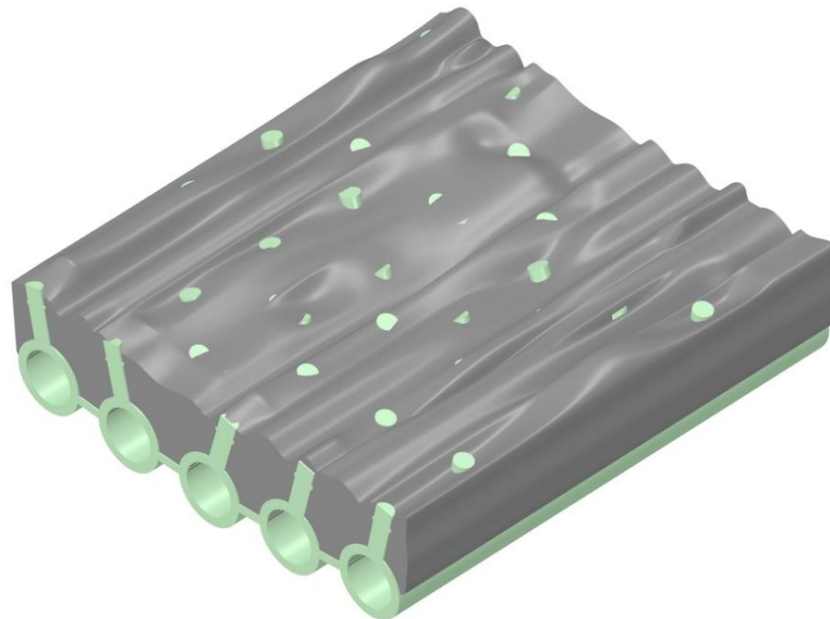


Figure 2-18. Wall erosion and anchor tip visibility and exposure to flue gas

As will be discussed in detail, this phenomenon will lead to a sharp increase in the thermal conductivity of the equivalent wall. EMA correlations cannot account for this occurrence because they assume that fillers are always fully embedded within the matrix volume. The most reliable approach is to use the FEM analysis, which is

a numerical analysis capable of solving heat transfer for any composite and homogenous material.

## 2.5. Final-model development

### 2.5.1. Wall properties using Finite Element Method (FEM)

Numerous researches are conducted on the heat transfer analysis and effective thermal conductivity calculation of the composite material using FEM analysis. Table 2-13 reports a short list of some studies.

Table 2-13. A summary of some studies on the application of FEM thermal analysis

Material	Load	Filler	Matrix	Application	Studied parameter	Reference
Carbon fibre reinforced plastic	Thermal-mechanical			Aerospace industry	Effective thermal conductivity	[67]
Fibre reinforced concrete	Thermal	Steel Plastic Fiberglass	Concrete	High thermal efficiency building	Effective thermal conductivity	[68]
Ceramic refractory	Thermal	Non	Magnesia-carbon brick	Ironmaking and Metallurgy	Crack propagation	[69]
Ceramic refractory	Thermal-mechanical	Non	Brick	Blast furnace lining	Stress response	[70]
Cu-diamond composite	Thermal	Copper	Diamond	High-power electronic devices	Effect of Particle Shape on the Thermal Conductivity	[71]
Aluminum alloy	Thermal	PPS/caco <sub>3</sub>	Sic <sub>p</sub> al	Aerospace industry	Effective thermal conductivity	[72]
Carbon/carbon composites	Thermal	Carbon bundle	Carbon	Aerospace structures (Thermal protection system-heat shield)	Effective thermal conductivity	[73]
Multiphase composites	Thermal	Carbon fibres	Polymer (polyacrylamide)	Engineering structures	Effective thermal conductivity	[74]
Rubber composites	Thermal	Carbon nanotubes (cnts), zinc oxide (zno) and alumina (Al <sub>2</sub> O <sub>3</sub> )	Emulsion-polymerized styrene-butadiene rubber (ESBR)	Aerospace industry Electronics packaging	Effective thermal conductivity	[75]
Cemented carbide shield	Thermal	Carbon nanotubes Graphene nano-platelets	WC-Co carbide	Heat shield	Effective thermal conductivity	[76]
Aluminium-reinforced composites	Thermal-mechanical	Sic	Aluminum alloy	Aviation, marine, electronic packaging, defence, automobile industries	Effective thermal conductivity	[77]
Woven composites	Thermal	Carbon fibre bundles	Epoxy resin	Structural engineering	Effective thermal conductivity	[78]
Woven Carbon/carbon composites	Thermal	Carbon fibre	Carbon	Aerospace and nuclear industries	Effective thermal conductivity	
Permeable-gas refractory ceramic	Thermal-mechanical	Non	Ceramic	Ironmaking and Metallurgy	Thermal shock	[79]
Refractory		Non	Magnesia and magnesia-chromite	Ironmaking and Metallurgy	Temperature and thermal stress distribution	[80]
Refractory lining of a steel ladle	Thermal	Non	Refractory concrete	Ironmaking and Metallurgy	Thermal shock damage	[81][82]
Refractory lining	Thermal	Non	Al <sub>2</sub> O <sub>3</sub> -sic-C brick	Ironmaking and Metallurgy	Thermal shock	[83]
Refractory linings	Thermal	Non	Refractory concrete	Ironmaking and Metallurgy	Cracking	[84]

To mention a few, Rashid et al. [66] have investigated and measured the thermal conductivity of burnt clay bricks reinforced with fibers using finite element analysis. Their study investigates the effect of filler material, volume fraction, length, and diameter on thermal conductivity, and their modelling results are validated against

experimental measurements. Nagy et al. [68] used FEM analysis to define the thermal properties (thermal conductivity, density, and specific heat capacity) of steel, plastic, and glass fiber reinforced concretes that are widely used for industrial floors. They reported the effect of filler type and volume fraction on the thermal properties of reinforced concrete. Andreev et al. [69] studied the thermo-mechanical response of the refractory materials to a service load, typical for a teeming ladle, utilizing FEM analysis. The model allows the detection of possible failure of the material during the heating-up period and cycling operation of the vessel. The influence of material parameters, the lining design, and parameters of the process are investigated. Gruber et al. [70] investigated the thermal behaviour of ceramic refractory materials applied to the lining of a blast furnace. They used the model to assist in material selection and lining design, considering the complex nature of refractories, which consist of several layers of different materials with various shapes and orientations. Their model allowed them to investigate the response of the lining to thermos-mechanical service loads and the interaction between the layers of the lining.

The following sections aim to develop the final CFD model using more precise thermos-physical properties of the equivalent wall and to correlate the wall thickness to other parameters that can be measured during the operations. Achieving this will give us an idea of the wall condition during the plant operation without directly measuring the wall thickness, which can be performed only during the plant shutdown.

### **2.5.2. Methodology**

Figure 2-19 shows the applied methodology and procedure to properly model the complex nature of the walls consisting of the following steps.

#### **Step 0:**

FEM analysis is performed to acquire effective thermal conductivity for different equivalent wall thicknesses.

#### **Step 1:**

A set of CFD calculations is performed for different equivalent wall thicknesses by assigning the thermal properties obtained by FEM analysis in Step 0 and for fixed

boundary conditions. For each given thickness, calculated parameters such as heat loss through the walls, the temperature at different points (A, B, and D in Figure 2-4), flue gas composition at various points (A and D in Figure 2-4), and carbon conversion are obtained.

### Step 2:

Each calculated parameter is plotted versus the equivalent wall thickness.

### Step3:

Ultimately, the plant-measured values for each parameter are mapped on the corresponding graphs from Step 2 to see at which thickness they intersect (see Figure 2-27). The obtained thickness is then compared to the measured one.

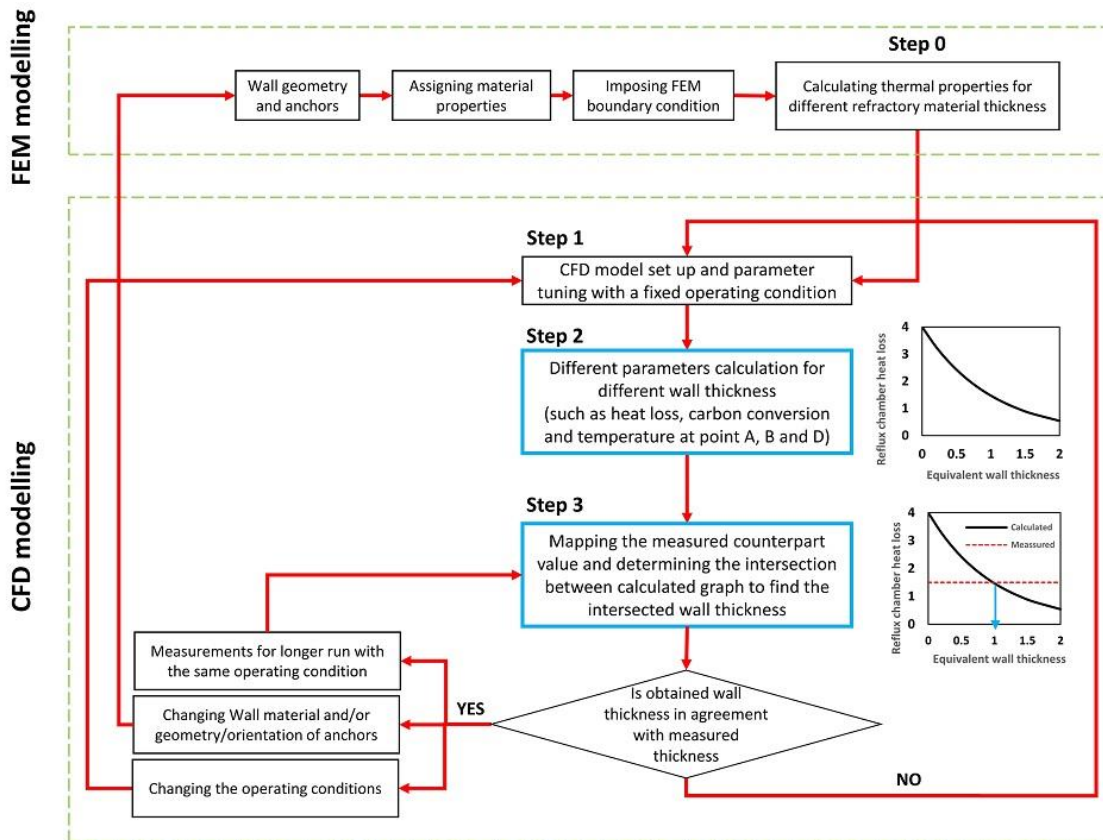


Figure 2-19. schematic representation of reflux chamber wall (A) and equivalent simplification (B) As will be discussed, this approach will lead to a fair prediction of wall thickness inside the reflux chamber (which is impossible to measure during the operation) using other parameters that can be measured during the operation (temperature, heat loss, etc.). It is important to note that this approach applies to a fixed operating period and the inlet condition. If there are changes in the inlet conditions, such as

inlet temperature, composition, and flow rate, or any other operating condition is changed (maybe after a long operation), Steps 1 to 3 will be repeated. This repetition is crucial because prolonged operation may lead to further reductions in wall thickness, potentially impacting the overall performance of the off-gas system. Additionally, if there are changes to the refractory wall material or modifications in the shape and orientation of the anchors, the entire flowchart, including FEM analysis, must be repeated.

### 2.5.3. FEM analysis

A steady state thermal analysis using FEM is performed to obtain properties of the equivalent refractory wall. A full-scale numerical analysis of large structures can be challenging and computationally expensive. However, this challenge can be mitigated by focusing on a smaller section that effectively represents the entire geometry. In this approach, the refractory wall with embedded anchors can be treated as a patterned array of identical cells, commonly referred to as unit cells or representative volume elements (RVE) [85]. In essence, a unit cell is a periodic representation that repeats itself throughout a larger geometry. The geometry and dimensions of the unit cell are illustrated in Figure 2-20.

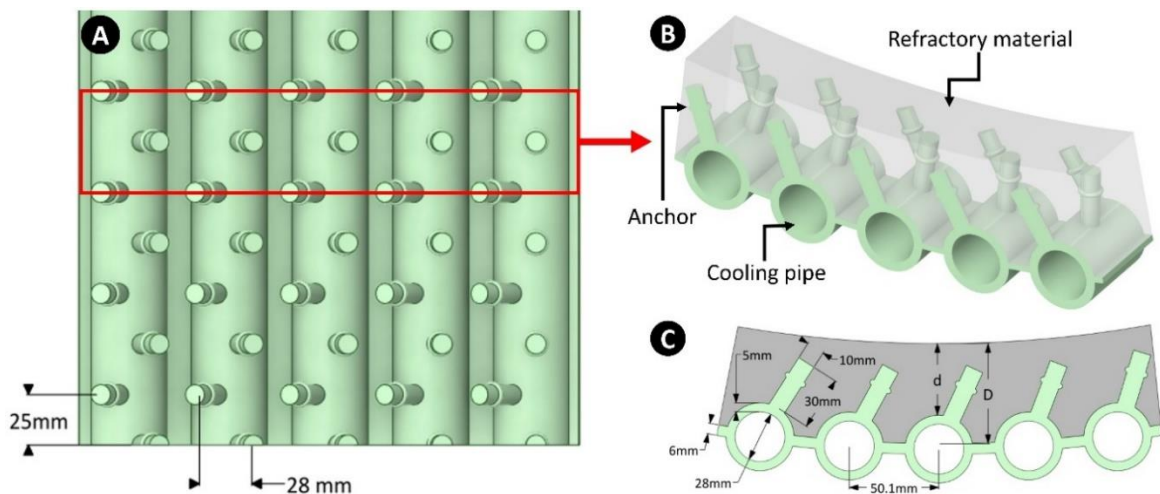


Figure 2-20. Part of the cooling pipe assembly (A); Unit cell with indicated components (B); Unit cell dimension and parameters (C) ( $d$ : tip thickness and  $D$ : base thickness)

As discussed, the anchors are covered by refractory material, and two different thicknesses, namely “ $d$ ” and “ $D$ ”, are defined for it (Figure 2-20.C). The pipes and anchors are made of steel (P235GH-TC1), and refractory is an alumina-silica material with the commercial name of Calde Stix 151. The material properties for



thermal analysis are taken from the Tata Steel commercial data sheet and listed in Table 2-14.

Table 2-14. material properties for FEM and CFD analysis (@ 293 K)

Material	$\rho$ [kg/m <sup>3</sup> ]	$k$ [W/m. K]	$C_p$ [j/kg K]	thickness [mm]
Refractory (Calde Stix 151)	2200	Figure 2-21	900	variable
Steel (P235GH-TC1)	7850	Figure 2-21	461	5

The thermal conductivities for both materials are considered as a function of temperature, as shown in Figure 2-21.

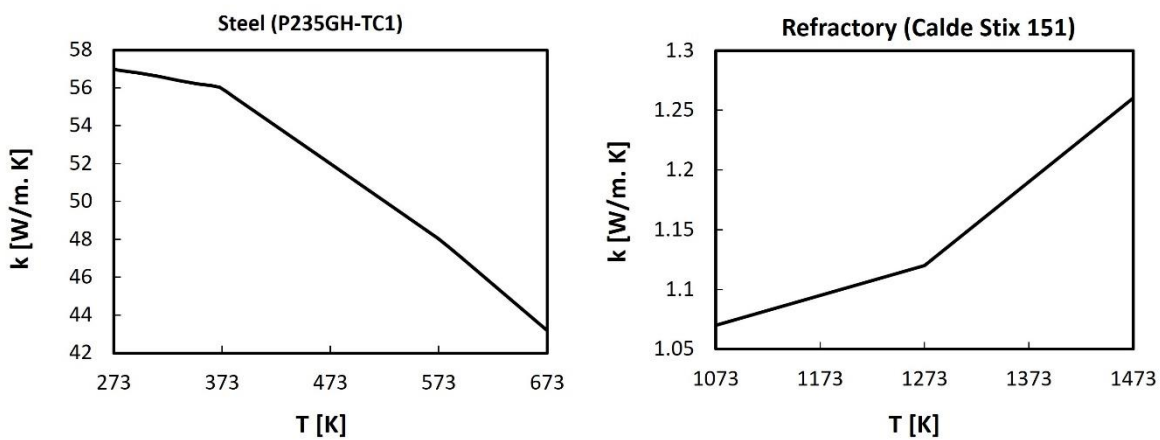


Figure 2-21. Temperature dependence of thermal conductivity for the FEM and CFD analysis

A finite element solver, SolidWorks®, is used to set up the model and calculate the temperature field within the unit cell by solving a three-dimensional conduction heat transfer equation as stated in Equation 2-64:

$$\frac{\partial}{\partial x} \left( k_x(T) \frac{\partial T}{\partial x} \right) + \frac{\partial}{\partial y} \left( k_y(T) \frac{\partial T}{\partial y} \right) + \frac{\partial}{\partial z} \left( k_z(T) \frac{\partial T}{\partial z} \right) + Q = \rho_s(T) C_p(T) \frac{\partial T}{\partial t} \quad (2-64)$$

Assuming the material is isotropic in steady state modelling without heat generation, Equation (2-64) can be simplified as Equation 2-65:

$$k(T) \left[ \frac{\partial^2 T}{\partial x^2} + \frac{\partial^2 T}{\partial y^2} + \frac{\partial^2 T}{\partial z^2} \right] = 0 \quad (2-65)$$

where  $k$  is isotropic thermal conductivity.



In addition to conductive heat transfer, heat can be transferred to the surroundings through convection. For instance, heat can be convected from the flue gas to the refractory surface or from the cooling pipes to the cooling water. To consider the heat transfer from the surfaces to the surroundings, convection boundary conditions are imposed according to Equation 2-66:

$$k(T) \left( \frac{\partial T}{\partial n} \right) + h(T - T_0) = 0 \quad (2-66)$$

Figure 2-22.A shows the convective boundary conditions considered for the simulations. The inner side of the unit cell is in touch with hot flue gas with an average temperature of 1673 K and a heat transfer coefficient of 200 W/m<sup>2</sup>. K. The heat transferred through the walls and pipe is absorbed by cooling water flowing through the pipes at an average temperature of 313 K and a high convective heat transfer coefficient of 5000 W/m<sup>2</sup>.K. The Outer surface of the cooling pipe is exposed to the surrounding air at a temperature of 298 K and a heat transfer coefficient of 40 W/m<sup>2</sup>.K.

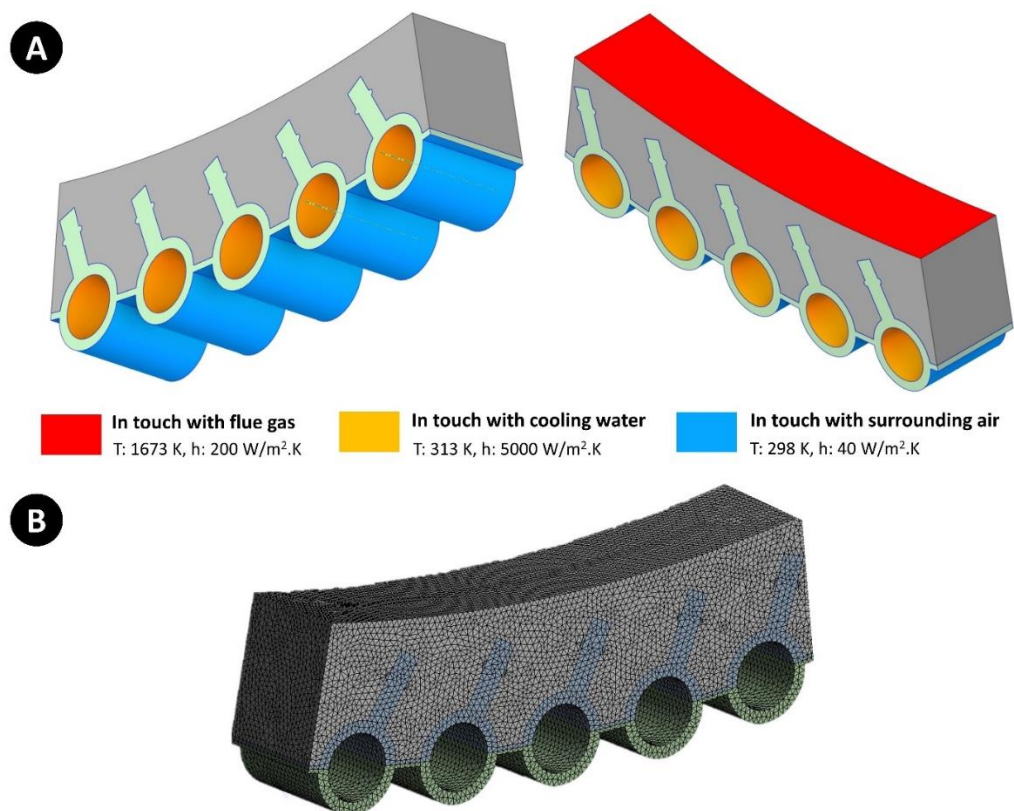


Figure 2-22. Thermal boundary conditions for FEM analysis of unit cell (A) and computational mesh grid (B)

The periodic boundary condition is imposed on the side walls. Figure 2-22.B illustrates the discretized computational domain with 750,000 tetrahedral cells (element size = 2.5 mm). The heat flux through the walls and surface temperatures are calculated and then used to estimate the effective thermal conductivity of the refractory and anchor composite.

#### 2.5.4. Effective thermal conductivity of equivalent wall (Step o)

The calculated surface temperature and heat flow for different refractory thicknesses of the unit cell are reported in Table 2-15. The effective thermal conductivity is estimated using the calculated temperature profiles and heat flow as stated in Equation 2-67:

$$k_{eff} = \frac{HF}{T_h - T_c} \cdot d_{eff} \quad (2-67)$$

where  $HF$  is the calculated heat flow,  $d_{eff}$  is the effective thickness of the refractory ( $\frac{d+D}{2}$ ),  $T_h$  is hot surface temperature and  $T_c$  is the outer surface temperature of the refractory wall in touch with the cooling pipes. Densities and heat capacities are calculated using mixing law and based on the anchor and refractory mass fractions as stated in Equations 2-55 and 2-56.

The values for effective thermal conductivity, based on the FEM analysis and reviewed EMA models, are shown in Figure 2-23 for different refractory thicknesses and filler volume fractions. Most of the EMA models have predicted a similar trend and values, which are in significant discrepancy with FEM analysis results.

Table 2-15. Obtained values for equivalent (composite) wall from FEM analysis

d [mm]	25*	30	35	40	45	50	60	70	80	90	100
D [mm]	44	49	54	59	64	69	79	89	99	109	119
$d_{eff}$ [mm]	34.5	39.5	44.5	49.5	54.5	59.5	69.5	79.5	89.5	99.5	109.5
HF [kW/m <sup>2</sup> ]	115	72.5	57.3	48.3	41.9	37.1	30.2	25.5	22.1	19.5	17.5
$T_c$ [K]	333	329	326	324	322	321	320	319	318	318	317
$T_h$ [K]	1258	1323	1387	1431	1463	1487	1522	1546	1563	1576	1586
$k_{eff}$ [W/m. K]	4.29	2.88	2.40	2.16	2.00	1.89	1.74	1.65	1.58	1.54	1.51
$\rho_{eff}$ [kg/m <sup>3</sup> ]	3251	3136	3044	2970	2908	2855	2771	2707	2657	2616	2583
$C_{p,eff}$ [J/kg. K]	818	827	834	840	845	849	856	861	865	868	870
* bare anchors											

Only the Rayleigh model has predicted values close to the FEM analysis; however, there is still a large difference between the two as Rayleigh predicts higher values than those obtained with FEM analysis. As it can be seen, for all analysis, there is an increase in thermal conductivity by decreasing refractory thickness. FEM analysis has predicted a sharp increase in effective thermal conductivity once the tip of the anchors becomes visible ( $d = 25$  mm). The effective thermal conductivity reaches a constant value close to the averaged conductivity of pure refractory ( $k = 1.15$  W/m.K) by increasing the refractory thickness. The values and results obtained using FEM analysis will be used and discussed for further analysis in CFD models.

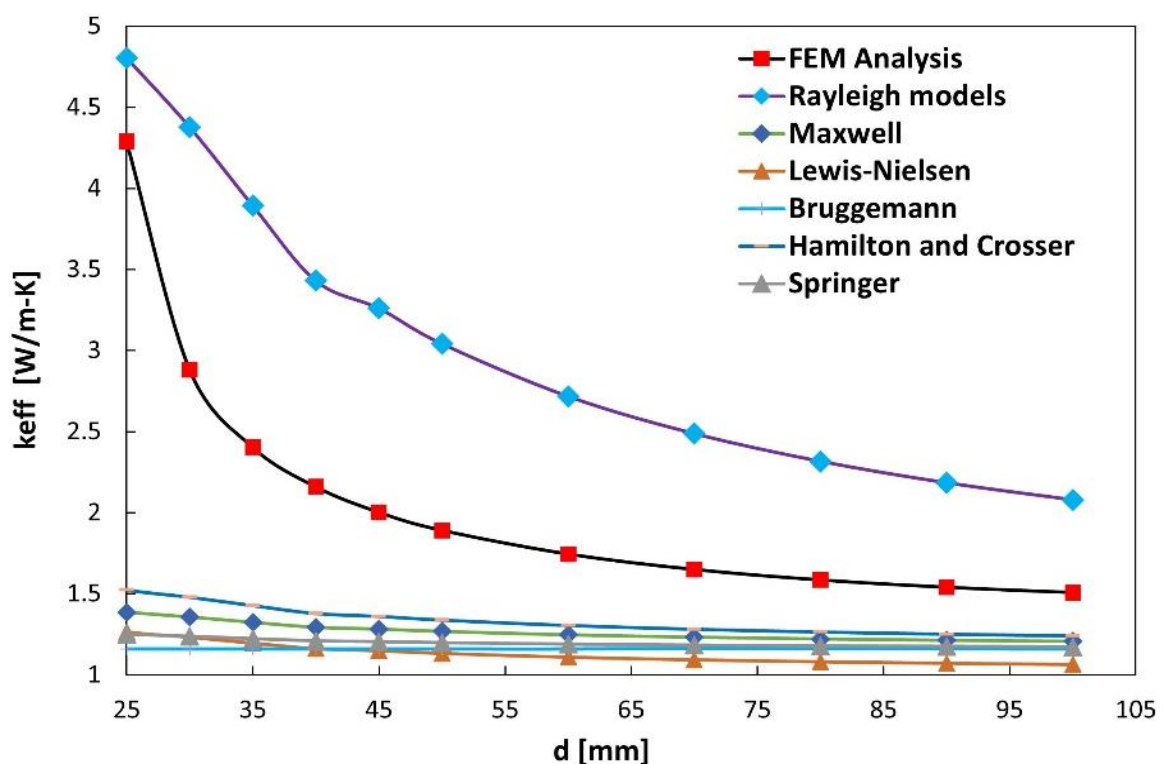


Figure 2-23. Calculated effective thermal conductivity using different models (in all calculations  $k_m=1.15$  W/m. K  $k_f=55$  W/m. K and the volume fraction of the filler is calculated for different refractory thickness)

Figure 2-24 shows the temperature distribution over the unit cell volume for different  $d$  values. As can be seen, the highest temperature occurs at the outer surface of the refractory, where it is in touch with hot flue gas. However, for the cases with lower wall thickness, the surface temperature of refractory reduces as more heat will flow through the wall thickness due to the higher thermal conductivity of the unit cell.

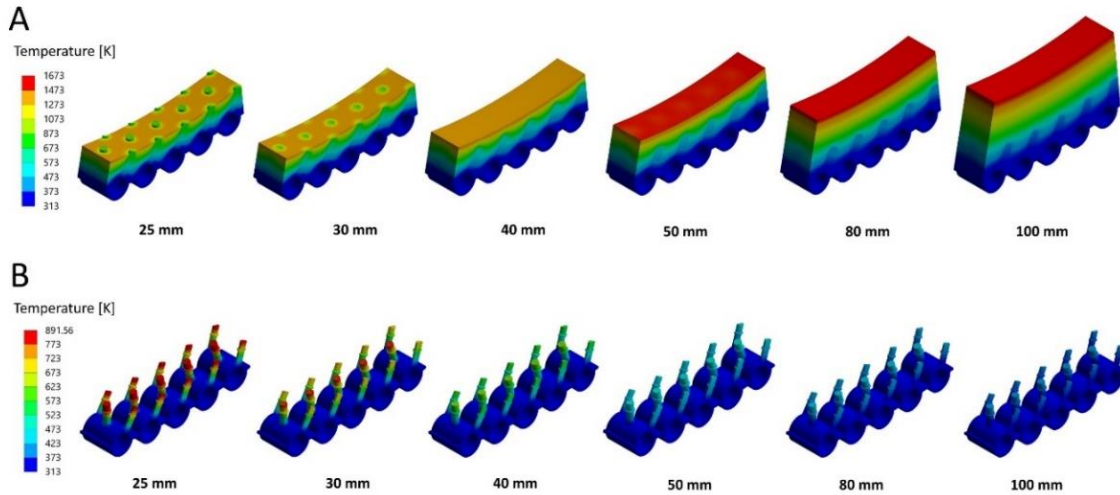


Figure 2-24. Calculated temperature contours for refractory and embedded anchors (A) and the anchors (B)

By reducing the refractory thickness, which acts as isolation, the tip of the anchors will be closer (or imposed) to the hot flue gas, and more heat will flow through the anchors and, therefore, through the whole wall.

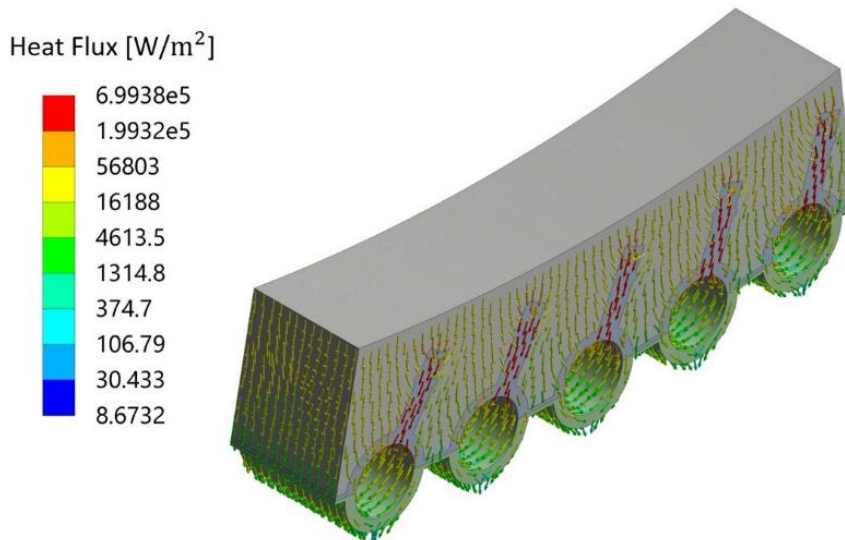


Figure 2-25. Calculated directional heat flux in the unit cell

The effective thermal conductivity increases for two main reasons. First, when the refractory thickness is reduced, the volume fraction of anchors (made of steel with significantly higher thermal conductivity) increases, leading to higher overall thermal conductivity. Secondly, a substantial portion of heat is conducted through the anchors to the cooling pipes, as illustrated in Figure 2-25, with the highest heat flux occurring near the anchor locations.

Another interesting finding is depicted in Figure 2-26.A, which shows the isotherm pattern for different temperatures. A clear relationship exists between the isotherms and the erosion pattern inside the reflux chamber (Figure 2-26.B). The isotherms illustrate that refractory regions near the tip of the anchors experience lower temperatures (due to higher heat flux) compared to regions farther away and vice versa. Consequently, regions near the tip of the anchors endure less thermal stress, contributing to their extended life cycle. However, it is important not to overlook the potential impact of thermal expansion in the anchors, which can lead to cracks and, ultimately, material loss in the wall. This phenomenon is responsible for the wavy isotherms that align with the observed erosion pattern.

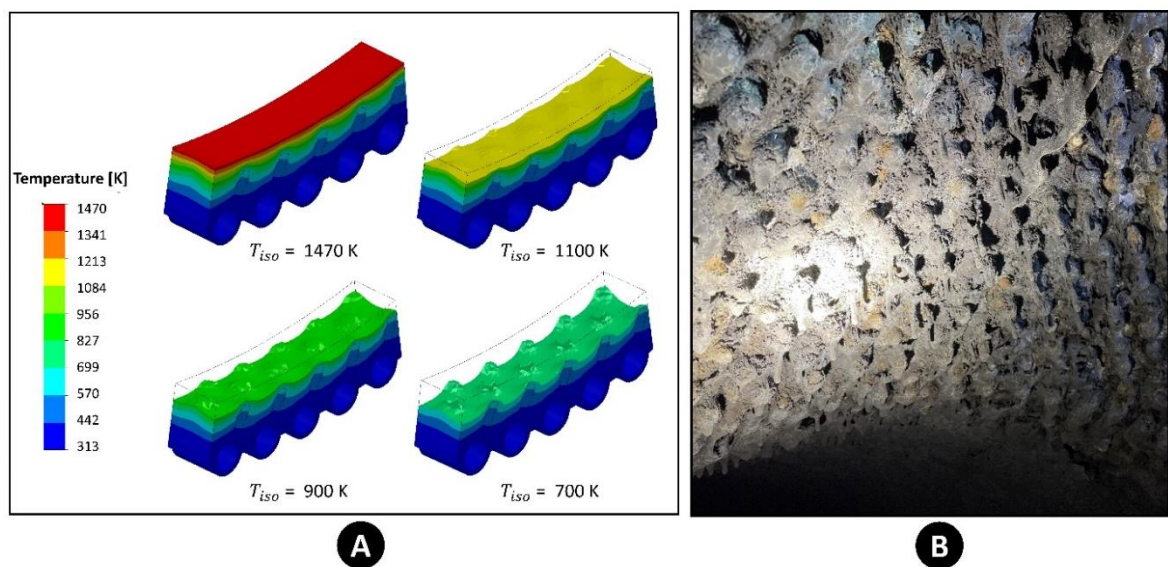


Figure 2-26. Predicted isotherm for different temperatures and observed erosion inside the reflux chamber

### 2.5.5. Sensitivity analysis using the final CFD model (Steps 1, 2, and 3)

CFD analysis of the entire off-gas system is performed using different wall boundary conditions inside the reflux chamber, where the wall is modelled with a two-layer approach. Five cases are considered for the equivalent wall layer (first layer), as highlighted in Table 2-15. For each case,  $k_{eff}$ ,  $c_{p,eff}$ ,  $\rho_{eff}$ ,  $d_{eff}$  are assigned for the effective thermal conductivity, heat capacity, density, and thickness of the layer, respectively.

The cases are named based on the tip thickness ( $d$ ) for simplicity of the analysis and plotting graphs. So, for example, a case with  $d = 40$  mm corresponds to a CFD case



where the equivalent wall thickness, thermal conductivity, density, and heat capacity are 49.5 mm, 2.16 W/m-K, 2970 kg/m<sup>3</sup>, 840 J/kg·K respectively. The pipe wall thickness (second layer) is steel material with known properties and is similar for all studied cases. The rest of the boundary conditions and model setup are the same for all cases. Figure 2-27 shows the calculated temperatures (points A, B, and D), O<sub>2</sub> mole fraction (point A), and heat losses in the reflux chamber and the rest of the off-gas system for different cases (based on correspondent  $d$  values).

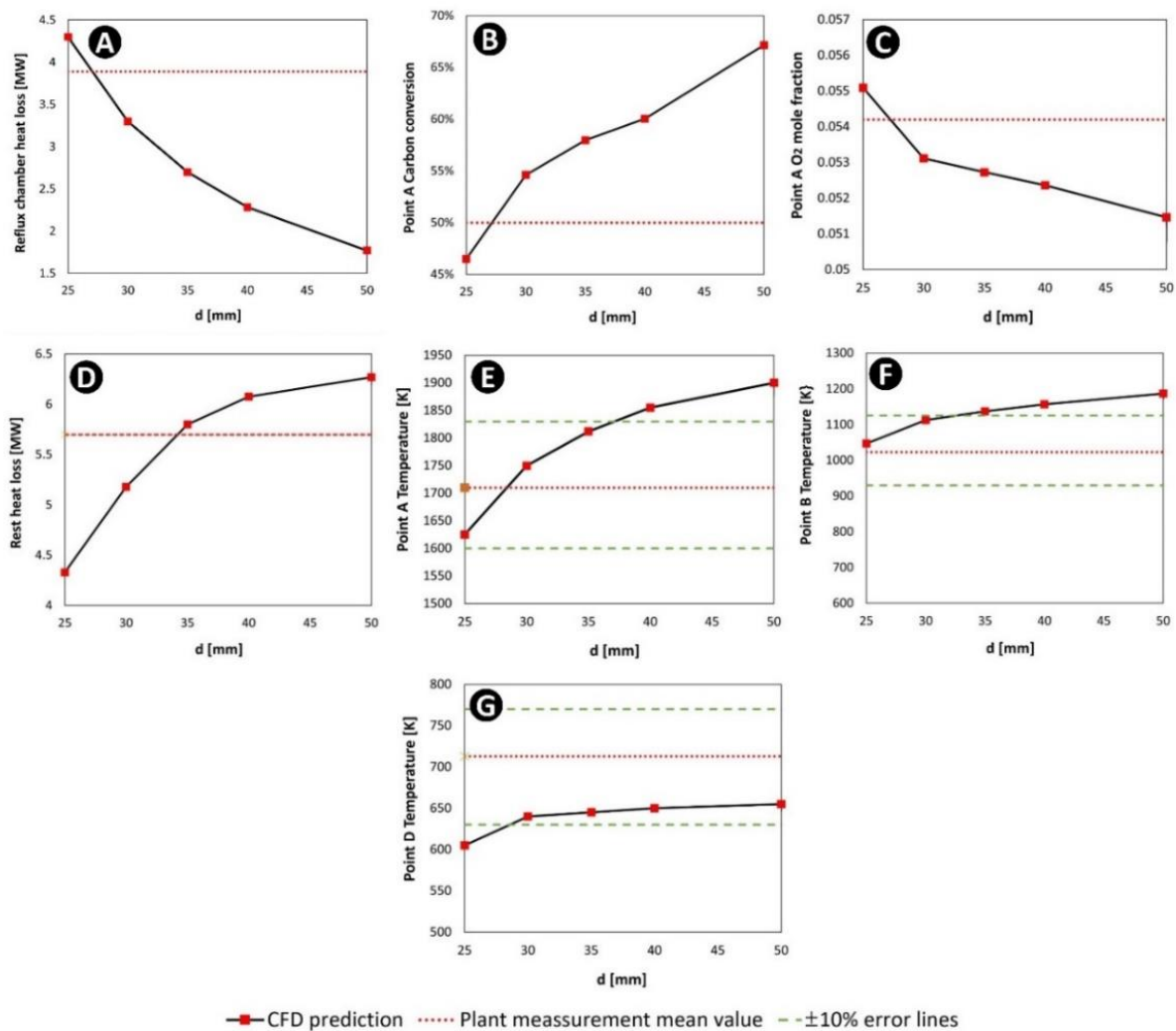


Figure 2-27. Predicted heat loss, O<sub>2</sub> mole fraction (dry basis), and the temperatures for different  $d$  values

The horizontal dot lines represent each parameter's measured values at the pilot plant. For temperature graphs,  $\pm 10\%$  measurement error is also shown with extra horizontal lines. As can be seen from Figure 2-27.A, by increasing the equivalent wall thickness in the models (and generally increasing refractory wall thickness), the

amount of heat loss from the reflux chamber walls is substantially reduced. On the other hand, lower heat loss will increase the temperature inside the reflux chamber and other parts of the off-gas system (Figure 2-27.D to F). Due to a higher temperature within the reflux chamber, one can expect an increase in the rate of CO-H<sub>2</sub> and carbon particle conversion (Figure 2-27.B) and, consequently, a reduction in O<sub>2</sub> amount (Figure 2-27.C) at the outlet of the reflux chamber.

Based on the Figure 2-27.A to E, the calculated curves and measured lines intersect at a “*d*” value between 25 and 35 mm. This interval corresponds to an effective wall thickness (*d<sub>eff</sub>*) between 34.5 and 44.5 mm (see Table 2-15), which is in good agreement with the measured average thickness of 32 to 38 mm during reflux chamber wall inspections. Calculated temperature graphs at points B and D (Figure 2-27.F and G) are also shown, and as it is evident, the measured mean values are falling outside the calculated range. However, the calculated graphs are still between the measured error lines. As can be comprehended, using the mentioned methodology (summarized in Figure 2-19), it is possible to have an approximate average refractory thickness and a general idea of the refractory condition without direct measurements and using parameters that can be measured during the operation without going into shut down.

Using these graphs, specifically those with the least errors (heat losses, O<sub>2</sub> composition, and carbon conversion), *d* = 27.5 mm, which corresponds to an averaged equivalent wall thickness (*d<sub>eff</sub>*) of 37 mm, seems to be a reasonable value for tuning the heat transfer in the final CFD model for the current operational and wall conditions.

The properties corresponding to the considered effective wall thickness are summarized in Table 2-16.

Table 2-16. Wall properties used in shell conduction model for tuned (used wall) CFD calculation

	Equivalent refractory (First layer)	Steel pipe thickness (Second layer)
<b><i>d<sub>eff</sub></i> [mm]</b>	37	5
<b><i>k<sub>eff</sub></i> [W/m. K]</b>	3.65	Function of temperature (see Figure 2-21)
<b><i>ρ<sub>eff</sub></i> [kg/m<sup>3</sup>]</b>	3010	7850
<b><i>cp<sub>eff</sub></i> [J/kg. K]</b>	836	461

Figure 2-28, Figure 2-29, and Table 2-17 summarize the calculated profiles and values for the initial, tuned, and final-model. As it can be seen, an overall improvement in predictions is achieved using the final-model.

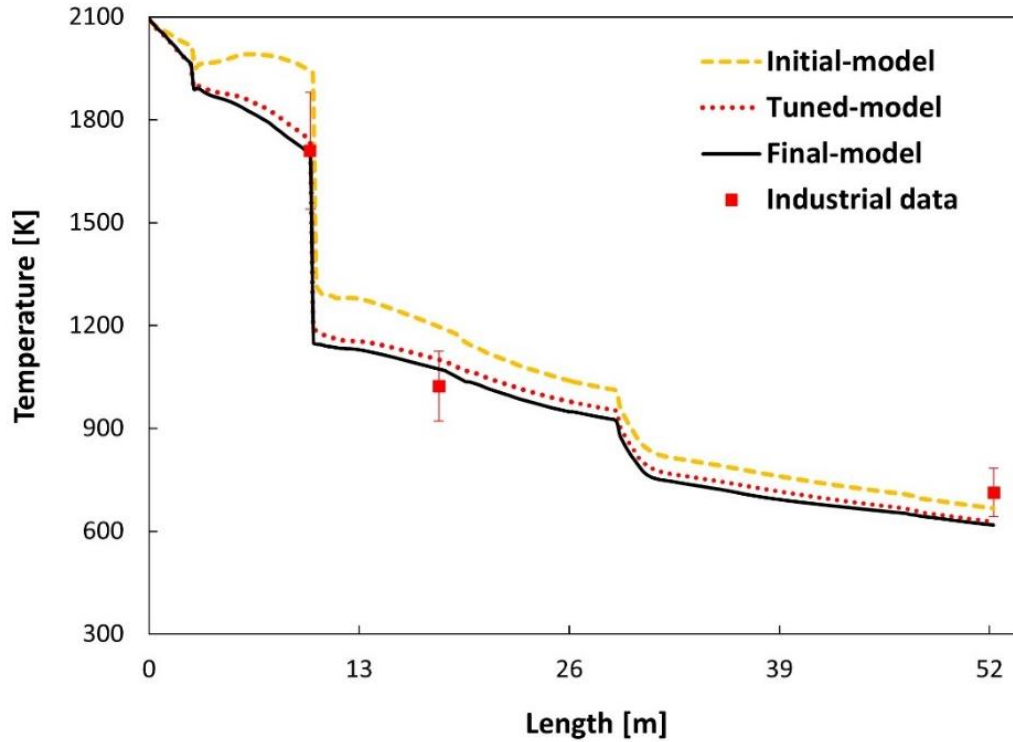


Figure 2-28. Calculated temperature profile for initial, tuned, and final-model

Another set of simulations is performed using the material properties of the fresh and used wall. Fresh wall refers to the case with original refractory thickness applied during the reflux chamber construction ( $d=40$  mm and  $d_{eff}=49.5$  mm).

Table 2-17. Calculated average temperature error at different measured points for different models

Temperature [K]	Error-Initial-model	Error-Tuned-model	Error-Final-model
Point A (length: 10 m)	16%	2%	1%
Point B (length: 18 m)	23%	10%	7%
Point D (length: 52 m)	10%	19%	21%
Heat loss [MW]			
Reflux chamber	56%	9%	1%
Rest	27%	11%	12%

Temperature profiles in Figure 2-30 exhibit a significant mismatch between the plant data and the predictions for a fresh wall, while there is a strong agreement with the case that incorporates the used wall condition.



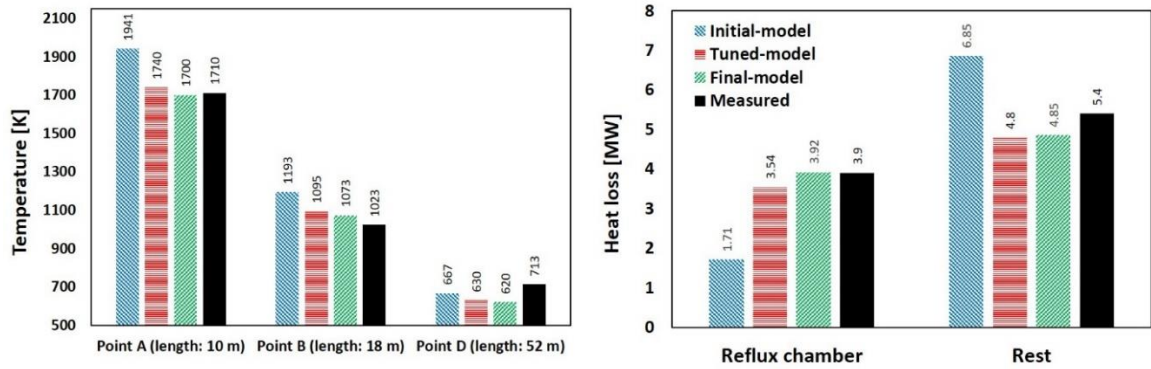


Figure 2-29. Calculated temperature at different measurement points and heat losses in different off-gas section

However, this discrepancy is either not visible or minor in the predicted gas composition profile, as demonstrated in Figure 2-31. Figure 2-32 provides a comprehensive view of the calculated and measured heat losses (at different regions), oxygen mole fraction, carbon conversion, and temperatures at various measurement points for more precise quantitative comparisons. These results consistently suggest that the refractory material thickness has changed and is no longer in a fresh condition, which aligns with the observations from the reflux chamber wall inspection, where local erosions and material loss have been identified. Reducing refractory material thickness will increase the thermal conductivity and thus the heat loss through the reflux chamber wall. This will reduce the local temperature profile and might affect the off-gas composition.

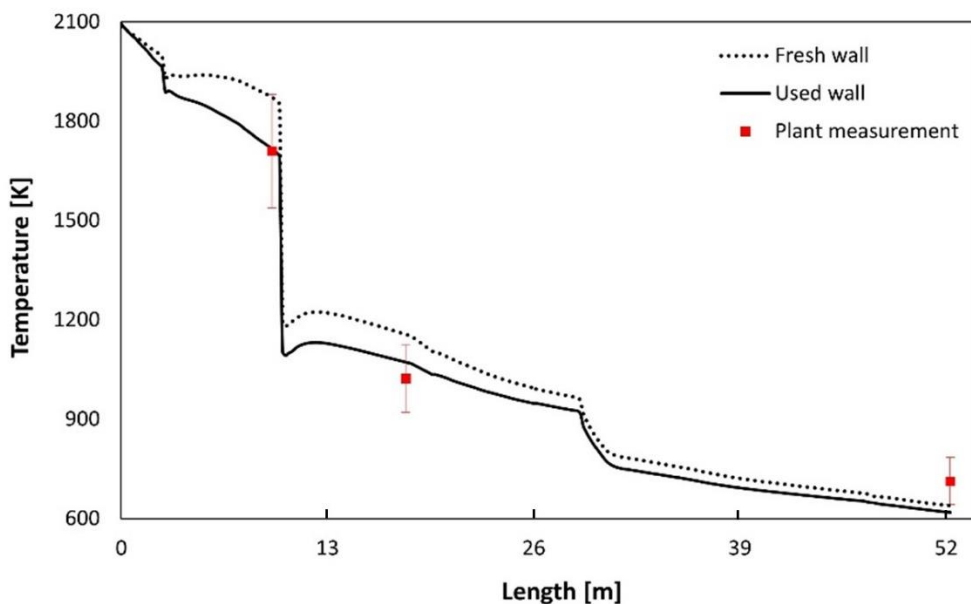


Figure 2-30. Predicted gas temperature profile using the tuned CFD model. Measured temperatures are shown with  $\pm 10\%$  error bars

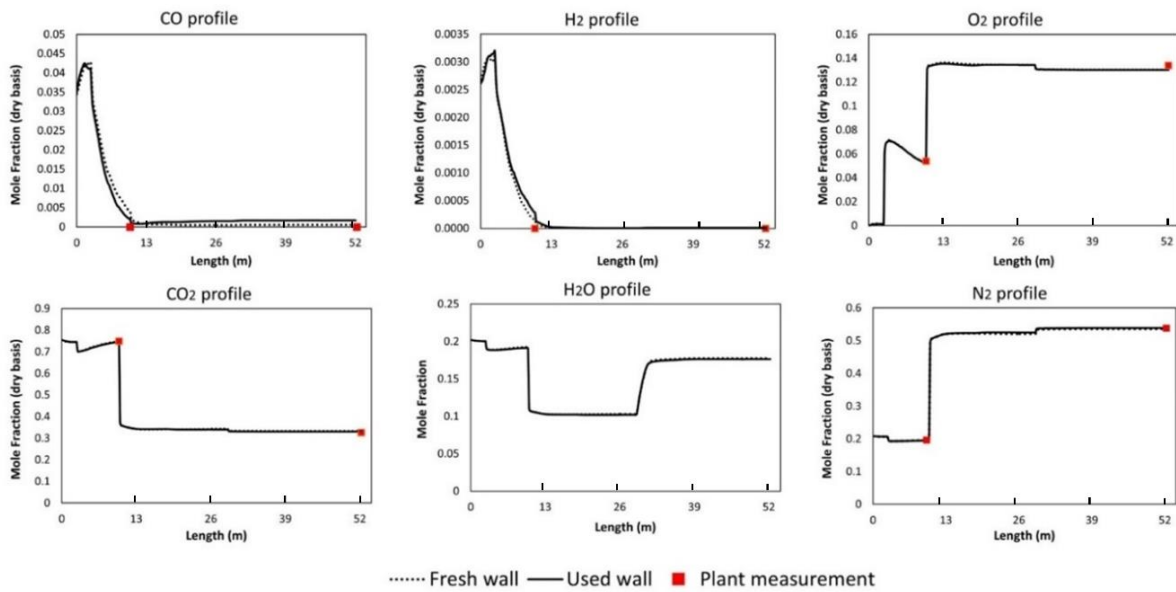


Figure 2-31. Predicted gas composition profiles using the tuned CFD mode

For example, using the fresh wall, which shows a higher local temperature, a higher carbon conversion at the outlet of the reflux chamber, and a slightly lower oxygen molar fraction is predicted. However, the change in off-gas composition is minor for this modelled operating condition.

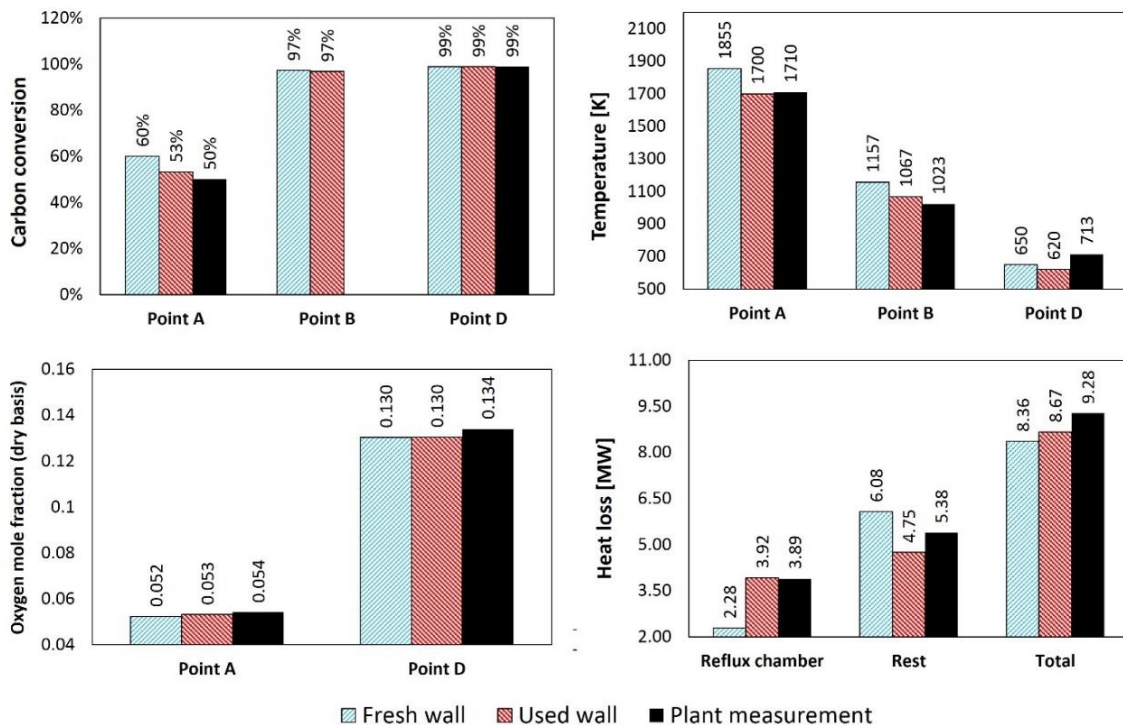


Figure 2-32. Calculated and measured parameters at different regions and measurement points ( $\pm 10\%$  plant measurement error for temperature is not shown).

## 2.6. Conclusion

In this chapter, a base model for the HIsarna off-gas system is developed using a detailed CFD approach. However, the results of the initial-model indicated noticeable discrepancies between the predictions, such as the temperature profile and heat losses, and the measured data.

The primary reason for these discrepancies was the inaccurate assignment of material properties to the various layers of the reflux chamber wall. The wall within the reflux chamber consists of steel cooling pipes with anchors to support an additional refractory layer, providing additional insulation. In contrast, the wall above the reflux chamber consists of cooling pipes without anchors and a refractory layer. Thus, the wall within the reflux chamber demands special attention for precise modeling.

Since the refractory layer includes embedded steel anchors, the assigned thermal conductivity for this layer cannot be the same as pure refractory, which is relatively low. The steel anchors embedded within the wall increase the effective thermal conductivity of this material layer. Consequently, this layer is regarded as a composite layer with the refractory material acting as a matrix and the embedded anchors functioning as fillers, and it is referred to as the equivalent wall.

EMA relations are employed to estimate the equivalent thermal conductivity of the wall. Utilizing this approach and taking into account the thermal influence of the embedded anchors, the calculated thermal conductivity of the equivalent wall (with a thickness of 40 mm) is significantly higher than that of the pure refractory material.

Using this value, the predicted temperature profiles and heat losses are in fair agreement with the measured values. However, with further inspection of the reflux chamber wall during the plant shut-down, it turned out that the thickness of the refractory material applied on top of the cooling pipes was no longer the same as the original thickness of 40 mm.

Hence, a reliable approach is necessary to determine effective thermos-physical properties and the effective equivalent wall thickness in order to improve the accuracy of model predictions. Based on the literature review, the FEM approach has been identified as the most suitable method for obtaining the equivalent wall

properties. A comprehensive FEM analysis of the reflux chamber walls, including the precise geometry of the embedded anchors, has been conducted. Effective thermal conductivity is estimated for various refractory material thicknesses, and CFD simulations are executed for each equivalent wall thickness.

Then, using the measured values, an approximate calculated wall thickness is obtained. The predicted thickness for the equivalent wall agrees with the measured values during the wall inspections. The corresponding thermo-physical property values for the equivalent wall are determined using the obtained thickness to set up the final-model.

This approach becomes particularly important when considering wall geometry changes, such as changes to anchor numbers, positions, and length. It also plays a crucial role in designing the reflux chamber for scaled-up cases, which will be discussed in detail in the upcoming chapters.

Besides the mentioned conclusions regarding the proposed methodology, the following can also be concluded based on the obtained results:

1. Wall modelling and thermo-physical properties assignment in the CFD model significantly affect temperature, composition, and heat loss profile prediction.
2. In the HIsarna off-gas system, the applied refractory inside the reflux chamber has a very low thermal conductivity; however, the embedded steel anchors inside the refractory material can increase the thermal conductivity by a factor of 3.
3. Refractory loss and thickness reduction increase the thermal conductivity of the wall.
4. Using the original refractory thickness (thickness during the reflux chamber construction), CFD models predict much lower heat losses and higher temperature profiles. These results suggest that the thickness of the refractory inside the reflux chamber is no longer the same as the original thickness. This conclusion is supported by direct measurements of the walls during the shutdown period.

5. FEM analysis is more reliable than the available EMA correlation for predicting the thermal conductivity of the reflux chamber walls, which can be considered as a composite of refractory matrix and anchor fillers.
6. Based on the proposed methodology, on average, an effective wall thickness of 37 mm predicts heat losses, temperature, and composition profiles, which is in excellent agreement with current plant measurements. The predicted wall thickness is in good agreement with the direct thickness measurements which was between 32 to 38 mm.
7. According to the proposed methodology, it is possible to indirectly measure the average refractory thickness from other measured values during the operations, such as heat loss, temperature, and gaseous compositions.

## References

- [1] C. Yigit, G. Coskun, E. Buyukkaya, U. Durmaz, H.R. Güven, CFD modeling of carbon combustion and electrode radiation in an electric arc furnace, *Appl Therm Eng.* 90 (2015) 831–837. <https://doi.org/10.1016/J.APPLTHERMALENG.2015.07.066>.
- [2] A. Cardarelli, M. De Santis, F. Cirilli, M. Barbanera, Computational fluid dynamics analysis of biochar combustion in a simulated ironmaking electric arc furnace, *Fuel.* 328 (2022) 125267. <https://doi.org/10.1016/J.FUEL.2022.125267>.
- [3] A.A. Ahmadi, M. Bahiraei, Thermohydraulic performance optimization of cooling system of an electric arc furnace operated with nanofluid: A CFD study, *J Clean Prod.* 310 (2021) 127451. <https://doi.org/10.1016/J.JCLEPRO.2021.127451>.
- [4] K.T. Karalis, N. Karkalos, N. Cheimarios, G.S.E. Antipas, A. Xenidis, A.G. Boudouvis, A CFD analysis of slag properties, electrode shape and immersion depth effects on electric submerged arc furnace heating in ferronickel processing, *Appl Math Model.* 40 (2016) 9052–9066. <https://doi.org/10.1016/J.APM.2016.05.045>.
- [5] Y. Chen, S. Ryan, A.K. Silaen, C.Q. Zhou, Simulation of Scrap Melting Process in an AC Electric Arc Furnace: CFD Model Development and Experimental Validation, *Metallurgical and Materials Transactions B.* 53 (2022) 2675–2694. <https://doi.org/10.1007/s11663-022-02559-6>.
- [6] T. Okosun, A.K. Silaen, G. Tang, B. Wu, C.Q. Zhou, CFD Analysis of Blast Furnace Operating Condition Impacts on Operational Efficiency, in: L. Nastac, L. Zhang, B.G. Thomas, M. Zhu, A. Ludwig, A.S. Sabau, K. Pericleous, H. Combeau (Eds.), *CFD Modeling and Simulation in Materials Processing 2016*, Springer International Publishing, Cham, 2016: pp. 75–82. [https://doi.org/10.1007/978-3-319-65133-0\\_10](https://doi.org/10.1007/978-3-319-65133-0_10).
- [7] D. Fu, Y. Chen, Y. Zhao, J. D'Alessio, K.J. Ferron, C.Q. Zhou, CFD modeling of multiphase reacting flow in blast furnace shaft with layered burden, *Appl Therm Eng.* 66 (2014) 298–308. <https://doi.org/10.1016/J.APPLTHERMALENG.2014.01.065>.
- [8] M. Vångö, C. Feilmayr, S. Pirker, T. Lichtenegger, Data-assisted CFD modeling of transient blast furnace tapping with a dynamic deadman, *Appl Math Model.* 73 (2019) 210–227. <https://doi.org/10.1016/J.APM.2019.04.024>.
- [9] S. Wang, Y. Shen, CFD-DEM modelling of raceway dynamics and coke combustion in an ironmaking blast furnace, *Fuel.* 302 (2021) 121167. <https://doi.org/10.1016/J.FUEL.2021.121167>.
- [10] Z. Miao, Z. Zhou, A.B. Yu, Y. Shen, CFD-DEM simulation of raceway formation in an ironmaking blast furnace, *Powder Technol.* 314 (2017) 542–549. <https://doi.org/10.1016/J.POWTEC.2016.11.039>.
- [11] H. Sun, J. Zhang, Z. Liu, J. Qiu, R. Mao, G. Wang, The Numerical Simulation of Flow-Field Inside the Raceway in Blast Furnace Based on CFD, in: F. Marquis (Ed.), *Proceedings of the 8th Pacific Rim International Congress on Advanced Materials and Processing*, Springer International Publishing, Cham, 2016: pp. 3051–3061.
- [12] H.-J. Odenthal, U. Thiedemann, U. Falkenreck, J. Schlueter, Simulation of Fluid Flow and Oscillation of the Argon Oxygen Decarburization (AOD) Process, *Metallurgical and Materials Transactions B.* 41 (2010) 396–413. <https://doi.org/10.1007/s11663-009-9335-y>.
- [13] A. Kemminger, F. Krause, H.-J. Odenthal, CFD simulation of top-blown converters, 2022.
- [14] W. Wei, P. Samuelsson, A. Tilliander, D.-Y. Sheng, P.G. Jönsson, Numerical Analysis of Fluid Flow and Temperature Distributions of O<sub>2</sub>/N<sub>2</sub> Gas Mixtures in AOD Nozzles, *ISIJ*

- International. 63 (2023) 319–329. <https://doi.org/10.2355/isijinternational.ISIJINT-2022-370>.
- [15] Y. Tang, T. Fabritius, J. Härkki, Mathematical modeling of the argon oxygen decarburization converter exhaust gas system at the reduction stage, *Appl Math Model.* 29 (2005) 497–514. <https://doi.org/10.1016/J.APM.2004.09.011>.
- [16] Z. Cheng, Y. Wang, A. Dutta, B. Blanpain, M. Guo, A. Malfliet, Numerical Study of Fluid Flow and Mixing in the Argon Oxygen Decarburization (AOD) Process, *ISIJ International.* 63 (2023) 492–503. <https://doi.org/10.2355/isijinternational.ISIJINT-2022-418>.
- [17] F.M. Najjar, B.G. Thomas, D.E. Hershey, Numerical study of steady turbulent flow through bifurcated nozzles in continuous casting, *Metallurgical and Materials Transactions B.* 26 (1995) 749–765. <https://doi.org/10.1007/BF02651721>.
- [18] P. Gardin, M. Brunet, J.F. Domgin, K. Pericleous, An experimental and numerical CFD study of turbulence in a tundish container, *Appl Math Model.* 26 (2002) 323–336. [https://doi.org/10.1016/S0307-904X\(01\)00064-6](https://doi.org/10.1016/S0307-904X(01)00064-6).
- [19] L. Zhang, S. Taniguchi, K. Cai, Fluid flow and inclusion removal in continuous casting tundish, *Metallurgical and Materials Transactions B.* 31 (2000) 253–266. <https://doi.org/10.1007/s11663-000-0044-9>.
- [20] C. Eastman, P. Glaws, D. Cao, Liquid Steel Flow and Interactions with Nonmetallic Phases in the Continuous Casting Tundish Using CFD & Physical Modeling, in: L. Nastac, L. Zhang, B.G. Thomas, M. Zhu, A. Ludwig, A.S. Sabau, K. Pericleous, H. Combeau (Eds.), *CFD Modeling and Simulation in Materials Processing 2016*, Springer International Publishing, Cham, 2016: pp. 27–34. [https://doi.org/10.1007/978-3-319-65133-0\\_4](https://doi.org/10.1007/978-3-319-65133-0_4).
- [21] T.D.A. Jones, R.I. Strachan, D.M. Mackie, M. Cooper, B. Frame, J.B. Vorstius, Computational fluid dynamic simulations of solidification for enhancing speed of continuous cast copper, *Engineering Science and Technology, an International Journal.* 24 (2021) 92–104. <https://doi.org/10.1016/J.JESTCH.2020.12.009>.
- [22] Z.Z. Cai, M.Y. Zhu, Simulation of air gap formation in slab continuous casting mould, *Ironmaking & Steelmaking.* 41 (2014) 435–446. <https://doi.org/10.1179/1743281213Y.0000000139>.
- [23] W. Yang, Z. Luo, Z. Zou, C. Zhao, Y. You, Modelling and analysis of bubble entrapment by solidification shell in steel continuous casting considering bubble interaction with a coupled CFD-DBM approach, *Powder Technol.* 390 (2021) 387–400. <https://doi.org/10.1016/J.POWTEC.2021.05.044>.
- [24] N. Arzpeyma, M. Ersson, P.G. Jönsson, Mathematical Modeling of Postcombustion in an Electric Arc Furnace (EAF), *Metals.* 9 (2019). <https://doi.org/10.3390/met9050547>.
- [25] R. Sripriya, T. Peeters, K. Meijer, C. Zeilstra, D. van der Plas, Computational fluid dynamics and combustion modelling of HISarna incinerator, *Ironmaking & Steelmaking.* 43 (2016) 192–202. <https://doi.org/10.1179/1743281215Y.0000000031>.
- [26] J. Arroyo, L. Pérez, V. Cuervo-Piñera, CFD Modeling and Validation of Blast Furnace Gas/Natural Gas Mixture Combustion in an Experimental Industrial Furnace, *Processes.* 11 (2023). <https://doi.org/10.3390/pr11020332>.
- [27] F. Trivellato, L. Labiscsak, The post-combustion chamber of steelmaking plants: Role of ambient air in reactant exhaust fumes, *Appl Math Model.* 39 (2015) 19–35. <https://doi.org/https://doi.org/10.1016/j.apm.2014.09.016>.
- [28] L. Labiscsak, G. Straffellini, C. Corbetta, M. Bodino, Fluid dynamics of a post-combustion chamber in electric arc steelmaking plants, 2011. <https://doi.org/10.2495/CMEM110191>.

- [29] X. Tang, M. Kirschen, M. Abel, H. Pfeifer, Modelling of EAF Off-Gas Post Combustion in Dedusting Systems using CFD Methods, *Steel Res Int.* 74 (2003) 201–210. <https://doi.org/https://doi.org/10.1002/srin.200300182>.
- [30] Y. Li, R.J. Fruehan, Computational fluid-dynamics simulation of postcombustion in the electric-arc furnace, *Metallurgical and Materials Transactions B.* 34 (2003) 333–343. <https://doi.org/10.1007/s11663-003-0079-9>.
- [31] G. Tang, W. Liu, A.K. Silaen, C.Q. Zhou, Modeling of Post-Combustion in an Electric Arc Furnace, (2017). <https://doi.org/10.1115/IMECE2017-72493>.
- [32] U. Becker-Lemgau, K.-H. Tacke, Mathematical model for post combustion in smelting reduction, *Steel Research.* 67 (1996) 127–137. <https://doi.org/https://doi.org/10.1002/srin.199605469>.
- [33] H. Gou, G.A. Irons, W.-K. Lu, Mathematical modeling of postcombustion in a KOBM converter, *Metallurgical Transactions B.* 24 (1993) 179–188. <https://doi.org/10.1007/BF02657884>.
- [34] M. Karbowniczek, THE ELECTRIC ARC FURNACE OFF-GASSES MODELING USING CFD, in: 2007.
- [35] K. Dong, W. Liu, R. Zhu, Study on Indirect Measuring Technology of EAF Steelmaking Decarburization Rate by Off-gas Analysis Technique in Hot State Experiment, *High Temperature Materials and Processes.* 34 (2015) 539–547. <https://doi.org/doi:10.1515/htmp-2014-0076>.
- [36] H.-J. Odenthal, A. Kemminger, F. Krause, L. Sankowski, N. Uebber, N. Vogl, Review on Modeling and Simulation of the Electric Arc Furnace (EAF), *Steel Res Int.* 89 (2017) 1700098. <https://doi.org/10.1002/srin.201700098>.
- [37] Q. Zhang, L. Chen, C. Zhao, Numerical Simulation of Combustion and Air Supply Process and Optimal Design of Traditional Top Combustion Hot Blast Stoves, *Steel Res Int.* 92 (2021) 2000311. <https://doi.org/https://doi.org/10.1002/srin.202000311>.
- [38] S. Gövert, V. Fratolocchi, J.B.W. Kok, Characterization of Low Frequency Combustion Dynamics of Hot Blast Stoves by Means of a Flame Transfer Function Based on CFD Forced Response Simulations: Comparison of Different Hot Blast Stove Designs, (2015). <https://doi.org/10.1115/GT2015-42198>.
- [39] V. Cuervo-Piñera, D. Cifrián-Riesgo, P.-D. Nguyen, V. Battaglia, M. Fantuzzi, A. Della Rocca, M. Ageno, A. Rensgard, C. Wang, J. Niska, T. Ekman, C. Rein, W. Adler, Blast Furnace Gas Based Combustion Systems in Steel Reheating Furnaces, *Energy Procedia.* 120 (2017) 357–364. <https://doi.org/https://doi.org/10.1016/j.egypro.2017.07.215>.
- [40] M. Kirschen, L. Voj, H. Pfeifer, NO<sub>x</sub> Emission from Electric Arc Furnace – Measurement and Modelling, 2005.
- [41] M. Aksyushin, M. Kalugin, G. Malikov, Y. Yaroshenko, Improvement of the Energy Efficiency of Hot Blast Stove Performance BT - Advanced Methods and Technologies in Metallurgy in Russia, in: S. Syngellakis, J.J. Connor (Eds.), Springer International Publishing, Cham, 2018: pp. 169–176. [https://doi.org/10.1007/978-3-319-66354-8\\_20](https://doi.org/10.1007/978-3-319-66354-8_20).
- [42] F. R. Menter, Two-equation eddy-viscosity turbulence models for engineering applications., *AIAA J.* 32 (1994) 1598–1605.
- [43] F.R. Menter, Zonal two equation k– $\epsilon$  turbulence models for aerodynamic flows, *AIAA Paper No. 93-2906.* (1993).
- [44] M. Modest, The Weighted-Sum-of-Gray-Gases Model for Arbitrary Solution Methods in Radiative Transfer, *J Heat Transfer.* 113 (1991) 650–656. <https://doi.org/10.1115/1.2910614>.



- [45] G. Krishnamoorthy, A new weighted-sum-of-gray-gases model for CO<sub>2</sub>-H<sub>2</sub>O gas mixtures, *International Communications in Heat and Mass Transfer*. 37 (2010) 1182–1186. <https://doi.org/https://doi.org/10.1016/j.icheatmasstransfer.2010.07.007>.
- [46] F. Cassol, R. Brittes, F.H.R. França, O.A. Ezekoye, Application of the weighted-sum-of-gray-gases model for media composed of arbitrary concentrations of H<sub>2</sub>O, CO<sub>2</sub> and soot, *Int J Heat Mass Transf.* 79 (2014) 796–806. <https://doi.org/https://doi.org/10.1016/j.ijheatmasstransfer.2014.08.032>.
- [47] O.J. Kim, T.-H. Song, Implementation of the weighted sum of gray gases model to a narrow band: application and validity, *Numerical Heat Transfer, Part B: Fundamentals*. 30 (1996) 453–468. <https://doi.org/10.1080/10407799608915093>.
- [48] Octave. Levenspiel, *Chemical reaction engineering*, New York Etc. Wiley. Vol. 2 (1972).
- [49] B.F. Magnussen, B.H. Hjertager, On mathematical modeling of turbulent combustion with special emphasis on soot formation and combustion, *Symposium (International) on Combustion*. 16 (1977) 719–729. [https://doi.org/10.1016/S0082-0784\(77\)80366-4](https://doi.org/10.1016/S0082-0784(77)80366-4).
- [50] B. MAGNUSSEN, On the structure of turbulence and a generalized eddy dissipation concept for chemical reaction in turbulent flow, in: *19th Aerospace Sciences Meeting, American Institute of Aeronautics and Astronautics*, 1981. <https://doi.org/doi:10.2514/6.1981-42>.
- [51] B. Mahmoodi, S.H. Hosseini, G. Ahmadi, A. Raj, CFD simulation of reactor furnace of sulfur recovery units by considering kinetics of acid gas (H<sub>2</sub>S and CO<sub>2</sub>) destruction, *Appl Therm Eng.* 123 (2017) 699–710. <https://doi.org/10.1016/J.APPLTHERMALENG.2017.05.148>.
- [52] A.A. Mofakham, G. Ahmadi, Improved Discrete Random Walk Stochastic Model for Simulating Particle Dispersion and Deposition in Inhomogeneous Turbulent Flows, *J Fluids Eng.* 142 (2020). <https://doi.org/10.1115/1.4047538>.
- [53] M. Ghosh, P. and Ghosh, CFD evaluation of thermal convection inside the DACON convection sensor in actual space flight, *Nat Sci (Irvine)*. 3 (2011) 419–425. <https://doi.org/10.4236/ns.2011.36057>.
- [54] A.H. al-abbas, Computational Fluid Dynamics (CFD) Modeling Study of Thermal Performance for Multipurpose Solar Heating System, *Al-Nahrain Journal for Engineering Sciences (NJES)*. Vol.20 (2017) pp.222-234.
- [55] J.S. Jayakumar, S.M. Mahajani, J.C. Mandal, P.K. Vijayan, R. Bhoi, Experimental and CFD estimation of heat transfer in helically coiled heat exchangers, *Chemical Engineering Research and Design*. 86 (2008) 221–232. <https://doi.org/https://doi.org/10.1016/j.cherd.2007.10.021>.
- [56] F. Popescu, R.A. Mahu, N.A. Antonescu, I. V Ion, CFD prediction of combustion in a swirl combustor, *IOP Conf Ser Mater Sci Eng.* 444 (2018) 82009. <https://doi.org/10.1088/1757-899x/444/8/082009>.
- [57] A. Frassoldati, T. Faravelli, E. Ranzi, The ignition, combustion and flame structure of carbon monoxide/hydrogen mixtures. Note 1: Detailed kinetic modeling of syngas combustion also in presence of nitrogen compounds, *Int J Hydrogen Energy*. 32 (2007) 3471–3485. <https://doi.org/10.1016/J.IJHYDENE.2007.01.011>.
- [58] J. Joliff, Y. , Belec, L. and Chailan, Finite Element Analysis of the Material's Area Affected during a Micro Thermal Analysis Applied to Homogeneous Materials, *J Surf Eng Mater Adv Technol.* 1 (2011) 1–8. <https://doi.org/10.4236/jsemat.2011.11001>.
- [59] K. Pietrak, T.S. Wiśniewski, A review of models for effective thermal conductivity of composite materials, *Journal of Power Technologies*; Vol 95 No 1 (2015). (2014). <https://papers.itc.pw.edu.pl/index.php/JPT/article/view/463>.

- [60] L.E. Nielsen, The Thermal and Electrical Conductivity of Two-Phase Systems, *Industrial & Engineering Chemistry Fundamentals*. 13 (1974) 17–20. <https://doi.org/10.1021/i160049a004>.
- [61] Lord Rayleigh, LVI. On the influence of obstacles arranged in rectangular order upon the properties of a medium, *The London, Edinburgh, and Dublin Philosophical Magazine and Journal of Science*. 34 (1892) 481–502. <https://doi.org/10.1080/14786449208620364>.
- [62] R. Landauer, The Electrical Resistance of Binary Metallic Mixtures, *J Appl Phys*. 23 (1952) 779–784. <https://doi.org/10.1063/1.1702301>.
- [63] I.H. Tavman, H. Akinci, Transverse thermal conductivity of fiber reinforced polymer composites, *International Communications in Heat and Mass Transfer*. 27 (2000) 253–261. [https://doi.org/https://doi.org/10.1016/S0735-1933\(00\)00106-8](https://doi.org/https://doi.org/10.1016/S0735-1933(00)00106-8).
- [64] H. Wang, Z. Rao, W. Wang, S. Liao, A reconstruction of Hamilton-Crosser model for effective thermal conductivity of nanofluids based on particle clustering and nanolayer formation, *Case Studies in Thermal Engineering*. 26 (2021) 101051. <https://doi.org/https://doi.org/10.1016/j.csite.2021.101051>.
- [65] Aklilu Tesfamichael Baheta and Abraham D. Woldeyohannes, Effect of Particle Size on Effective Thermal Conductivity of Nanofluids, *Asian J Sci Res*. (2013) 339–345. <https://doi.org/10.3923/ajsr.2013.339.345>.
- [66] K. Rashid, E.U. Haq, M.S. Kamran, N. Munir, A. Shahid, I. Hanif, Experimental and finite element analysis on thermal conductivity of burnt clay bricks reinforced with fibers, *Constr Build Mater*. 221 (2019) 190–199. <https://doi.org/https://doi.org/10.1016/j.conbuildmat.2019.06.055>.
- [67] R. Rolfes, J. Noack, M. Taeschner, High performance 3D-analysis of thermo-mechanically loaded composite structures, *Compos Struct*. 46 (1999) 367–379. [https://doi.org/https://doi.org/10.1016/S0263-8223\(99\)00101-4](https://doi.org/https://doi.org/10.1016/S0263-8223(99)00101-4).
- [68] B. Nagy, S.G. Nehme, D. Szagri, Thermal Properties and Modeling of Fiber Reinforced Concretes, *Energy Procedia*. 78 (2015) 2742–2747. <https://doi.org/https://doi.org/10.1016/j.egypro.2015.11.616>.
- [69] K. Andreev, H. Harmuth, FEM simulation of the thermo-mechanical behaviour and failure of refractories—a case study, *J Mater Process Technol*. 143–144 (2003) 72–77. [https://doi.org/https://doi.org/10.1016/S0924-0136\(03\)00322-4](https://doi.org/https://doi.org/10.1016/S0924-0136(03)00322-4).
- [70] D. Gruber, K. Andreev, H. Harmuth, FEM simulation of the thermomechanical behaviour of the refractory lining of a blast furnace, *J Mater Process Technol*. 155–156 (2004) 1539–1543. <https://doi.org/https://doi.org/10.1016/j.jmatprotec.2004.04.249>.
- [71] H. Guo, Y.Y. Han, X.M. Zhang, F.Z. Yin, Y.M. Fan, P.P. Wang, Finite Element Analysis of the Effect of Particle Shape on the Thermal Conductivity in Diamond/Cu Composites, *Materials Science Forum*. 788 (2014) 689–692. <https://doi.org/10.4028/www.scientific.net/MSF.788.689>.
- [72] L. Qian, X. Pang, J. Zhou, J. Yang, S. Lin, D. Hui, Theoretical model and finite element simulation on the effective thermal conductivity of particulate composite materials, *Compos B Eng*. 116 (2017) 291–297. <https://doi.org/https://doi.org/10.1016/j.compositesb.2016.10.067>.
- [73] M. Zahid, R. Sharma, A.R. Bhagat, S. Abbas, A. Kumar, P. Mahajan, Micro-structurally informed finite element analysis of carbon/carbon composites for effective thermal conductivity, *Compos Struct*. 226 (2019) 111221. <https://doi.org/https://doi.org/10.1016/j.compstruct.2019.111221>.

- [74] M. Ahmadi, R. Ansari, M.K. Hassanzadeh-Aghdam, Finite element analysis of thermal conductivities of unidirectional multiphase composites, *Compos Interfaces*. 26 (2019) 1035–1055. <https://doi.org/10.1080/09276440.2019.1578588>.
- [75] Z. Li, W. Wu, H. Chen, Z. Zhu, Y. Wang, Y. Zhang, Thermal conductivity of micro/nano filler filled polymeric composites, *RSC Adv*. 3 (2013) 6417–6428. <https://doi.org/10.1039/C3RA22482A>.
- [76] Z. Li, W. Xiao, X. Ruan, A Finite Element Analysis of the Effects of Graphene and Carbon Nanotubes on Thermal Conductivity of Co Phase in WC-Co Carbide., *Materials (Basel)*. 14 (2021). <https://doi.org/10.3390/ma14247656>.
- [77] P. Gurusamy, T. Sathish, V. Mohanavel, A. Karthick, M. Ravichandran, O. Nasif, S. Alfarradj, V. Manikandan, S. Prasath, Finite Element Analysis of Temperature Distribution and Stress Behavior of Squeeze Pressure Composites, *Advances in Materials Science and Engineering*. 2021 (2021) 8665674. <https://doi.org/10.1155/2021/8665674>.
- [78] Y. Zhao, L. Song, J. Li, Y. Jiao, Multi-Scale Finite Element Analyses of Thermal Conductivities of Three Dimensional Woven Composites, *Applied Composite Materials*. 24 (2017) 1525–1542. <https://doi.org/10.1007/s10443-017-9601-0>.
- [79] H.Z. Gu, A. Huang, H.Z. Wang, Finite Element Analysis on Temperature-Stress of Permeable Refractory Ceramic under Working Process in Ladle, *Key Eng Mater*. 434–435 (2010) 154–157. <https://doi.org/10.4028/www.scientific.net/KEM.434-435.154>.
- [80] N.S. Köksal, M. Toparlı, Calculation of Temperature and Thermal Stress in Refractory Materials Quenched in Water Using Finite Element Methods , *Key Eng Mater*. 264–268 (2004) 1783–1786. <https://doi.org/10.4028/www.scientific.net/KEM.264-268.1783>.
- [81] F. Damhof, W.A.M. Brekelmans, M.G.D. Geers, Predictive FEM simulation of thermal shock damage in the refractory lining of steelmaking installations, *J Mater Process Technol*. 211 (2011) 2091–2105. <https://doi.org/https://doi.org/10.1016/j.jmatprotec.2011.07.005>.
- [82] S. Yilmaz, Thermomechanical Modelling for Refractory Lining of a Steel Ladle Lifted by Crane, *Steel Res Int*. 74 (2003) 485–490. <https://doi.org/https://doi.org/10.1002/srin.200300221>.
- [83] A.P. de M. Mati, R.A. Freire, S.L.C. da Silva, P.R. Brandão, The effect of key aspects on the thermomechanical behaviour of torpedo ladle bricks using finite element analysis, *Tecnol. Metal. Mater. Min*. 16 (2019) 268–278. <https://doi.org/10.17504/protocols.io.36wq76p5vk5/v1>.
- [84] P. Boisse, A. Gasser, J. Rousseau, Computations of refractory lining structures under thermal loadings, *Advances in Engineering Software*. 33 (2002) 487–496. [https://doi.org/https://doi.org/10.1016/S0965-9978\(02\)00064-9](https://doi.org/https://doi.org/10.1016/S0965-9978(02)00064-9).
- [85] J.-J. Gou, Y.-J. Dai, S. Li, W.-Q. Tao, Numerical study of effective thermal conductivities of plain woven composites by unit cells of different sizes, *Int J Heat Mass Transf*. 91 (2015) 829–840. <https://doi.org/https://doi.org/10.1016/j.ijheatmasstransfer.2015.07.074>.



# Chapter 3

## SENSITIVITY ANALYSIS AND MODEL SELECTION

### Why this one and not that?

This chapter is based on the following paper:

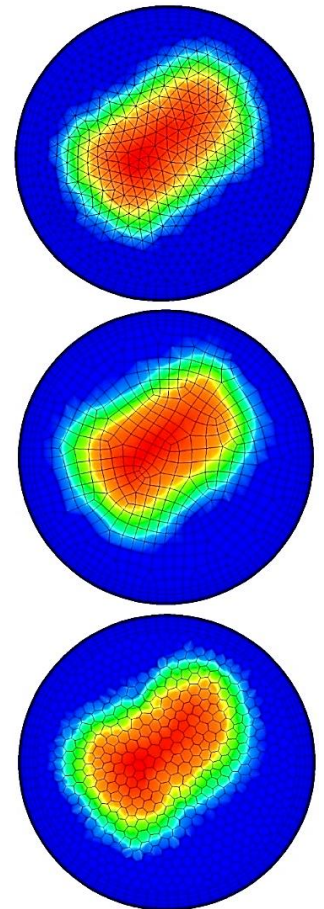
Hosseini, A.; Hage, J.L.T.; Meijer, K.; Offerman, E.; Yang, Y. **On the Importance of Model Selection for CFD Analysis of High Temperature Gas-Solid Reactive Flow; Case Study: Post Combustion Chamber of Hisarna Off-Gas System.** *Processes* 2023, 11, 839. <https://doi.org/10.3390/pr11030839>

During the current Ph.D. research, many comments were received on the CFD model setup and sub-model selection details.

For example, questions like:

- Why is radiation included? Is it even necessary to be considered?
- Why detailed kinetic mechanism is employed instead of a global mechanism? Is it even essential to consider kinetics?
- Why expensive turbulent chemistry interaction models (combustion models) are used? etc.

A comprehensive parametric study has been conducted to address these questions and establish the reliability of the developed model presented in previous chapters. The study explores the significance of various parameters, including different mesh types (tetrahedral, hexahedral, and polyhedral), mesh grid sizes (coarse, medium, and fine grid), radiation models (Rosseland, P<sub>1</sub>, and discrete ordinate model), turbulent models (k-epsilon and k-omega), kinetic mechanisms, TCI models (eddy dissipation, finite rate-eddy dissipation, eddy dissipation concept model), on the precision of the developed model.





### 3.1. Introduction

Generally speaking, computational fluid dynamics (CFD) modelling is based on fluid mechanics principles that utilize numerical methods and algorithms to solve governing equations of fluid flow dynamics [1]. The governing equations are transport equations derived from conservation laws for extensive mass, energy, and momentum properties. They are differential equations to describe the spatial and temporal distribution of intensive quantities instead of the extensive ones [2]. The basic governing equations that are solved in any CFD codes are called the Navier-Stokes (NS) equations. It is a set of continuity equations and Newton's second law, known as the momentum equation, to obtain pressure, velocity, and density field [3]. These equations are necessary for any CFD computation regardless of the application, number of phases, and level of problem complexity. For more complex flow, other governing equations such as energy, species transport, radiative transport, and turbulent transport might be added depending on the physics of the problem.

The governing equations are replaced by discrete approximations at grid points which represent the computational domain (geometry) in a form that can be solved by a computer using finite differences (FDM), finite volumes (FVM), and finite element (FEM) method, linking the different grid points together [4]. It is possible to study almost any phenomenon at any scale and geometry complexity using CFD tools. It is suited for all types of problems where knowledge of the spatial distribution of flow quantities is desired [5]. CFD modelling can be considered a tool of general interest in diverse engineering fields such as metallurgy, chemical processes, biomechanics and biomedical engineering, meteorology, renewables, civil engineering, architecture, or any fluid flow field. CFD modelling is indeed an iterative design procedure with a large number of parametric variations.

Setting up a Computational Fluid Dynamics (CFD) model involves several general steps. However, providing a universally valid, simple checklist is challenging as the complexity and setup steps are highly case-dependent. Additionally, different simplifications of the actual situation are typically applied at various stages of the setup and solution process. Ultimately, numerous parameter variations may be conducted to achieve a well-defined setup.

Nevertheless, every CFD case necessitates a minimum amount of input information to initiate the solving procedure. The following steps outline the essential requirements:

1. Geometry (also known as computational domain) preparation
2. mesh generation (Discretising the domain into computational cells)
3. model selection to represent physical phenomena occurring within the domain
4. Boundary condition, inlet and outlet, selection and knowledge of boundary values of parameters that are supposed to be solved within the domain
5. Selecting a discretization method to discretize governing equations for a numerical procedure
6. Solver and iterative method to solve the governing equations
7. Monitoring relative error for the iterative solution to reach a minimum designated value
8. Visualization and post-processing of the obtained results
9. Model validation with available measured data for the same studied geometry and phenomena

After establishing an initial CFD model, the decision to enhance the model can be made based on post-processed results and a comparison with available measured data, if applicable. Improvements to the CFD model may involve modifying sub-models, increasing model complexity by incorporating additional transport equations and sub-models, adjusting boundary conditions, enhancing mesh resolution, increasing computational cell numbers, and so on.

However, incorporating more details into a CFD model can impact the solution procedure, stability, and computation time. There exists a trade-off between the complexity of a CFD model and its computational cost (simulation time). Figure 3-1 provides a graphical representation of this trade-off, indicating that higher complexity results in higher computational costs, yet it allows for greater accuracy and more detailed results. Recent advancements in CFD modeling approaches aim to optimize the solving procedure to achieve the same level of detail and accuracy with reduced cost. A great example could be the development of polyhedral cells, which significantly decrease the cell count and simulation time while maintaining accuracy.



The accuracy and cost of a CFD model highly depend on the proper selection of mesh cell type and proper mesh generation (step 2) and choosing parameters and sub-models that can represent the physics of the problem (step 3). However, proper setup of steps 2 and 3 does not guarantee high accuracy results but plays a major role compared to the other steps.

The crucial aspect of developing a CFD model is the final step, namely the validation step. A CFD model is valid only for cases within the parameter range of successful verification.

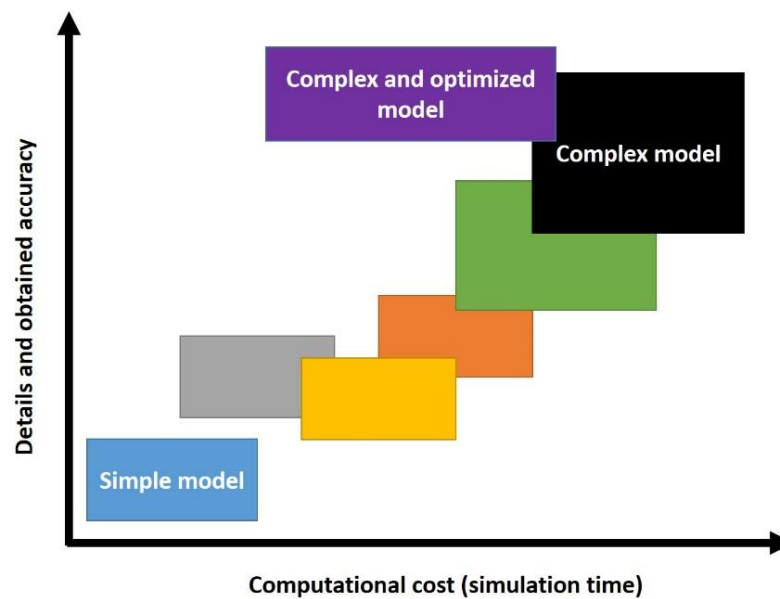


Figure 3-1. Trade-off between the method complexity and the results information content

In this chapter, the off-gas system of HIsarna is utilized to discuss the importance of steps 2 and 3 in more detail. A comprehensive literature review for selecting mesh cell type, turbulent models, radiation model, turbulent chemistry intersection model, solid particle modelling, and the importance of wall boundary conditions are presented. The selection of each sub-model is justified via literature review and comparing them in the current case study.

### 3.2. Effect of mesh cell type

The precision, credibility, and stability of a CFD model highly depend on the computational grid generation. Grid cell type, size, and orientation can significantly influence the simulation time, as well as the accuracy of the results.

The most efficient and classic of all is called structured grid, mainly composed of well-aligned hexahedral cells. An example of a structured grid for an industrial case is shown in Figure 3-2.A.

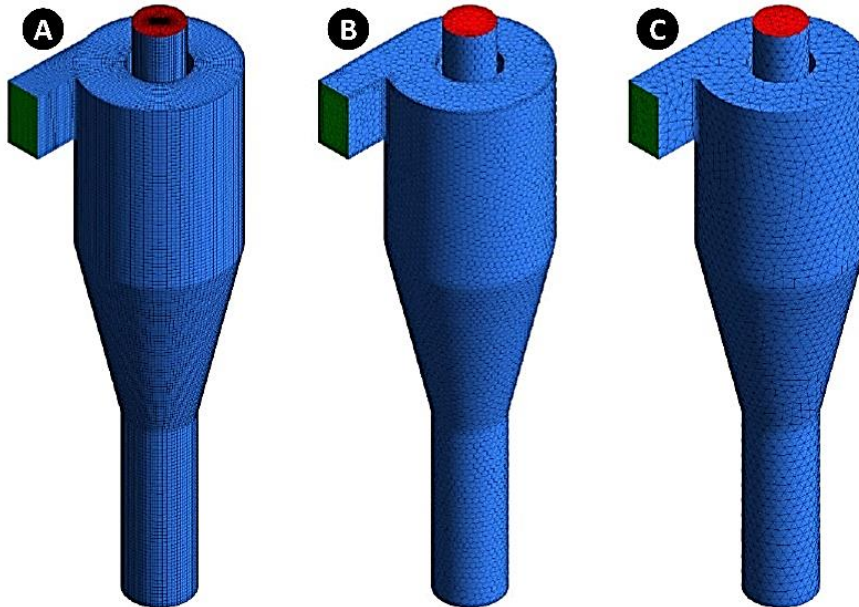


Figure 3-2. Large scale mesh – A) Structured hexahedral, B) Polyhedral, C) Unstructured tetrahedral mesh [6]

A Structured grid refers to a grid with implicit connectivity whose structure allows for easy identification of elements and nodes and easy data storage and access within cells [7]. However, in the case of complex geometries with sharp edges and curved boundaries, the use of structured grids tends to decrease mesh quality, resulting in high cell non-orthogonality, low orthogonal quality, and high skewness. This, in turn, can lead to unreliable results that may significantly differ from measured values. Additionally, generating a structured mesh for complex geometries involves manually dividing the domain into smaller subdomains to conduct the meshing process separately. This is a time-consuming task that demands advanced skills. The limitations of structured meshes become even more pronounced in complex industrial and large-scale applications [7,8]. An alternative to a structured grid is an unstructured one in which tetrahedral cells are commonly used. Tetrahedral cells can be positioned and assembled freely within the computational domain. The main drawback of the tetrahedral cells is their limitation to excessive stretch, which can significantly increase the number of elements compared to structured mesh [8].

One solution to reduce the cell count is to use hybrid mesh, which combines different element types. Hybrid meshes can provide maximal flexibility in matching mesh cells with the boundary surfaces and allocating cells of various element types in other parts of the complex flow regions where hexahedral cells cannot be allocated or would result in poor-quality regions.

Another solution would be creating polyhedral mesh by combining tetrahedral cells into polyhedral cells, as depicted in Figure 3-3.

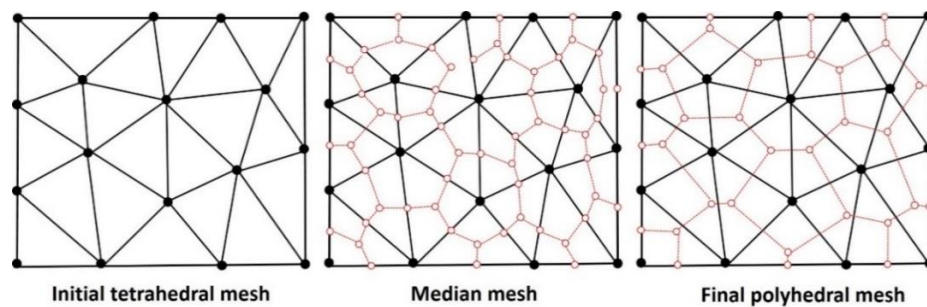


Figure 3-3. Tetrahedral grid conversion into the polyhedral grid [9]

This conversion results in a considerable reduction in cell count and an increase in mesh quality, ultimately leading to more accurate final results [10]. A clear potential benefit of applying polyhedral mesh is that it allows the flexibility of an unstructured mesh to be applied to a complex geometry without the computational overheads associated with a large tetrahedral mesh [7]. Another benefit of polyhedral mesh is that each cell will have more faces and, therefore, more neighboring cells. This is beneficial when it comes to gradient approximation. It also allows mass interchange over more faces, reducing numerical diffusion effects caused by non-perpendicular flow on cell faces, specifically in flow fields where no prevailing flow direction can be identified [8].

Different indicators can be defined to evaluate a grid quality. Among them, orthogonal quality and skewness are essential quality indicators that must be checked before proceeding to the model setup and simulation. The concept of mesh orthogonality relates to how close the angles between adjacent element faces (or adjacent element edges) are to some optimal angle.

It is defined as:

$$\text{Orthogonal quality} = \min \left( \frac{A_i \cdot f_i}{|\vec{A}_i| |\vec{f}_i|}, \frac{A_i \cdot c_i}{|\vec{A}_i| |\vec{c}_i|} \right)$$

$\vec{A}_i$  is the vector normal to the cell face,  $\vec{c}_i$  is a vector connecting cell centroids and  $\vec{f}_i$  is the vector connecting the cell centroid to the center of the cell faces. It varies between 0 (worst) and 1 (best). Examples of cell arrangements with orthogonal quality equal to and lower than unity are shown in Figure 3-4.

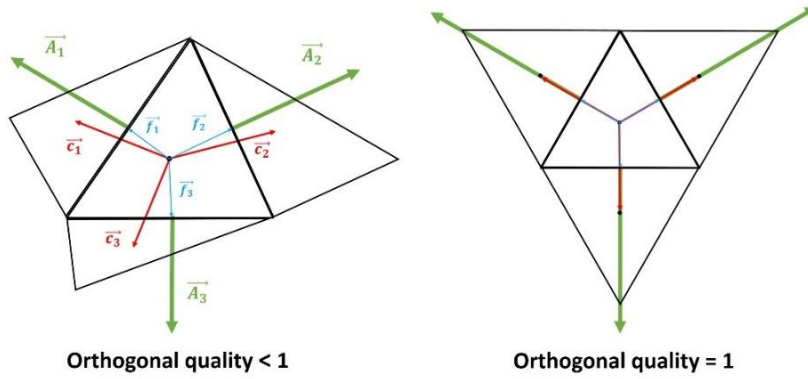


Figure 3-4. A schematic view of cells and corresponding vectors for orthogonal quality calculation

Cell skewness is the measure of how stretched a cell is. For all cell types, equiangular skewness is applied, which may be calculated as:

$$\text{Skewness} = \max\left(\frac{\theta_{max} - \theta_e}{180 - \theta_e}, \frac{\theta_e - \theta_{min}}{\theta_e}\right)$$

where  $\theta_{max}$  and  $\theta_{min}$  are the maximum and minimum cell angles and  $\theta_e$  is the equiangular face/cell (60 degrees for tetrahedral and 90 degrees for hexahedral cell).

The skewness value ranges from 0 (good) to 1 (bad), as it is depicted for some cells in Figure 3-5. The concept of skewness does not apply to polyhedral mesh; however, any polyhedral mesh has substantially lower skewness than its equivalent tetrahedral grid.

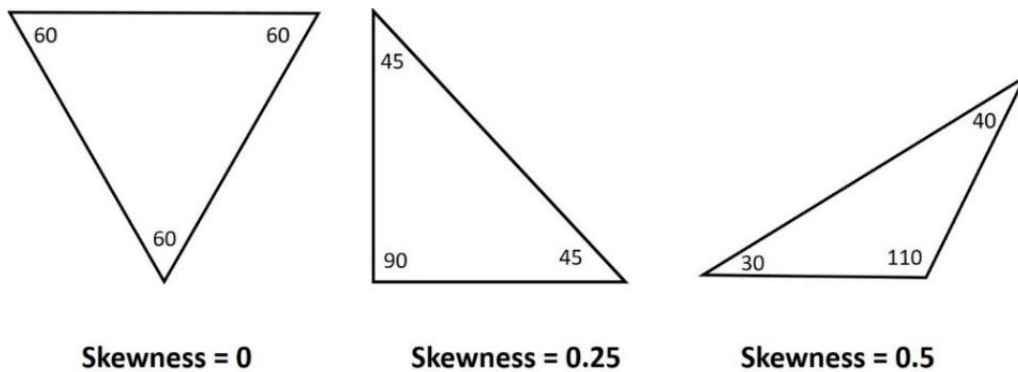


Figure 3-5. Skewness value for a perfect and highly skewed cell

There have been numerous studies on the effect of cell type on cell counts, grid quality, simulation time, accuracy of prediction, and residuals [8,11–15]. Here, the same parameters are studied for different cell types using the reflux chamber geometry.

Two grids with the same cell size (40 mm) are generated using tetrahedral and polyhedral cells. Figure 3-6 shows the cell count for each cell type, and as can be seen, with the same cell size, tetrahedral cells lead to a noticeably higher cell count. Due to the sharp edges and relatively complex geometry of the off-gas system, the generation of hexahedral or structured mesh is quite complex, ultimately leading to poor-quality mesh. Therefore, the hexahedral/structural mesh grid is omitted in comparisons.

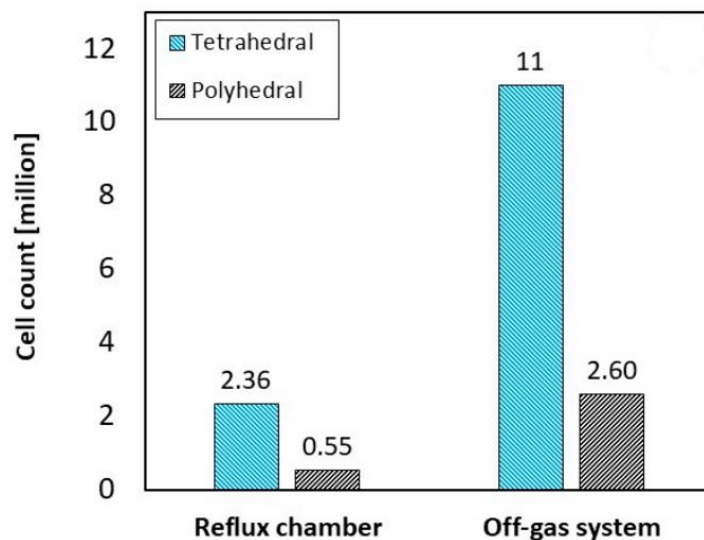


Figure 3-6. Cell count for different cell types

Figure 3-7 shows the skewness and orthogonal quality contour in the mid-plane of the reflux chamber. As can be seen, tetrahedral mesh exhibits higher skewness and lower orthogonal qualities than the other cells. Among them, polyhedral mesh showed the best and highest average orthogonal quality, as reported in Table 3-1.

Table 3-1. Averaged skewness and orthogonal quality for reflux chamber volume

	<b>Tetrahedral</b>	<b>Polyhedral</b>
Orthogonal quality	0.7891	0.9725
Skewness	0.21	-

High skewness and low orthogonal quality will reduce the accuracy of the interpolations on the surfaces and increase the gradient calculation errors [11]. It is

possible to reduce the skewness by increasing cell count; however, it will come at the cost of increasing simulation time.

For both cell types, low orthogonal quality was observed near the wall and turns, which can be associated with sharp edges that lead to difficulties in maintaining high mesh quality, especially with prism layers. The same observation is reported in the study of Wang et al. [16]. Nevertheless, both generated grids have a good and acceptable quality for CFD calculations.

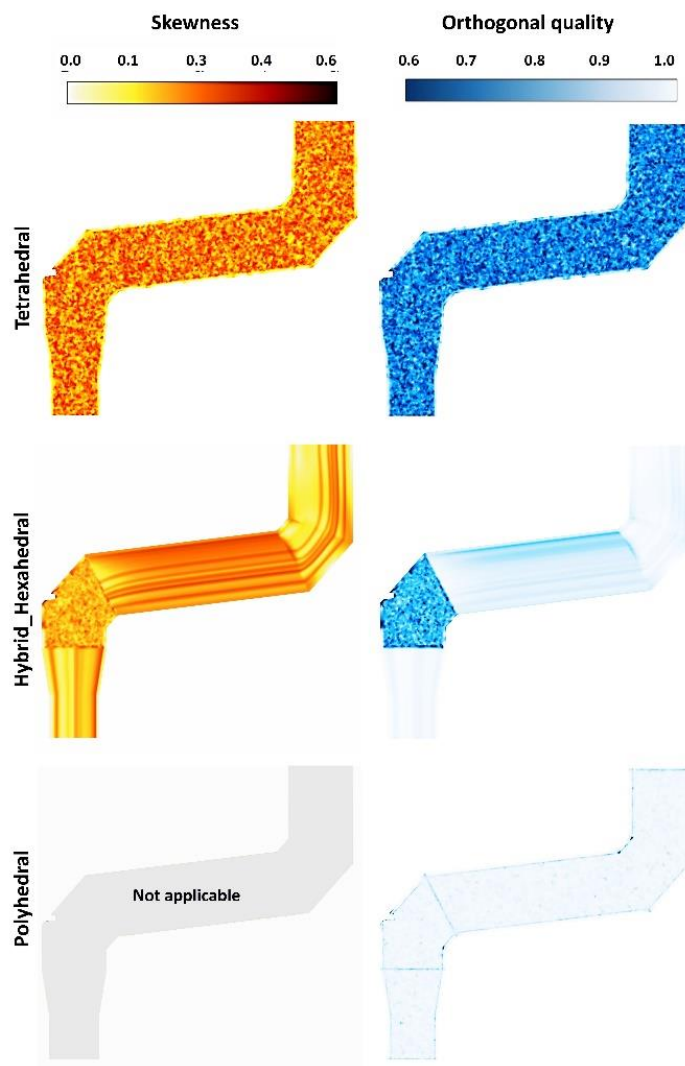


Figure 3-7. Skewness and orthogonal quality contours

Figure 3-8 shows the continuity residuals during steady state iterations for different cell types. The simulations are performed for 2000 iterations, and particles are injected at iteration 820, which led to a small residual spike and instability in the simulation. As it can be seen, the polyhedral mesh converges to the set value of around  $10^{-4}$  after 2000 iterations, while the tetrahedral mesh still needs more



iteration to reach the convergence criteria. Considering a residual value of  $10^{-3}$ , polyhedral mesh satisfies this criterion after 570 iterations, while it is met after 2000 iterations for tetrahedral mesh.

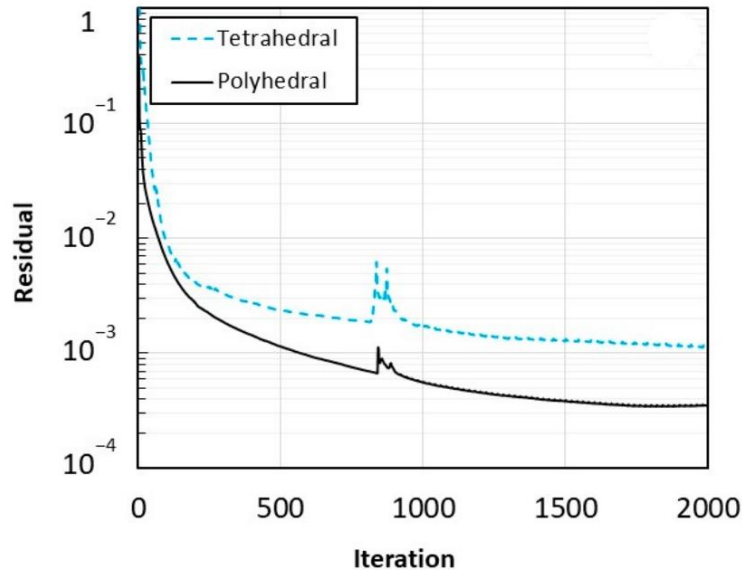


Figure 3-8. Residuals and convergence for different cell types

The reason is mainly related to the lower cell count and higher quality of the polyhedral compared to the tetrahedral mesh. The other disadvantage of tetrahedral mesh is the higher required simulation time (due to the higher number of cells) which is depicted as normalized time in Figure 3-9. The polyhedral grid shows noticeably lower time than the tetrahedral mesh grid for total time and time spent for DPM iterations.

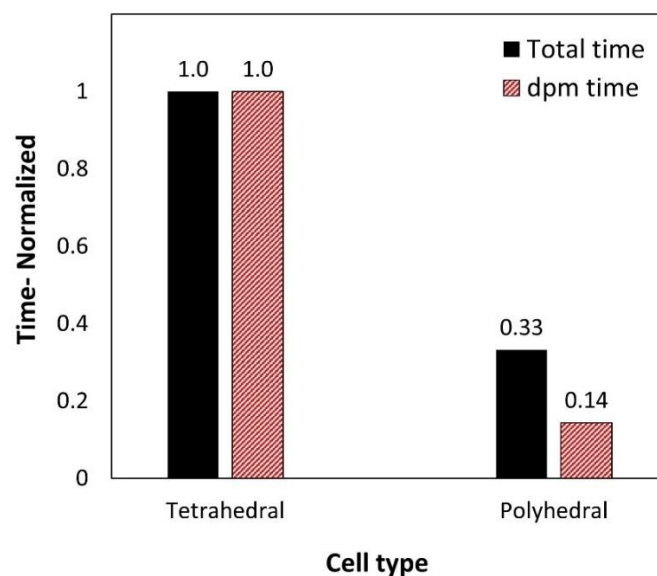


Figure 3-9. Simulation time for different cell types

Figure 3-10 shows the predicted temperature and CO composition profile along the reflux chamber length. As can be seen, both grids predict more or less the same profiles with an outlet temperature close to the plant measurement. The carbon conversions for the tetrahedral and polyhedral grid at the chamber outlet are 56% and 54%, respectively (plant measurement is 50%).

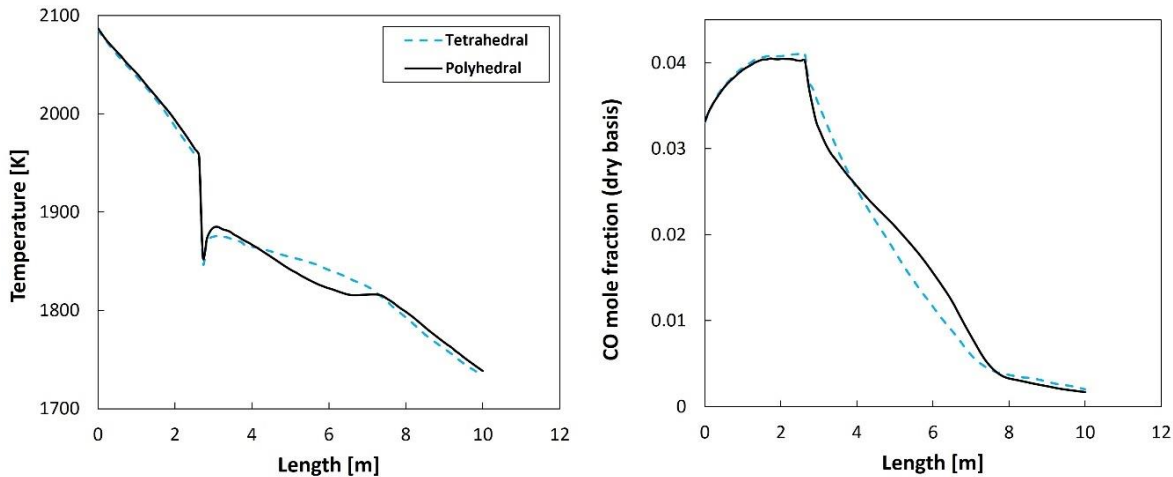


Figure 3-10. Predictions of different cell types for off-gas temperature and CO model fraction profile

Altogether, the performed analysis shows that the polyhedral cells hold great promise in producing equivalent accuracy results compared to other mesh types with the added benefits of:

- Lower cell count, most economical
- Faster converge in fewer iterations
- Convergence to lower residual values
- Faster solution run-time

### 3.3. Effect of mesh cell count (mesh sensitivity analysis)

Apart from the cell type, the cell count is crucial in optimal mesh design to ensure analysis accuracy and computational feasibility [1]. A coarse grid can yield inaccurate results and instability in analyses; therefore, it is important to use a sufficiently refined grid to ensure the adequacy of the calculations. Moreover, in any CFD calculation, one must ensure that the obtained solution is grid-independent. This means that a numerical solution tends toward a unique value as grid density is



increased. A solution is considered grid-independent when further grid refinement produces a negligible change in the solution. Based on this definition, five different polyhedral meshes are selected (as reported in Table 3-2), and simulation with the same settings as the base model is performed for each mesh.

Table 3-2. Mesh specification for mesh sensitivity analysis

Zone	Cell Size [mm]			Cell count [million]
	Reflux chamber	Air quench	Up/down leg	
Very coarse	65	55	75	0.88
Coarse	55	45	65	1.05
Medium	40	30	50	2.69
Fine	30	25	40	2.3
Very fine	25	20	35	3.3

Figure 3-11 shows the calculated temperature and composition profile for each grid refinement.

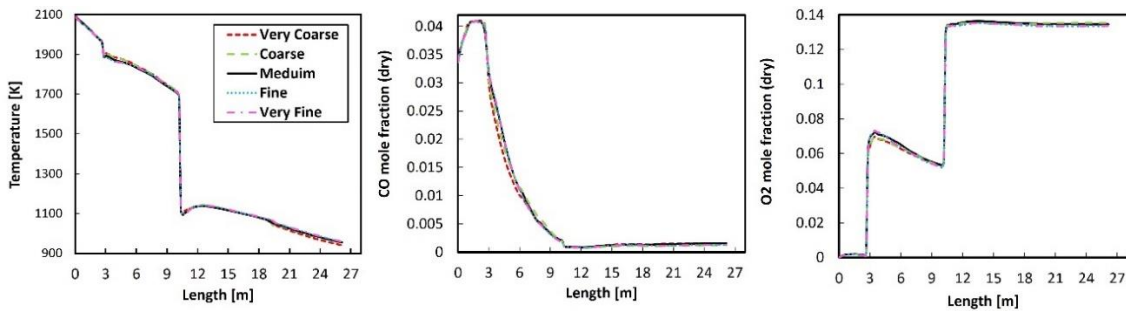


Figure 3-11. Temperature, CO, and O<sub>2</sub> profile prediction for different mesh refinements

As it is evident, medium, fine, and very fine grids show the same accuracy; however, coarse grids show a slight deviation compared to medium and fine grids. The discrepancies are mainly observed in the reflux chamber where oxygen is injected (between lengths of 3 to 10 m). It is an important region where most of the oxidation reactions occur. Nevertheless, the solution seems to be grid-independent after the coarse grid. Hence, a medium-sized grid is used for the base model and the rest of the analysis since finer grids require substantially higher simulation time for the same obtained accuracy.

### 3.4. Selection of turbulence model

For industrial cases, k-ε and k-ω are among the most common models to describe the turbulence nature of the flow. Both models can take into account the turbulence

parameter with proper accuracy. In this section, the intention is not to compare the accuracy of predictions but rather to point out an issue the author faced during the calculations. Even though the  $k-\omega$  model is proven to be more accurate and robust in capturing the details of turbulent flows, for final model development in this study,  $k-\varepsilon$  is preferred for two reasons.

The first and main reason is the higher number of cells required by the  $k-\omega$  model. To properly predict the velocity profile and subsequent thermal properties using the  $k-\omega$  model, a  $y^+ \leq 1$  near the walls must be maintained during the calculations. Low  $y^+$  requires higher grid resolution and more inflation layer near the wall region, consequently, higher cell count. Depending on the computational resources, this could be a great disadvantage in industrial applications with large geometries. However, for the  $k-\varepsilon$  model, a  $y^+$  value above 30 and up to 300 needs to be maintained, requiring a much coarser grid resolution near the wall regions. Indeed,  $k-\varepsilon$  models use wall functions to correlate the profiles near the walls. For standard wall function, one should make sure the  $y^+$  is either below 5 or above 30 to avoid putting the first cell in the buffer region. A  $y^+$  value of either lower than 2 or higher than 30 is required for enhanced wall treatment. It is worth mentioning that all wall functions predict similar results for  $y^+ > 30$ . Nevertheless, the enhanced wall treatment function is quite  $y^+$  insensitive and can still predict near-wall region properties with great accuracy for any  $y^+$  values. Besides mesh resolution, another problem was raised regarding using the  $k-\omega$  model. To the author's best knowledge, the issue faced while choosing turbulence models is not reported in any other literature. When carbon particles are included in the model, the trajectories of particles are calculated in each cell. To fulfill proper trajectory calculations, the size of all cells in the grid needs to be larger than the particle diameter. In other words, all cells should have enough volume to host a single particle. For a stable calculation, it is necessary to keep the cell size at least three times larger than the diameter of particles; however, larger cells might be needed for specific cases.

In the current case, using the  $k-\omega$  model and obtaining  $y^+ < 1$  led to cell layers with a size smaller than the particle diameter. Therefore, during the calculations, the solver failed to complete the trajectory calculation and removed some particles from the domain by marking them as "incomplete". Removing carbon particles from the domain causes a reduction in the initial injected flow rate of particles, which

ultimately can lead to a wrong prediction of carbon conversion, gaseous composition, and temperature profiles, especially when the carbon particle flow rate is high. Table 3-3 summarizes the mesh size and the number of incomplete particle trajectories for different generated grids with different  $y^+$  values.

Table 3-3. Tracked and incomplete particle trajectory for different  $y^+$  (regardless of the utilized turbulent model) – particle size is fixed and equal to 0.12 mm

Mesh	First layer thickness [mm]	Number of inflation layers	Mesh size (Reflux chamber)	Mesh size (off-gas system)	$y^+$	Tracked particle	Incomplete Particle (average)
Mesh 1	0.2	14	880 K	5.31 M	0.38	9185	880 (10%)
Mesh 2	0.3	12	840 K	4.8 M	0.6	8800	686 (8%)
Mesh 3	0.5	10	750 K	4.1 M	0.95	7600	356 (5%)
Mesh 4	1	8	645 K	3.58 M	1.9	6315	230 (4%)
Mesh 5	2	5	627 K	3.12 M	4.6	5900	117 (2%)
Mesh 6	10	4	485 K	2.6 M	34	4516	0

It can be seen that lower  $y^+$  values require lower first-layer thicknesses, which increases the number of fine cells and overall cell number. There are still incomplete trajectories even for a  $y^+$  value as high as 2. However, for  $y^+ = 34$ , which is used for all discussed models in this thesis, all particle trajectories are calculated without missing particles. To recap, using the k- $\epsilon$  model for the current case seems to be a better choice for two reasons. It requires lower cell count as it needs higher  $y^+$  values near the wall region, and consequently, cell size will be large enough for safe particle path calculations.

### 3.5. Effect of turbulent-chemistry interaction models

As mentioned before, the flue gas from the CCF enters the reflux chamber containing CO-H<sub>2</sub> mixture and carbon particles, which must be removed to avoid emissions. The combustion of the mixture happens inside the reflux chamber by injecting oxygen. The most crucial aspect in modeling systems involving reactive flow is to accurately predict the combustion behavior of the gaseous and gas-solid mixture. Among the various phenomena, the mass transfer phenomenon and its modeling are indispensable, playing a vital role in achieving a well-tuned CFD model capable of adequately predicting the behavior of a reactive flow. To correctly describe mass transfer and reactions, the following are required:

1. Detailed kinetic data and reaction mechanism,
2. Proper selection of turbulence-chemistry interaction (TCI) model.

The current studied system is a gas-solid reactive flow. Since the carbon particles are ultimately converted into H<sub>2</sub> and CO, special attention is given to the gaseous reactions. A proper selection of the TCI models (also known as combustion models) substantially influences the gas phase behaviour, composition, and temperature distribution [17]. There have been numerous studies on reaction mechanisms and kinetic database development for CO-H<sub>2</sub> mixture combustion. Table 3-4 summarizes some of the available literature on the reaction mechanism development and their applications in CFD models.

Table 3-4. Summary of utilized mechanisms for different reactive flow modelling

Fuel mixture	Oxidizer	Pressure [atm]	Mechanism	Number of Species	Number of reactions	Reference
CO-H <sub>2</sub> O	Air	1-20	Detailed	13	28	[18]
CO-H <sub>2</sub> -H <sub>2</sub> O	Air	1	Detailed	8	31	[19]
CO/H <sub>2</sub>	O <sub>2</sub>	21-500	Detailed (reduced GRI)	30	171	
CO/H <sub>2</sub> /CH <sub>4</sub>	Air	1	Detailed (reduced GRI)	15	49	
CO/H <sub>2</sub> /CH <sub>4</sub>	Air	1	Detailed (GRI)	53	325	[20]
CO/H <sub>2</sub>	Air/O <sub>2</sub>	1	Detailed	14	30	[21]
CO/H <sub>2</sub>	Air	40-200	Detailed	12	27	[22]
CO/H <sub>2</sub>		1-20	Detailed	14	30	[23]
CH <sub>4</sub> /CO/H <sub>2</sub>	Air	1	Detailed (GRI)	53	325	[24]
CH <sub>4</sub> /CO/H <sub>2</sub>	Air	1	Detailed (GRI)	53	325	[25]
CH <sub>4</sub> /CO/H <sub>2</sub>	Air	1	Detailed (USC II)	111	784	[25]
CO/H <sub>2</sub>	Air	1-5	Detailed GRI and mechanism from [21]	53	325	[26]
CO/H <sub>2</sub>	Air/O <sub>2</sub>	1-10	Detailed	14	33	[27]
CH <sub>4</sub> /CO/H <sub>2</sub>		1-40	Detailed GRI Reduced GRI NUIG [28] Heghes [29] Frenklach[30][31]			[32-34]
CO/H <sub>2</sub>	Air	1	Detailed from [18]	13	28	[22]
CO/H <sub>2</sub>	Air	1	Detailed		74	[35]
CO/H <sub>2</sub>	Air/O <sub>2</sub>	1	Detailed	14	33	[36,37]
CH <sub>4</sub> /CO	Air	1	Global 3 step Westbrook-Dryer mechanism	5	3	[38]
CH <sub>4</sub> /CO/H <sub>2</sub>	Air	1	Global 4 step Jones-Lindstedt mechanism	6	4	[38]
CH <sub>4</sub> /CO/H <sub>2</sub>	Air	1	Global 6 step modified Jones- Lindstedt mechanism	9	6	[38]
CO/H <sub>2</sub>	Air/O <sub>2</sub>	1-20	Global 5 step	8	5	[39]
CH <sub>4</sub> /CO/H <sub>2</sub>	Air	1	Global 6 step	7	6	[26]

Reaction mechanisms can have limited numbers of species and reactions involved, which are usually referred to as global or multi-step mechanisms. On the other hand, a detailed mechanism is a set of elementary reactions forming a complex network. For instance, for a mixture of CH<sub>4</sub>-CO-H<sub>2</sub>, Westbrook and Dryer [40] have proposed a simple three-step global mechanism, as stated in Table 3-5.

Jones and Lindstedt have proposed a four-step mechanism to include the effect of hydrogen content, as reported in Table 3-6. Frassoldati et al. [38] compared these

two global mechanisms with detailed mechanism (DKM) in laminar flow. Their comparison results are shown in Figure 3-12.

Table 3-5. Westbrook-Dryer mechanism (WD) - rate coefficients in the form  $k=A \cdot T^n \cdot \exp(-E_a/RT)$  - A units: mol/l/s/K;  $E_a$  units: cal/mol

	Reaction	Kinetic rate expression
1	$CH_4 + 1.5O_2 \rightarrow CO + 2H_2O$	$r_1 = 5 \times 10^{11} e^{-\frac{47800}{RT}} [CH_4]^{0.7} [O_2]^{0.8}$
2	$CO + 0.5O_2 \rightarrow CO_2$	$r_2 = 2.24 \times 10^{12} e^{-\frac{40700}{RT}} [CO][H_2O]$
3	$CO_2 \rightarrow CO + 0.5O_2$	$r_3 = 5 \times 10^8 e^{-\frac{40700}{RT}} [CO_2]$

Table 3-6. Jones-Lindstedt mechanism (JL)- rate coefficients in the form  $k=A \cdot T^n \cdot \exp(-E_a/RT)$  - A units: mol/l/s/K;  $E_a$  units: cal/mol

	Reaction	Kinetic rate expression
1	$CH_4 + 0.5O_2 \rightarrow CO + 2H_2$	$r_1 = 4.4 \times 10^{11} e^{-\frac{30000}{RT}} [CH_4]^{0.5} [O_2]^{1.25}$
2	$CH_4 + H_2O \rightarrow CO + 3H_2$	$r_2 = 3 \times 10^8 e^{-\frac{30000}{RT}} [CH_4][H_2O]$
3	$CO + H_2O \leftrightarrow CO_2 + H_2$	$r_3 = 2.75 \times 10^9 e^{-\frac{20000}{RT}} [CO][H_2O]$
4	$H_2 + 0.5O_2 \leftrightarrow H_2O$	$r_4 = 6.8 \times 10^{15} \cdot T^{-1} e^{-\frac{40000}{RT}} [H_2]^{0.25} [O_2]^{1.5}$

They have reported a large discrepancy between global and detailed mechanism predictions and also with experimental temperature and composition profiles from a small-scale gas burner.

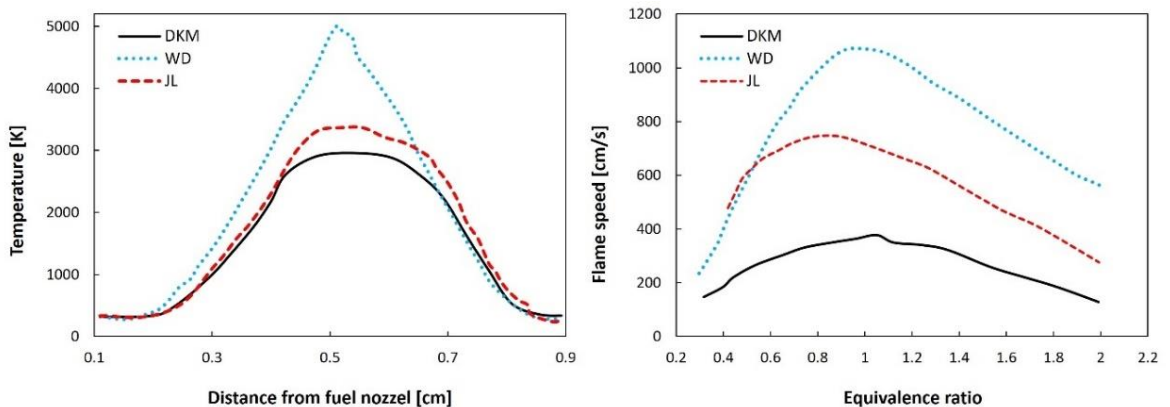


Figure 3-12. Calculated temperature and flame speed via the global and detailed mechanism [38]

Ultimately, they have proposed a modified JL mechanism with tuned kinetic parameters, which matches well with predictions from the detailed mechanism, as shown in Figure 3-13.

Table 3-7. Modified Jones-Lindstedt mechanism (JL-modified)- rate coefficients in the form  $k=A \cdot T^n \cdot \exp(-E_a/RT)$  - A units: mol/l/s/K;  $E_a$  units: cal/mol

Reaction	Kinetic rate expression
1 $CH_4 + 0.5O_2 \rightarrow CO + 2H_2$	$r_1 = 3.06 \times 10^{11} e^{-\frac{30000}{RT}} [CH_4]^{0.5} [O_2]^{1.3}$
2 $CH_4 + H_2O \rightarrow CO + 3H_2$	$r_2 = 3.84 \times 10^9 e^{-\frac{30000}{RT}} [CH_4][H_2O]$
3 $CO + H_2O \leftrightarrow CO_2 + H_2$	$r_3 = 2.01 \times 10^9 e^{-\frac{20000}{RT}} [CO][H_2O]$
4 $H_2 + 0.5O_2 \leftrightarrow H_2O$	$r_4 = 8.03 \times 10^{16} \cdot T^{-1} e^{-\frac{40000}{RT}} [H_2]^{0.3} [O_2]^{1.55}$
5 $O_2 \leftrightarrow 2O$	$r_5 = 1.5 \times 10^9 e^{-\frac{113000}{RT}} [O_2]$
6 $H_2O \leftrightarrow H + OH$	$r_6 = 2.3 \times 10^{22} e^{-\frac{120000}{RT}} [H_2O]$

In another study, Graca et al. [41] studied the combustion of methane-air mixture using a detailed and reduced mechanism and compared it to the Westbrook-Dryer global mechanism and reported poor performance and prediction of the global mechanism. The same is reported by other researchers [32–34,38]. From the mentioned comparative studies, two important conclusions can be derived:

1. Increasing the number of species and intermediate reactions will improve the performance of a global mechanism
2. Detailed mechanisms will perform better, and obtained results can be used as a reference to improve global mechanisms in the absence of experimental data.

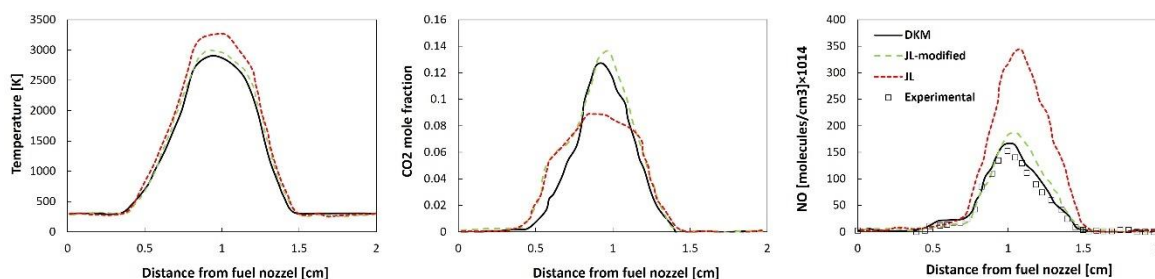


Figure 3-13. Obtained results from the proposed modified mechanism of Frassoldati et al. [38]

With detailed mechanisms, it is possible to study phenomena such as ignition temperature, ignition delay, laminar flame speed, etc., in more detail, resulting in more reliable predictions. The most comprehensive mechanism for the combustion of  $CH_4$ - $CO$ - $H_2$  mixture (or  $CO$ - $H_2$  mixture) is known as the GRI (Gas Research Institute) mechanism, which was originally designed for  $CH_4$  combustion by researchers at the combustion laboratory of the University of California, Berkeley [42]. The recently developed GRI mechanism (GRI 3.0) contains 325 reactions with 55 species and can be directly used to study  $CO$ - $H_2$  mixture (no  $CH_4$ ) [26,39] and  $NO_x$  formation [43–48].

The precision of detailed mechanisms comes at a higher computational cost as they include more species and reactions in the CFD calculations. For example, most researchers have used a reduced GRI mechanism where some species and reactions might be eliminated depending on specific reactive flow conditions [49–52][53]. Other researchers have proposed their own detailed mechanism with much fewer species and reactions, but for kinetic data, they have mainly referred to the GRI mechanism [18,19,21–23,27,28,30–37]. As mentioned in Chapter 2, for the current off-gas system analysis, the proposed mechanism by Frassoldati et al. [36] is used (14 species and 33 reactions), which can be easily imported as CHEMKIN format with a reasonable computational cost. The list of the reactions and related Arrheniusian parameters is reported in Table 3-8.

Table 3-8. CO/H<sub>2</sub>/O<sub>2</sub> mechanism with rate coefficients in the form  $k=A \cdot T^n \cdot \exp(-E_a/RT)$ ,  
A units: mol/l/s/K; E<sub>a</sub> units: cal/mol

	<b>Reaction</b>	<b>A</b>	<b>n</b>	<b>E<sub>a</sub></b>
1	H+O <sub>2</sub> =OH+O	2.21E+11	0	16 650
2	O+H <sub>2</sub> =OH+H	4.33E+10	0	10 000
3	H+O <sub>2</sub> + $[M]$ =HO <sub>2</sub> + $[M]$	4.65E+09	-0.8	0
4	H+O <sub>2</sub> +O <sub>2</sub> =HO <sub>2</sub> +O <sub>2</sub>	8.90E+08	0	-2822
5	OH+HO <sub>2</sub> =H <sub>2</sub> O+O <sub>2</sub>	5.00E+10	0	1000
6	H+HO <sub>2</sub> =OH+OH	2.50E+11	0	1900
7	O+HO <sub>2</sub> =O <sub>2</sub> +OH	3.25E+10	0	0
8	OH+OH=O+H <sub>2</sub> O	7.36E+09	0	1100
9	H <sub>2</sub> + $[M]$ =H+H+ $[M]$	2.23E+11	0	96 081
10	O <sub>2</sub> + $[M]$ =O+O+ $[M]$	1.55E+11	0	115 120
11	H+OH+ $[M]$ =H <sub>2</sub> O+ $[M]$	4.50E+16	-2	0
12	H+HO <sub>2</sub> =H <sub>2</sub> +O <sub>2</sub>	2.50E+10	0	700
13	HO <sub>2</sub> +HO <sub>2</sub> =H <sub>2</sub> O <sub>2</sub> +O <sub>2</sub>	2.11E+09	0	0
14	OH+OH+ $[M]$ =H <sub>2</sub> O <sub>2</sub> + $[M]$	7.40E+10	-0.37	0
15	O+OH+ $[M]$ =HO <sub>2</sub> + $[M]$	1.00E+10	0	0
16	H+H <sub>2</sub> O=H <sub>2</sub> +OH	4.00E+07	1	19 000
17	H <sub>2</sub> O <sub>2</sub> +H=H <sub>2</sub> O+OH	2.41E+10	0	3970
18	H <sub>2</sub> O <sub>2</sub> +H=H <sub>2</sub> +HO <sub>2</sub>	6.03E+10	0	7950
19	HO <sub>2</sub> +H <sub>2</sub> O→H <sub>2</sub> O <sub>2</sub> +OH	5.39E+05	2	28 780
20	OH+H <sub>2</sub> O <sub>2</sub> →H <sub>2</sub> O+HO <sub>2</sub>	3.20E+05	2	-4170
21	O+H <sub>2</sub> O <sub>2</sub> →OH+HO <sub>2</sub>	1.08E+06	2	-1657
22	CO+O+ $[M]$ =CO <sub>2</sub> + $[M]$	9.64E+07	0	3800
23	CO+OH=CO <sub>2</sub> +H	9.60E+08	0.14	7352
24	CO+HO <sub>2</sub> =CO <sub>2</sub> +OH	3.01E+10	0	23 000
25	CO+H <sub>2</sub> O=CO <sub>2</sub> +H <sub>2</sub>	2.00E+08	0	38 000
26	O <sub>2</sub> +CO=CO <sub>2</sub> +O	2.53E+09	0	47 700
27	HCO+ $[M]$ =CO+H+ $[M]$	1.20E+14	-1	17 000
28	HCO+O=CO <sub>2</sub> +H	3.00E+10	0	0
29	HCO+H=H <sub>2</sub> +CO	1.00E+11	0	0
30	HCO+OH=H <sub>2</sub> O+CO	5.00E+10	0	0
31	HCO+HO <sub>2</sub> =H <sub>2</sub> O <sub>2</sub> +CO	4.00E+08	0	0
32	O <sub>2</sub> +HCO=HO <sub>2</sub> +CO	1.00E+09	0	0
33	HCO+HO <sub>2</sub> ⇒H+OH+CO <sub>2</sub>	3.00E+10	0	0

To justify the selection of this mechanism for the rest of the study, a set of simulations is performed to compare GRI 3.0 (325 reactions with 55 species), GRI 1.2 (177 reactions with 32 species), and Frassoldati mechanism (14 species and 33 reactions). Figure 3-14.A and Figure 3-14.B show the predicted temperature and CO mole fraction profiles. As can be seen, all studied mechanisms predict the same trend for the profiles. The predicted carbon conversions at the outlet of the reflux chamber (point A) are 53%, 54%, and 52% for Frassoldati, GRI 1.2, and GRI 3.0, respectively.

However, as mentioned before, the higher number of reactions will lead to a higher simulation cost. Figure 3-14.C shows the normalized simulation time for all three mechanisms for the same iterations. As can be seen, compared to the Frassoldati mechanism, GRI 3.0 and GRI 1.2 exhibit simulation times 15.6 and 3.5 times higher, respectively, while obtaining similar predicted profiles and carbon conversions. According to these results, the computational costs grow exponentially by increasing the number of reactions in the mechanism. Considering the obtained results, utilizing the detailed Frassoldati mechanism seems more reasonable.

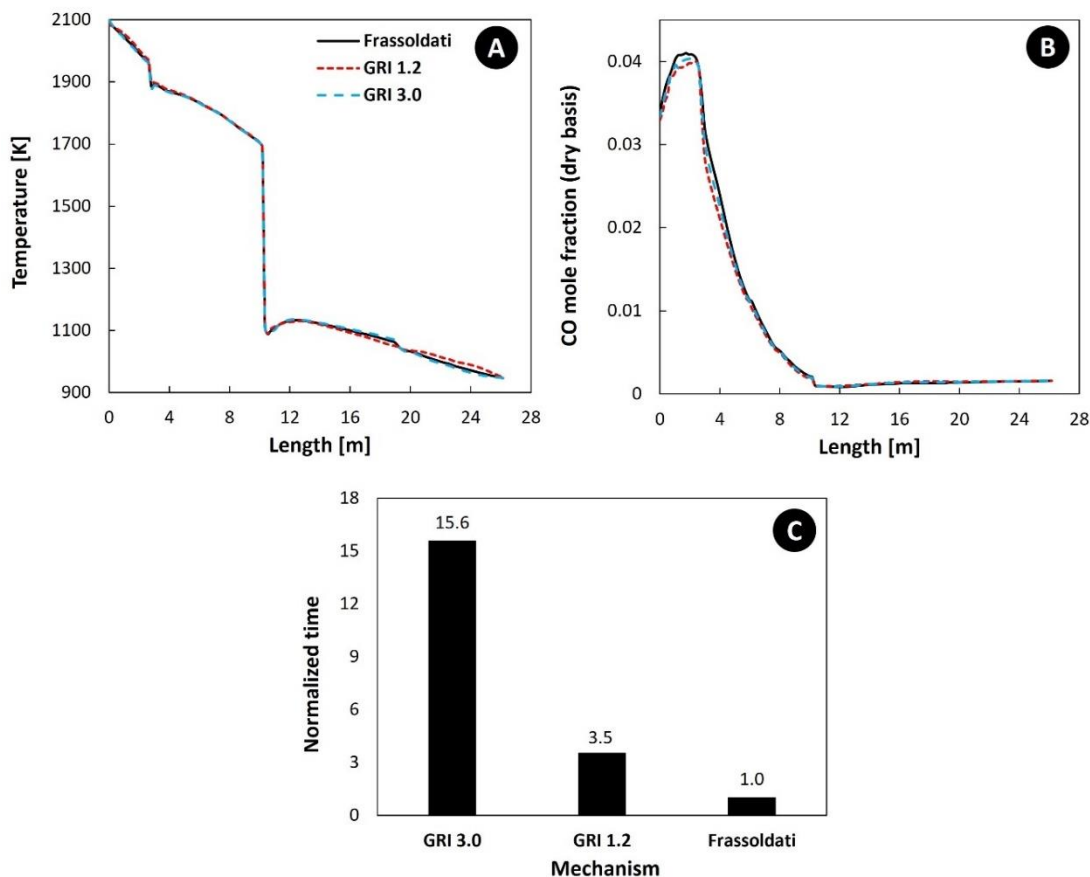


Figure 3-14. Temperature and CO profile prediction for different kinetic mechanisms



After selecting the reaction mechanism, a proper TCI model needs to be selected. Among the available TCI models, the eddy dissipation model (EDM), finite rate/eddy dissipation model (FR-EDM), relaxed to equilibrium finite rate/eddy dissipation model (FR-EDM-relax), and eddy dissipation concept model (EDC) are considered for comparison. All of the mentioned models are extensions of the EDM. Detailed discussion on the mathematical formulation of each model is presented in Chapter 2. However, a brief reminder is presented here.

EDM model calculates the overall reaction rate, assuming that the rate of each reaction is fully controlled by turbulent mixing and the chemical reaction is fast. In fact, EDM bypasses the kinetic data and will not consider finite rate effects in reaction rate calculations. The FR-EDM model calculates the reaction rate of a species as the minimum between the turbulent mixing rate and finite rate from Arrhenius parameters.

The FR-EDM-relaxed is similar to the FR-EDM. However, in this variant, thermodynamic equilibrium is considered in each computational cell at the end of calculations, relaxing the species fractions to their calculated equilibrium values. Last but not least, the EDC assumes that combustion occurs in the flow regions where turbulent kinetic energy dissipation occurs (fine structures). These regions can be described as perfectly stirred tank reactors (PST) at constant pressure, where the reactions advance according to a chemical residence time, defined as a function of turbulence parameters [54].

There are many studies where the above-mentioned TCI models have been utilized to simulate different gaseous and gas-solid reactive flows in small and large-scale applications. Table 3-9 summarizes some of the available literature on the reaction mechanism development and their applications in CFD models. To the authors' best knowledge, only a few studies compared the TCI models.

Musa et al. [55] have compared EDM and FR-EDM to model the gaseous phase combustion process in a ramjet engine with swirling flow. According to their paper, both TCI models predict similar results; however, FR-EDM is preferred in such combustors with non-premixed flames. Emami et al. [83] have investigated the effect of EDM and EDC model on the behaviour of a laboratory scale hydrogen-fuelled, dual-stage high-velocity oxy-fuel (HVOF) and reported the superiority of the

EDC model over EDM. They have reported an overheating of the flow and extra heat release near the fuel-rich regions for the EDM model. The same overestimation of temperature is reported by other researchers [54,91–93].

Table 3-9. Summary of utilized TCI models for different reactive flow modelling at different scales

Application	Scale	Fuel mixture	Mechanism	TCI model	Reference
Hydrogen jet	Experimental	H <sub>2</sub>	Detailed (16 and 37 reactions)	EDM/EDC	[56]
Gas burner	Pilot	C <sub>2</sub> H <sub>6</sub> /CH <sub>4</sub> /CO/H <sub>2</sub>	Reduced GRI	EDC	[57]
Gas burner	Experimental	CH <sub>4</sub> /CO/H <sub>2</sub>	GRI	EDC	[58][59][60]
Wood pellet burner	Domestic	Solid biomass CO-H <sub>2</sub>	Global	EDC	[61]
Sulfur recovery unit (SRU)	Industrial	H <sub>2</sub> S/CH <sub>4</sub>	Detailed (432 reactions)	EDC	[62]
Gas burner	Pilot	CH <sub>4</sub> /H <sub>2</sub>	GRI DRM-22 [63]	EDC	[64][65]
Gas burner	Industrial	CH <sub>4</sub> /H <sub>2</sub>	Global DRM-19 [63] GRI	EDC/FR-EDM	[66]
Entrained flow coal gasifier	Experimental /pilot	Coal /CO/H <sub>2</sub>	Global[67][40][68] GRI CRECK [69]	EDC/FR-EDM	[17]
Cyclonic gas burner	Experimental	C <sub>3</sub> H <sub>8</sub>	San Diego [70]	EDC	[71]
JHC burner	Experimental	ethylene/H <sub>2</sub>	GRI POLIMI [72]	EDC	[73]
Gas burner	Experimental	CH <sub>4</sub>	GRI DRM 19 global	EDC	[40]
Burner	Experimental	CH <sub>4</sub> /CO	SFM KEE	EDC	[74]
Burner	Pilot	H <sub>2</sub>		EDM	[75]
Pulsejet engine	Experimental	C <sub>12</sub> H <sub>23</sub> /CH <sub>4</sub>		EDM	[76]
Furnace	Experimental	CH <sub>4</sub> /CO/H <sub>2</sub>	DRM19	EDC	[77]
Rocket combustion chamber	Experimental	CH <sub>4</sub> /CO/H <sub>2</sub>	detailed (18 reactions) [78]	EDC	[79]
Coal burner	Experimental	pulverized coal/CO/H <sub>2</sub>	Detailed frank	EDM/EDC	[54]
Furnace	Industrial	Natural gas	Global 4 step	EDM	[80]
Entrained flow gasifier	Pilot	Coal/CO/H <sub>2</sub>	Reduced GRI	EDC	[81]
Entrained bed gasifier	Pilot	Coal/CO/H <sub>2</sub>	Detailed	FR-EDM	[82]
High-velocity oxy-fuel	Experimental	H <sub>2</sub>	Global 2 step	EDM/EDC	[83]
Thermal cracking	Pilot	C <sub>2</sub> H <sub>6</sub> /C <sub>3</sub> H <sub>8</sub> /C <sub>4</sub> H <sub>10</sub>	Detailed (23 reactions)	FR-EDM	[84]
Thermal cracking	Pilot	C <sub>3</sub> H <sub>8</sub>	Detailed (23 reactions) [85]	EDC	[86]
Micro mixing	Experimental	Boric acid	Global 3 step	FR-EDM	[87]
Solid fuel ramjet	Experimental	C <sub>2</sub> H <sub>4</sub>	Global 3 step	EDM/FR-EDM	[55]
Ethylene cracking furnaces	Pilot		Detailed (22 reactions)	FR-EDM	[88]
Steam methane reforming furnace	Industrial	CH <sub>4</sub>	Global (3 step)	EDC	[89]
Steam methane reforming furnace	Industrial	CH <sub>4</sub>	Global (3 step)	FR-EDM	[90]

The primary reason for this discrepancy lies in how EDM links the calculation of reaction rates to turbulence effects. EDM calculates the reaction rate exclusively based on turbulence parameters, disregarding kinetic data [83,92,93]. Due to this neglect of chemical kinetics, the impacts of intermediate species and endothermic dissociation reactions are overlooked, resulting in an over-prediction of temperature. This over-prediction is particularly pronounced in highly turbulent and fuel-rich regions. [83,94]. For example, Emami et al. [83] have reported

temperature overestimation by the EDM for a rich mixture (equivalence ratio =1.4); however, this over-prediction was minor for a leaner mixture (equivalence ratio =1). The other drawback is the poor prediction of ignition and reactions where chemical kinetics may limit the rate as there is no kinetic control of the reactions [95].

Moreover, the EDM calculates the same turbulent rate for all reactions; therefore, including a detailed mechanism would not make any specific difference compared to a global mechanism. In fact, the EDM should only be used with global mechanisms [17,66,83,96]. In conclusion, EDM assumes mixing is the only parameter that controls the combustion rate and heat release, leading to unphysical overheating, temperature increase, and poor prediction of ignition properties.

In another interesting research, Parente et al. [66] have the effect of FR-EDM and EDM using experimental and numerical analysis of industrial burner. They reported that the FR-EDM model cannot capture the main features of the MILD reaction zone, while the EDC model with a detailed chemical mechanism performs satisfactorily. As can be seen in Figure 3-15, FR-EDM predicts an overshoot of temperature when compared to EDC with both global and detailed mechanisms. Temperature overshoot is more pronounced near the flame region with rich fuel content.

Figure 3-16 shows NO<sub>x</sub> prediction by different TCI models and again points to EDC superiority in predictions. In another study, the EDC eminence was confirmed by Mularski et al. [17] by investigating the impact of chemical reaction mechanisms and turbulence–chemistry interaction approaches on coal gasification in entrained flow reactors in three different configurations. Since the gas-solid reaction is modelled using the multiple surface reaction approach in the current case, applying EDM is impossible. To begin the comparisons, the simulations were performed using the FR-EDM with the detailed mechanism. However, the reactions were not initiated during the calculations, and all kinetic rates were zero. This is actually one of the shortcomings of both EDM and FR-EDM, which fail a precise prediction of the ignition. The same issue is reported by Sripriya et al. [95] for post-combustion of CO-H<sub>2</sub> mixture. They have included artificial heat point sources inside the computational domain as source terms to resolve this issue. This way, the source terms act like the ignition sources to guarantee the persistence of the reactions and flame formation (if there are any).

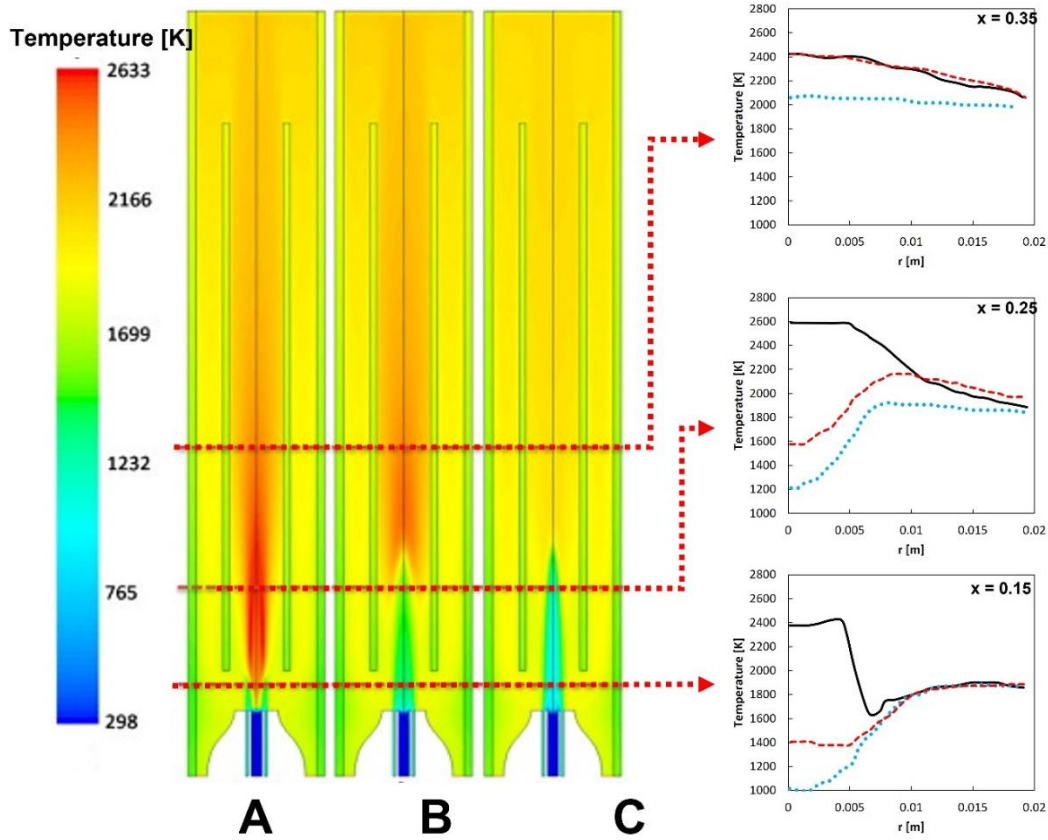


Figure 3-15. Temperature distribution in the burner fed for the study of Parente et al. [65] with  $\text{CH}_4/\text{H}_2$  predicted by (A) ED/FR with global chemistry, (B) EDC with global chemistry, (C) EDC with detailed GRI mechanism [66]

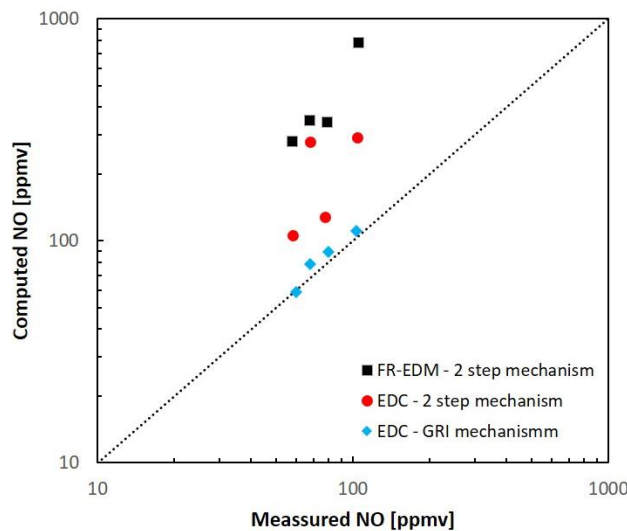


Figure 3-16. Predicted  $\text{NO}_x$  formation by different TCI models and mechanisms [66]

In the current study, the problem of the reaction initiation is resolved by using FR-EDM and then relaxing the calculated composition to their chemical equilibrium, also known as relaxed to equilibrium calculations (FR-EDM-rer). This approach initiates the reaction and ignition without artificial heat sources.

Figure 3-17.A shows the predicted temperature and CO mole fraction profile for EDC and FR-EDM-rer (other sub-models are the same for both TCI models).

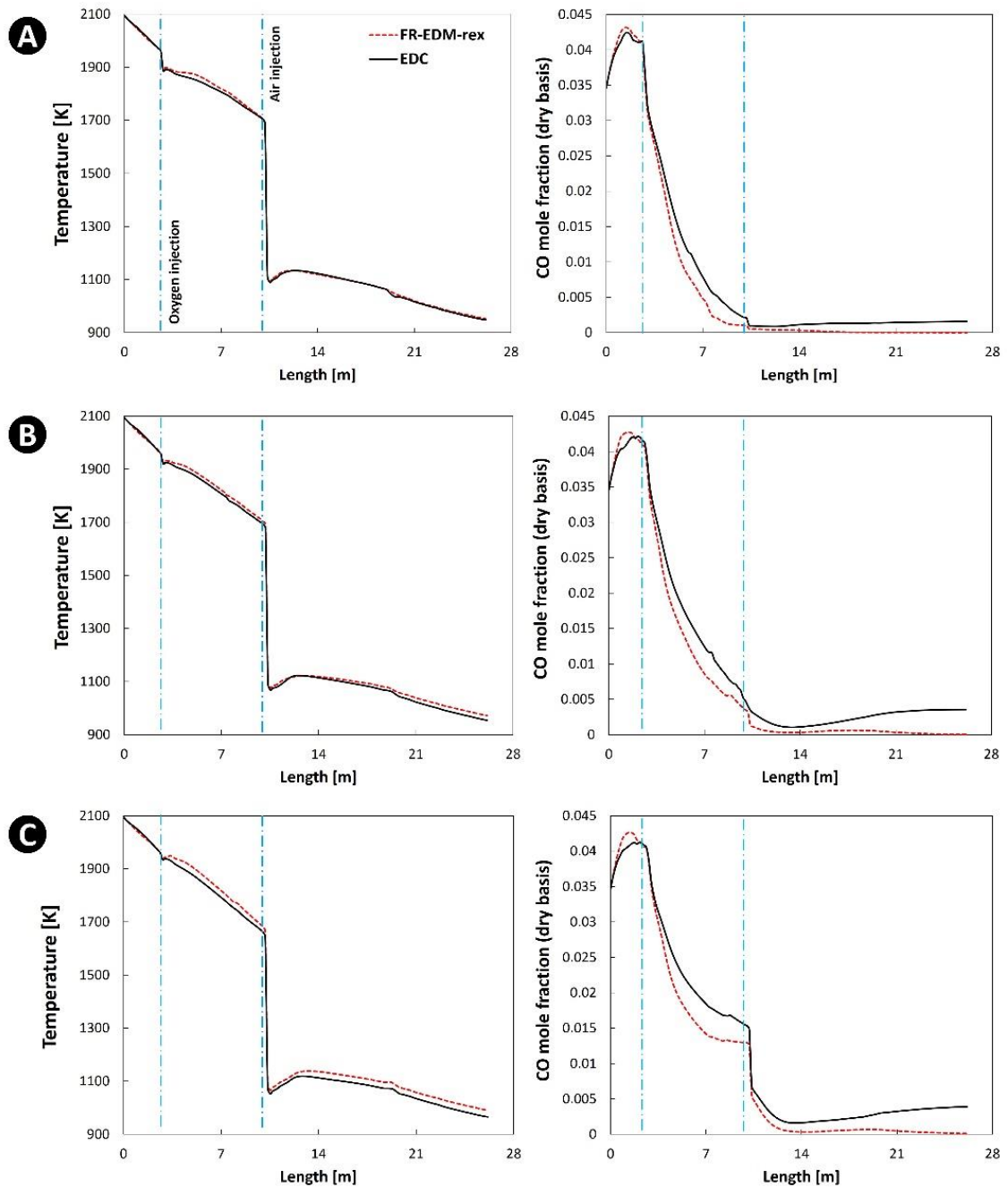


Figure 3-17. Temperature and CO profile for different oxygen reduction cases; A) 0% reduction, B) 60% reduction, C) 80% reduction

As illustrated, the predictions for both models are quite similar; however, the FR-EDM-rer predicts a slightly higher temperature in the oxygen injection region of the reflux chamber where the CO combustion occurs. A more pronounced discrepancy can also be seen for the CO profile in the same region where FR-EDM-rer predicts

a lower CO mole fraction (higher CO conversion). This means that FR-EDM-rer predicts a higher reaction rate, which is also reported by other reviewed studies.

The consistency in predictions among TCI models has been previously reported by Rebola et al. [96], which assessed the performance of several turbulence and combustion models in the numerical simulation of a flameless combustor. Their obtained results are shown in Figure 3-18. Even though the EDC has shown the best performance, FR-EDM has predicted similar profiles.

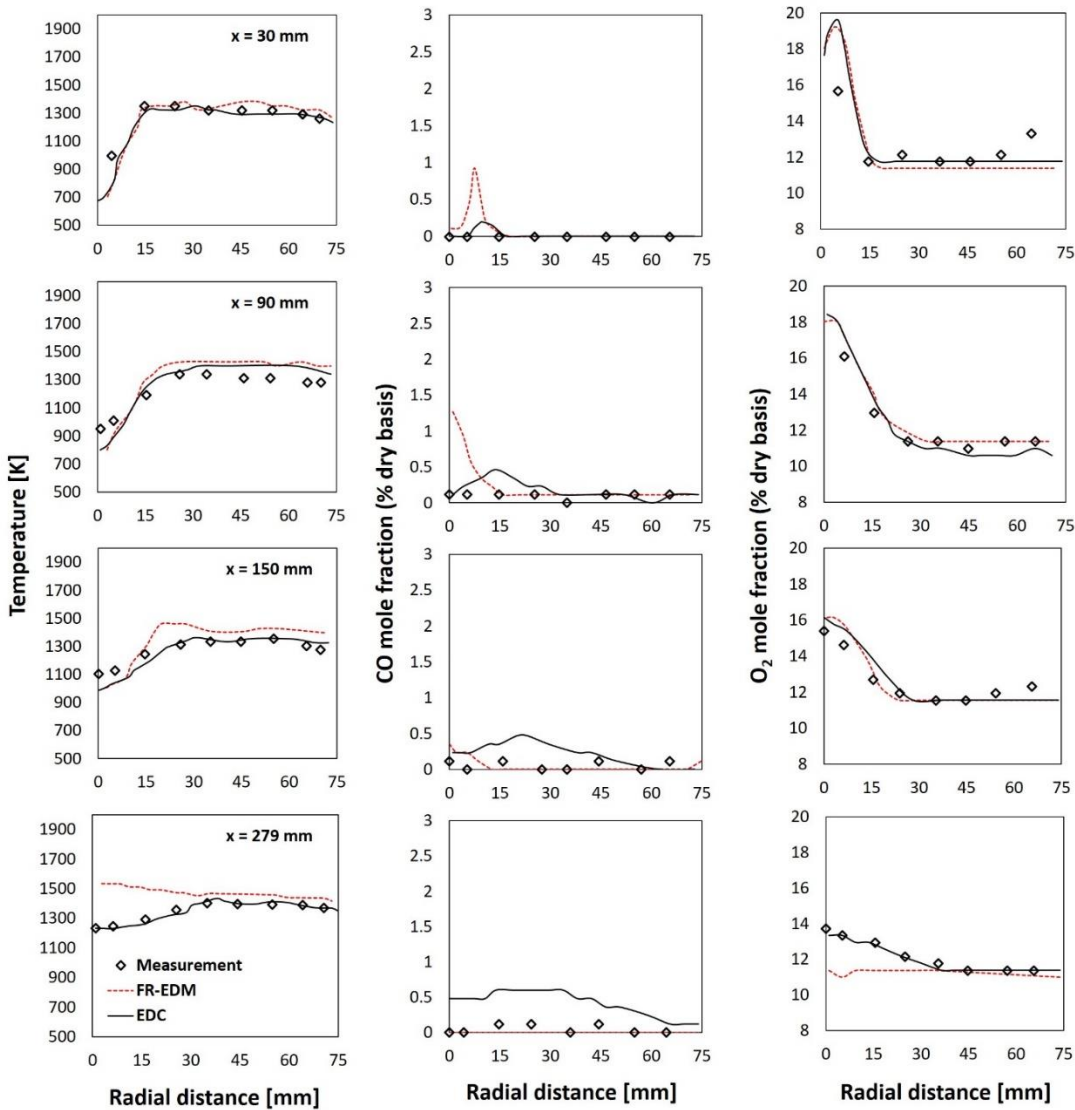


Figure 3-18. Measured and predicted radial temperature, O<sub>2</sub>, and CO molar fraction profiles for different TCI models from the study of Rebola et al. [96]

In another study, Chen et al. [89] reported a similar and comparable temperature contour by the EDM, FR-EDM, and EDC models (Figure 3-19). However, they have chosen the EDC to further investigate their case study.

To have a better analysis, a set of simulations is performed by creating a fuel-rich environment inside the reflux chamber and reducing the oxygen injection by 60% and 80%. The discrepancies between the two TCI models become more evident as depicted in Figure 3-17.B and Figure 3-17.C for 60 % and 80% oxygen reduction, respectively.

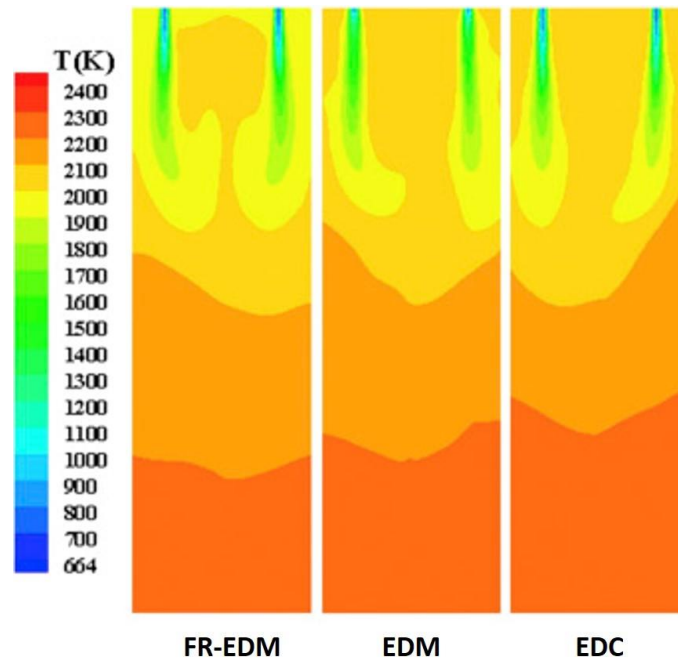


Figure 3-19. Contours of gas temperature distributions of different combustion models from the study of Chen et al. [89]

Again, FR-EDM-rer predicts higher reaction rates, lower CO mole fraction, and slightly higher temperature along the off-gas system length than EDC. The discrepancies in the predicted CO profile are more pronounced in the up-leg/down-leg region of the off-gas system, where full combustion of CO (escaped from the reflux chamber or generated by escaped carbon gasification) is predicted by FR-EDM-rer. In contrast, the EDC predicts almost no combustion (as the temperature is getting lower and lower) but an increase in CO content due to the conversion of the remaining carbon in the flow.

The discrepancies between the two models can also be seen in Figure 3-20, where temperature, carbon conversion, and CO mole fraction at the outlet of the reflux chamber are shown. Even though the difference in temperature and carbon conversion is minor, the CO composition is predicted quite differently for fuel-rich cases.



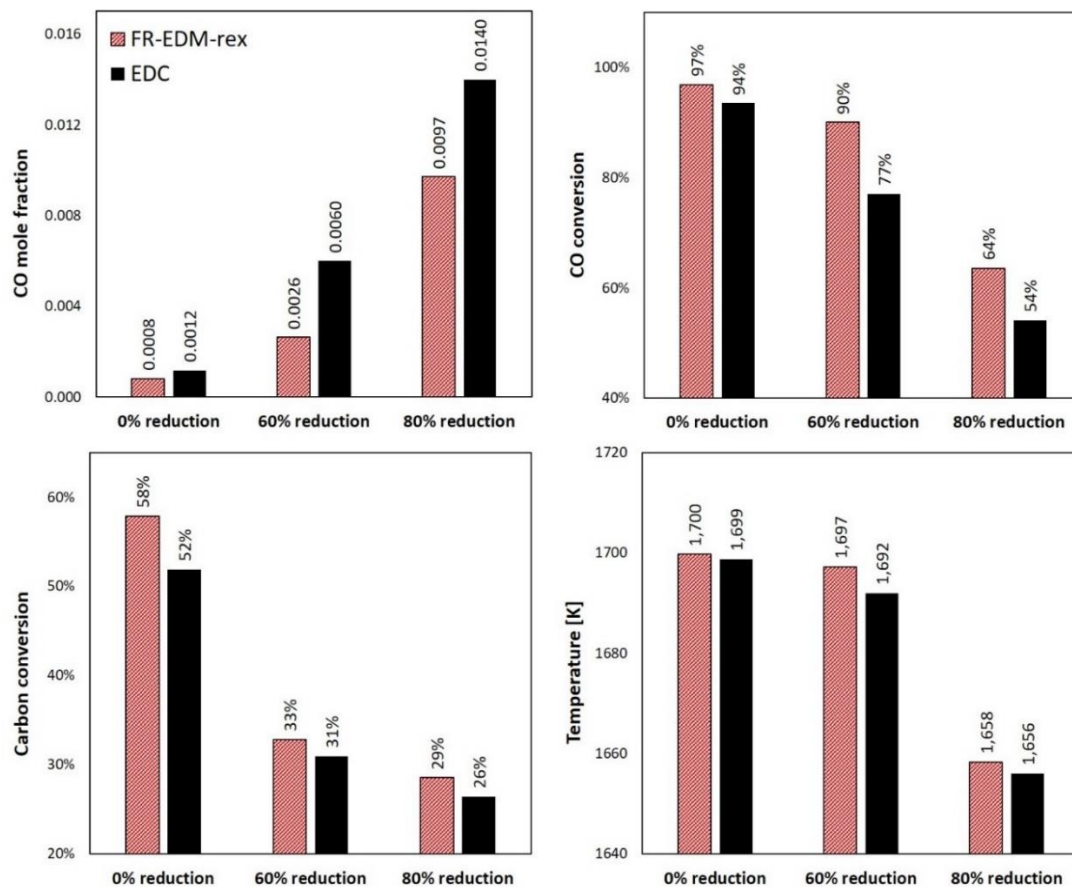


Figure 3-20. Reflux chamber outlet temperature, CO mole fraction, CO conversion, and carbon conversion for different oxygen reduction cases

Nevertheless, for the current case, FR-EDM-rex and EDC predict quite similar temperature profiles, composition profiles, and carbon conversion for the fuel-lean mixture. However, the two TCI model discrepancies become more pronounced for the fuel-rich mixture.

From the literature review and performed analysis for the current case, the following can be deduced regarding TCI model selection:

- The EDM and FR-EDM are better using a global mechanism (with few steps) as the mixing rate is considered the same for all included reactions.
- The EDM predicts temperature overshoot in fuel-rich zones and regions where turbulent mixing is high since it bypasses the kinetic mechanism and computes the same mixing rate for all reactions.
- The FR-EDM considers the effect of finite rate chemistry. However, it still predicts temperature overshoot in fuel-rich zones.



- Like EDM, FR-EDM is best used with global kinetic mechanisms, with the same turbulent rate for all reactions. Therefore, if detailed chemistry is considered, the FR-EDM model will likely produce incorrect results since the rate of production/destruction of the species has to be controlled by the Arrhenius parameters through an accurate description of turbulence/chemistry interactions. Moreover, using the FR-EDM approach with detailed kinetic schemes could lead to numerical instabilities, and it could result in sudden variations of the controlling rates within the reaction zone [66].
- Using the FR-EDM, the ignition of reactions might be predicted poorly, and the reactions might not start, even at very high temperatures. An artificial ignition source might be required to initiate the reaction chain.
- The performance of The FR-EDM can be improved by considering equilibrium calculation.
- The FR-EDM-rex and EDC predict similar results for a fuel-lean mixture with a slight difference. The discrepancies between the two increase for fuel-rich mixtures.

### 3.6. Effect of gas-solid (carbon particles) reaction

Incorporating carbon combustion reactions in the model will change the temperature and composition profile compared to a case without considering any gas-solid reaction. To explain the importance of this consideration, a simulation is performed where only gaseous reactions are considered, neglecting carbon particle flow and reactions in the model. The temperature and composition profiles are illustrated in Figure 3-21, and as is shown, it shifts up by considering the carbon particle reaction as the overall gas-solid reaction is highly exothermic.

When gas-solid reactions are considered, the temperatures at points A, B, and D are around 60 °C higher. The effect is also notable in CO and H<sub>2</sub> profiles, which are higher by considering carbon particles as they participate in H<sub>2</sub>-CO generation. It also has a considerable effect on the O<sub>2</sub> profile. When carbon particles are not considered, the profile in the reflux chamber is constant as oxygen consumption halts when the CO-H<sub>2</sub> mixture is fully combusted. When carbon particles are

considered, the oxygen inside the chamber is reduced along the length as it is constantly reacted by produced CO-H<sub>2</sub> from carbon reaction with O<sub>2</sub>, H<sub>2</sub>O, and CO<sub>2</sub>.

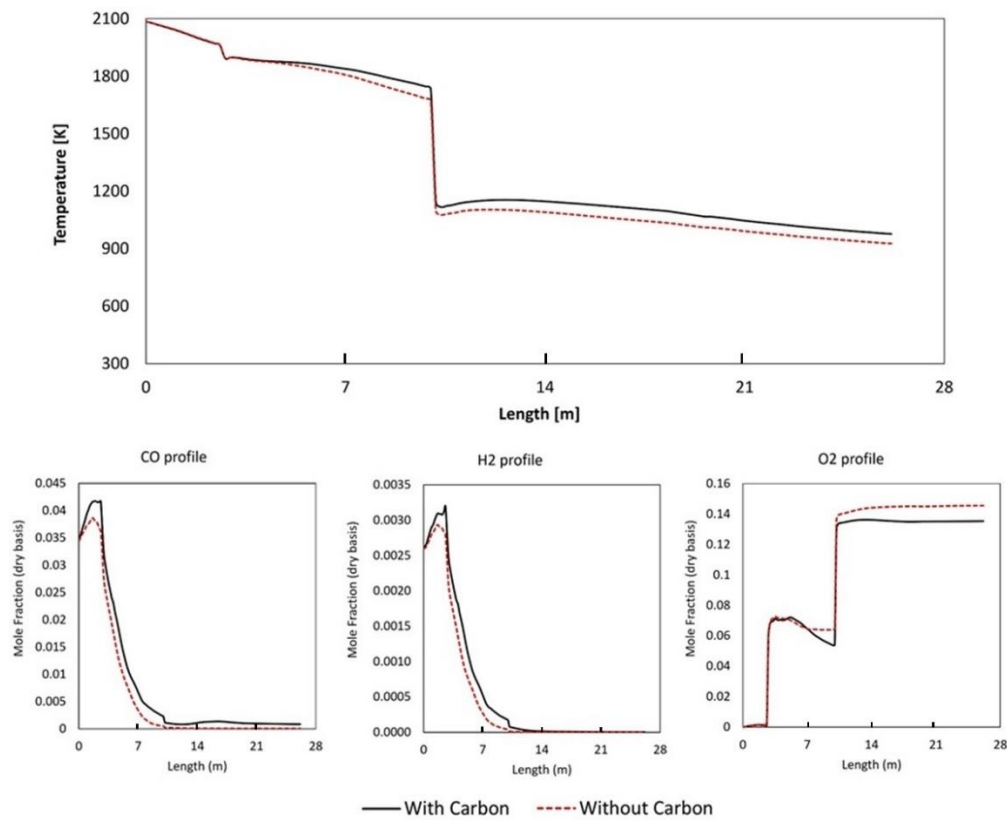


Figure 3-21. Effect of gas-solid (carbon) reaction on averaged cross-section composition and temperature profiles (modelled up to Point C)

In conclusion, considering carbon particles in the model has a notable effect on temperature and composition profiles, leading to a better fit with industrial measurements. However, incorporating gas-solid reactions using the DPM model can significantly increase the calculation time. For example, for the current case, DPM calculation time is around 30% of the total calculation time to reach a convergence of  $10^{-4}$  and a steady state calculated temperature and compositions at monitored points.

### 3.7. Effect of carbon particle dispersion

The turbulent dispersion of particles is considered using the DRW model mentioned in Chapter 2. Using this model, it is possible to control the number of injected particles. To precisely consider the effect of particles in the flow, enough representative particles must be injected. The higher the number of particles, the

better the representation and the closer the modelled particle flow to reality. Therefore, there is no limit to the maximum number of particles. However, the higher number of particles requires more computational time to calculate the trajectories. A sensitivity analysis is required to set a minimum number of particles to represent the actual particles.

The number of injected particles can be controlled by a parameter called NTs (number of tries). Table 3-10 shows the effect of NTs on different calculated values.

Table 3-10. Effect of NTs on predicated values

	Experimental			Calculated		
Number of tries []	-	1	3	5	10	20
Injected particles []	-	923	2769	4615	9230	15640
Reflux chamber outlet carbon flowrate [kg/s]	-	0.0141	0.0137	0.0136	0.0135	0.0135
<b>Reflux chamber outlet carbon conversion [%]</b>	50	50%	52%	52%	53%	52%
Reflux chamber outlet temperature [K]	1710	1692	1698	1702	1695	1702.4
<b>Reflux chamber outlet molar composition (dry basis)</b>						
CO	0.00	0.002	0.0021	0.002	0.00192	0.002
O <sub>2</sub>	0.054	0.0535	0.0532	0.0534	0.0533	0.0534
<b>Heat loss</b>						
Reflux chamber [MW]	3.9	3.89	3.88	3.89	3.92	3.91
Rest of the off-gas system [MW]	5.4	2.87	2.8	2.8	2.83	2.83

For better visualization, Figure 3-22 shows the reflux chamber outlet oxygen, temperature, and carbon conversion for different NTs. As can be seen, after five tries, the values are not changing, and it seems the current case is NTs insensitive. However, higher NTs comes at a higher computational cost. Figure 3-23 shows the normalized simulation time (normalized over the longest simulation time) for cases with different NTs. As can be deduced from the graph, the simulation time is growing exponentially, though at a low rate.

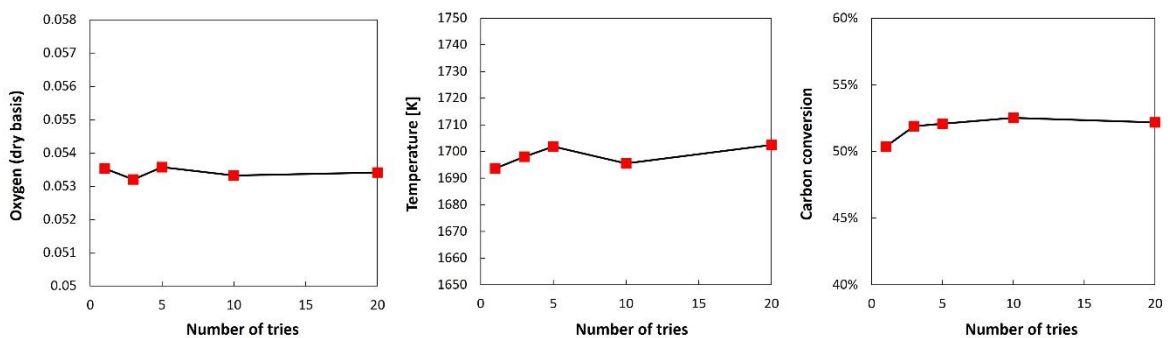


Figure 3-22. Predicted reflux chamber outlet values for different NTs

In cases where the computational resources are limited, it is suggested to perform sensitivity studies to see a possible reduction in NTs and computational costs. It is worth mentioning that for all simulations performed in this study, an NTs = 20 is considered.

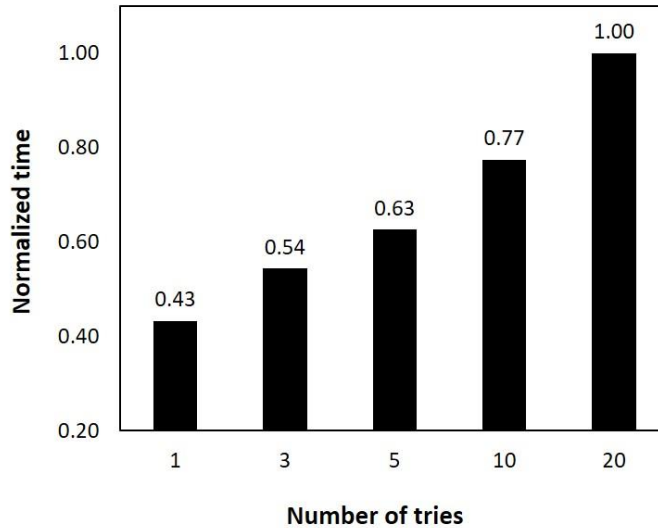


Figure 3-23. Normalized simulation time for different NTs

### 3.8. Effect of the radiation model

Radiative heat transfer can be dominant for systems involving high-temperature phenomena and contribute as high as 95% of total heat transfer [97–99].

This means that in high-temperature applications, the effect of radiative heat transfer cannot be neglected and must be considered during numerical calculations. This is because the rates at which thermal energy is transferred by conduction and convection are known to be approximately proportional to the difference in temperature. In contrast, the rate of thermal energy transferred by radiation is proportional to the difference between the temperatures raised to the fourth power. The temperature at the off-gas system inlet could sometimes reach as high as 2200 K, which is further increased after post-combustion (2600 K) due to the exothermic reactions in the reflux chamber. In such cases, and generally, in combustion chambers, the temperature difference between the flue gas and water-cooled walls is very large; thus, the radiative heat transfer plays a vital role [100]. In this section, four different cases are considered to compare the effect of radiation inside the reflux chamber (only chamber geometry is modelled). In three cases, Rosseland, P1,

and Discrete Ordinate (DOM) radiation models are used to account for the radiation effect, and one case is set up without any radiation model. Detailed mathematical formulation for each of the mentioned radiation models is demonstrated in Chapter 2. Table 3-11 shows some high-temperature industrial scale applications and respective utilized radiation models.

Table 3-11. Summary of utilized radiation modelling for different high temperature reactive flow applications

Application	Scale	Temperature range [K]	Fuel	Radiation model	Reference
Steam methane reforming furnace	Pilot	1100-1400	CH <sub>4</sub>	DOM	[101]
Ethylene cracking furnaces	Pilot	300-2100	n-Paraffins/i-Paraffins/Olefins	DOM	[88]
Ethylene furnace	Industrial	300-2150	CH <sub>4</sub> /H <sub>2</sub> – complex feed	DOM	[102]
Post-combustion chamber	Pilot	300-2000	CO/H <sub>2</sub>	P1	[95]
Methane combustor	pilot	300-2325	CH <sub>4</sub> /H <sub>2</sub>	P1	[103]
Sulphur removal unit	Industrial		H <sub>2</sub> S	DOM	[62]
hydrogen production reformer	Industrial	650-2500	CH <sub>4</sub>	P1	[89]
naphtha thermal cracking furnaces	Industrial	300-1550	CH <sub>4</sub> /C <sub>2</sub> H <sub>4</sub> /C <sub>2</sub> H <sub>6</sub> /C <sub>3</sub> H <sub>8</sub> /H <sub>2</sub>	DOM	[104]
semi-suspension biomass-fired industrial	Industrial	300-1600	Bagasse	DOM	[105]
Steam methane reforming furnace	Industrial	500-2000	CH <sub>4</sub>	DOM	[90]
Mild combustor	Industrial	300-2519	CH <sub>4</sub> /H <sub>2</sub>	DOM	[66]
Gas burner	Industrial	-	C <sub>2</sub> H <sub>6</sub> /CH <sub>4</sub> /CO/H <sub>2</sub>	DOM	[80]
entrained-flow gasifier	Industrial	300-2250	Coal/CO/H <sub>2</sub>	P1	[81]
Gasifier	Industrial	600-1100	Wood chips	DOM	[106]

Most of the available literature has used the P1 and DOM models to include the radiation effect. There are different criteria for choosing a proper radiation model. The most reliable way is the comparison method, where different radiation models are used and compared with measured values. However, once there is a lack of proper measurements, there are still some rules of thumb to consider for radiation model selection. A good indicator is the optical thickness or opacity of the medium fluid (in the current case, the off-gas flow). Optical thickness can be calculated according to Habibi et al. [107]:

$$\text{optical thickness} = a \times L_s$$

where  $a$  is the absorption coefficient and  $L_s = \frac{k^{1.5}}{\varepsilon}$  is the length scale based on the turbulent parameter of the  $k$ - $\varepsilon$  model. The length scale could also be the diameter of the chamber. The P1 model should typically be used for optical thicknesses  $>1$  [89,90,107]. For optical thickness  $>3$ , the Rosseland model is computationally

cheaper and more efficient. On the other hand, DOM works across all ranges of optical thicknesses but is substantially more computationally expensive than P1 and Rosseland models [108]. Figure 3-24 and Figure 3-25 show the predicted temperature contour and averaged cross-sectional temperature along the reflux chamber length, respectively, for different studied cases.

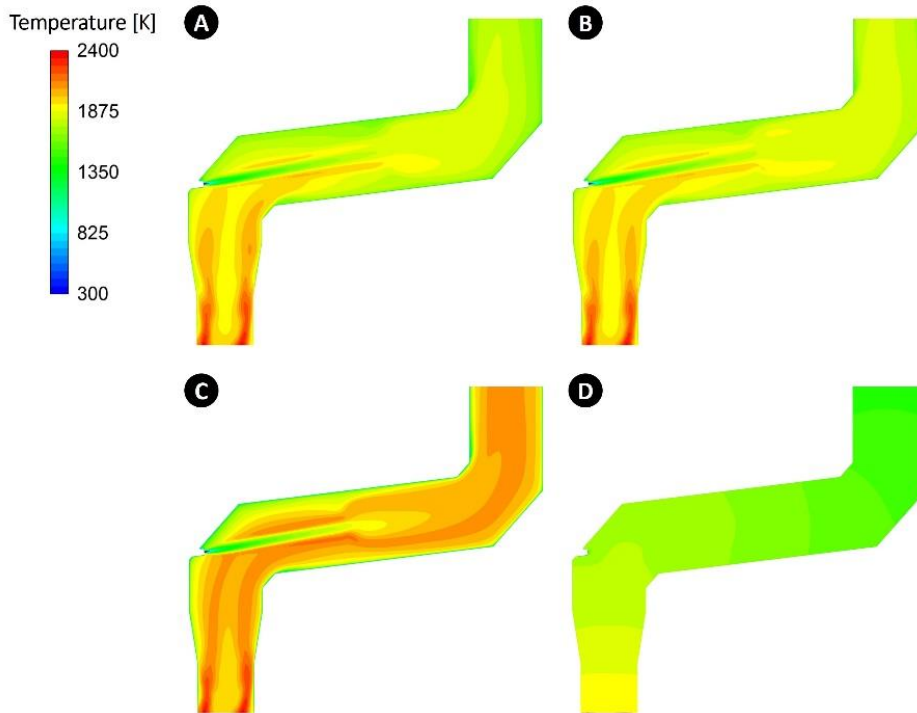


Figure 3-24. Predicted contour of temperature for DOM (A), P1 (B), No Radiation(C) and Rosseland (D) model

The predicted contour and profile for the Rosseland model are unrealistic, and the temperature falls rapidly under 1750 K before hitting the oxygen-rich zone. Moreover, the outlet temperature of the reflux chamber shows a 20% error with respect to the mean measured values and out of the measurement uncertainty in Figure 3-25. The temperature is highly over-predicted for the case without the radiation model, once again illustrating the importance of the radiation effect.

P1 and DOM show similar predictions; however, P1 predicts slightly higher temperatures around and after the oxygen injection zone with a difference of 65 °C compared to the DOM model. Nevertheless, both models predict an outlet temperature within the measurement uncertainty. The wall temperature profile (inner wall in contact with hot flue gas) is comparable for P1 and DOM; however, it is anticipated to be higher for the Rosseland model.

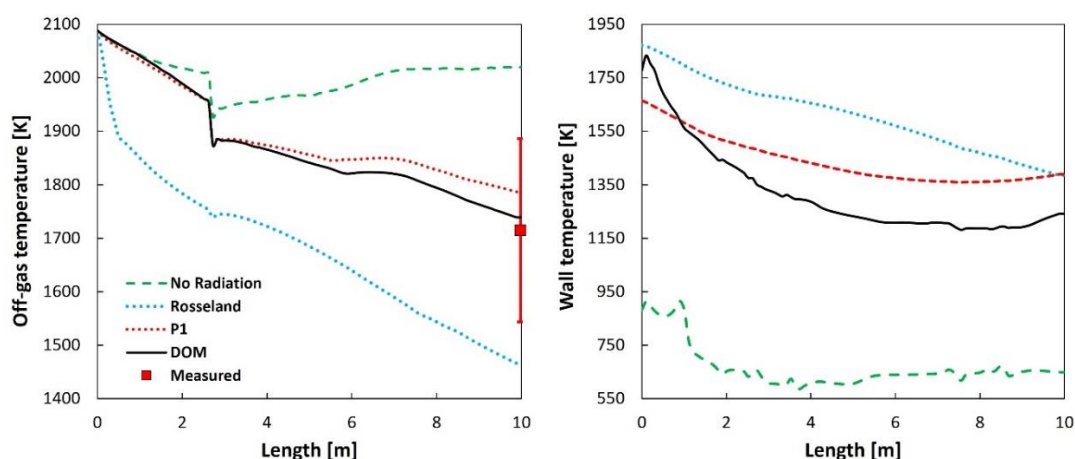


Figure 3-25. Flow and wall temperature across the reflux chamber length for different radiation models

The case without a radiation model exhibits a significant discrepancy with other models, resulting in a higher flow temperature and substantially lower heat losses through the wall.

The same conclusion is derived by Habibi et al. [107], who studied the effect of different radiation models for CFD simulation of a steam cracking furnace. They have reported unrealistic flame formation for the Rosseland and the adiabatic case (without radiation model) but similar predictions for P1 and DOM. They have attributed the lower temperature profile of the Rosseland model to its limitation in predicting radiation intensity accurately. In the Rosseland model, the radiation intensity is not derived from a distinct transport equation, resulting in an inaccurate temperature profile and flame structure [107].

Figure 3-26 shows the predicted contour of the CO mole fraction, which is quite similar for all cases. To have a better analysis, Figure 3-27 shows the averaged cross sectional profile of CO and O<sub>2</sub>, and as can be seen, P1 and DOM models predict similar profiles.

In all cases, the concentration of CO increases before reaching the oxygen injection zone due to CO<sub>2</sub> dissociation at high temperatures and in the absence of oxygen. The scenario without a radiation model predicts a slightly higher CO formation, which is associated with the higher calculated temperature, as discussed in Figure 3-25. This high temperature contributes to a higher dissociation of CO<sub>2</sub> into CO. On the other hand, the Rosseland model showed the highest deviation from other models.

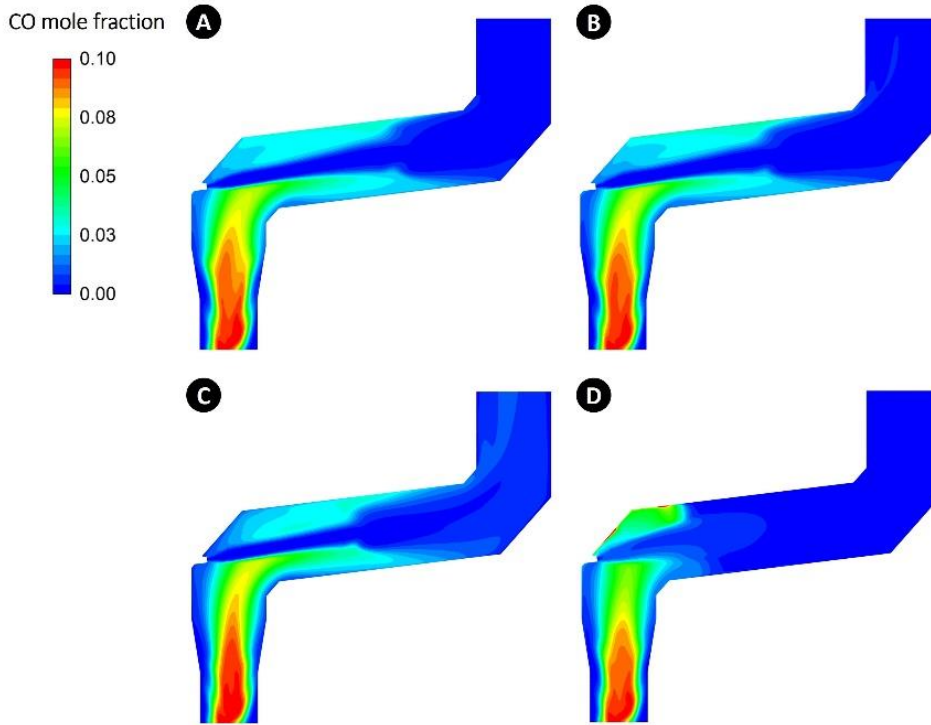


Figure 3-26. Predicted CO contour for different radiation models of DOM (A), P1 (B), No Radiation(C), and Rosseland (D) model

As the temperature experiences a sharp drop in the inlet section of the reflux chamber in this model, the predicted dissociation rate of CO<sub>2</sub> is significantly lower compared to other models. Consequently, the concentration of CO remains nearly constant before reaching the oxygen injection zone.

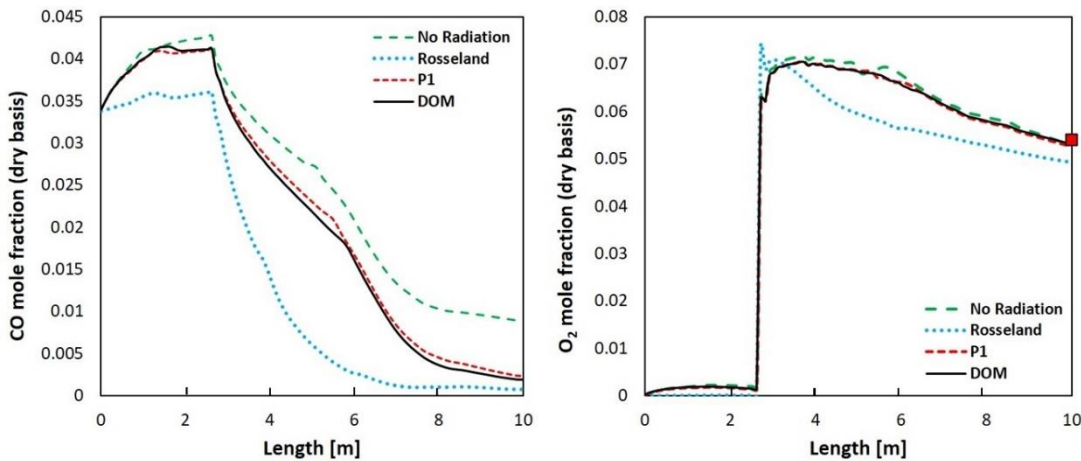


Figure 3-27. Predicted average cross-sectional CO and O<sub>2</sub> profile along the reflux chamber

Additionally, the amount of CO is noticeably lower than in other models at each cross section and the outlet of the reflux chamber. This is again due to a lower predicted average temperature across the reflux chamber for the Rosseland model,



which favors CO conversion into CO<sub>2</sub>. This effect can also be seen in the oxygen profile, which is predicted to be lower at any cross section due to a higher CO conversion. Figure 3-28 and Figure 3-29 show the contour and profile of the optical thickness. As can be seen, the optical thickness value is lower than 1 in all regions for all studied radiation models illustrating an optically thin medium.

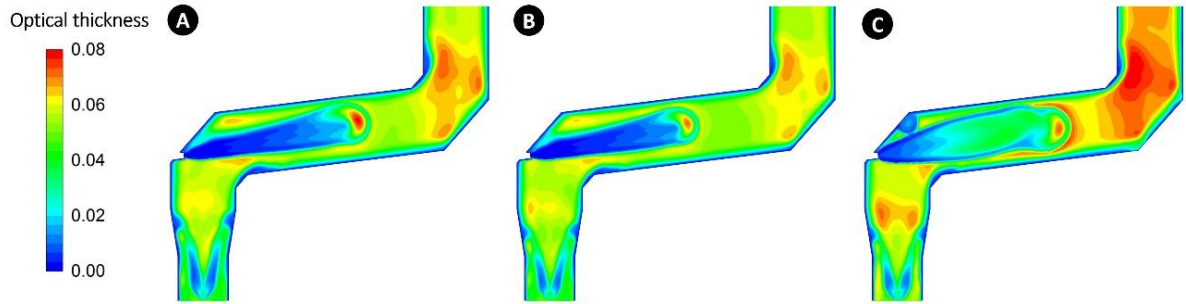


Figure 3-28. Predicted optical thickness for different radiation models of DOM (A), P1 (B), and Rosseland (C) model

The predicted opacities indicate that the Rosseland model shall not be used for this case. All models show a very low optical thickness near the combustion zone but much higher values in the upper parts. Even though the P1 model is suitable for cases with optical thickness >1, it predicts values and profiles much closer to the DOM, which is suitable for all ranges of optical thickness.

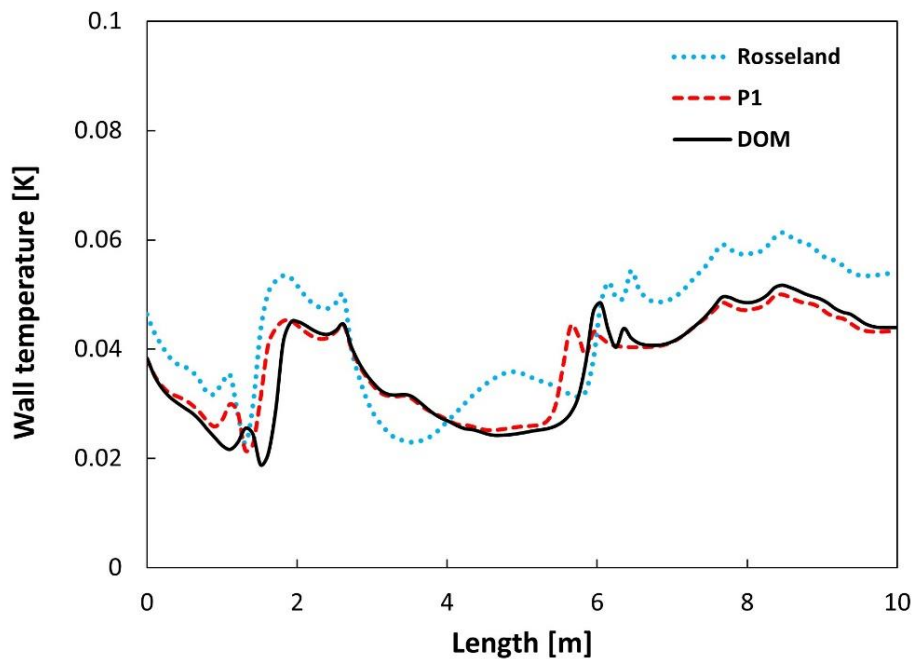


Figure 3-29. Predicted average cross-sectional optical thickness for different radiation models

Nevertheless, DOM predictions are in better agreement with the measured values, as shown in Figure 3-30. The heat losses through the reflux chamber walls are predicted to be much lower than the measured loss due to a very low prediction of the wall temperature (Figure 3-25) for the case without the radiation model. The Rosseland model has predicted much higher heat loss due to a lower flue gas temperature and higher wall temperature prediction inside the reflux chamber.

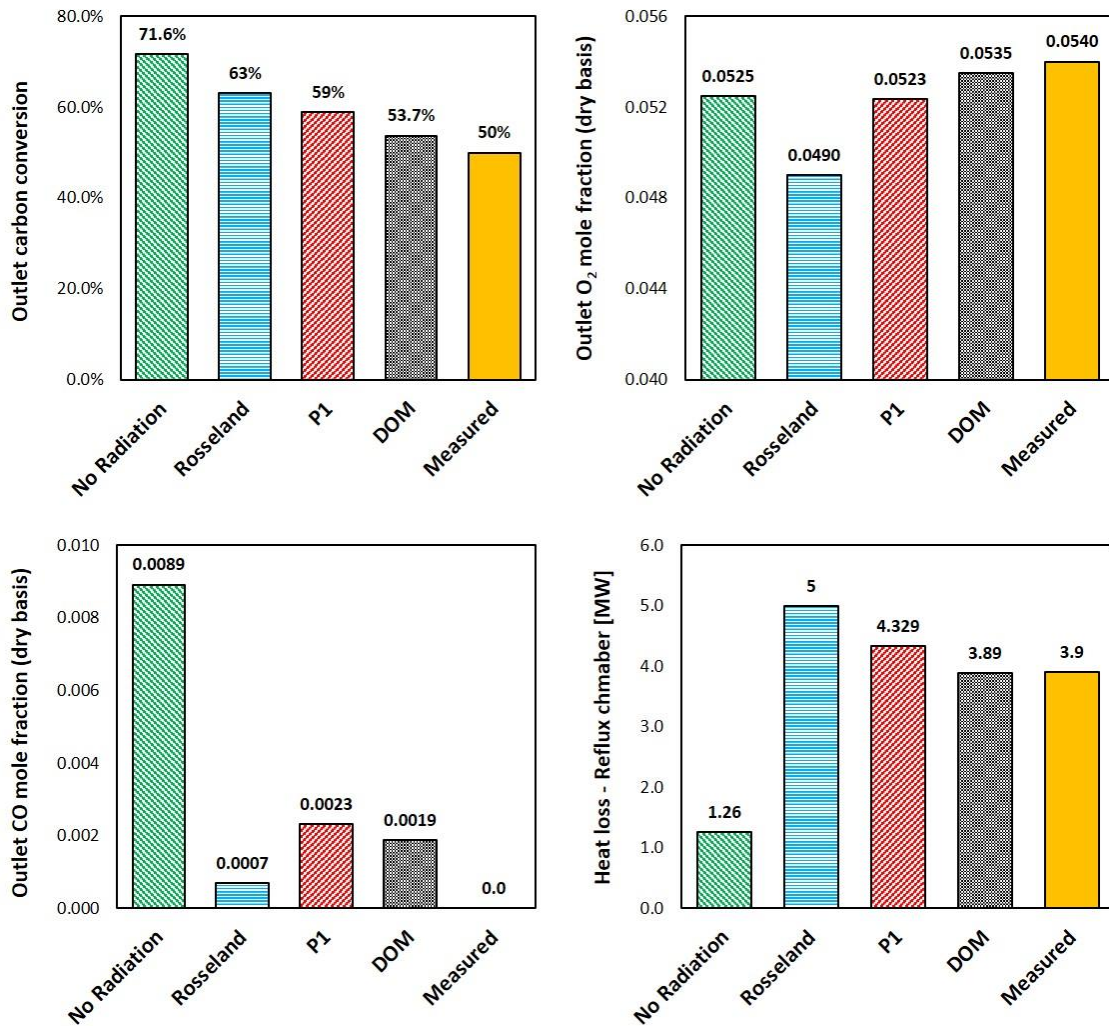


Figure 3-30. Predicted (different radiation mode) and measured values for different outlet parameters

This enhances the driving force for heat transfer to the cold side of the wall (the outer wall in contact with cooling water). The carbon conversion is highest for the case without the radiation model, a direct result of the extremely high temperature, leading to a higher conversion rate of carbon particles. In the Rosseland model, despite having the lowest temperature along the chamber, a higher carbon conversion is predicted compared to P1 and DOM. This might be attributed to the

lower predicted CO partial pressure for the Rosseland model across the reflux chamber, resulting in a slightly higher carbon conversion. The predictions closely align with the measured carbon conversion for the P1 and DOM radiation models.

The same can be seen for CO outlet mole fractions. Due to a very high predicted temperature profile for the case without radiation model, higher carbon is converted into CO. On the other hand, as mentioned before, very high temperature is detrimental to CO conversion and will lead to CO<sub>2</sub> dissociation into CO. Therefore, higher carbon conversion, low CO conversion, and high CO<sub>2</sub> dissociation all contribute to a much higher CO value at the outlet once the effect of radiation is omitted (72% CO conversion). For the Rosseland model, the lowest outlet CO is predicted due to a much lower predicted temperature profile, which is a favourable atmosphere for CO combustion.

Ultimately, a comparison of simulation time for each radiation model is presented in Figure 3-31. As can be seen, including radiation models increases the simulation time by 13%, 11%, and 30% for Roseland, P1, and DOM, respectively with respect to the case without radiation. The DOM model requires the longest simulation time, while the P1 model was computationally the cheapest. The same has been reported in numerous studies [100,107]; however, the relative increase in simulation time for each model is quite case-dependent.

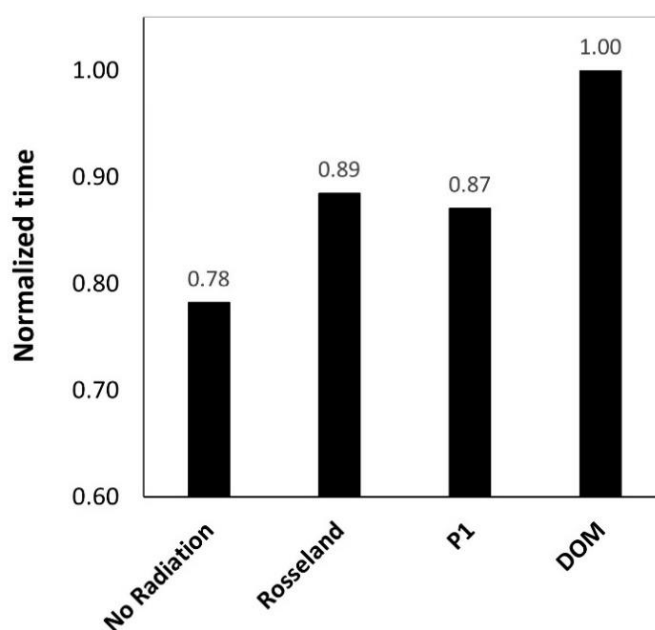


Figure 3-31. Normalized simulation time for different radiation model

The following conclusions can be derived from the above analysis for different studied radiation models:

- Radiative heat transfer plays an important and dominant role in the current system and generally systems with combustion processes or cases with a noticeable temperature difference between fluid medium and solid surface. The case without the radiation model shows unrealistic and large deviations from measured values.
- The Rosseland model must be used for optically thick mediums ( $>3$ ) and is unsuitable for the current case where the computed local optical thickness at any point is lower than 0.1.
- The P1 model can predict and capture the main features of the flow and is very close to the predicted values by the DOM; however, there are still discrepancies between P1 predictions and the measured values.
- According to the current findings and references [109][107], the P1 model is deemed accurate for optically thick media. However, it tends to produce inaccurate results for thinner (transparent) media, particularly near boundaries and when the radiation field is anisotropic. The model can also falter in cases involving complex geometry, such as congested spaces or systems with many and large openings.
- The P1 model is computationally cheaper, leading to a lower calculation time than DOM.

### 3.9. Conclusion

Many factors can affect the performance of a CFD model. In this chapter, it was shown that improving only one factor would not necessarily guarantee a proper model with reliable predictions, but all sub-models and parameters must be optimized. There may be some rule of thumb for sub-model and parameter selections; however, the model selection is quite case-dependent, and sensitivity analysis for specific cases is always required to ensure that a model works fine. From the whole analysis performed in this chapter, the following conclusions can be derived:

#### *Mesh cell type and count*

- For coarse meshes, cell type plays an important role in prediction accuracy, but the cell type effect can be ignored for fine meshes.
- The polyhedral mesh grid is preferred over other types, especially for large-scale and industrial cases with complex geometries and, more importantly, when computational resources are limited. This is because polyhedral mesh exhibits the same accuracy with a much lower mesh count and, thus, a higher simulation speed.

### ***Turbulence model***

- Even though the  $k-\omega$  model is more precise for predicting the turbulent nature of the flow, the  $k-\varepsilon$  model is still preferred in industrial and large-scale cases as it requires a lower mesh count.

### ***Reactions and TCI model***

- TCI model and kinetic mechanism selection are important to any reactive flow modelling. Based on the literature review and also performed analysis for the current case, the eddy dissipation concept (EDC) model seems to be the most reliable TCI model to predict a correct species profile in the reactive flows.
- Detailed kinetic mechanisms are preferred over global ones for their accuracy. However, using a detailed mechanism comes at a higher computational cost. According to the findings, the computational cost considerably grows with the number of reactions in a mechanism.
- Including gas-solid reactions also plays a vital role in predicting the correct temperature and composition profiles for highly exothermic reactions like carbon oxidation. A sensitivity analysis is needed to include enough particles in the calculations to properly represent the particle flow rate in the reactive flow.

### ***Radiation model***

- For high-temperature applications, radiation might play an important role. Including a proper radiation model is necessary to consider the radiation effects, especially for internal flows with a high temperature difference between the walls and the main flow stream. It becomes even more important

for the current case where the reactive flow includes highly exothermic reactions (combustion of CO-H<sub>2</sub> and carbon mixture).

- Omitting or selecting an improper radiation model will lead to predictions that are in discrepancies with the measured values, especially for the heat loss and temperature profile.
- According to the current results and also the literature reviews, the discrete ordinate model (DOM) is more reliable than other available models (P<sub>1</sub> and Rosseland model) and is applicable for all temperature and fluid optical thickness ranges; however, using the DOM model comes at a higher computational cost compared to the other studied models.

## Reference

- [1] D.A. Tillman, D.N.B. Duong, N.S. Harding, Chapter 7 - Modeling and Fuel Blending, in: D.A. Tillman, D.N.B. Duong, N.S.B.T.-S.F.B. Harding (Eds.), Butterworth-Heinemann, Boston, 2012: pp. 271–293. <https://doi.org/https://doi.org/10.1016/B978-0-12-380932-2.00007-6>.
- [2] I. Uriz, G. Arzamendi, P.M. Diéguez, L.M. Gandía, Chapter 17 - Computational Fluid Dynamics as a Tool for Designing Hydrogen Energy Technologies, in: L.M. Gandía, G. Arzamendi, P.M.B.T.-R.H.T. Diéguez (Eds.), Elsevier, Amsterdam, 2013: pp. 401–435. <https://doi.org/https://doi.org/10.1016/B978-0-444-56352-1.00017-9>.
- [3] E.R. Vasquez, T. Eldredge, 18 - Process modeling for hydrocarbon fuel conversion, in: M.R.B.T.-A. in C.H.F.P. Khan (Ed.), Woodhead Publishing Series in Energy, Woodhead Publishing, 2011: pp. 509–545. <https://doi.org/https://doi.org/10.1533/9780857093783.5.509>.
- [4] G. Tryggvason, Chapter 6 - Computational Fluid Dynamics, in: P.K. Kundu, I.M. Cohen, D.R.B.T.-F.M. (Sixth E. Dowling (Eds.), Academic Press, Boston, 2016: pp. 227–291. <https://doi.org/https://doi.org/10.1016/B978-0-12-405935-1.00006-X>.
- [5] A. MOSER, A. SCHÄULIN, L. DAVIDSON, V. CORRADO, V. DORER, M. KOSCHENZ, 11 - DESIGN WITH MODELING TECHNIQUES, in: H. Goodfellow, E.B.T.-I.V.D.G. Tähti (Eds.), Academic Press, San Diego, 2001: pp. 1025–p3. <https://doi.org/https://doi.org/10.1016/B978-012289676-7/50014-X>.
- [6] M. Sosnowski, J. Krzywanski, R. Gnatowska, Polyhedral meshing as an innovative approach to computational domain discretization of a cyclone in a fluidized bed CLC unit, E3S Web Conf. 14 (2017).
- [7] J. Tu, G.-H. Yeoh, C. Liu, Chapter 6 - Practical Guidelines for CFD Simulation and Analysis, in: J. Tu, G.-H. Yeoh, C.B.T.-C.F.D. (Second E. Liu (Eds.), Butterworth-Heinemann, 2013: pp. 219–273. <https://doi.org/https://doi.org/10.1016/B978-0-08-098243-4.00006-8>.
- [8] M. Sosnowski, R. Gnatowska, K. Grabowska, J. Krzywański, A. Jamrozik, Numerical Analysis of Flow in Building Arrangement: Computational Domain Discretization, Applied Sciences . 9 (2019). <https://doi.org/10.3390/app9050941>.
- [9] R. V Garimella, J. Kim, M. Berndt, Polyhedral Mesh Generation and Optimization for Non-manifold Domains BT - Proceedings of the 22nd International Meshing Roundtable, in: J. Sarrate, M. Staten (Eds.), Springer International Publishing, Cham, 2014: pp. 313–330.
- [10] H. Zhang, S. Tang, H. Yue, K. Wu, Y. Zhu, C. Liu, B. Liang, C. Li, Comparison of Computational Fluid Dynamic Simulation of a Stirred Tank with Polyhedral and Tetrahedral Meshes, Iranian Journal of Chemistry and Chemical Engineering (IJCCE). 39 (2020) 311–319. <https://doi.org/10.30492/ijcce.2019.34950>.
- [11] F. Juretić, A.D. Gosman, Error Analysis of the Finite-Volume Method with Respect to Mesh Type, Numerical Heat Transfer, Part B: Fundamentals. 57 (2010) 414–439. <https://doi.org/10.1080/10407791003685155>.
- [12] R. Duan, W. Liu, L. Xu, Y. Huang, X. Shen, C.-H. Lin, J. Liu, Q. Chen, B. Sasanapuri, Mesh Type and Number for the CFD Simulations of Air Distribution in an Aircraft Cabin, Numerical Heat Transfer, Part B: Fundamentals. 67 (2015) 489–506. <https://doi.org/10.1080/10407790.2014.985991>.
- [13] G. Yu, B. Yu, S. Sun, W.-Q. Tao, Comparative Study on Triangular and Quadrilateral Meshes by a Finite-Volume Method with a Central Difference Scheme, Numerical Heat Transfer, Part B: Fundamentals. 62 (2012) 243–263. <https://doi.org/10.1080/10407790.2012.709416>.

- [14] B. Xie, F. Xiao, A multi-moment constrained finite volume method on arbitrary unstructured grids for incompressible flows, *Journal of Computational Physics*. 327 (2016) 747–778. <https://doi.org/https://doi.org/10.1016/j.jcp.2016.09.054>.
- [15] B. Xie, X. Deng, S. Liao, High-fidelity solver on polyhedral unstructured grids for low-Mach number compressible viscous flow, *Computer Methods in Applied Mechanics and Engineering*. 357 (2019) 112584. <https://doi.org/https://doi.org/10.1016/j.cma.2019.112584>.
- [16] W. Wang, Y. Cao, T. Okaze, Comparison of hexahedral, tetrahedral and polyhedral cells for reproducing the wind field around an isolated building by LES, *Building and Environment*. 195 (2021) 107717. <https://doi.org/https://doi.org/10.1016/j.buildenv.2021.107717>.
- [17] J. Mularski, N. Modliński, Impact of Chemistry–Turbulence Interaction Modeling Approach on the CFD Simulations of Entrained Flow Coal Gasification, *Energies*. 13 (2020). <https://doi.org/10.3390/en13236467>.
- [18] T.J. Kim, R.A. Yetter, F.L. Dryer, New results on moist CO oxidation: high pressure, high temperature experiments and comprehensive kinetic modeling, *Symposium (International) on Combustion*. 25 (1994) 759–766. [https://doi.org/10.1016/S0082-0784\(06\)80708-3](https://doi.org/10.1016/S0082-0784(06)80708-3).
- [19] W. Wang, B. Rogg, Reduced kinetic mechanisms and their numerical treatment I: Wet CO flames, *Combustion and Flame*. 94 (1993) 271–292. [https://doi.org/https://doi.org/10.1016/0010-2180\(93\)90074-D](https://doi.org/https://doi.org/10.1016/0010-2180(93)90074-D).
- [20] C.M. Vagelopoulos, F.N. Egolfopoulos, Laminar flame speeds and extinction strain rates of mixtures of carbon monoxide with hydrogen, methane, and air, *Symposium (International) on Combustion*. 25 (1994) 1317–1323. [https://doi.org/https://doi.org/10.1016/S0082-0784\(06\)80773-3](https://doi.org/https://doi.org/10.1016/S0082-0784(06)80773-3).
- [21] S.G. Davis, A. V. Joshi, H. Wang, F. Egolfopoulos, An optimized kinetic model of H<sub>2</sub>/CO combustion, *Proceedings of the Combustion Institute*. 30 (2005) 1283–1292. <https://doi.org/10.1016/J.PROCI.2004.08.252>.
- [22] W. Li, C. Zou, H. Yao, Q. Lin, R. Fu, J. Luo, An optimized kinetic model for H<sub>2</sub>/CO combustion in CO<sub>2</sub> diluent at elevated pressures, *Combustion and Flame*. 241 (2022) 112093. <https://doi.org/https://doi.org/10.1016/j.combustflame.2022.112093>.
- [23] P. Saxena, F.A. Williams, Testing a small detailed chemical-kinetic mechanism for the combustion of hydrogen and carbon monoxide, *Combustion and Flame*. 145 (2006) 316–323. <https://doi.org/https://doi.org/10.1016/j.combustflame.2005.10.004>.
- [24] D. Singh, T. Nishiie, S. Tanvir, L. Qiao, An experimental and kinetic study of syngas/air combustion at elevated temperatures and the effect of water addition, *Fuel*. 94 (2012) 448–456. <https://doi.org/https://doi.org/10.1016/j.fuel.2011.11.058>.
- [25] Y. He, Z. Wang, L. Yang, R. Whiddon, Z. Li, J. Zhou, K. Cen, Investigation of laminar flame speeds of typical syngas using laser based Bunsen method and kinetic simulation, *Fuel*. 95 (2012) 206–213. <https://doi.org/https://doi.org/10.1016/j.fuel.2011.09.056>.
- [26] J. Natarajan, T. Lieuwen, J. Seitzman, Laminar flame speeds of H<sub>2</sub>/CO mixtures: Effect of CO<sub>2</sub> dilution, preheat temperature, and pressure, *Combustion and Flame*. 151 (2007) 104–119. <https://doi.org/https://doi.org/10.1016/j.combustflame.2007.05.003>.
- [27] H. Sun, S.I. Yang, G. Jomaas, C.K. Law, High-pressure laminar flame speeds and kinetic modeling of carbon monoxide/hydrogen combustion, *Proceedings of the Combustion Institute*. 31 (2007) 439–446. <https://doi.org/https://doi.org/10.1016/j.proci.2006.07.193>.
- [28] D. Healy, N.S. Donato, C.J. Aul, E.L. Petersen, C.M. Zinner, G. Bourque, H.J. Curran, Isobutane ignition delay time measurements at high pressure and detailed chemical kinetic



- simulations, *Combustion and Flame*. 157 (2010) 1540–1551. <https://doi.org/https://doi.org/10.1016/j.combustflame.2010.01.011>.
- [29] C. Heghes, Soot formation modeling during hydrocarbon pyrolysis and oxidation behind shock waves, (2006).
- [30] M. Frenklach, Reaction mechanism of soot formation in flames, *Physical Chemistry Chemical Physics*. 4 (2002) 2028–2037.
- [31] H. Wang, M. Frenklach, A detailed kinetic modeling study of aromatics formation in laminar premixed acetylene and ethylene flames, *Combustion and Flame*. 110 (1997) 173–221. [https://doi.org/https://doi.org/10.1016/S0010-2180\(97\)00068-0](https://doi.org/https://doi.org/10.1016/S0010-2180(97)00068-0).
- [32] M. Fischer, X. Jiang, An investigation of the chemical kinetics of biogas combustion, *Fuel*. 150 (2015) 711–720. <https://doi.org/https://doi.org/10.1016/j.fuel.2015.01.085>.
- [33] M. Fischer, X. Jiang, An assessment of chemical kinetics for bio-syngas combustion, *Fuel*. 137 (2014) 293–305. <https://doi.org/https://doi.org/10.1016/j.fuel.2014.07.081>.
- [34] M. Fischer, X. Jiang, A chemical kinetic modelling study of the combustion of CH<sub>4</sub>–CO–H<sub>2</sub>–CO<sub>2</sub> fuel mixtures, *Combustion and Flame*. 167 (2016) 274–293. <https://doi.org/https://doi.org/10.1016/j.combustflame.2016.02.001>.
- [35] U. Maas, J. Warnatz, Ignition processes in carbon-monoxide-hydrogen-oxygen mixtures, *Symposium (International) on Combustion*. 22 (1989) 1695–1704. [https://doi.org/https://doi.org/10.1016/S0082-0784\(89\)80182-1](https://doi.org/https://doi.org/10.1016/S0082-0784(89)80182-1).
- [36] A. Frassoldati, T. Faravelli, E. Ranzi, The ignition, combustion and flame structure of carbon monoxide/hydrogen mixtures. Note 1: Detailed kinetic modeling of syngas combustion also in presence of nitrogen compounds, *International Journal of Hydrogen Energy*. 32 (2007) 3471–3485. <https://doi.org/10.1016/J.IJHYDENE.2007.01.011>.
- [37] A. Cuoci, A. Frassoldati, G. Buzzi Ferraris, T. Faravelli, E. Ranzi, The ignition, combustion and flame structure of carbon monoxide/hydrogen mixtures. Note 2: Fluid dynamics and kinetic aspects of syngas combustion, *International Journal of Hydrogen Energy*. 32 (2007) 3486–3500. <https://doi.org/10.1016/j.ijhydene.2007.02.026>.
- [38] A. Frassoldati, A. Cuoci, T. Faravelli, E. Ranzi, C. Candusso, D. Tolazzi, Simplified kinetic schemes for oxy-fuel combustion, (2009).
- [39] Z.M. Nikolaou, J.-Y. Chen, N. Swaminathan, A 5-step reduced mechanism for combustion of CO/H<sub>2</sub>/H<sub>2</sub>O/CH<sub>4</sub>/CO<sub>2</sub> mixtures with low hydrogen/methane and high H<sub>2</sub>O content, *Combustion and Flame*. 160 (2013) 56–75. <https://doi.org/10.1016/J.COMBUSTFLAME.2012.09.010>.
- [40] C.K. Westbrook, F.L. Dryer, Simplified reaction mechanisms for the oxidation of hydrocarbon fuels in flames, *Combustion Science and Technology*. 27 (1981) 31–43.
- [41] M. Graça, A. Duarte, P.J. Coelho, M. Costa, Numerical simulation of a reversed flow small-scale combustor, *Fuel Processing Technology*. 107 (2013) 126–137. <https://doi.org/https://doi.org/10.1016/j.fuproc.2012.06.028>.
- [42] GRI mechanism, (n.d.). <http://combustion.berkeley.edu/gri-mech/overview.html> (accessed April 8, 2022).
- [43] S. Iavarone, A. Parente, NO<sub>x</sub> Formation in MILD Combustion: Potential and Limitations of Existing Approaches in CFD, *Frontiers in Mechanical Engineering*. 6 (2020).
- [44] B.B. Dally, A.N. Karpetis, R.S. Barlow, Structure of turbulent non-premixed jet flames in a diluted hot coflow, *Proceedings of the Combustion Institute*. 29 (2002) 1147–1154. [https://doi.org/https://doi.org/10.1016/S1540-7489\(02\)80145-6](https://doi.org/https://doi.org/10.1016/S1540-7489(02)80145-6).

- [45] C.J. Sung, C.K. Law, J.-Y. Chen, Augmented reduced mechanisms for NO emission in methane oxidation, *Combustion and Flame*. 125 (2001) 906–919. [https://doi.org/https://doi.org/10.1016/S0010-2180\(00\)00248-0](https://doi.org/https://doi.org/10.1016/S0010-2180(00)00248-0).
- [46] H. Xu, F. Liu, Z. Wang, X. Ren, J. Chen, Q. Li, Z. Zhu, A Detailed Numerical Study of NO<sub>x</sub> Kinetics in Counterflow Methane Diffusion Flames: Effects of Fuel-Side versus Oxidizer-Side Dilution, *Journal of Combustion*. 2021 (2021) 6642734. <https://doi.org/10.1155/2021/6642734>.
- [47] T. Weydahl, I. Ertesvåg, I. Gran, B. Magnussen, P. Kilpinen, Prediction of Nitrogen Oxide Formation in Ammonia-Doped Turbulent Syngas Jet Flames, (2022).
- [48] S. Zahirović, R. Scharler, P. Kilpinen, I. Obernberger, Validation of flow simulation and gas combustion sub-models for the CFD-based prediction of NO<sub>x</sub> formation in biomass grate furnaces, *Combustion Theory and Modelling*. 15 (2010) 61–87. <https://doi.org/10.1080/13647830.2010.524312>.
- [49] X.Z. Hu, Q.B. Yu, Y.M. Li, Skeletal and Reduced Mechanisms of Methane at O<sub>2</sub>/CO<sub>2</sub> Atmosphere, *Chem. J. Chin. Univ.* 39 (2018) 95–101.
- [50] W. Wang, Studies on the Efficient Reduction Methods for the Combustion Chemical Kinetic Mechanism of Fuel, (2016).
- [51] X.-L. GOU, W. WANG, Y. GUI, Methane Reaction Mechanism Reduction Using Paths Flux Analysis of Three Generations Method, *Journal of Engineering Thermophysics*. (2014).
- [52] H. Liu, F. Chen, H. LIU, Z.H. Zheng, S.H. Yang, 18-step reduced mechanism for methane/air premixed supersonic combustion, *Journal of Combustion Science and Technology*. 18 (2012) 467–472.
- [53] H. Lu, F. Liu, Y. Wang, X. Fan, J. Yang, C. Liu, G. Xu, Mechanism Reduction and Bunsen Burner Flame Verification of Methane, *Energies*. 12 (2019). <https://doi.org/10.3390/en12010097>.
- [54] M. Vascellari, G. Cau, Influence of turbulence–chemical interaction on CFD pulverized coal MILD combustion modeling, *Fuel*. 101 (2012) 90–101. <https://doi.org/https://doi.org/10.1016/j.fuel.2011.07.042>.
- [55] O. Musa, C. Xiong, Z. Changsheng, Z. Min, O. Musa, Combustion modeling of unsteady reacting swirling flow in solid fuel ramjet, in: 2017 International Conference on Mechanical, System and Control Engineering (ICMSC), 2017: pp. 115–120. <https://doi.org/10.1109/ICMSC.2017.7959454>.
- [56] O.S. Vankova, Comparison of turbulence/chemistry interaction models in the problem of ignition a parallel hydrogen jet in a supersonic air flow, *AIP Conference Proceedings*. 2351 (2021) 40052. <https://doi.org/10.1063/5.0053925>.
- [57] M.T. Lewandowski, J. Pozorski, Assessment of turbulence–chemistry interaction models in the computation of turbulent non-premixed flames, *Journal of Physics: Conference Series*. 760 (2016) 12015. <https://doi.org/10.1088/1742-6596/760/1/012015>.
- [58] F.C. Christo, B.B. Dally, Modeling turbulent reacting jets issuing into a hot and diluted coflow, *Combustion and Flame*. 142 (2005) 117–129. <https://doi.org/https://doi.org/10.1016/j.combustflame.2005.03.002>.
- [59] A. De, E. Oldenhof, P. Sathiah, D. Roekaerts, Numerical Simulation of Delft-Jet-in-Hot-Coflow (DJHC) Flames Using the Eddy Dissipation Concept Model for Turbulence–Chemistry Interaction, *Flow, Turbulence and Combustion*. 87 (2011) 537–567. <https://doi.org/10.1007/s10494-011-9337-0>.

- [60] A. De, A. Dongre, Assessment of Turbulence-Chemistry Interaction Models in MILD Combustion Regime, *Flow, Turbulence and Combustion*. 94 (2015) 439–478. <https://doi.org/10.1007/s10494-014-9587-8>.
- [61] S. Chapela, J. Porteiro, M. Costa, Effect of the Turbulence–Chemistry Interaction in Packed-Bed Biomass Combustion, *Energy & Fuels*. 31 (2017) 9967–9982. <https://doi.org/10.1021/acs.energyfuels.7b00516>.
- [62] B. Mahmoodi, S.H. Hosseini, G. Ahmadi, A. Raj, CFD simulation of reactor furnace of sulfur recovery units by considering kinetics of acid gas (H<sub>2</sub>S and CO<sub>2</sub>) destruction, *Applied Thermal Engineering*. 123 (2017) 699–710. <https://doi.org/10.1016/J.APPLTHERMALENG.2017.05.148>.
- [63] DRM mechanism, (n.d.). <http://combustion.berkeley.edu/drm/> (accessed April 1, 2022).
- [64] A. Mardani, Optimization of the Eddy Dissipation Concept (EDC) model for turbulence-chemistry interactions under hot diluted combustion of CH<sub>4</sub>/H<sub>2</sub>, *Fuel*. 191 (2017) 114–129. <https://doi.org/https://doi.org/10.1016/j.fuel.2016.11.056>.
- [65] A. Mardani, S. Tabejamaat, M.B. Mohammadi, Numerical study of the effect of turbulence on rate of reactions in the MILD combustion regime, *Combustion Theory and Modelling*. 15 (2011) 753–772. <https://doi.org/10.1080/13647830.2011.561368>.
- [66] A. Parente, C. Galletti, L. Tognotti, Effect of the combustion model and kinetic mechanism on the MILD combustion in an industrial burner fed with hydrogen enriched fuels, *International Journal of Hydrogen Energy*. 33 (2008) 7553–7564. <https://doi.org/https://doi.org/10.1016/j.ijhydene.2008.09.058>.
- [67] W.P. Jones, R.P. Lindstedt, Global reaction schemes for hydrocarbon combustion, *Combustion and Flame*. 73 (1988) 233–249. [https://doi.org/https://doi.org/10.1016/0010-2180\(88\)90021-1](https://doi.org/https://doi.org/10.1016/0010-2180(88)90021-1).
- [68] D.J. HAUTMAN, F.L. DRYER, K.P. SCHUG, I. GLASSMAN, A Multiple-step Overall Kinetic Mechanism for the Oxidation of Hydrocarbons, *Combustion Science and Technology*. 25 (1981) 219–235. <https://doi.org/10.1080/00102208108547504>.
- [69] E. RANZI, A. FRASSOLDATI, A. STAGNI, M. PELUCCHI, A. CUOCI, T. FARAVELLI, Reduced Kinetic Schemes of Complex Reaction Systems: Fossil and Biomass-Derived Transportation Fuels, *International Journal of Chemical Kinetics*. 46 (2014) 512–542. <https://doi.org/https://doi.org/10.1002/kin.20867>.
- [70] San Diego Mechanism, (n.d.). <https://web.eng.ucsd.edu/mae/groups/combustion/mechanism.html> (accessed February 2, 2022).
- [71] G. Sorrentino, P. Sabia, M. de Joannon, R. Ragucci, A. Cavaliere, U. Göktolga, J. van Oijen, P. de Goey, Development of a Novel Cyclonic Flow Combustion Chamber for Achieving MILD/Flameless Combustion, *Energy Procedia*. 66 (2015) 141–144. <https://doi.org/https://doi.org/10.1016/j.egypro.2015.02.079>.
- [72] E. Ranzi, A. Frassoldati, R. Grana, A. Cuoci, T. Faravelli, A.P. Kelley, C.K. Law, Hierarchical and comparative kinetic modeling of laminar flame speeds of hydrocarbon and oxygenated fuels, *Progress in Energy and Combustion Science*. 38 (2012) 468–501. <https://doi.org/https://doi.org/10.1016/j.pecs.2012.03.004>.
- [73] S.R. Shabaniyan, P.R. Medwell, M. Rahimi, A. Frassoldati, A. Cuoci, Kinetic and fluid dynamic modeling of ethylene jet flames in diluted and heated oxidant stream combustion conditions, *Applied Thermal Engineering*. 52 (2013) 538–554. <https://doi.org/https://doi.org/10.1016/j.applthermaleng.2012.12.024>.

- [74] B. Danon, W. de Jong, D.J.E.M. Roekaerts, Experimental and Numerical Investigation of a FLOX Combustor Firing Low Calorific Value Gases, *Combustion Science and Technology*. 182 (2010) 1261–1278. <https://doi.org/10.1080/00102201003639284>.
- [75] Y. Halouane, A. Dehbi, CFD simulations of premixed hydrogen combustion using the Eddy Dissipation and the Turbulent Flame Closure models, *International Journal of Hydrogen Energy*. 42 (2017) 21990–22004. <https://doi.org/https://doi.org/10.1016/j.ijhydene.2017.07.075>.
- [76] A. Agarwal, I. Pitso, Modelling & numerical exploration of pulsejet engine using eddy dissipation combustion model, *Materials Today: Proceedings*. 27 (2020) 1341–1349. <https://doi.org/https://doi.org/10.1016/j.matpr.2020.02.620>.
- [77] N. Romero-Anton, X. Huang, H. Bao, K. Martin-Eskudero, E. Salazar-Herran, D. Roekaerts, New extended eddy dissipation concept model for flameless combustion in furnaces, *Combustion and Flame*. 220 (2020) 49–62. <https://doi.org/https://doi.org/10.1016/j.combustflame.2020.06.025>.
- [78] G. Dong, Y. Huang, Y. CHEN, Study of effects of different chemical reaction mechanisms on computation results for methane jet turbulence diffusion flame, *Journal of Fuel Chemistry and Technology*. 28 (2000) 49–54.
- [79] J. Wei, M. Ye, S. Zhang, J. Qin, O.J. Haidn, Modeling of a 7-elements GOX/GCH<sub>4</sub> combustion chamber using RANS with Eddy-Dissipation Concept model, *Aerospace Science and Technology*. 99 (2020) 105762. <https://doi.org/https://doi.org/10.1016/j.ast.2020.105762>.
- [80] P. Józwiak, J. Hercog, A. Kiedrzyńska, K. Badyda, CFD analysis of natural gas substitution with syngas in the industrial furnaces, *energy*. 179 (2019) 593–602. <https://doi.org/https://doi.org/10.1016/j.energy.2019.04.179>.
- [81] A. Richter, M. Vascellari, P.A. Nikrityuk, C. Hasse, Detailed analysis of reacting particles in an entrained-flow gasifier, *Fuel Processing Technology*. 144 (2016) 95–108. <https://doi.org/https://doi.org/10.1016/j.fuproc.2015.12.014>.
- [82] S.S. Park, H.J. Jeong, J. Hwang, 3-D CFD Modeling for Parametric Study in a 300-MWe One-Stage Oxygen-Blown Entrained-Bed Coal Gasifier, *Energies*. 8 (2015). <https://doi.org/10.3390/en8054216>.
- [83] S. Emami, H. Jafari, Y. Mahmoudi, Effects of Combustion Model and Chemical Kinetics in Numerical Modeling of Hydrogen-Fueled Dual-Stage HVOF System, *Journal of Thermal Spray Technology*. 28 (2019) 333–345. <https://doi.org/10.1007/s11666-019-00826-8>.
- [84] N. Zhang, B. Chen, T. Qiu, CFD simulation of cracking tube with internal twisted slices, in: I.A. Karimi, R.B.T.-C.A.C.E. Srinivasan (Eds.), *11 International Symposium on Process Systems Engineering*, Elsevier, 2012: pp. 905–909. <https://doi.org/https://doi.org/10.1016/B978-0-444-59506-5.50012-2>.
- [85] K.M. Sundaram, G.F. Froment, Modeling of Thermal Cracking Kinetics. 3. Radical Mechanisms for the Pyrolysis of Simple Paraffins, Olefins, and Their Mixtures, *Industrial & Engineering Chemistry Fundamentals*. 17 (1978) 174–182. <https://doi.org/10.1021/i160067a006>.
- [86] N. ZHANG, T. QIU, B. CHEN, CFD Simulation of Propane Cracking Tube Using Detailed Radical Kinetic Mechanism, *Chinese Journal of Chemical Engineering*. 21 (2013) 1319–1331. [https://doi.org/https://doi.org/10.1016/S1004-9541\(13\)60619-9](https://doi.org/https://doi.org/10.1016/S1004-9541(13)60619-9).
- [87] Y. Ouyang, Y. Xiang, H. Zou, G. Chu, J. Chen, Flow characteristics and micromixing modeling in a microporous tube-in-tube microchannel reactor by CFD, *Chemical Engineering Journal*. 321 (2017) 533–545. <https://doi.org/https://doi.org/10.1016/j.cej.2017.03.151>.

- [88] H. Guihua, W. Honggang, Q. Feng, Numerical simulation on flow, combustion and heat transfer of ethylene cracking furnaces, *Chemical Engineering Science*. 66 (2011) 1600–1611. <https://doi.org/https://doi.org/10.1016/j.ces.2010.12.028>.
- [89] P. Chen, W. Du, M. Zhang, F. Duan, L. Zhang, Numerical studies on heat coupling and configuration optimization in an industrial hydrogen production reformer, *International Journal of Hydrogen Energy*. 44 (2019) 15704–15720. <https://doi.org/https://doi.org/10.1016/j.ijhydene.2018.10.238>.
- [90] A. Tran, A. Aguirre, H. Durand, M. Crose, P.D. Christofides, CFD modeling of a industrial-scale steam methane reforming furnace, *Chemical Engineering Science*. 171 (2017) 576–598. <https://doi.org/https://doi.org/10.1016/j.ces.2017.06.001>.
- [91] S. May, S. Karl, O. Bo, Development of an Eddy Dissipation Model for the use in Numerical Hybrid Rocket Engine Combustion Simulation, in: n.d.
- [92] Elwina, Yunardi, Y. Bindar, Syukran, Simulation of the Influence of Air Preheat Combustion on the Temperature of Propane Turbulent Flame Using Probability Density Function Approach and Eddy Dissipation Model, *Advanced Materials Research*. 871 (2014) 95–100. <https://doi.org/10.4028/www.scientific.net/AMR.871.95>.
- [93] B. Rohani, M.A. Wahid, M.M. Sies, K.M. Saqr, Comparison of eddy dissipation model and presumed probability density function model for temperature prediction in a non-premixed turbulent methane flame, *AIP Conference Proceedings*. 1440 (2012) 384–391. <https://doi.org/10.1063/1.4704240>.
- [94] T. Poinso, D. Veynante, *Theoretical and numerical combustion*, RT Edwards, Inc., 2005.
- [95] R. Sriprya, T. Peeters, K. Meijer, C. Zeilstra, D. van der Plas, Computational fluid dynamics and combustion modelling of HISarna incinerator, *Ironmaking & Steelmaking*. 43 (2016) 192–202. <https://doi.org/10.1179/1743281215Y.0000000031>.
- [96] A. Rebola, P.J. Coelho, M. Costa, Assessment of the Performance of Several Turbulence and Combustion Models in the Numerical Simulation of a Flameless Combustor, *Combustion Science and Technology*. 185 (2013) 600–626. <https://doi.org/10.1080/00102202.2012.739222>.
- [97] A. Olivieri, F. Vegliò, Process simulation of natural gas steam reforming: Fuel distribution optimisation in the furnace, *Fuel Processing Technology*. 89 (2008) 622–632. <https://doi.org/https://doi.org/10.1016/j.fuproc.2007.12.001>.
- [98] G. Liesche, K. Sundmacher, Radiation-based model reduction for the optimization of high temperature tube bundle reactors: Synthesis of hydrogen cyanide, *Computers & Chemical Engineering*. 127 (2019) 186–199. <https://doi.org/https://doi.org/10.1016/j.compchemeng.2019.05.007>.
- [99] Z. Yu, E. Cao, Y. Wang, Z. Zhou, Z. Dai, Simulation of natural gas steam reforming furnace, *Fuel Processing Technology*. 87 (2006) 695–704. <https://doi.org/https://doi.org/10.1016/j.fuproc.2005.11.008>.
- [100] L. Labiscsak, G. Straffellini, C. Corbetta, M. Bodino, Fluid dynamics of a post-combustion chamber in electric arc steelmaking plants, 2011. <https://doi.org/10.2495/CMEM110191>.
- [101] M. Tutar, C.E. Üstün, J.M. Campillo-Robles, R. Fuente, S. Cibrián, I. Arzua, A. Fernández, G.A. López, Optimized CFD modelling and validation of radiation section of an industrial top-fired steam methane reforming furnace, *Computers & Chemical Engineering*. 155 (2021) 107504. <https://doi.org/https://doi.org/10.1016/j.compchemeng.2021.107504>.
- [102] X. Lan, J. Gao, C. Xu, H. Zhang, Numerical Simulation of Transfer and Reaction Processes in Ethylene Furnaces, *Chemical Engineering Research and Design*. 85 (2007) 1565–1579. [https://doi.org/https://doi.org/10.1016/S0263-8762\(07\)73201-X](https://doi.org/https://doi.org/10.1016/S0263-8762(07)73201-X).

- [103] M. İlbaz, İ. Yılmaz, Y. Kaplan, Investigations of hydrogen and hydrogen–hydrocarbon composite fuel combustion and NO<sub>x</sub> emission characteristics in a model combustor, *International Journal of Hydrogen Energy*. 30 (2005) 1139–1147. <https://doi.org/https://doi.org/10.1016/j.ijhydene.2004.10.016>.
- [104] M. Rezaeimanesh, A. Asghar Ghoreyshi, S.M. Peyghambarzadeh, S. Hassan Hashemabadi, A coupled CFD simulation approach for investigating the pyrolysis process in industrial naphtha thermal cracking furnaces, *Chinese Journal of Chemical Engineering*. 44 (2022) 528–542. <https://doi.org/https://doi.org/10.1016/j.cjche.2021.03.028>.
- [105] R. Laubscher, S. van der Merwe, Heat transfer modelling of semi-suspension biomass fired industrial watertube boiler at full- and part-load using CFD, *Thermal Science and Engineering Progress*. 25 (2021) 100969. <https://doi.org/https://doi.org/10.1016/j.tsep.2021.100969>.
- [106] T. Gruber, R. Scharler, I. Obernberger, Application of an empirical model in CFD simulations to predict the local high temperature corrosion potential in biomass fired boilers, *Biomass and Bioenergy*. 79 (2015) 145–154. <https://doi.org/https://doi.org/10.1016/j.biombioe.2015.02.024>.
- [107] A. Habibi, B. Merci, G.J. Heynderickx, Impact of radiation models in CFD simulations of steam cracking furnaces, *Computers & Chemical Engineering*. 31 (2007) 1389–1406. <https://doi.org/https://doi.org/10.1016/j.compchemeng.2006.11.009>.
- [108] Ansys Fluent user guide, ANSYS Inc. Southpointe 275 Technology Drive Canonsburg, PA 15317, (2013).
- [109] E.P. Keramida, H.H. Liakos, M.A. Founti, A.G. Boudouvis, N.C. Markatos, Radiative heat transfer in natural gas-fired furnaces, *International Journal of Heat and Mass Transfer*. 43 (2000) 1801–1809. [https://doi.org/https://doi.org/10.1016/S0017-9310\(99\)00244-6](https://doi.org/https://doi.org/10.1016/S0017-9310(99)00244-6).

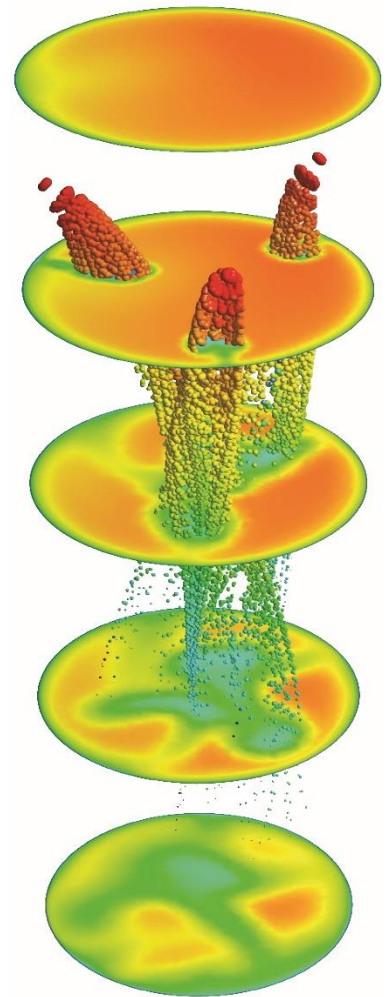
# Chapter 4

## OFF-GAS SYSTEM FLOW ANALYSIS

This chapter is partially based on the following published paper:

Ashkan Hosseini, Vinod Dhiman, Koen Meijer, Christiaan Zeilstra, Johannes Hage, Tim Peeters, Erik Offerman & Yongxiang Yang (2022) CFD modelling of the off-gas system of HIsarna iron-making process. Part 1: model development using detailed reaction mechanism for post-combustion of CO–H<sub>2</sub> mixture and carbon particles, *Ironmaking & Steelmaking*, 49:8, 828-844, DOI: 10.1080/03019233.2022.2062929

In this chapter, flow analysis by post-processing the obtained result from the final CFD model is presented. Different parameters are varied to see the effect on the flow behaviour and performance of the off-gas system. Parameters such as injected post-combustion oxygen variation, water injection for quenching, and inlet composition variation are considered to investigate their effects on the temperature, composition profiles, heat losses, wall temperature distributions etc.



## 4.1. CFD model summary and review

A detailed description of the CFD model development and optimization is given in Chapter 2 and Chapter 3. A quick review is presented before using the model to investigate different operational parameters. The flow field inside the off-gas system is considered a gaseous medium with solid particles. Volumetric and gas-solid reactions are considered using the eddy dissipation concept model. For both volumetric and gas-solid reactions, a detailed kinetic mechanism is considered. The radiative nature of the flow is taken into account using the discrete ordinate model. Particle flow is modeled using the discrete phase model. Both gas-solid reaction and evaporation are considered for carbon particles and water droplets. The turbulent nature of the flow is modeled using the realizable  $k$ - $\epsilon$  model with enhanced wall treatment formulation for near-wall velocity profile estimation. Wall boundary conditions are modeled by considering the shell conduction model, and thermo-physical properties are obtained from finite element analysis of the detailed geometry. Ultimately, the final CFD model is validated against pilot plant operational data.

## 4.2. Flow and wall temperature

Now that we have constructed a well-defined model, we can thoroughly examine the various phenomena that occur within the off-gas system. To begin the analysis, the contours of compositions and temperature are shown in Figure 4-1 (up to point C in Figure 2.4).

As it can be seen from profiles and contours (see also Figure 2.30 and 2.31), the amount of CO and H<sub>2</sub> is increasing before the oxygen injection area (length: 3 m). This is primarily attributed to the carbon reaction with the H<sub>2</sub>O-CO<sub>2</sub> mixture and the thermal dissociation of CO<sub>2</sub>-H<sub>2</sub>O into CO and H<sub>2</sub>. Along the same length, the temperature consistently decreases due to factors such as heat losses through the wall, the endothermic dissociation of CO<sub>2</sub> and H<sub>2</sub>O, and the endothermic reaction of carbon with the H<sub>2</sub>O-CO<sub>2</sub> mixture. Subsequently, there is a sharp increase in oxygen concentration when oxygen is injected (at a length of 3 meters) into the



reflux chamber, accompanied by a drop in temperature. CO and H<sub>2</sub> then undergo combustion, resulting in a sudden drop in the mole fraction profile.

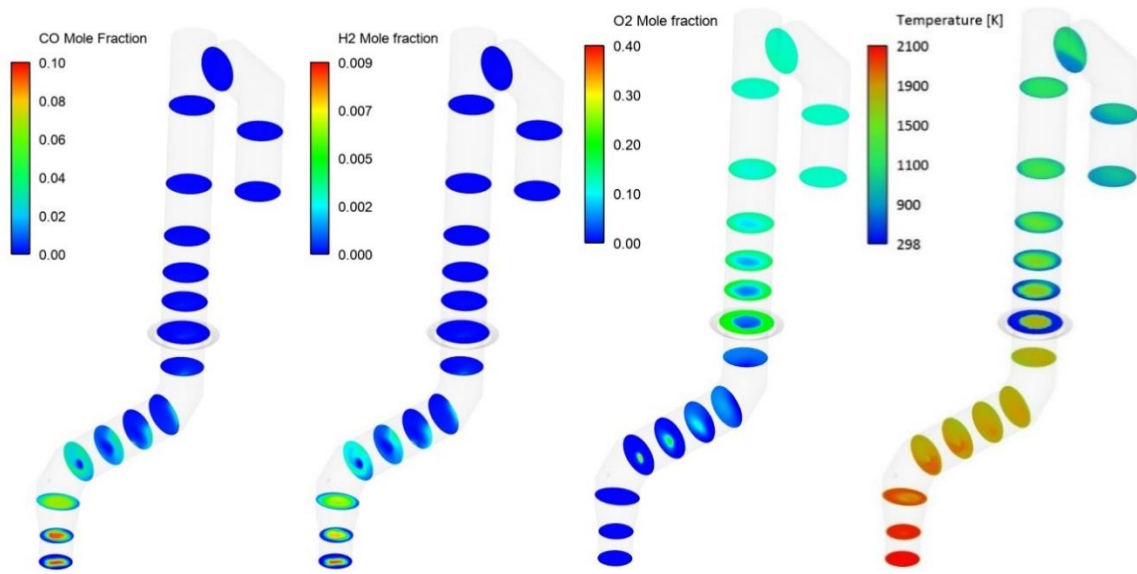


Figure 4-1. Composition and temperature contours at different cross section over the off-gas system length

As combustion proceeds, oxygen is progressively consumed, resulting in a reduction of available oxygen. Simultaneously, the levels of CO<sub>2</sub> and H<sub>2</sub>O increase as combustion byproducts. Initially, the temperature remains constant after the injection of oxygen, owing to the heat generated during combustion. However, temperature starts to decrease as a result of heat losses through the walls and other endothermic reactions. A notable surge in the oxygen profile occurs further downstream, coinciding with a drop in temperature. This is associated with the injection of air through air quench channels (length 10 m).

As previously mentioned, in addition to quenching the flow, another advantage of using air for quenching is the ability to solidify molten particles escaping from the CCF and reflux chamber. As illustrated by the temperature contour, the introduction of air forms a cold ring near the chamber's wall. When the particles come into contact with this colder area, they rapidly freeze. These frozen particles are subsequently carried away by the flue gas and do not accumulate on the chamber's walls.

This can also be seen in Figure 4-2, where flow streamlines colored by flow temperature are shown. The swirl motion of the flow at the inlet can also be confirmed from the streamlines (swirl number = 0.6).

Downstream, where flue gas is quenched with water (length 29 m), there will be another step reduction in temperature due to evaporative cooling. More discussion on water quenching is presented in section 4.4.

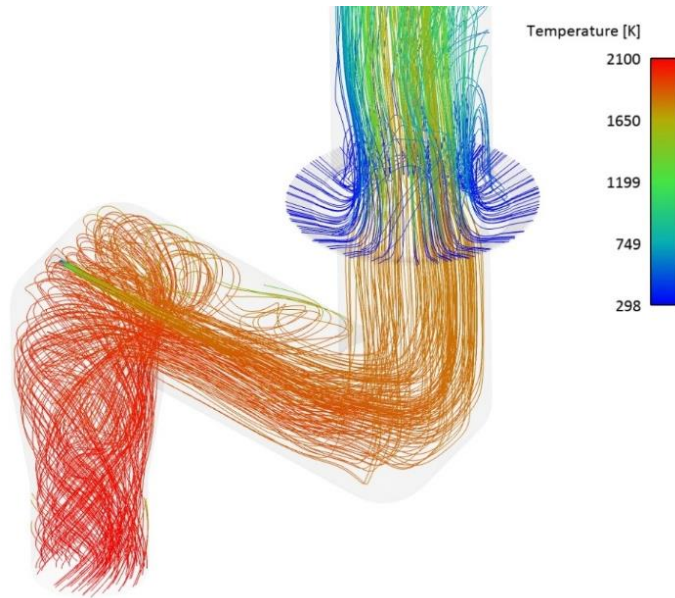


Figure 4-2. Flow streamlines coloured by temperature – effect of swirl motion

The contours of wall temperatures are shown in Figure 4-3 and Figure 4-4 for the reflux chamber and air quench, respectively. The inner wall refers to the wall layer in contact with flue gas, and the outer wall is in touch with cooling water. The average temperature values are reported in Table 4-1.

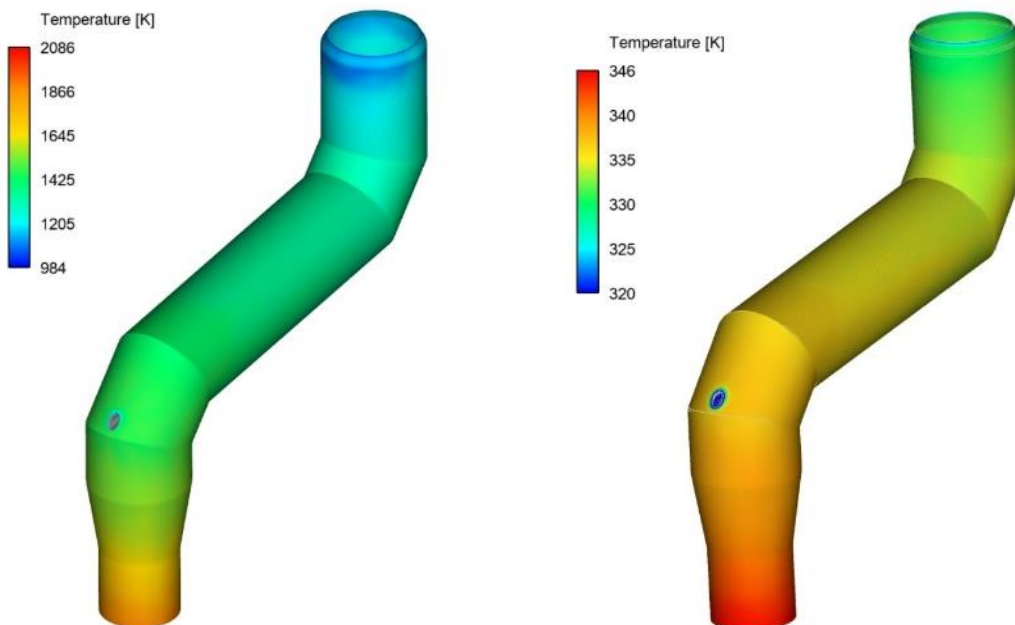


Figure 4-3. Reflux chamber inner (left) and outer (right) wall temperature distribution

There is a noticeable temperature difference between the inner and outer walls of the reflux chamber (1070 °C difference), which shows the excellent isolation properties of the refractory.

Table 4-1. Average wall temperature – model prediction

	Inner wall [K]	Outer wall [K]
<b>Reflux chamber</b>	1310	335
<b>Air quench</b>	323	320
<b>Up-leg</b>	320	318
<b>Down-leg</b>	318	317

Above the reflux chamber, a slight temperature difference exists between the inner and outer walls due to the quenching process, and only steel tubes are used to cool the walls with a very thin thickness of 5 mm.

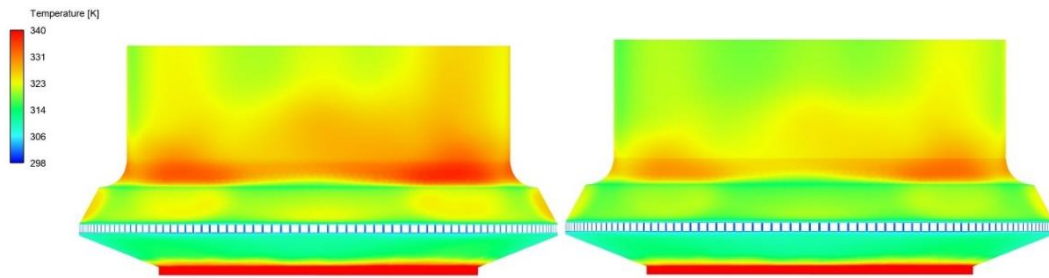


Figure 4-4. Air quench inner (left) and outer (right) wall temperature

### 4.3. Carbon track and conversion

Figure 4-5 shows the carbon particle tracks, scaled and colored by particle diameter. As illustrated, the particles are gradually depleted of carbon and reach a minimum diameter. The maximum carbon conversion ( $conversion = \frac{m_{inlet} - m_{loc}}{m_{inlet}}$ ,  $m_{loc}$  is the conversion at any location) at different points (A, B, C) are reported in Figure 4-5. The conversion of carbon is highest inside the reflux chamber, considering its shorter length compared to the up-leg and down-leg. This is due to pure oxygen injection inside the reflux chamber at a higher gas temperature, which causes the gas-solid reactions to proceed at a higher rate. The air quench also plays an important role in combusting carbon particles and CO-H<sub>2</sub> mixture. Essentially, any remaining carbon material from the reflux chamber is safely burned within the up-leg and down-leg sections. As a result, all carbon is completely consumed before reaching the water-quenched zone (Point C).

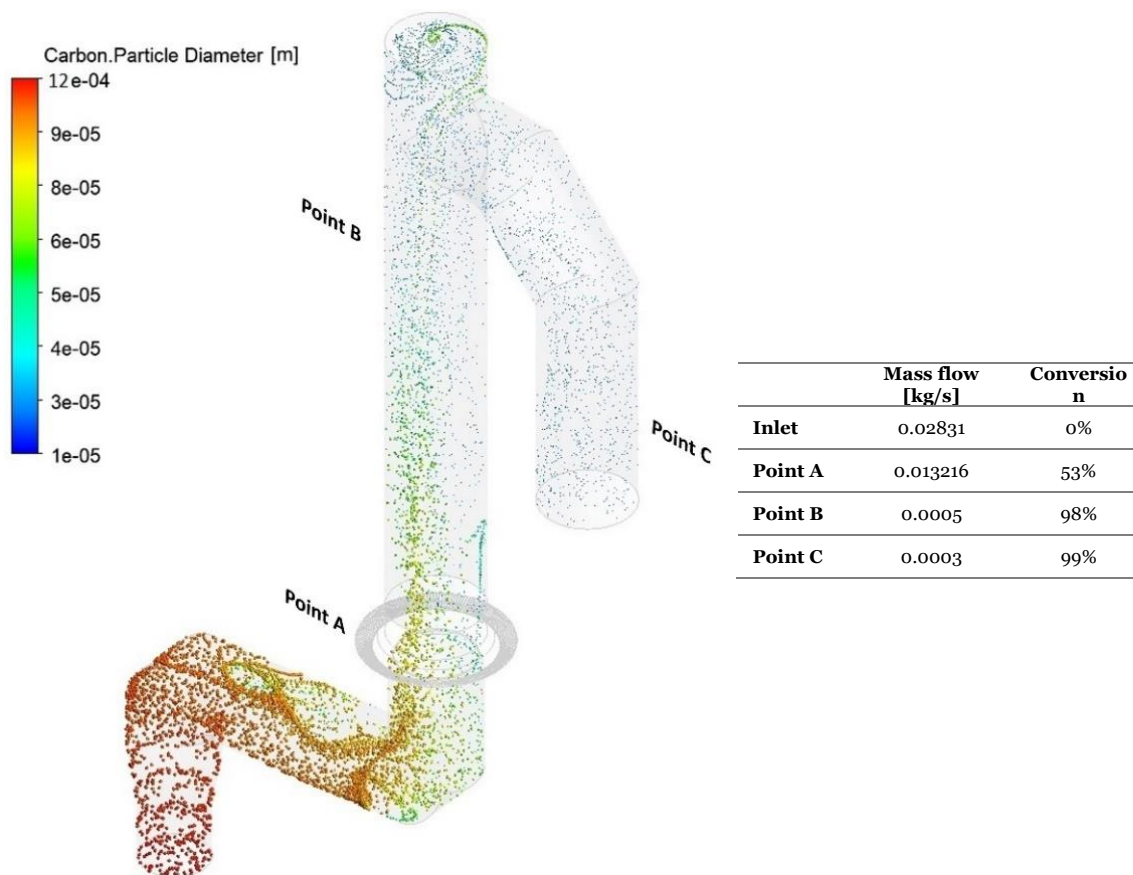


Figure 4-5. Carbon particle tracks and predicted conversions at measurement points

#### 4.4. Effect of water injection

Figure 4-6 shows a graphical representation of how the water spray is modelled inside the off-gas system. The gradual decrease of droplet diameter due to evaporation is also very well shown.

The amount of heat removed by evaporative cooling is considerable (1.2 MW). The water injection can make a temperature difference of 120 °C compared to a case without water injection (quenched only with nitrogen), as shown in the temperature profile of Figure 4-7. For a better graphical representation, the effect of water quenching on temperature and water vapor contours is also shown in Figure 4-8 and in Figure 4-10, which show cross sectional temperature profiles over the pipe diameter ratio ( $d/D$ ).

Since the spray angle is not wide and also due to the high flow rate of the flue gas, the water droplets are not well-spread at the beginning of the injection, and cold spots with much lower temperatures than the surrounding are formed.

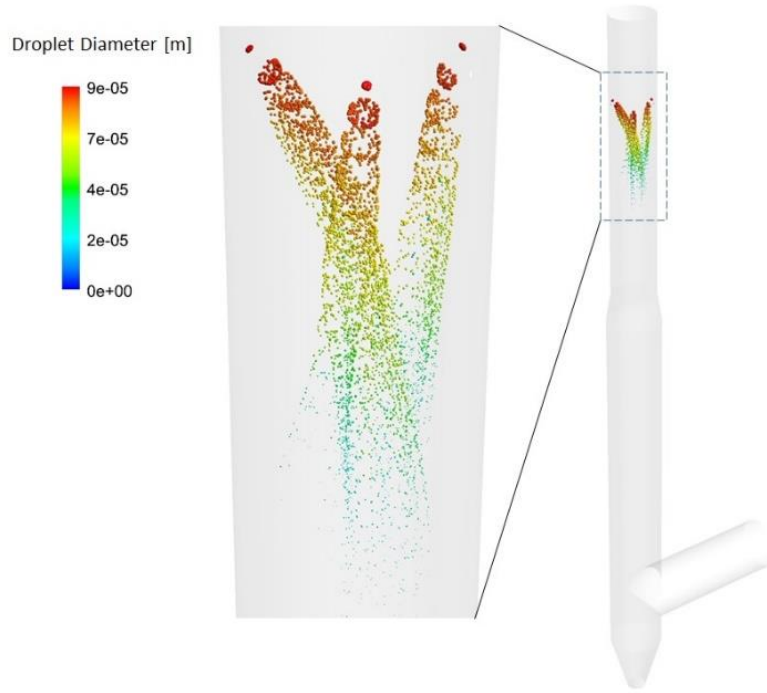


Figure 4-6. Water injection through cone spray model - droplet tracks in down-leg

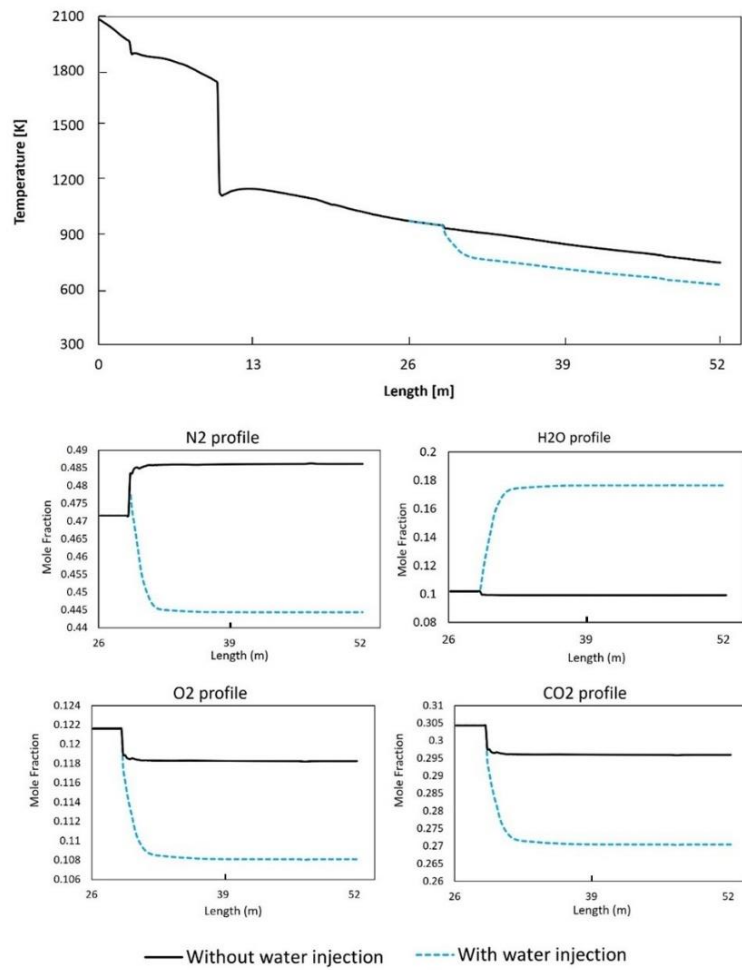


Figure 4-7. Effect of water injection on composition and temperature profiles in down-leg

Because the water is sprayed into a high-flow-rate flue gas with a narrow angle, the formed droplets do not effectively disperse at the initial stage of injection, resulting in the formation of cold spots with significantly lower temperatures compared to the surroundings. This can be seen in Figure 4-10, where the temperature drops fast and takes a V-shaped profile with a low local temperature at the center. This phenomenon is better shown in the temperature contours of Figure 4-8.

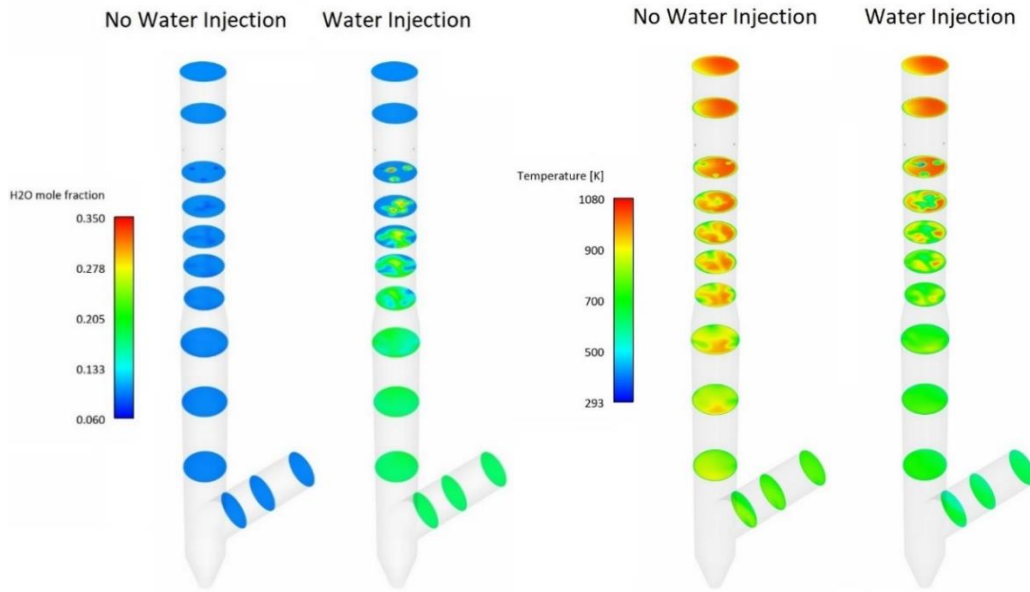


Figure 4-8. Composition and temperature contours at different cross section in down-leg – effect of water injection

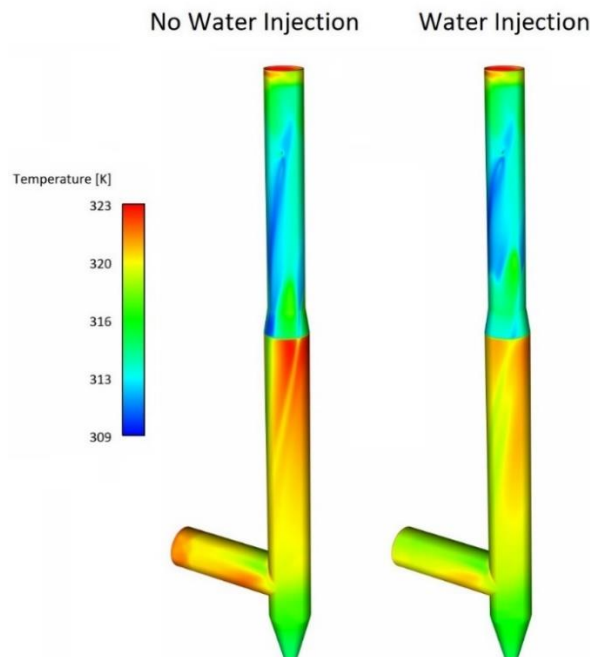


Figure 4-9. Down-leg inner wall temperature distribution – effect of water injection



At each cross section, the temperature profile becomes uniform (a constant value) downstream as the water is fully evaporated. While water injection locally reduces the wall temperature, as depicted in Figure 4-9, the overall change in average wall temperature is insignificant.

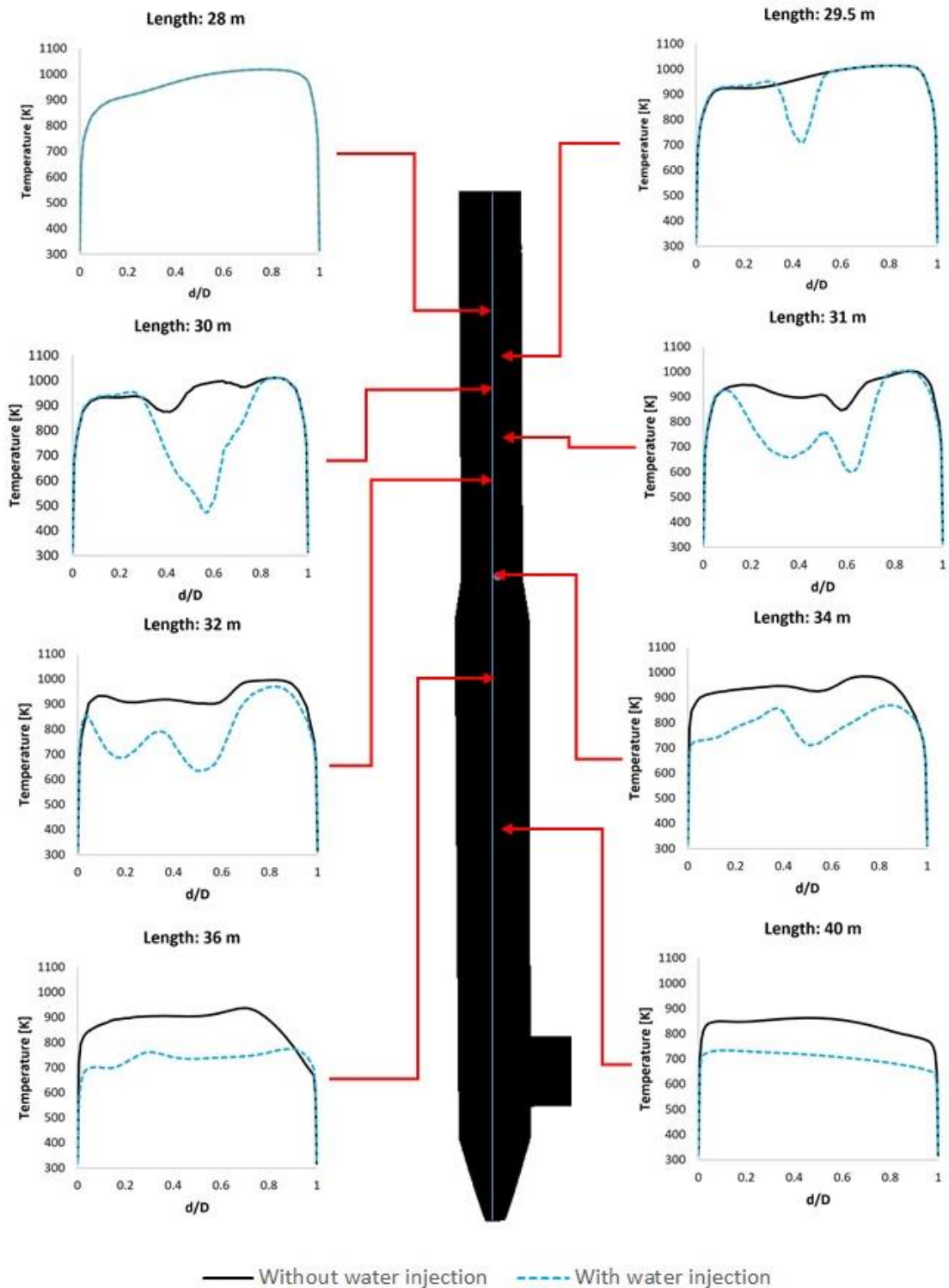


Figure 4-10. Temperature profile at central line on different cross section and at different lengths

## 4.5. Effect of oxygen injection

The calculated oxygen composition profile (see Figure 2-31) demonstrates a significant increase in the oxygen mole fraction in the reflux chamber, reaching 5.4% oxygen at the outlet. A basic theoretical calculation for the overall reactions of  $\text{H}_2 + 0.5 \text{O}_2 \rightarrow \text{H}_2\text{O}$  and  $\text{CO} + 0.5 \text{O}_2 \rightarrow \text{CO}_2$  reveals that the stoichiometric oxygen required for complete combustion of the CO-H<sub>2</sub> mixture, with the current inlet and composition values, is 0.058 kg/s.

For the complete combustion of carbon particles (0.0282 kg/s) using a single-step reaction of  $\text{C} + \text{O}_2 \rightarrow \text{CO}_2$ , 0.074 kg/s of oxygen is required. To fully combust the CO-H<sub>2</sub>-carbon mixture, 0.133 kg/s of oxygen is needed, considering this stoichiometric value. As a result, the excess oxygen injection will be at 120%

Due to the limited length of the reflux chamber in the current plant installation, achieving complete combustion of unwanted elements is not feasible. The combustion process in the reflux chamber is only partial, resulting in approximately 55% and 95% conversion for carbon and CO-H<sub>2</sub>, respectively.

The remaining uncombusted elements are effectively burned in the up-leg since the temperature there remains sufficiently high, and there is an abundant supply of oxygen due to air injection through the air quench system. Therefore, leakage of CO and carbon from the reflux chamber is acceptable as long as these fractions are fully combusted downstream.

On the other hand, the oxygen is injected in pure form (99.5 % purity) into the reflux chamber, which involves certain costs, unlike air quench, which uses cost-free ambient air. Thus, it is desired to reduce pure oxygen injection to reduce operating costs as much as possible.

A series of simulations were conducted to assess the impact of reducing the oxygen injection (at 20%, 40%, and 60% reduction) on CO-H<sub>2</sub>-carbon mixture combustion. Figure 4-11 shows the CO and O<sub>2</sub> mole fraction at different measuring points along with CO and carbon conversion. As demonstrated, reducing oxygen injection leads to an increase in CO mole fraction, a decrease in O<sub>2</sub> mole fraction, and consequently, a reduction in CO and carbon conversion at the reflux chamber outlet (point A). Up to a 40% reduction in oxygen, carbon is still fully combusted before reaching point



C, as shown in Figure 4-12 which illustrates the particle tracks colored by the particle diameter. However, carbon escapes when oxygen injection is reduced by 60% and enters the water-quenched zone (97% conversion). The CO mole fraction at point C increases (indicating lower conversion) due to the reduction in oxygen injection into the reflux chamber.

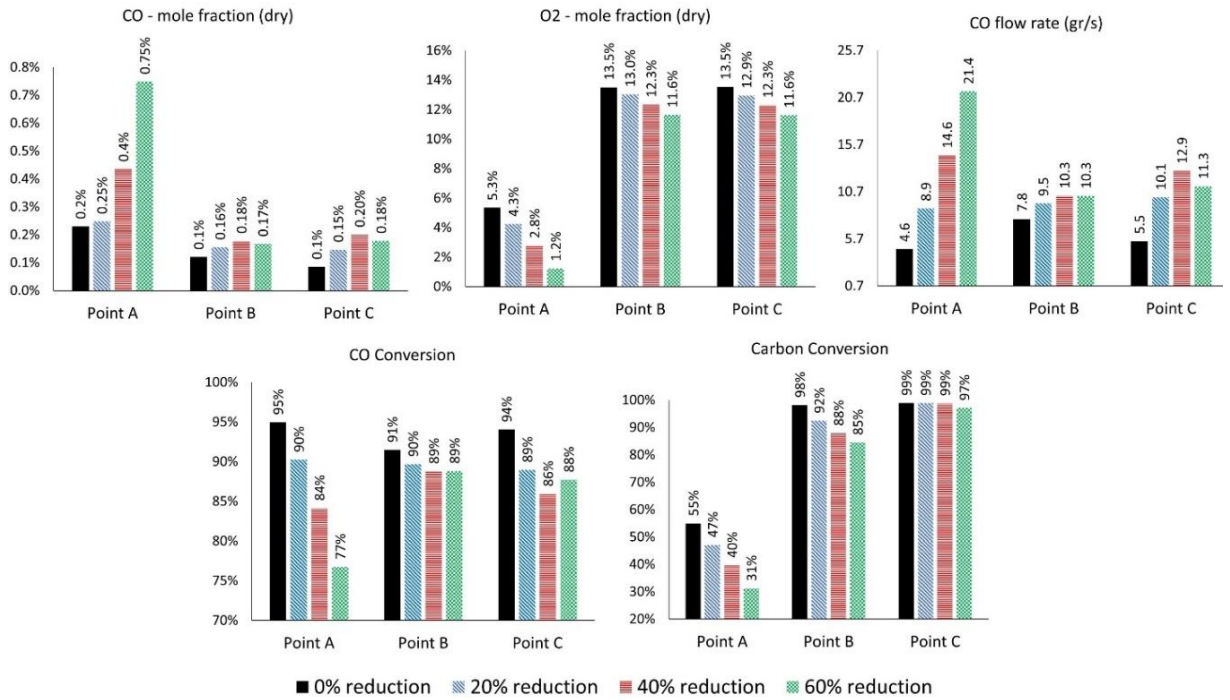


Figure 4-11. CO-O<sub>2</sub> mole fraction and carbon conversion for different oxygen reduction cases

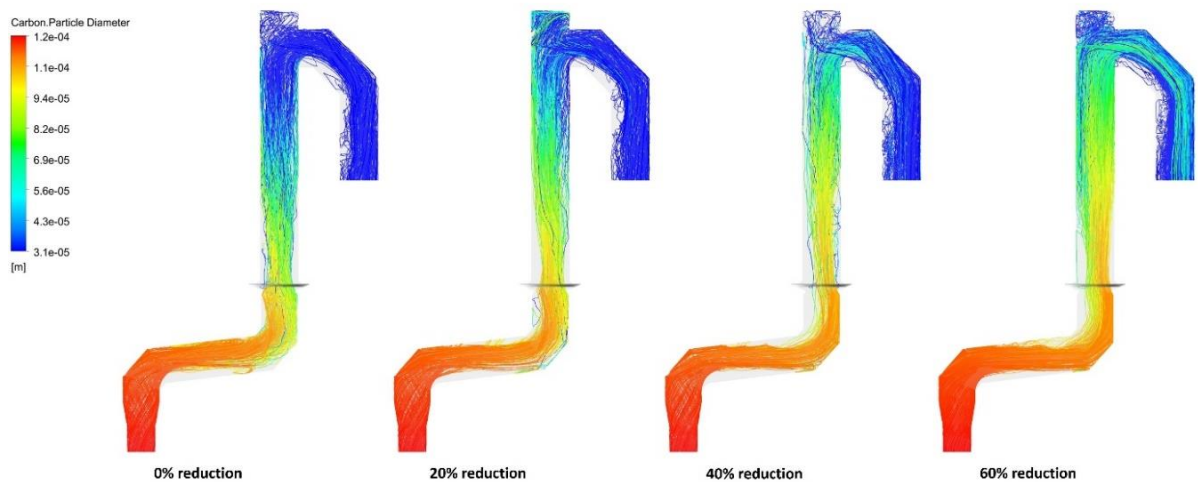


Figure 4-12. Carbon particle track, colored by particle diameter for different oxygen reduction cases. Allowing a substantial amount of CO to enter the water-quenched zone is risky, as combustion is more likely to cease there, given the rapid temperature drop below the auto-ignition point of CO (882 K).

To have a better understanding, a simple analysis using CHEMKIN software, where a mixture containing a certain amount of CO (same as point B) with the same combustion mechanism as used in the CFD models, is performed to investigate the auto-ignition properties using closed homogeneous reactor model. The initial temperature of the mixture is fixed, and temperature increase and CO consumption are monitored. The results are shown in Figure 4-13. As it can be concluded, the ignition (increase in temperature and initiation of CO consumption) is delayed by reducing the temperature, and there is no ignition below the temperature of 882 (609 °C). At 882 K, even though the ignition starts, the consumption rate of CO and temperature increase rate are quite low, and for the time analyzed (30 sec), full consumption of CO could not be achieved. A higher temperature than the auto-ignition temperature (around 200 °C higher) is needed to ensure that all CO is combusted.

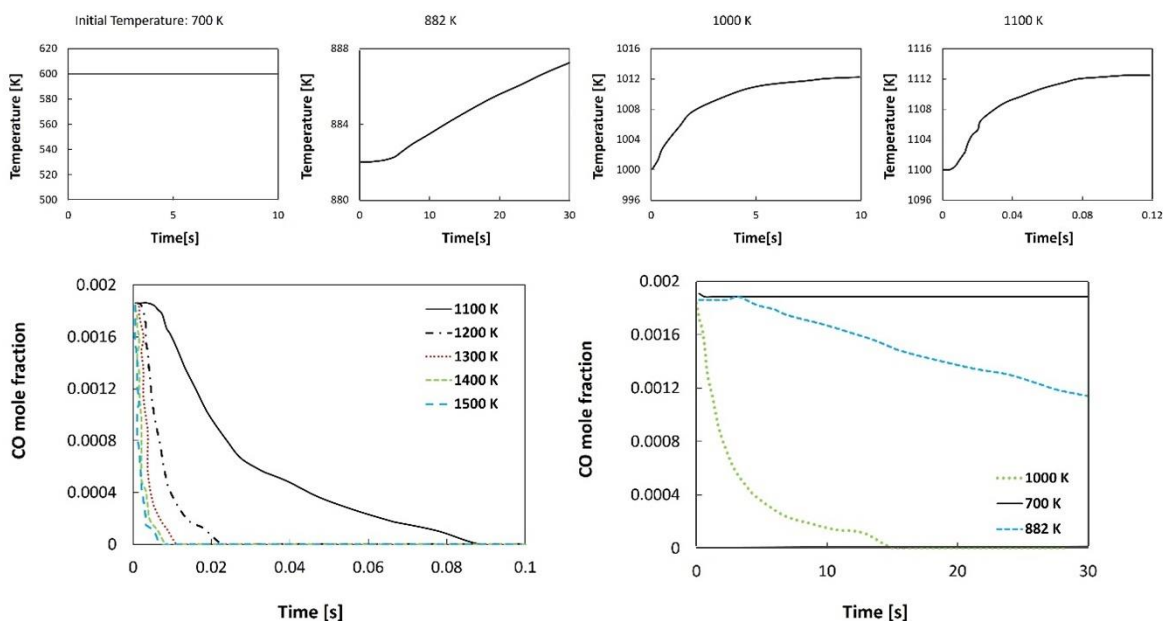


Figure 4-13. Temperature and CO mole fraction transient profile for auto-ignition analysis

Therefore, reducing oxygen injection is possible, but it should be in a quantity that the unwanted species (CO and carbon) are still combusted at a higher temperature than the auto-ignition point. From model predictions, any reduction in oxygen injection will increase the CO flow rate (and mole fraction) entering the low-temperature region of the off-gas system with a high risk of emission into the environment. Further reduction in oxygen injection is also investigated and reported in Figure 4-14. As the flow rate is decreased, the velocity is reduced, leading to lower penetration of oxygen into the bulk flue gas. This occurs because the oxygen

flow is displaced away from the center, with the flue gas stream pushed upward, as shown in Figure 4-14 (short circuit or channeling of oxygen). This will allow CO-H<sub>2</sub> to escape without being mixed with the oxygen stream.

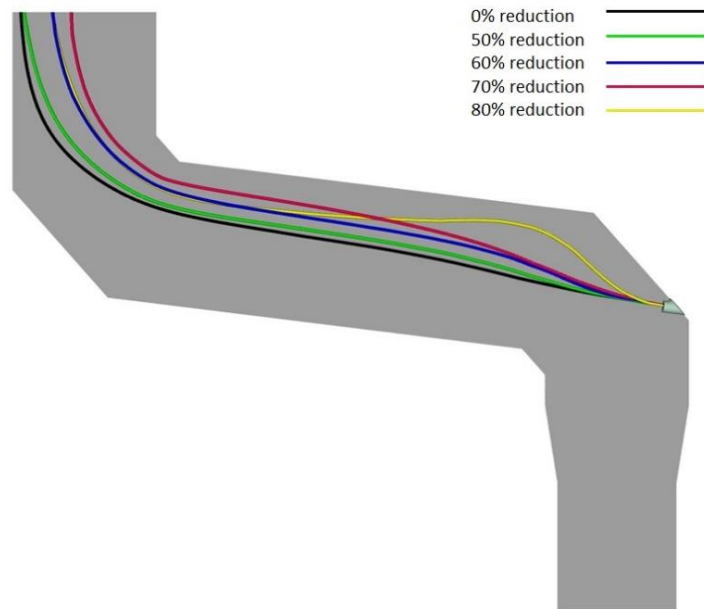


Figure 4-14. Oxygen mean streamlines for different oxygen reduction cases

## 4.6. Effect of inlet CO content

The HISarna process exhibits a transient nature. The inlet boundary conditions employed in all steady-state models consist of averaged values over a fixed operating period. However, it is important to note that all values will fluctuate around these averaged values during actual operations. For example, the amount of CO may vary between 0% and 10% (molar) at certain times, depending on the CCF post-combustion ratio. The same variability applies to O<sub>2</sub>, which can reach levels of up to 5% at the inlet of the reflux chamber.

A set of simulations is performed to see the effect of inlet composition change by varying the amount of CO and O<sub>2</sub>. Figure 4-15 below shows the effect of CO molar fraction at the inlet of the off-gas system (for 2.5% and 10% CO content) on temperature, composition, carbon conversion, and heat of reaction profiles. As can be seen, increasing CO content provides more fuel to the post-combustion region, and much more heat is generated (nearly five times more). Higher CO content at the inlet will lead to a sudden release of heat in a short interval once reaching the oxygen-rich zone (near the injector), which might increase the risk of the explosion

inside the off-gas system and higher temperature across the whole off-gas system. Subsequently, the heat loss through the reflux chamber and the rest of the off-gas system walls will be higher. The higher CO content consumes more oxygen, which is evident from the O<sub>2</sub> profile.

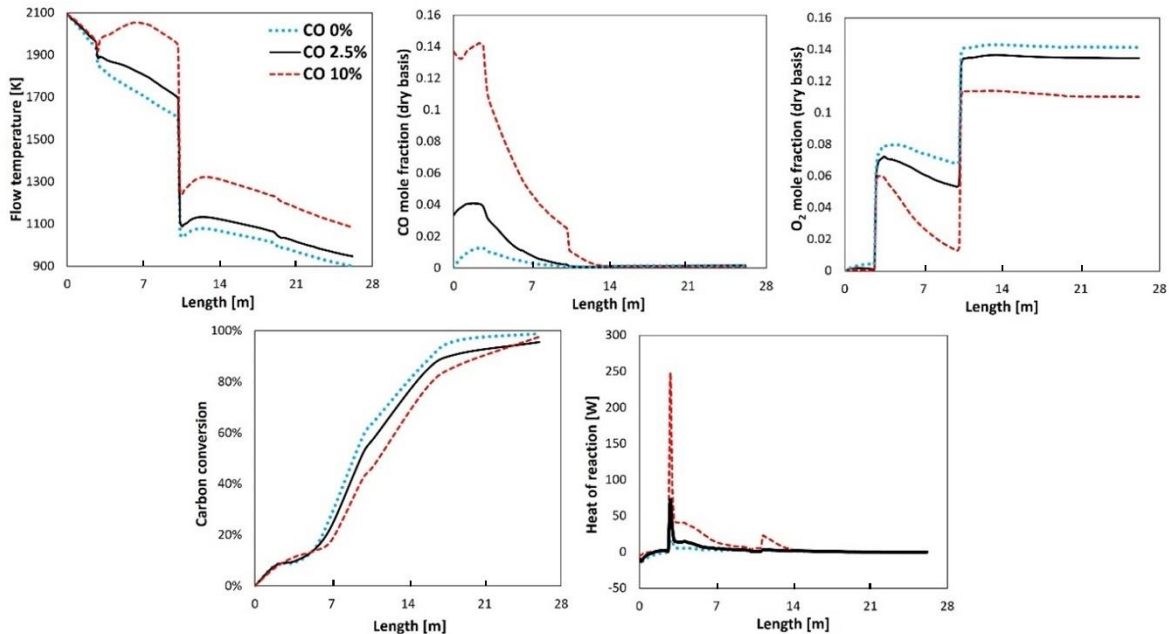


Figure 4-15. Effect of CO inlet content on different calculated parameters

From the same figure, it is evident that increasing CO content reduces local carbon conversion. This is primarily due to the higher oxygen consumption resulting from the gaseous reactions, which occur more easily and rapidly than the solid surface reactions. Additionally, following Le Chatelier's principle, the increase in CO partial pressure negatively affects the forward rate of the carbon gasification reactions.

Nevertheless, the current oxygen injection and system configuration can still remove all unwanted species. However, the possibility of oxygen injection reduction which was discussed in section 4.5, is valid for average inlet values, and increasing CO content might limit the possibilities of oxygen reduction.

## 4.7. Effect of inlet O<sub>2</sub> content

Figure 4-16 shows the effect of the O<sub>2</sub> content of inlet flue gas on the temperature, composition, carbon conversion, and heat of reaction profiles. The graph shows the favorable impact of oxygen presence at the inlet on the removal and conversion of

unwanted species. The presence of oxygen from the inlet leads to the earlier consumption of CO content and an early increase in temperature. Additionally, it is noticeable that the peak of heat release near the oxygen injection area is moderated, and the peak of released heat is reduced by introducing oxygen at the reflux chamber's inlet, reducing the potentially explosive nature of the high CO content flow. Furthermore, there is a significant improvement in carbon conversion, reaching 99% at a shorter length of just 14 meters.

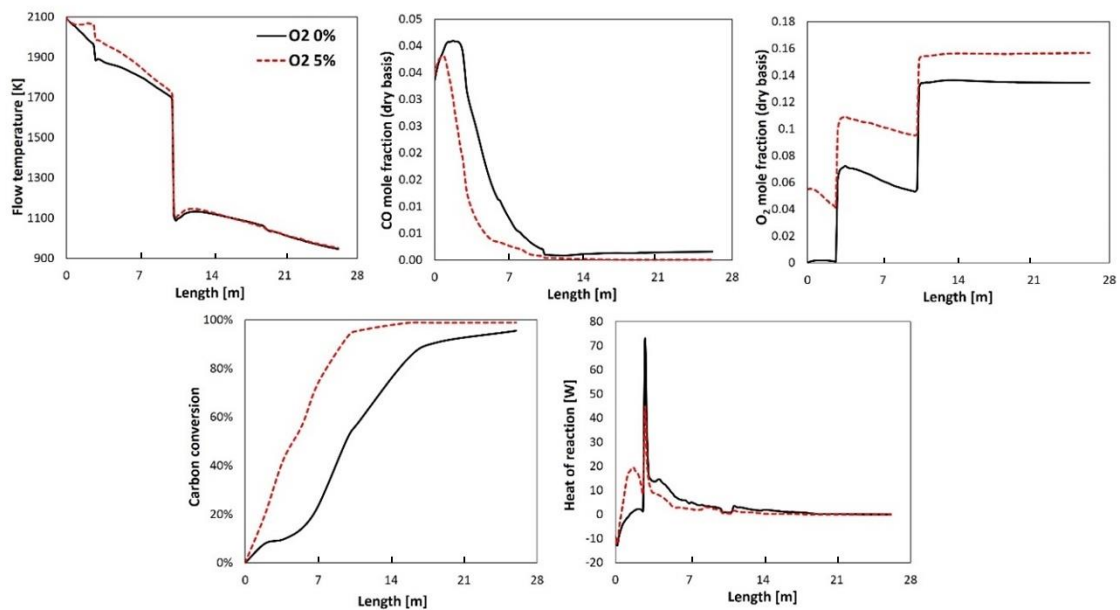


Figure 4-16. Effect of CO inlet content on different calculated parameters

## 4.8. Conclusion

A 3D CFD simulation of the HIsarna off-gas system is performed and the effects of different operating parameters are investigated. The developed CFD model can provide detailed information on the flow behaviour, conversion of unwanted species, and heat transfer within the off-gas system, and the predictions are in good agreement with available plant data.

The water injection has a noticeable effect on the composition and temperature profile in the down-leg. Due to poor dispersion of the sprayed droplets, the formation of cold spots along the flue gas flow is predicted. The overall temperature reduction is predicted to be around 100 °C once the water is injected, which makes the flue gas condition proper for further cooling and ultimate treatments.

Oxygen is injected with a 120% excess to ensure the complete conversion of unwanted species. Despite this excess, both plant data and model results indicate that achieving complete conversion of CO and carbon in the reflux chamber is challenging.

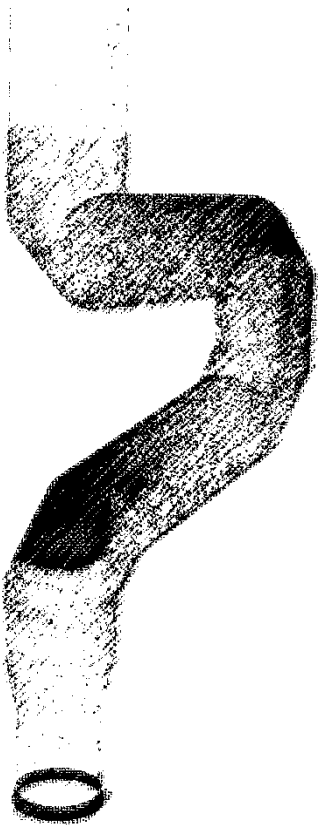
The CO and carbon that escape the reflux chamber are subsequently combusted in the up/down-leg where the temperature and oxygen concentration remain sufficiently high for the reactions to occur. However, model predictions suggest that oxygen injection could be reduced while still achieving full conversion downstream.

Excessive reduction in oxygen injection results in CO and carbon entering the water-quenched zone, where temperatures fall below the auto-ignition point of CO, potentially leading to unwanted pollutant emissions.

Depending on the content of O<sub>2</sub> and CO in the inlet off-gas, the temperature and composition profile can drastically differ from the base case. Higher CO content means higher available fuel to burn. For the case with a CO content of 10%, a sharp increase in released heat is predicted near the oxygen-rich region of the reflux chamber, which can cause an explosive flow behavior. Therefore, a very high value of CO content at the inlet of the reflux chamber is not desired. This sharp increase can be mitigated by including oxygen at the inlet. With the inclusion of oxygen, the combustion of CO commences earlier, even before reaching the oxygen-rich region. This results in a reduced amount of CO available to burn near the oxygen lance.

# Chapter 5

## BEHAVIOUR OF PRE-REDUCED MOLTEN ORE PARTICLES



A general model has been developed to describe the flow behavior of molten iron ore particles within the off-gas system. Based on plant inspections, it was observed that particle accretion and the formation of a molten layer primarily occur within the reflux chamber. The fundamental model was validated using average plant measurements and subsequently used to suggest modifications aimed at improving particle capture efficiency by the reflux chamber's wall. The calculated results demonstrate an enhanced particle capture efficiency, increasing from 74% with the current design to 85% with the modified geometry.



### 5.1. Introduction

One of the main issues in the HIsarna process is the loss of injected fine ore from the main reactor. The losses are from CCF to the reflux chamber and then to the up/down-leg, which ultimately end up in the bag house with other impurities such as lime and carbon particles. In this chapter, possible solutions to reduce the loss of iron ore from the reflux chamber are investigated. To fulfill that, a CFD model is developed to predict the behaviour of particles within the off-gas system.

The behavior of molten ore particles and their interactions with flue gas and the chamber wall is modeled as multiphase dispersed flow. Approaches for multiphase flow modeling are categorized in Figure 5-1. Currently, two main approaches exist for modeling multiphase flows: the Euler-Lagrange and Euler-Euler approach [1].

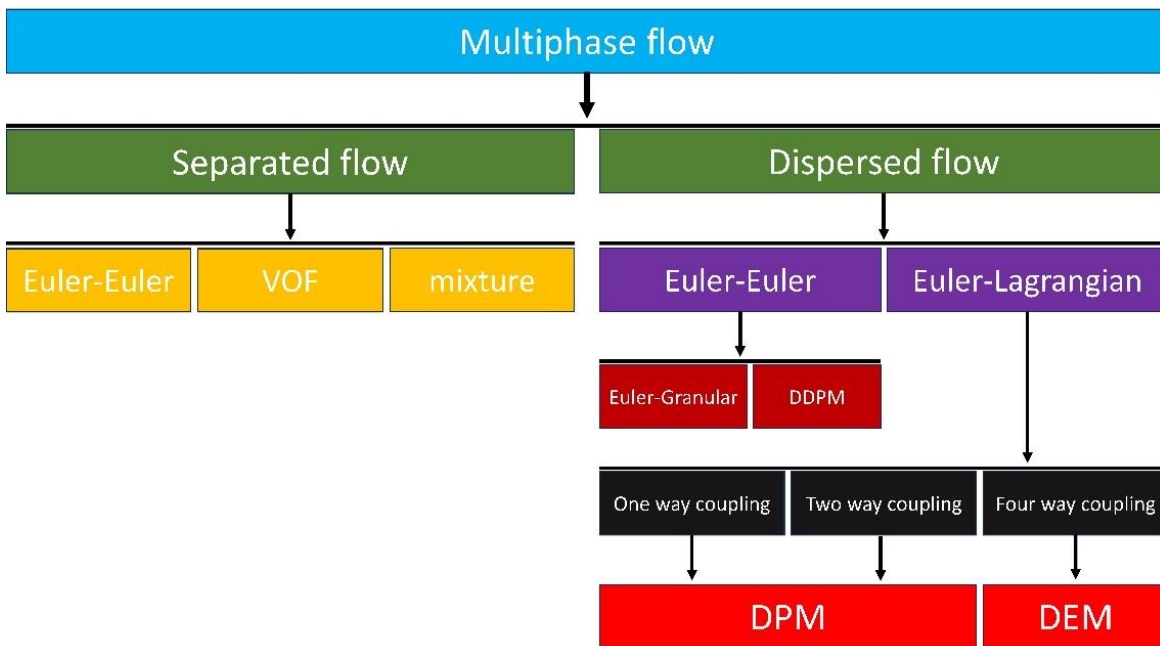


Figure 5-1. Multiphase flow modelling approaches

The Euler-Euler model treats both the fluid and granular phases as a continuous medium and typically utilizes the kinetic theory of granular flow (KTGF) to describe granular interactions. particles are statistically characterized through a concentration function, with their temporal evolution governed by a convection-diffusion equation. The basic property of the Euler-Euler model is a consequence of the temporal and spatial averaging, and each fluid as a continuum occupies the entire domain [2].



In contrast, the Euler-Lagrange approach treats the fluid phase as a continuous medium through the solution of the Navier-Stokes equations, whereas the dispersed phase is individually tracked, with each particle having its own coordinates and corresponding equations of motion (which is based on Newton's second law). The dispersed phase can represent a broad range of substances, including solid particles in a gas, liquid droplets in a gas, or air bubbles in a liquid. The dispersed phase can exchange momentum, mass, and energy with the fluid phase. Figure 5-2 shows the visual difference between the two approaches for a fluidized bed model. As can be observed, in the Euler-Euler approach, the bulk of particles is represented with an averaged concentration, while the Euler-Lagrange approach resolves individual particles, offering a closer analogy to experimental data.

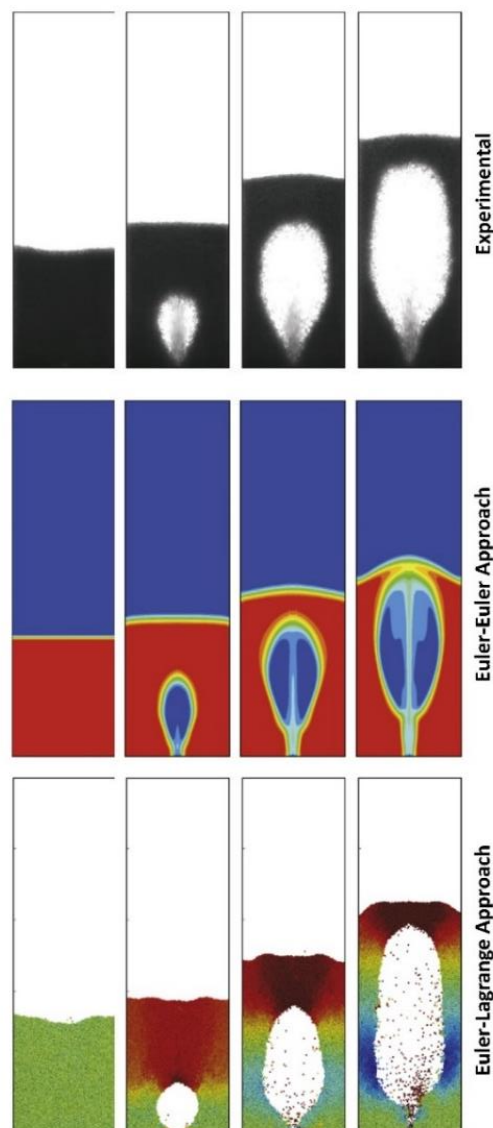


Figure 5-2. DPM and DEM modelling of a fluidized bed

A notable limitation of the Euler-Lagrange approach is the substantial computational effort it demands when handling systems with a high number of particles. Consequently, this approach is often constrained to applications involving downsized equipment and low flow rates. In contrast, the Euler-Euler approach has demonstrated success in predicting fluid-particle dynamics in a variety of processes [3]. The Euler-Lagrange approach can be further categorized based on the interactions between flow constituents and the way their effects are coupled.

In one-way coupling, the discrete phase is simulated based on the flow field of the continuous phase. One-way coupling is also known as the uncoupled approach, signifying that only the continuous phase influences the behavior of the discrete phase. In other words, there are no interchange terms with one-way coupling, including mass, momentum, and heat transfer from the discrete phase to the continuum.

In two-way coupling, both phases mutually influence each other, resulting in mass, momentum, and heat exchange between the discrete and continuous phases. In four-way coupling, in addition to the above considerations, particle collisions are also taken into account, where one particle can affect the motion of others.

Table 5-1. Summary of a few performed studies on the application of DPM modelling

<b>Particle - fluid</b>	<b>application</b>	<b>reference</b>
Polyethylene Pellets - Air	Pneumatic conveying of polyethylene pellets	[1]
Dust Particle - Air	Ascensional and descensional ventilation	[4]
Diesel Particulate Matter - Air	Mine ventilation	[5-10]
-	Rotor-stator particle agglomeration reactor	[11]
Pellet - Gas	Biomass grate combustion	[12]
Limestone Particles - Air	Plane air classifier	[13]
Pneumatically Conveyed Particles - Gas	Mitigating elbow erosion	[14]
Particle-Gas	Particle settling in a horizontal air stream	[15]

The initial volume fraction of the dispersed phase plays a pivotal role in determining the level of coupling between the phases. When the volume fraction is below 10%, particle-particle interactions can be safely disregarded, making it suitable for utilizing the discrete phase model with one and two-way coupling. In cases where the volume fraction exceeds 10%, particle collisions become significant, and the discrete element method (DEM), which involves four-way coupling, may be

employed. Since the current scenario can be classified as a diluted particulate flow with a volume fraction of less than 10%, interactions between particles can be omitted. The Discrete Phase Model (DPM) concept has been widely applied to model particulate flows using various approaches, some of which are outlined in Table 5-1.

## 5.2. Governing equation

The governing equation regarding DPM modelling is already discussed in Chapter 2, section 2.2. The same concept is applied for the molten ore particle flow as discussed for carbon and water droplet particles. In this approach, the following equation is solved for each discrete particle to obtain the velocity by calculating each force on the particle:

$$m \frac{d\vec{u}}{dt} = \vec{F}_{drag} + \vec{F}_{Pressure} + \vec{F}_{virtual} + \vec{F}_{gravitation} + \vec{F}_{other} \quad (5-1)$$

Then, using the obtained velocity, the trajectory of the particles is calculated by integrating the following:

$$\frac{dx}{dt} = u_p \quad (5-2)$$

## 5.3. Phenomena description

According to mass balance calculations, approximately 10% of the injected ore escapes from the CCF and enters the reflux chamber. These particles remain in a molten state, and the wall of the reflux chamber can capture them using the same mechanism as described for the CCF. Upon impact with the wall, these particles accumulate and form a running film, which then refluxes back into the CCF. The capturing efficiency of the reflux chamber is approximately 60%, and about 4% of the total injected ore into the process escapes from the reflux chamber.

Above the reflux chamber, due to quenching, the particles solidify, and no further capturing by the walls is possible. The entire wall of the reflux chamber functions as a capturing unit because the temperature inside the reflux chamber remains higher than the particle solidification temperature. Most of the particles are in the form of  $\text{Fe}_3\text{O}_4$  and minor  $\text{FeO}$ , with melting temperatures of 1870 K and 1650 K, respectively. However, due to impurities in the ore, the slag-forming temperature

decreases to a range of 1600 to 1700 K, which is lower than the average flue gas temperature across the reflux chamber.

No information and experimental data are available on the molten ore interaction with solid walls. Therefore, to develop the model, a few basic assumptions are considered:

**Assumption 1:** The particles are in a molten state and maintain this state inside the reflux chamber for the majority of the operating time, as the temperature within the chamber exceeds the solidification temperature (1650 K for this study). This assertion is supported by CFD model predictions, as illustrated in Figure 5-3, which demonstrates temperatures exceeding the solidification temperature of 1650 K. In cases of low CO content, the temperature may drop below the solidification point. However, due to the consistent presence of the liquid film on the wall, there remains a high likelihood of particle capture even at lower flue gas temperatures. It is important to note that the simulations are steady-state and not transient, so an average behavior is considered in this analysis.

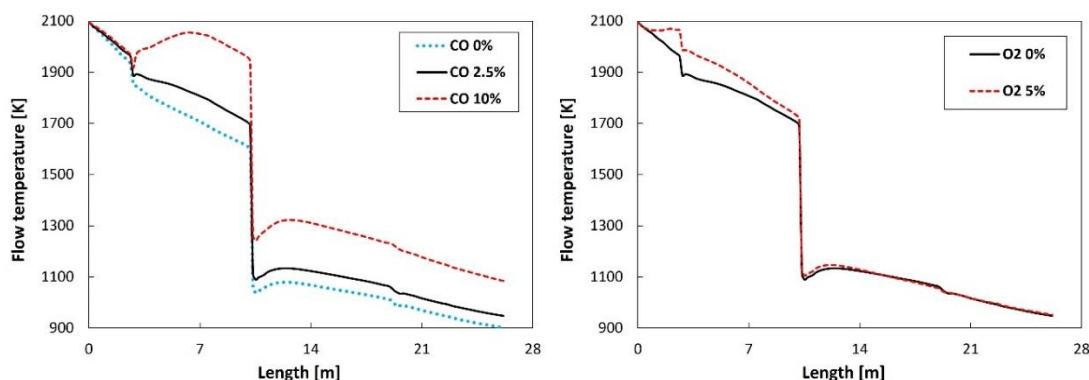


Figure 5-3. Calculated temperature profile for different CO-O<sub>2</sub> inlet compositions for dog-leg geometry

**Assumption 2:** The entire reflux chamber wall surface can capture the molten particles and are covered by a molten running film of liquid iron ore. This is a fair assumption based on the recent inspections. Figure 5-4 illustrates the formation of the slag layer on the wall surfaces within the chamber.

**Assumption 3:** Above the reflux chamber, the particles solidify, and there is no further wall-based capturing. This results from a cold air layer forming around the wall above the air quench. Any particles that come into contact with this cold layer will solidify and be carried away by the flue gas. Figure 5-5 shows the wall of the off-

gas system taken from the bottom of the second bend of the reflux chamber. It is evident that the build-up is no longer forming above the reflux chamber. Hence, the modelling and consideration of particle capturing are focused exclusively on the reflux chamber geometry.

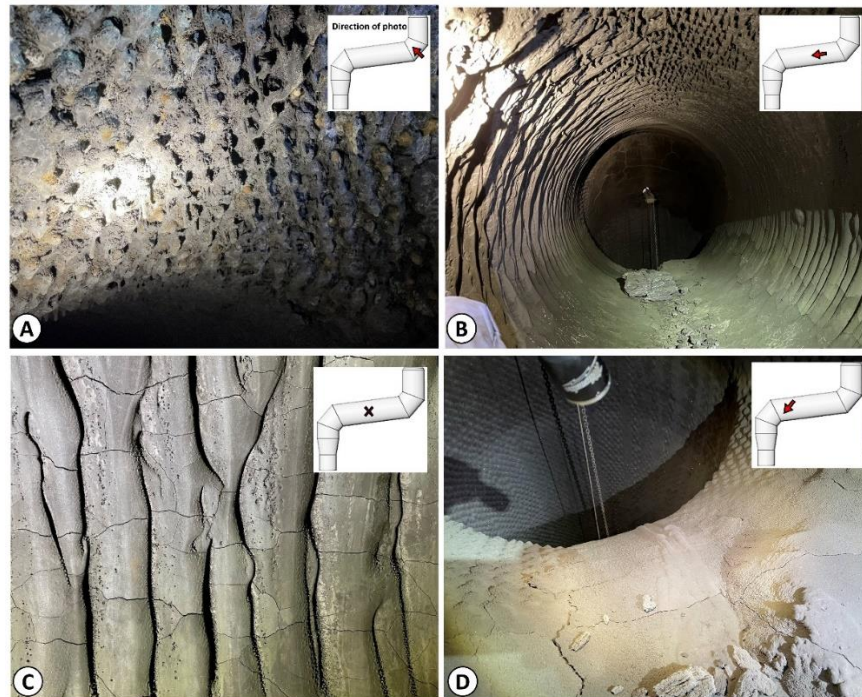


Figure 5-4. Accretion build-up on the reflux chamber wall surface (inspection 2021)

A simple model is developed based on these assumptions and validated against the measured data. The model will then be used to investigate the effect of geometrical modification of the reflux chamber to increase particle capturing, achieving higher conversion of CO-H<sub>2</sub> and carbon mixture and reducing the formation of zinc ferrite, which will be discussed in detail in the coming chapters.

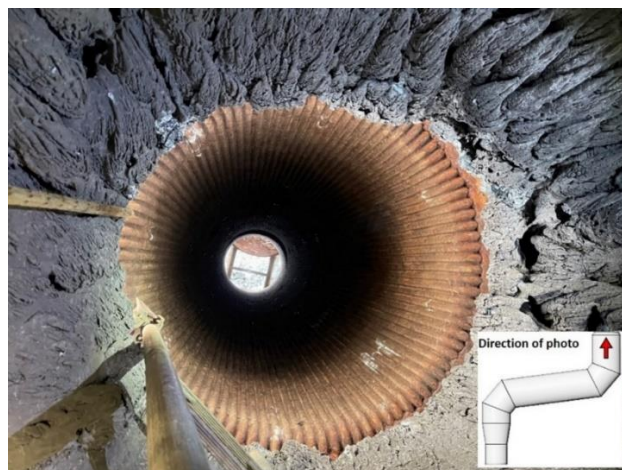


Figure 5-5. Clean wall of the off-gas system above the air quench

## 5.4. Geometry, mesh, and boundary conditions

The reflux chamber geometry and mesh will be the same as discussed in Chapter 2, section 2.3.2. The inlet boundary condition for gaseous flow is similar to the previously developed CFD model (Chapter 2, section 2.3.3). In the current model, an extra particle flow representing the molten iron oxide particles is added with properties reported in Table 5-2. It is assumed that 10% of the injected mass of particles (CCF injection: 8 tone/hr or 2.23 kg/s) are escaping from CCF and entering the reflux chamber.

Table 5-2. molten ore particle properties (obtained from TATA Steel Ijmuiden R&D)

Parameters	Value
Density [kg/m <sup>3</sup> ]	5000
Heat capacity [J/kg-K]	922
Injected ore into CCF [kg/s]	2.23
Reflux Chamber inlet [kg/s]	0.223

Another important consideration is particle size distribution (PSD). It is infeasible to have precise information on escaped PSD from CCF as there are no possibilities of sampling due to high temperatures and the liquid nature of particles. Hence, the used particle size distribution (PSD) is taken from CFD models developed for CCF, as shown in Figure 5-6. Thermal boundary conditions for the walls are the same as in Chapter 2 (see Figure 2.11). The boundary conditions for particles are set to “trap” so that any particle impacting the wall is captured and subsequently removed from the calculations.

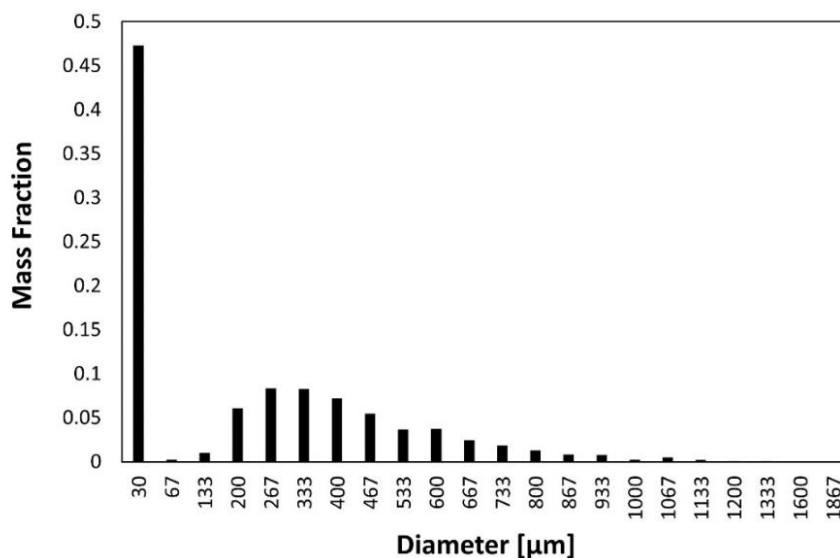


Figure 5-6. Inlet PSD of ore particles for DPM modelling

## 5.5. Base model: dog-leg geometry

Figure 5-7 shows the calculated escaped particle flow rate and outlet PSD.

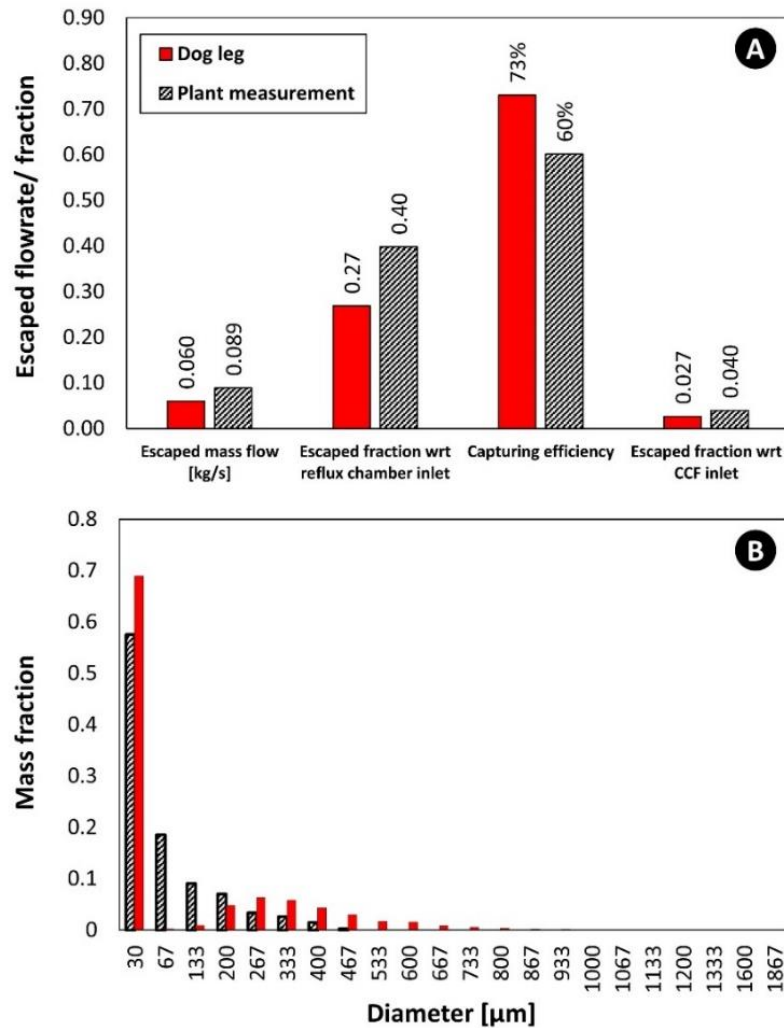


Figure 5-7. Calculated escaped flow rate (A) and outlet PSD (B)

The results are in fair agreement with the counterpart plant measurement. Figure 5-8 shows the flow rate of the tracked particles and captured particles by the wall of the reflux chamber. The bend, where the post-combustion oxygen lance is situated, effectively captures most larger particles.

As particles enter the curve, they must overcome the force of momentum to change their direction from the straight path they were initially following. Due to their greater acquired momentum, larger particles tend to maintain their original trajectory. Consequently, it becomes more challenging for larger particles to change their path during the curved section of the geometry, resulting in collisions with the walls and subsequent capture. This observation aligns with findings from plant



inspections. Figure 5-9 shows the wall of the reflux chamber around the oxygen lance (first bend), and as can be seen, there are small dents on the wall, indicating erosions due to the particle impact.

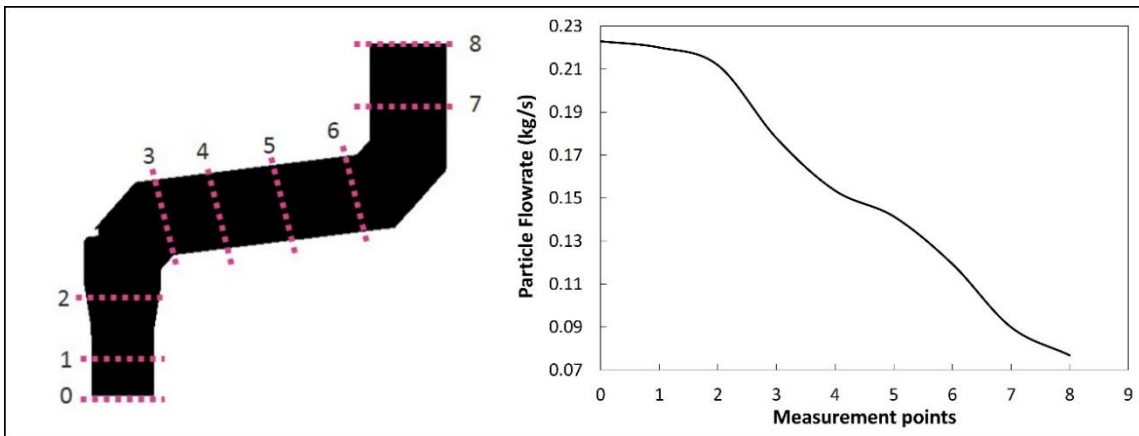


Figure 5-8. Predicted particle track and accretion on the walls



Figure 5-9. Wall condition around the oxygen lance and first bend of the dog-leg geometry (inspection 2019)

## 5.6. Reflux chamber geometry modification

The walls inside the reflux chamber are responsible for particle capturing. Therefore, to enhance particle capture efficiency, a physical (geometrical) modification is preferable. This preference is due to the fact that changes in operational parameters (such as temperature or flue gas flow rate) have only a slight or negligible impact on the flow behavior. Moreover, operational modifications would necessitate significant alterations to the process.



However, given the very high temperatures inside the reflux chamber, options for physical and geometrical modifications are limited. As previously mentioned, the reflux chamber's dog-leg geometry was designed to capture particles in their molten state and create a film on the walls that runs back to the main reactor, reducing ore loss. Therefore, any geometrical modifications must adhere to these criteria and ensure that escaped particles are refluxed to the CCF. Among the ideas to modify the geometry of the reflux chamber, “frog-leg” geometry has been the best candidate, as shown in Figure 5-10.

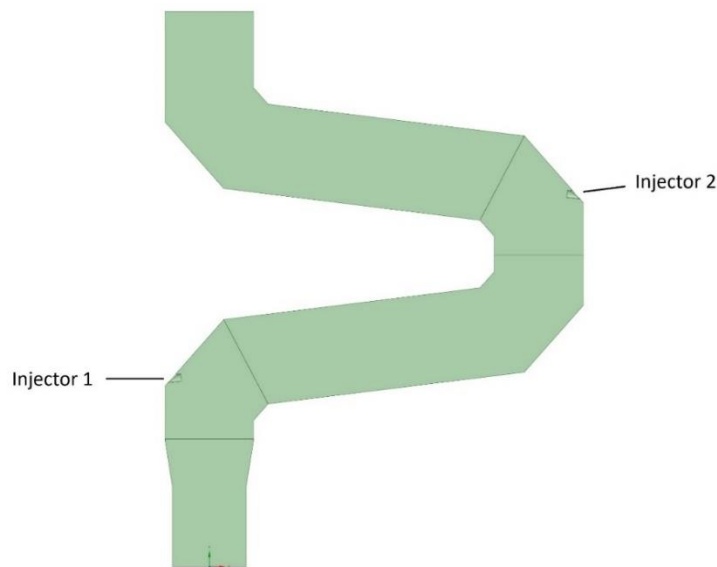


Figure 5-10. Frog-leg geometry for modified reflux chamber

It is formed simply by adding a second bend to the original geometry. In the frog-leg configuration, two sets of oxygen injection nozzles can be placed at two different elevations, which is an added advantage to the original geometry.

The same developed base model is used to see the particle behaviour; however, temperature profiles must be acquired to ensure that the temperature remains high throughout the reflux chamber so that the “trap” wall boundary condition is valid for different inlet boundary conditions.

Figure 5-11 shows the temperature profile for different inlet CO contents, which fluctuates during the operation. As can be seen, the temperature for most of the frog-leg length remains high enough to form the molten layer on the wall surface. Therefore, the assumption of the “trap” wall boundary condition remains valid for the frog-leg configuration. Figure 5-12 shows the outlet result of calculated particle flow for frog-leg geometry. As can be seen, there is a noticeable improvement in

capturing efficiency for the modified geometry. Injecting oxygen at two different elevations for frog-leg geometry is possible; however, the results showed that the oxygen injection has no specific effect on particle behaviour.

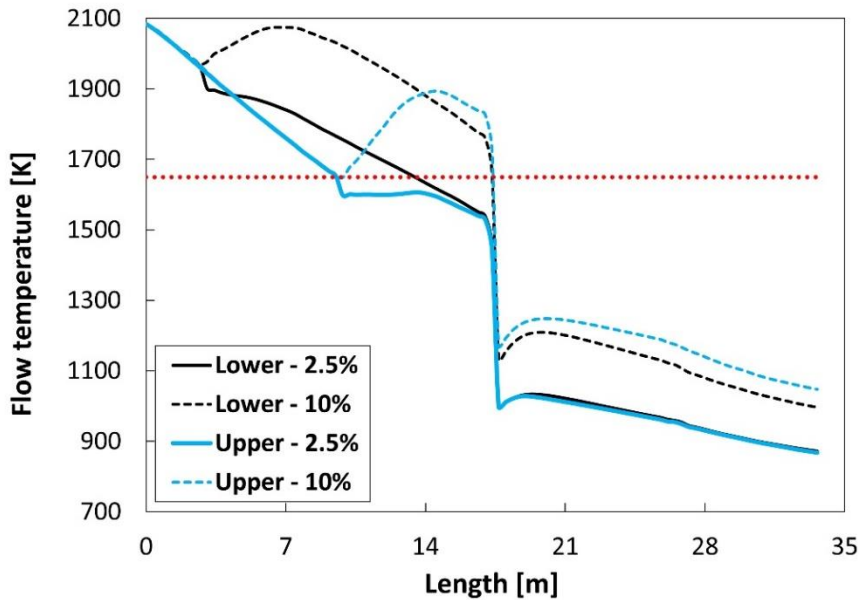


Figure 5-11. temperature profile for different CO inlet compositions (frog-leg geometry)

The escaped particles from the first bend (same as the dog-leg outlet) will again hit the second bend and are captured, showing the effectiveness of the turns in the geometry. Figure 5-13 clearly shows the effect of the second bend on the particle track and capturing behaviour of the walls as the particle flow rate continues to decrease.

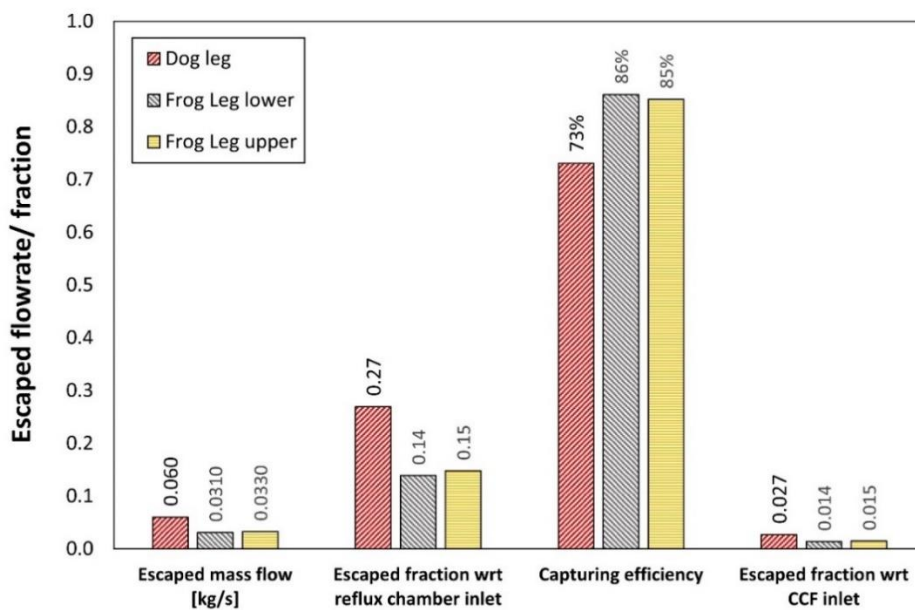


Figure 5-12. Calculated escaped flow rate and capturing efficiency for frog leg geometry

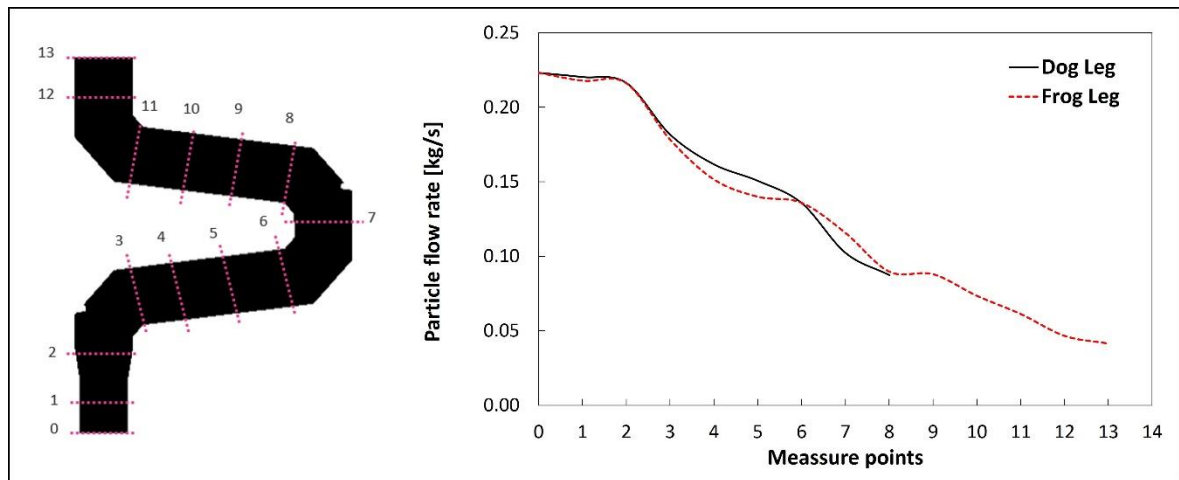


Figure 5-13. Predicted particle track and accretion on the walls for the frog-leg geometry

## 5.7. Further modifications

The positive effect of the bent geometry became evident from the results for both dog-leg and frog-leg configurations. The frog-leg geometry offers more flexibility for additional geometrical variations, as depicted in Figure 5-14. Shortening the upper length reduces the heat loss through the walls, maintaining a higher temperature. This is important to ensure that particles retain their liquid-state to be captured by the walls. The other modification could be adding another bend to the frog-leg to increase the chance of particle capturing.

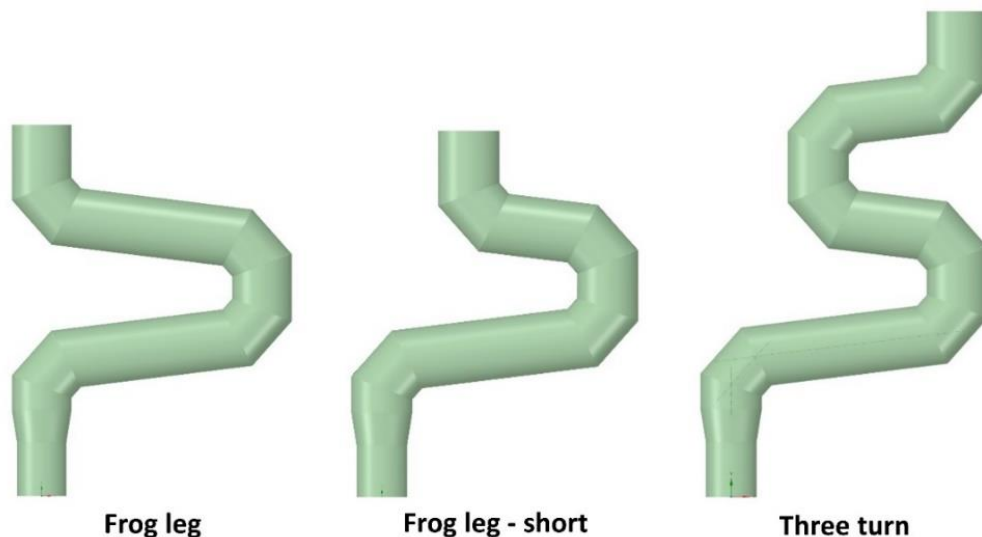


Figure 5-14. further geometrical modification of frog-leg geometry

Figure 5-15 shows the escaped flow rate of particles for each modification presented so far. For “Three turn” geometry, it is assumed that the temperature inside the reflux chamber stays above the solidification temperature. It is worth reiterating

that the temperature profile must be calculated before any geometrical modification to ensure that particles retain their molten-state while traveling inside the reflux chamber.

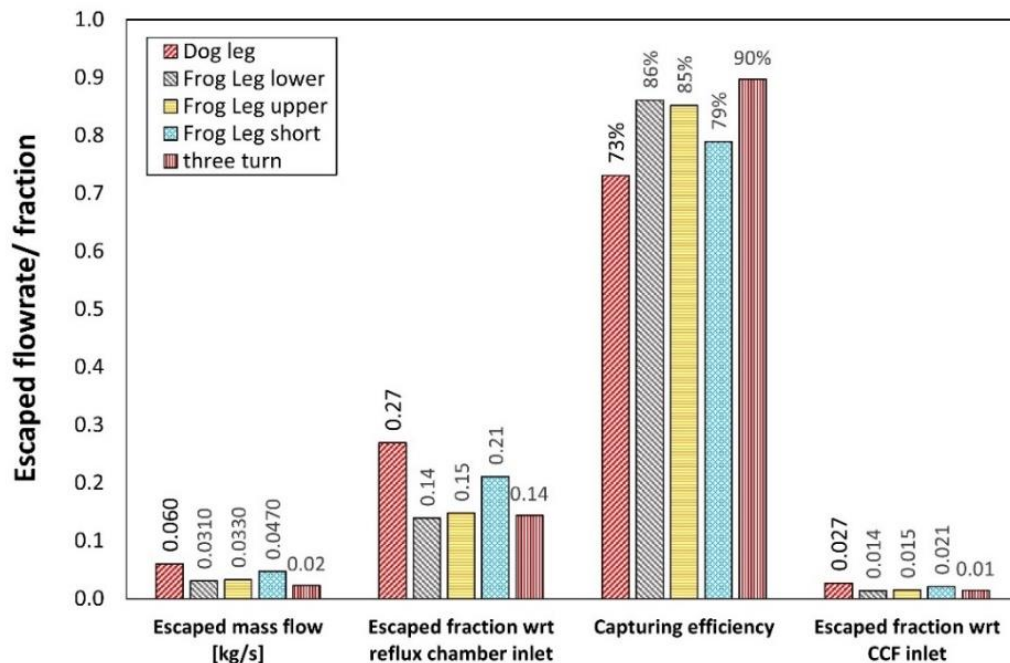


Figure 5-15. Calculated escaped flow rate and capturing efficiency for different reflux chamber geometries

As mentioned before, the HIsarna process is transient with fluctuating temperature and composition profiles at the inlet of the reflux chamber. For example, a slight change in CO composition has a noticeable effect on the temperature profile, as depicted in Figure 5-11. Of course, only one variation of inlet condition is mentioned in this study. During the plant operation, the temperature can vary from 1900 to 2400 K, significantly affecting the temperature and composition profiles inside the off-gas system. Variations in oxygen levels can also alter the profiles within the reflux chamber (see Figure 5-3 for dog-leg geometry). Additionally, the carbon flow rate can be higher than the 0.0283 kg/s considered for all base models. For a more in-depth understanding of the impact of carbon particles, please refer to Chapter 3, Figure 3-21. As presented in Figure 5-11, for low CO content of flue gas entering the reflux chamber, the temperature falls under the solidification temperature, which is the case for both upper and lower oxygen injection.

One solution to ensure a higher temperature within the reflux chamber is to increase the thickness of the refractory wall. Figure 5-16 shows the temperature profile of

frog-leg configuration with upper oxygen injection for different refractory wall thicknesses.

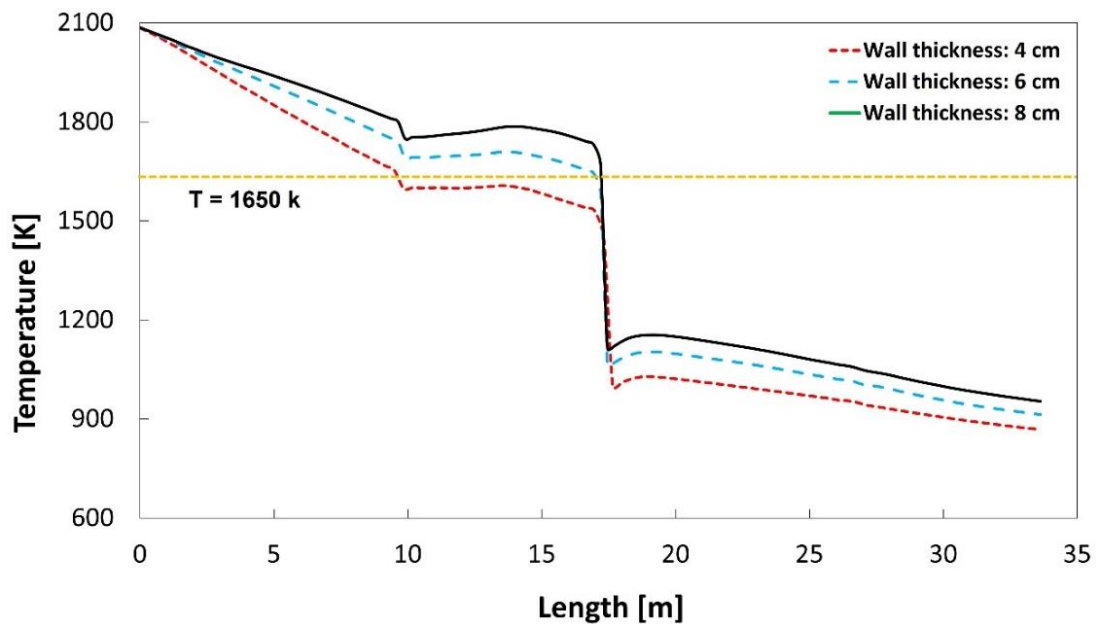


Figure 5-16. Effect of refractory wall thickness on the calculated temperature profile of frog-leg geometry with oxygen upper injection

As can be seen, a thicker wall increases the temperature profile by reducing heat losses through the walls. However, given the harsh conditions inside the reflux chamber (discussed before), the wall is subjected to various thermo-chemical-mechanical stresses that can lead to refractory material loss and gradual thinning of the refractory. As a result, this solution necessitates ongoing monitoring of the wall's condition and, if required, refractory renewal to ensure a consistently high temperature inside the reflux chamber.

## 5.8. Conclusion and future improvement

A basic CFD model to describe the behaviour of partially-reduced molten iron ore is developed and validated using measured data from plant operation. The walls can still capture the molten ore particles escaping from the CCF and entering the reflux chamber. Particles hitting the wall surface create a molten layer which is refluxed to the CCF. The developed model assumes that the particles remain in the liquid-state inside the reflux chamber. This way, once a particle hits the wall, it will be captured and removed from the calculations. The mentioned assumption is valid based on the plant data and temperature profile prediction for different inlet compositions.

Based on the calculated particle trajectories and captured particles on the surface, it was concluded that the bend performs most of the particle capturing. The validated model is utilized to modify the dog-leg configuration to see the possibility of a further increase in capturing efficiency. The proposed modified geometry, called frog-leg, is a simple modification of the original reflux chamber geometry by adding a second bend. Based on the calculations, the capturing efficiency is increased from 73% for the dog-leg configuration to 85% for the modified geometry.

It can be concluded that any proposed geometry must meet two requirements:

1. Since the particle capturing is solely performed by the wall surface, the particles must stay liquid inside the modified reflux chamber.
2. The modified geometry should be designed to provide enough inclination for the formed liquid to flow back to the CCF.

Possible model improvement can be made by considering the effect of velocity and dimensionless numbers such as Weber ( $We$ ) number on particle wall interaction. Many empirical relations and particle-wall interaction criteria exist for common liquids like water. However, there is a lack of experimental and numerical data for high-viscosity and high-density liquid particles, such as slag. Nevertheless, the existing relations can still be useful in avoiding the assumption that the entire wall surface acts as an absolute capturing medium. It is likely that some of the molten particles may bounce off the walls due to their impact velocity and direction.

## References

- [1] M. Mezhericher, T. Brosh, A. Levy, Modeling of Particle Pneumatic Conveying Using DEM and DPM Methods, *Particulate Science and Technology - PARTICULATE SCI TECHNOLOGY*. 29 (2011) 197–208. <https://doi.org/10.1080/02726351003792914>.
- [2] L. Meng, S. Gao, D. Wei, Q. Zhao, B. Cui, Y. Shen, Z. Song, Particulate flow modelling in a spiral separator by using the Eulerian multi-fluid VOF approach, *Int J Min Sci Technol*. 33 (2023) 251–263. <https://doi.org/https://doi.org/10.1016/j.ijmst.2022.09.016>.
- [3] D. dos Santos, S. Baluni, A. Bück, Eulerian Multiphase Simulation of the Particle Dynamics in a Fluidized Bed Opposed Gas Jet Mill, *Processes*. 8 (2020). <https://doi.org/10.3390/pr8121621>.
- [4] G. Zhou, Y. Liu, Y. Kong, Y. Hu, R. Song, Y. Tian, X. Jia, B. Sun, Numerical analysis of dust pollution evolution law caused by ascensional/descensional ventilation in fully mechanized coal mining face based on DPM-DEM model, *J Environ Chem Eng*. 10 (2022) 107732. <https://doi.org/https://doi.org/10.1016/j.jece.2022.107732>.
- [5] P. Chang, G. Xu, F. Zhou, B. Mullins, S. Abishek, Comparison of underground mine DPM simulation using discrete phase and continuous phase models, *Process Safety and Environmental Protection*. 127 (2019) 45–55. <https://doi.org/https://doi.org/10.1016/j.psep.2019.04.027>.
- [6] M. Thiruvengadam, Y. Zheng, J.C. Tien, DPM simulation in an underground entry: Comparison between particle and species models, *Int J Min Sci Technol*. 26 (2016) 487–494. <https://doi.org/https://doi.org/10.1016/j.ijmst.2016.02.018>.
- [7] H. Zhang, L. Fava, M. Cai, N. Vayenas, E. Acuña, A hybrid methodology for investigating DPM concentration distribution in underground mines, *Tunnelling and Underground Space Technology*. 115 (2021) 104042. <https://doi.org/https://doi.org/10.1016/j.tust.2021.104042>.
- [8] P. Chang, G. Xu, J. Huang, Numerical study on DPM dispersion and distribution in an underground development face based on dynamic mesh, *Int J Min Sci Technol*. 30 (2020) 471–475. <https://doi.org/https://doi.org/10.1016/j.ijmst.2020.05.005>.
- [9] P. Chang, G. Xu, F. Zhou, B. Mullins, S. Abishek, D. Chalmers, Minimizing DPM pollution in an underground mine by optimizing auxiliary ventilation systems using CFD, *Tunnelling and Underground Space Technology*. 87 (2019) 112–121. <https://doi.org/https://doi.org/10.1016/j.tust.2019.02.014>.
- [10] R. Morla, A. Godbole, S. Karekal, R.M. Bhattacharjee, N. Balasubrahmanyam, Fundamental understanding of diesel-operated man riding vehicle DPM dispersion – A case study, *Journal of Sustainable Mining*. 17 (2018) 105–110. <https://doi.org/https://doi.org/10.1016/j.jsm.2018.04.004>.
- [11] B. Oyegbile, G. Akdogan, M. Karimi, Modelling the Dynamics of Granular Particle Interactions in a Vortex Reactor using a Coupled DPM-KTGF Model, *S Afr J Chem Eng*. 34 (2020) 31–46. <https://doi.org/https://doi.org/10.1016/j.sajce.2020.05.008>.
- [12] S. Somwangthanoj, S. Fukuda, CFD modeling of biomass grate combustion using a steady-state discrete particle model (DPM) approach, *Renew Energy*. 148 (2020) 363–373. <https://doi.org/https://doi.org/10.1016/j.renene.2019.10.042>.
- [13] H.A. Petit, C.I. Paulo, O.A. Cabrera, E.F. Irassar, Modelling and optimization of an inclined plane classifier using CFD-DPM and the Taguchi method, *Appl Math Model*. 77 (2020) 617–634. <https://doi.org/https://doi.org/10.1016/j.apm.2019.07.059>.

- [14] R. Li, Z. Sun, A. Li, Y. Li, Z. Wang, Design optimization of hemispherical protrusion for mitigating elbow erosion via CFD-DPM, *Powder Technol.* 398 (2022) 117128. <https://doi.org/https://doi.org/10.1016/j.powtec.2022.117128>.
- [15] L. Stone, D. Hastie, S. Zigan, Using a coupled CFD – DPM approach to predict particle settling in a horizontal air stream, *Advanced Powder Technology.* 30 (2019) 869–878. <https://doi.org/https://doi.org/10.1016/j.appt.2019.02.001>.



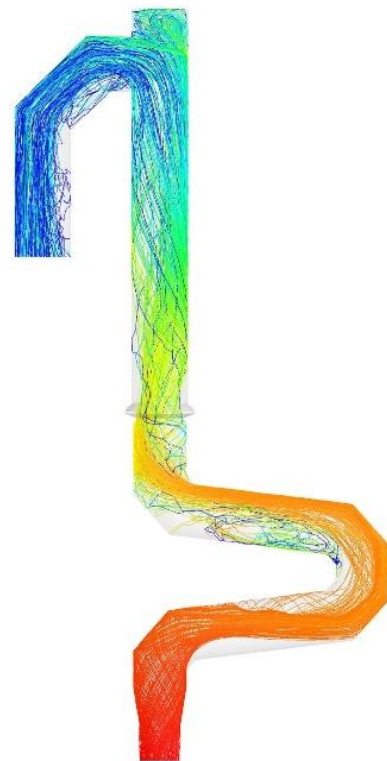
# Chapter 6

## FLOW ANALYSIS OF MODIFIED REFLUX CHAMBER

**This chapter is based on the following paper:**

Ashkan Hosseini, Vinod Dhiman, Koen Meijer, Christiaan Zeilstra, Johannes Hage, Tim Peeters, Erik Offerman & Yongxiang Yang (2022), **CFD modelling of the off-gas system HISarna iron making process part 2: reflux chamber geometry modification and effects on flow behaviour**, *Ironmaking & Steelmaking*, 49:8, 783-794, DOI: 10.1080/03019233.2022.2060457

**In this chapter, the focus will be on the effect of frog-leg geometry on the fluid behaviour and operating conditions inside the off-gas system. As mentioned in Chapter 5, the performed geometrical modification increases the capturing efficiency of the escaped iron ore particles injected into the main HISarna. It is important to understand the effect of this modification on heat loss, temperature profile, carbon conversion, and gaseous phase composition. The same model developed for “dog-leg” geometry is used to investigate the above-mentioned parameters for the modified geometry. It is shown that “frog-leg” geometry leads to a higher heat loss through the reflux chamber walls, which can change the temperature profile and consequently local species composition of the off-gas. The “frog-leg” geometry also allows for injecting oxygen at different elevations. The simulation results indicate that injecting oxygen at the lower part of the “frog-leg” can increase the carbon combustion rate and reduce CO escaping the reflux chamber to the air quench section of the off-gas system.**



## 6.1. Introduction

As mentioned in the introduction chapter, fine iron ore and pure oxygen are injected into the CCF. The oxygen is needed as an oxidizer to partly combust the CO-H<sub>2</sub> mixture from the Smelting Reduction Vessel (SRV). The combustion process provides heat to pre-reduce and melt the iron ore during the flight time and ultimately deposited against the wall of the furnace. The accumulation of the molten particles on the wall creates a liquid film that drips along the wall and falls into the SRV's molten iron bath.



Figure 6-1. Scheme of current reflux chamber installation

During the fly time, a portion of the injected ore is carried away by the flue gas and escapes the CCF. Plant measurements and model predictions indicate that nearly 10% of the ore injected into the CCF escapes and enters the off-gas system. In the previous design, the off-gas system consisted of a straight vertical pipe with an incinerator for burning unwanted compounds. As previously mentioned, the design has been altered, and a special component has been introduced to the system, known as the reflux chamber.

This modification fulfills two important tasks:

- Post-combusting of the remaining CO and H<sub>2</sub> from CCF by injecting O<sub>2</sub> and eliminating the downstream incinerator.

- Capturing the particles using the added bend and horizontal section (reflux chamber). Once the molten pre-reduced ore particles are carried with flue gas, they hit the upper wall of the reflux chamber and form a film that can flow back to the CCF and then SRV. This material remains liquid as the temperature at the reflux chamber remains high (for most of the length) and above the melting point of pre-reduced ore.

The current reflux chamber geometry is called “Dog-Leg” and is capable of increasing the capturing efficiency of the escaped particles from the CCF. Further increase in capturing efficiency can be achieved by modifying the dog-leg and adding a second bend. The modified geometry is called “Frog-Leg” (see Figure 6-2.C).

The CFD model for dog-leg geometry is used to investigate the off-gas system performance with frog-leg configuration for the reflux chamber.

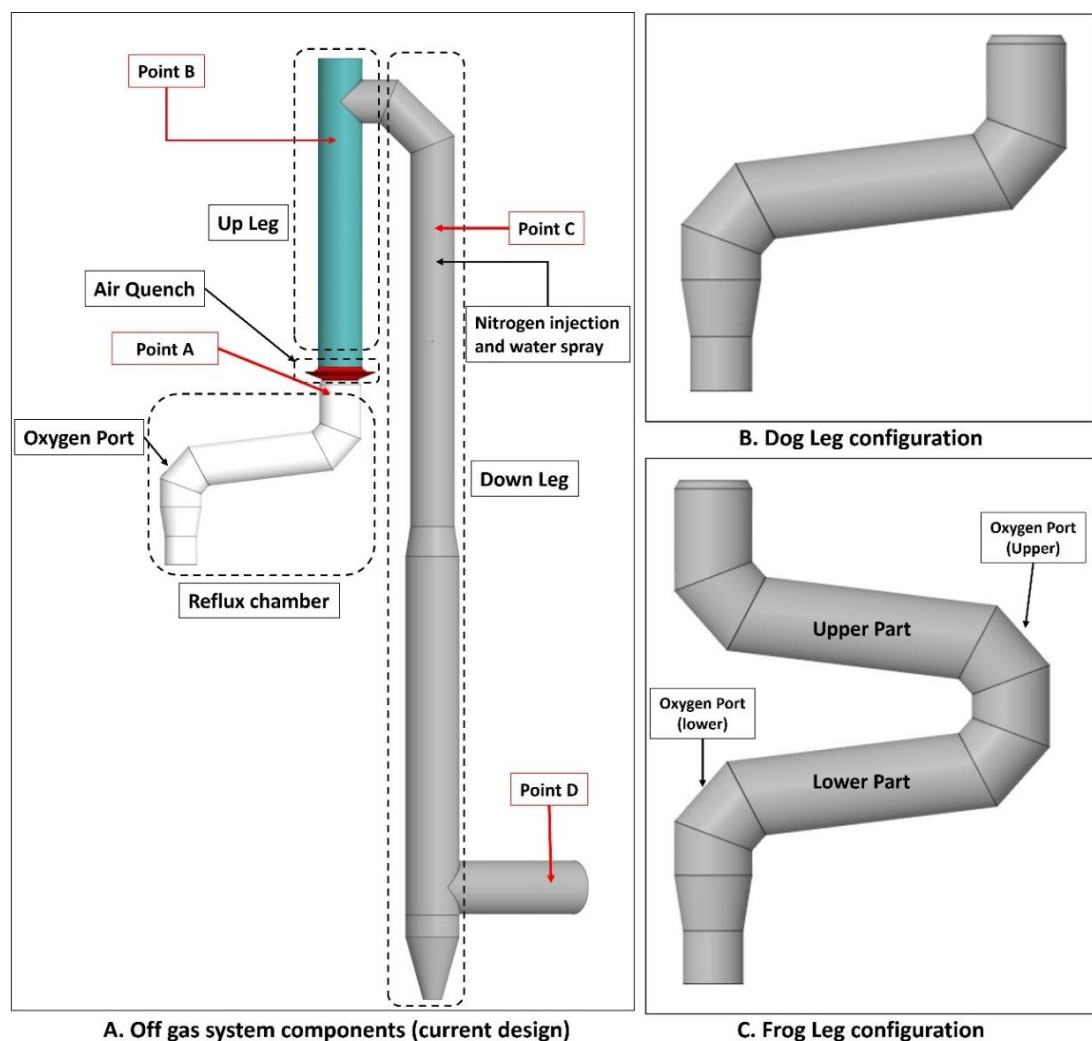


Figure 6-2. Off-gas system components and data acquisition points

## 6.2. Temperature and composition profiles

Figure 6-3 shows the temperature and composition profile for dog-leg and frog-leg geometry.

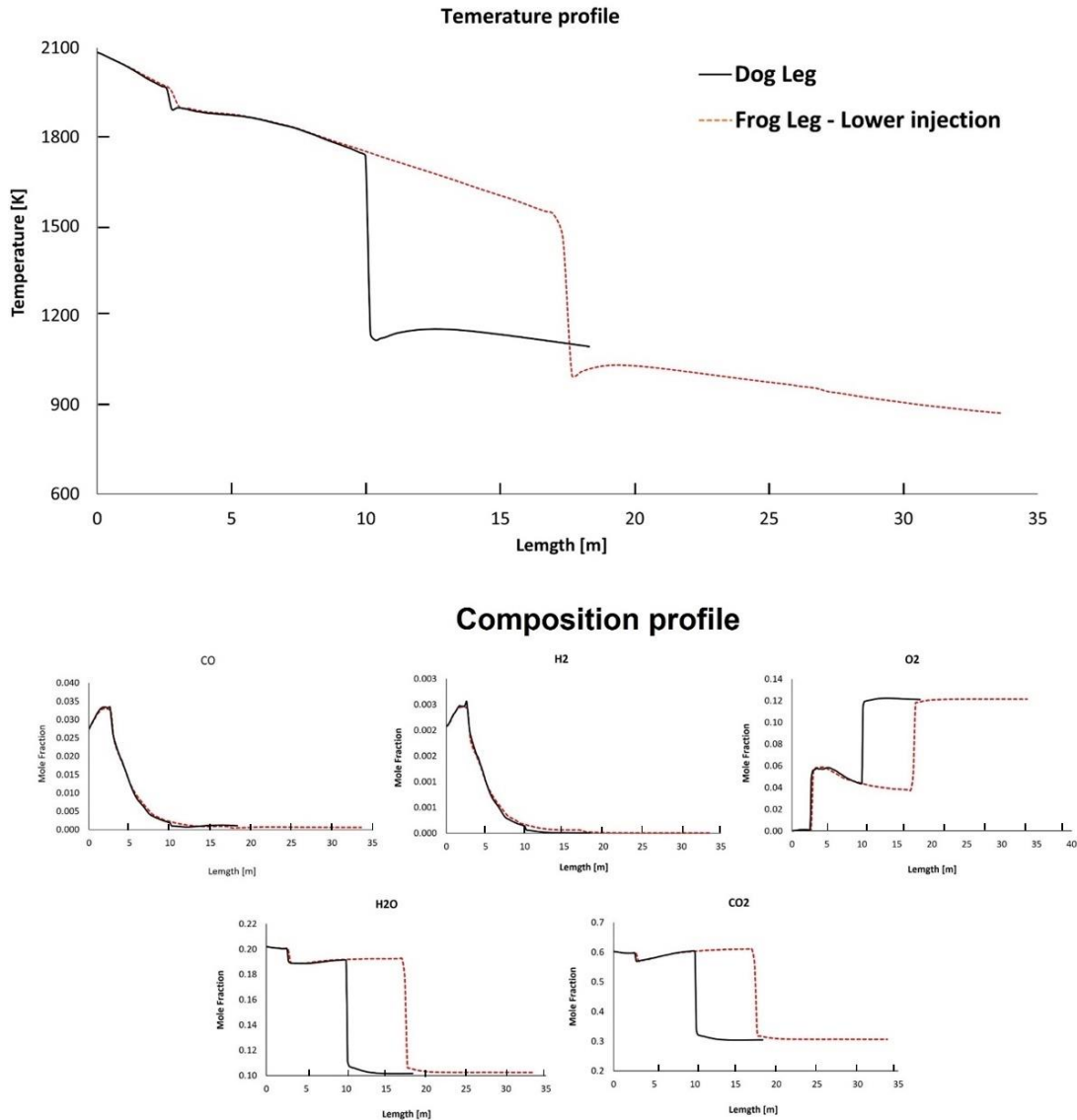


Figure 6-3. Temperature and composition profile for off-gas system – model prediction for “dog-leg” and “frog-leg” geometry from inlet to Point C

The oxygen injection position is the same as in dog-leg geometry (lower position), and as can be seen, the profile trends are the same at the beginning of the reflux chamber length. In the frog-leg geometry, the temperature reduction continues, and the flue gas enters the air quench section at a significantly lower temperature, with a difference of 210°C, primarily because of the higher heat loss in the reflux chamber (Figure 6-5). As shown in Figure 6-2.C, injecting oxygen at two different elevations

using the frog-leg design is possible. Figure 6-4 illustrates the temperature and composition profile for different positions of the oxygen injection inside the frog-leg geometry. From these graphs, a major difference can be seen between the two designs. Once the oxygen is injected at the lower part, the temperature stays higher inside the reflux chamber (compared to the upper injection).

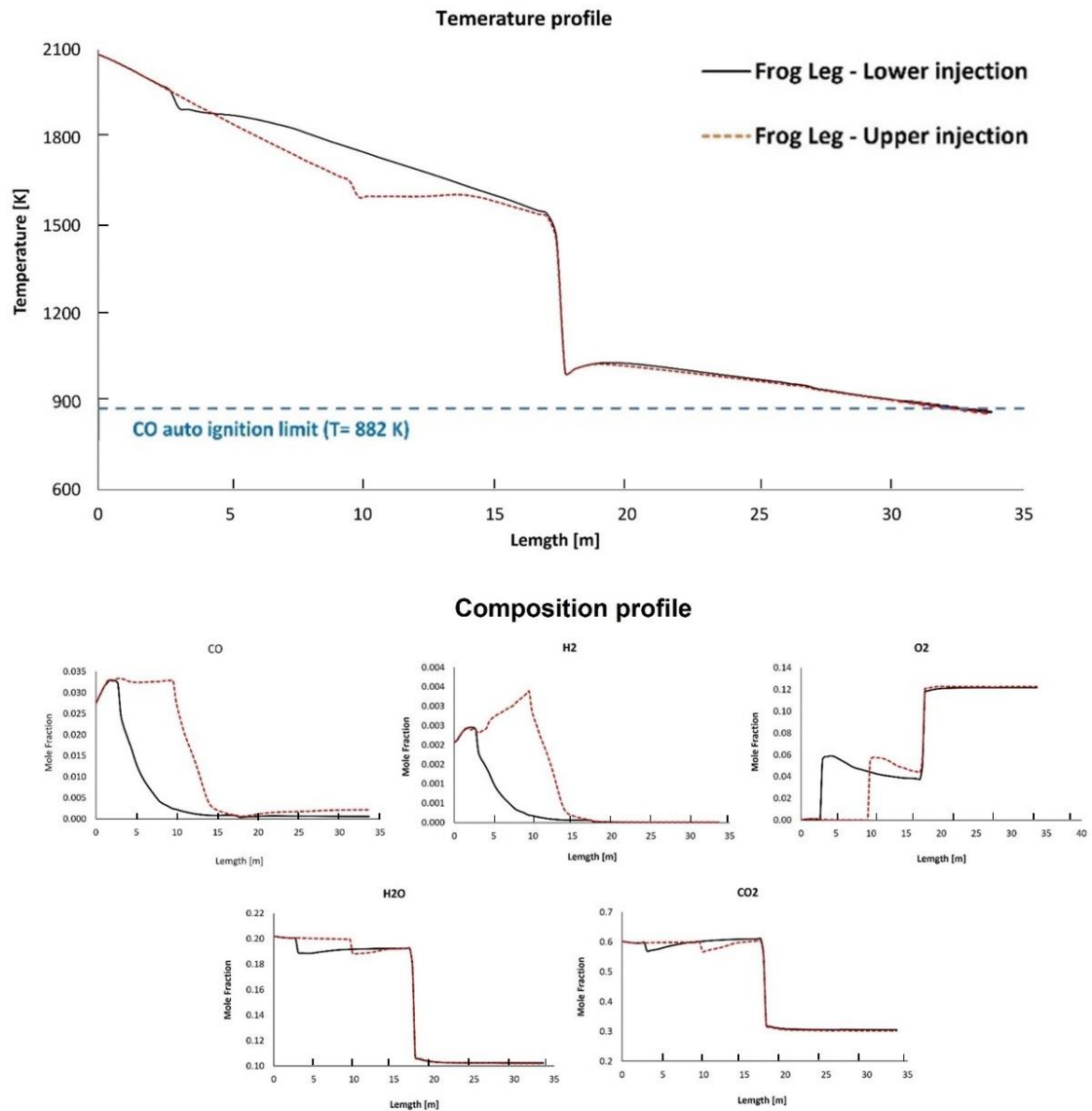


Figure 6-4. Temperature and composition profiles for the off-gas system – model prediction for “frog-leg” geometry with different oxygen injection levels – from inlet to Point C

This is an advantage since CO and carbon will be combusted at a higher rate at higher temperatures. Ultimately, both designs lead to the same temperature at the reflux chamber outlet (also at points B and C) and similar heat losses, as presented in Figure 6-5. The modified design leads to a lower average temperature at various measuring points than the dog-leg design due to higher wall heat loss.

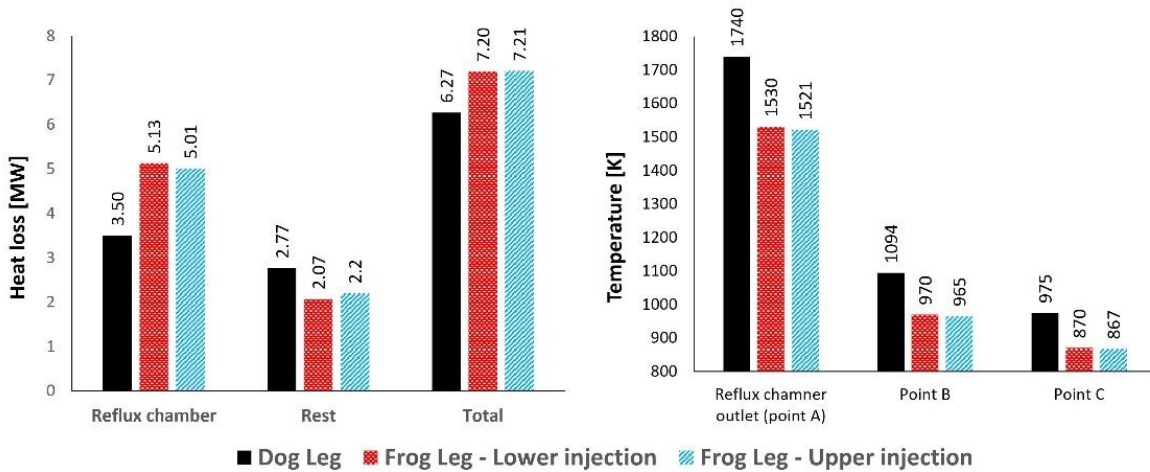


Figure 6-5. Calculated heat loss (left) and temperature at different measurement points (right) for different designs

When oxygen is injected at the upper region, unwanted CO and H<sub>2</sub> combustion is delayed in the lack of oxygen at the lower part of the reflux chamber. An increase of CO and H<sub>2</sub> is observed at the lower part as carbon can react with H<sub>2</sub>O and CO<sub>2</sub> to produce H<sub>2</sub> and CO, respectively.

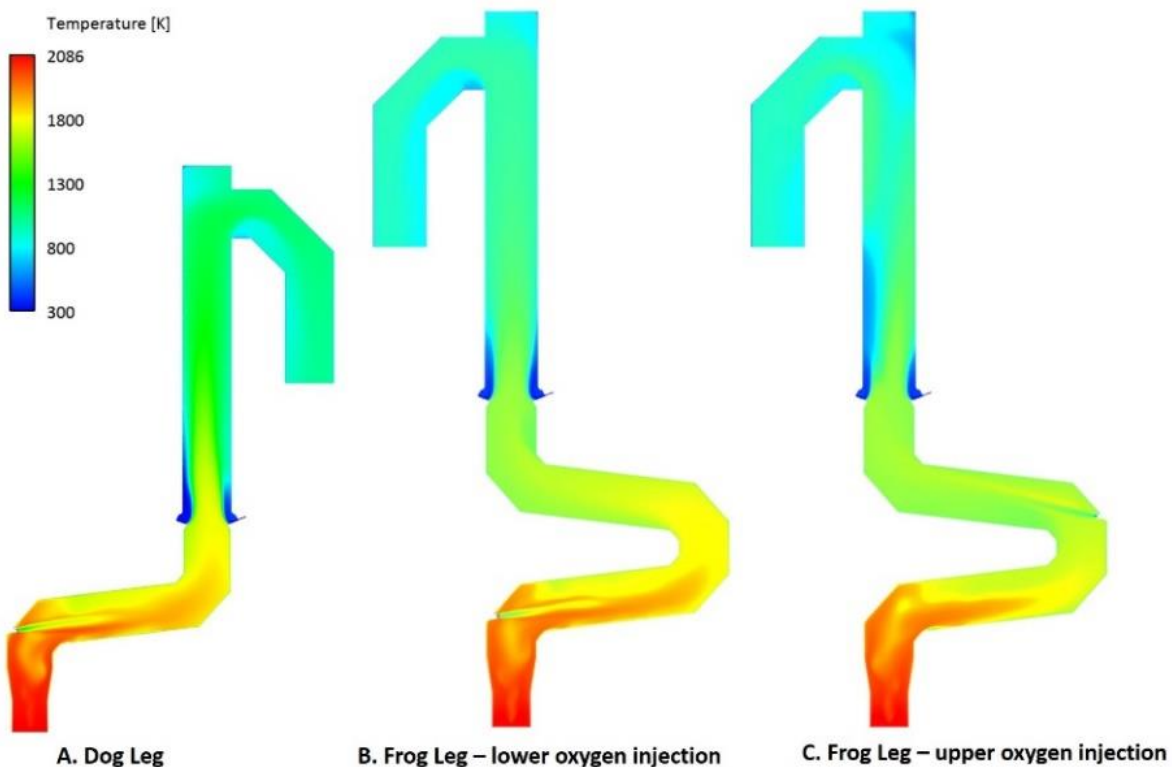


Figure 6-6. Temperature contours for different off-gas design



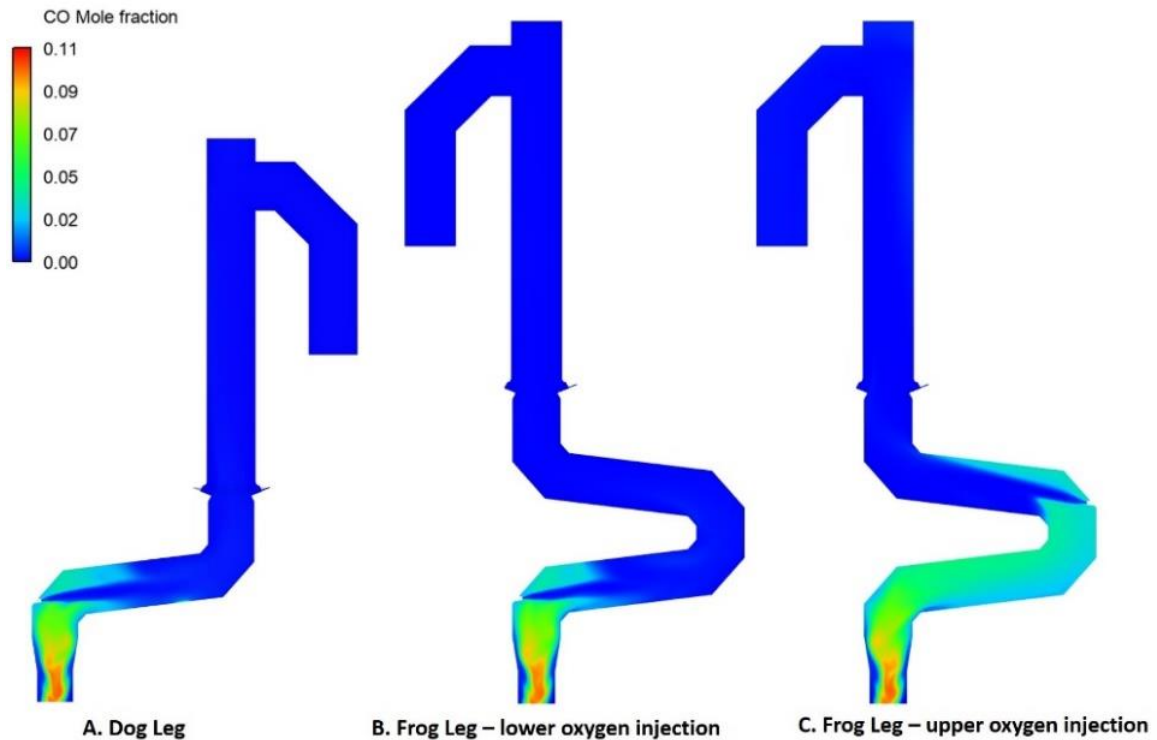


Figure 6-7. CO contours for different off-gas design

### 6.3. Carbon and CO conversion

As mentioned before, the frog-leg geometry with varying oxygen injection positions exhibits distinct CO mole fraction profiles along the length of the reflux chamber.

For the case with lower injection, the oxygen is injected at an early stage (3 m from the inlet), and the combustion of CO and carbon particles proceeds immediately after entering the reflux chamber. Because of the longer length compared to the dog-leg geometry, the unwanted species will have a higher residence time inside the reflux chamber and mix for a longer time with the flue gas. This will increase CO and carbon conversion inside the reflux chamber, as reported in Figure 6-9 at different measurement points.

Species conversion is defined as:

$$conversion = \frac{m_{in} - m_L}{m_{in}}$$

where  $m_{in}$  and  $m_L$  are species mass flow rates at the inlet and random location of the reflux chamber, respectively.

This conclusion can also be seen in Figure 6-10, where the carbon particle track, coloured by particle diameter, is shown. Notably, carbon particles in the frog-leg geometry reach their minimum diameter at a shorter length compared to the dog-leg geometry.

The other option is injecting oxygen at the upper level of the reflux chamber. In this case, the combustion and conversion of CO and carbon particles with oxygen is delayed. However, the carbon conversion still proceeds by reacting with H<sub>2</sub>O and CO<sub>2</sub>, and a negative conversion (increase in flow rate from 91 g/s to 110 g/s) of CO is predicted. The maximum conversion of carbon particles before reaching the oxygen port (length: 9.5 m) is 20%, with a reduced flow rate from 28.2 g/s to 23 g/s.

Due to the heat loss through the wall and the endothermic reaction of carbon particles with the H<sub>2</sub>O-CO<sub>2</sub> mixture, the temperature constantly decreases and reaches as low as 1650 K before mixing with oxygen at the injection point. Notably, the temperature increase upon mixing with oxygen is significantly lower compared to the lower injection scenario, where the flue gas and oxygen mix at a temperature of 1945 K. Therefore, carbon reaction with oxygen inside the reflux chamber is performed at a lower temperature for the upper injection case, leading to a lower reaction rate and conversion (52%), as depicted in Figure 6-8, which is 35% less than the lower injection case.

The escaped carbon enters the air quench at a low temperature where the flue gas is further quenched. Carbon particles will still react with oxygen (and H<sub>2</sub>O-CO<sub>2</sub> mixture) to produce CO. But, the reaction rate of CO combustion is low due to a lower temperature in up/down-leg; hence, the CO consumption rate will be lower than the production rate, and the accumulation of CO will occur.

Also, a complete conversion of carbon is not predicted, even though the flow rate is constantly decreasing, and ultimately, 8% of carbon particles enter point C and inside the water-quenched zone. The increase in CO flow rate can be seen in Figure 6-8 and Figure 6-9 (decreasing conversion profile). As reported in Figure 6-9, the flow rate of CO and carbon is higher for other designs at point C before entering the water-quenched zone. Further conversion of CO cannot happen since the flue gas temperature falls below the auto-ignition temperature of CO (882 K) before reaching Point C, as shown in Figure 6-4. This is true for both frog-leg cases, but for



dog-leg design, the temperature is still higher than the auto-ignition temperature, and CO conversion proceeds even after Point C.

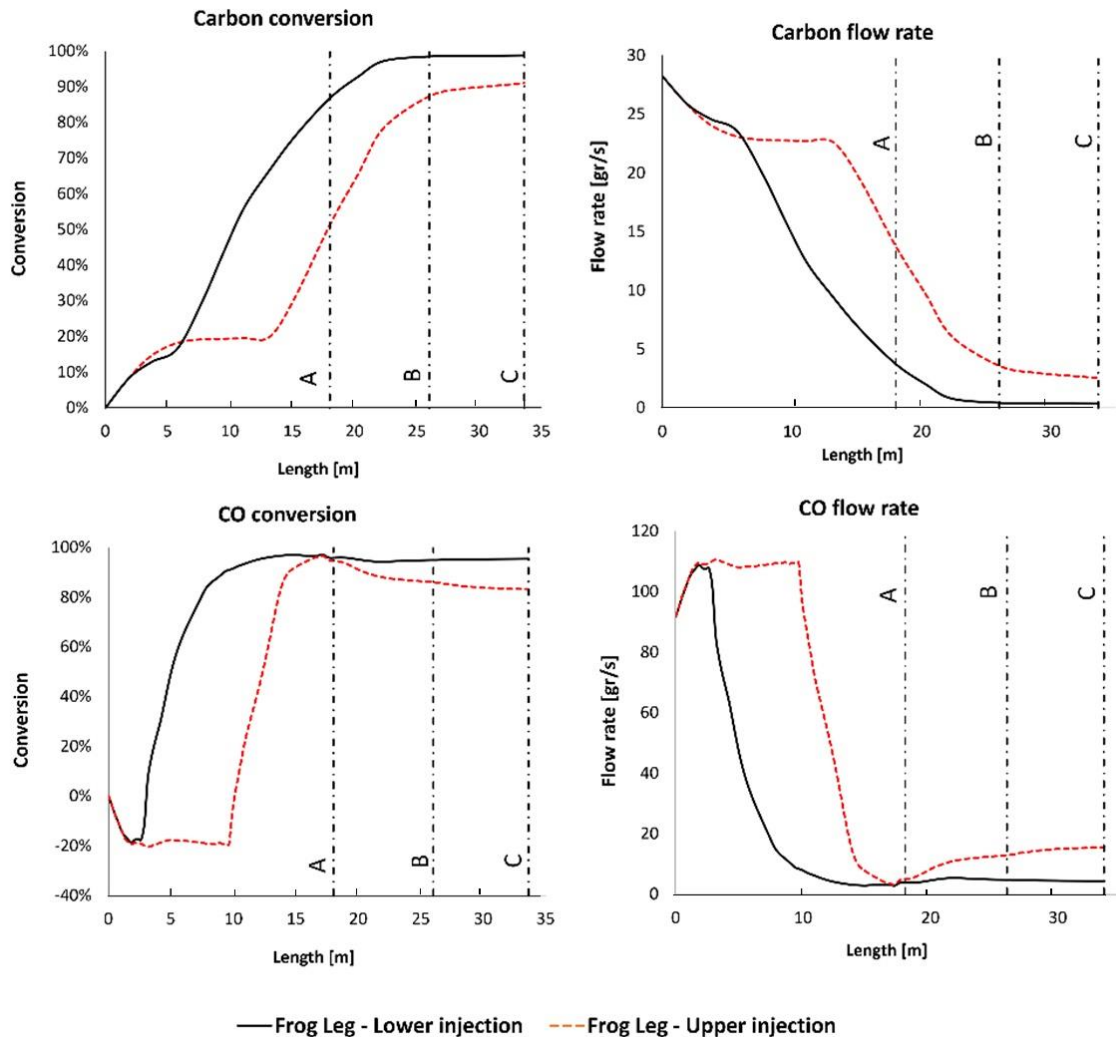


Figure 6-8. CO, carbon, conversion, and flow rate profile along the off-gas system length for “Frog Leg” geometry. (Points A, B, and C are shown). Positive conversion means consumption, and negative means the production of species.

For the case with lower oxygen injection, the escaped fraction of carbon from the reflux chamber is much lower (13% compared to 48% for upper injection), and CO conversion is already 96%. Due to a lower carbon emission from the reflux chamber, the produced CO inside the up/down-leg is insignificant and safely combusted with 95% conversion. The carbon reaches full conversion at Points B and C, as reported in Figure 6-9 and visualized in Figure 6-10.

To sum up, the reflux chamber performance is vital to the overall system performance regarding the unwanted species removal. It is desired to perform all possible removal inside the reflux chamber and at a high temperature.

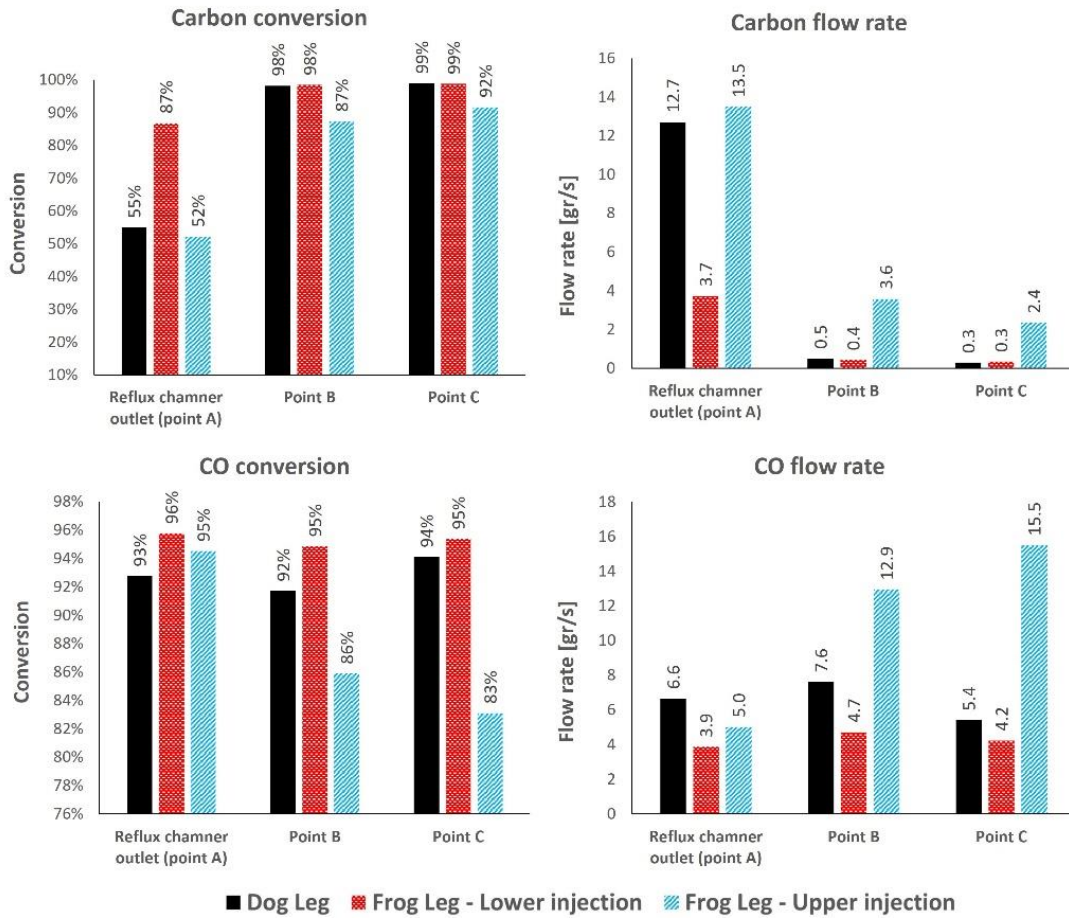


Figure 6-9. CO and carbon, conversion and flow rate at different measurement points for different design

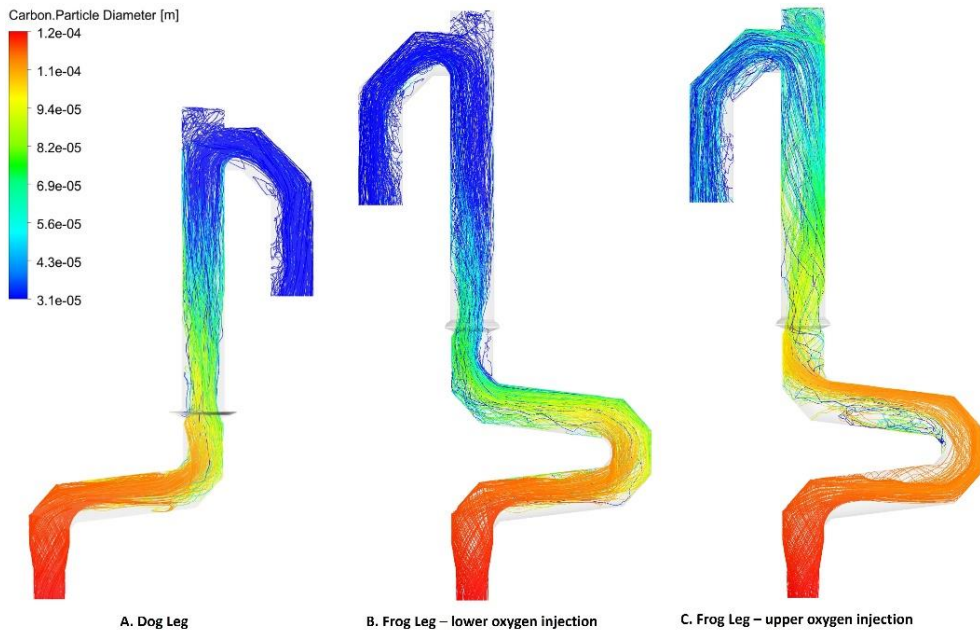


Figure 6-10. carbon particle tracks coloured by particle diameter for different off-gas design

It is important to reach maximum CO and carbon combustion (preferably full combustion) before Point C to avoid any leakage of unwanted species into the water-

quenched zone. Based on the model predictions, the frog-leg geometry with lower oxygen injection can achieve this scenario with maximum CO and carbon conversion.

## 6.4. Further modification of frog-leg geometry

As discussed, the frog-leg design with upper oxygen injection leads to CO and carbon particle emission into the water-quenched zone. However, further modification makes it possible to reach a better or the same performance as other designs.

This can be acquired by keeping the temperature as high as possible inside the reflux chamber. One possible solution is decreasing the heat loss inside the reflux chamber by increasing the refractory wall thickness. A set of simulations is performed to investigate the effect of wall thickness on the reflux chamber performance for frog leg geometry with upper oxygen injection.

Figure 6-11 shows the temperature, CO, and carbon profiles for conversion and flow rate. As derived from both profiles, increasing wall thickness will improve the isolation quality of the walls, thus raising the local temperature inside the reflux chamber. This will lead to a higher consumption rate and lower emission of CO and carbon into regions with low temperatures. The carbon conversion inside the reflux chamber increases from 51% for the original thickness to 60% and 74% for 6 and 8 cm of wall thickness, respectively (see Figure 6-12). Since the temperature is still high for thicker refractory walls, a full conversion of carbon is predicted before reaching Point C for both increased thicknesses. Carbon monoxide conversion is high, around 95% for all cases, at the outlet of the reflux chamber. However, it remains high only for wall thickness of 8 cm, and it is as low as 86% and 83% for 6 and 4 cm of wall thickness due to a higher carbon emission from the reflux chamber. The emitted carbon will still be converted to CO, but the CO conversion rate will be low with a lower temperature inside the up/down-leg.

The same modification can also be performed for frog-leg geometry with lower oxygen injection to reach the maximum possible conversion of the unwanted species (not presented here). Increasing the temperature inside the reflux chamber will offer another benefit. As mentioned before, the reason for modification from dog-leg to frog-leg geometry is mainly increasing particle capturing efficiency. Once molten

ore particles (escaped from CCF) hit the wall, they form a liquid surface that flows back into the CCF. The particles need to remain in the liquid phase (or semi-liquid) to be captured by the wall.

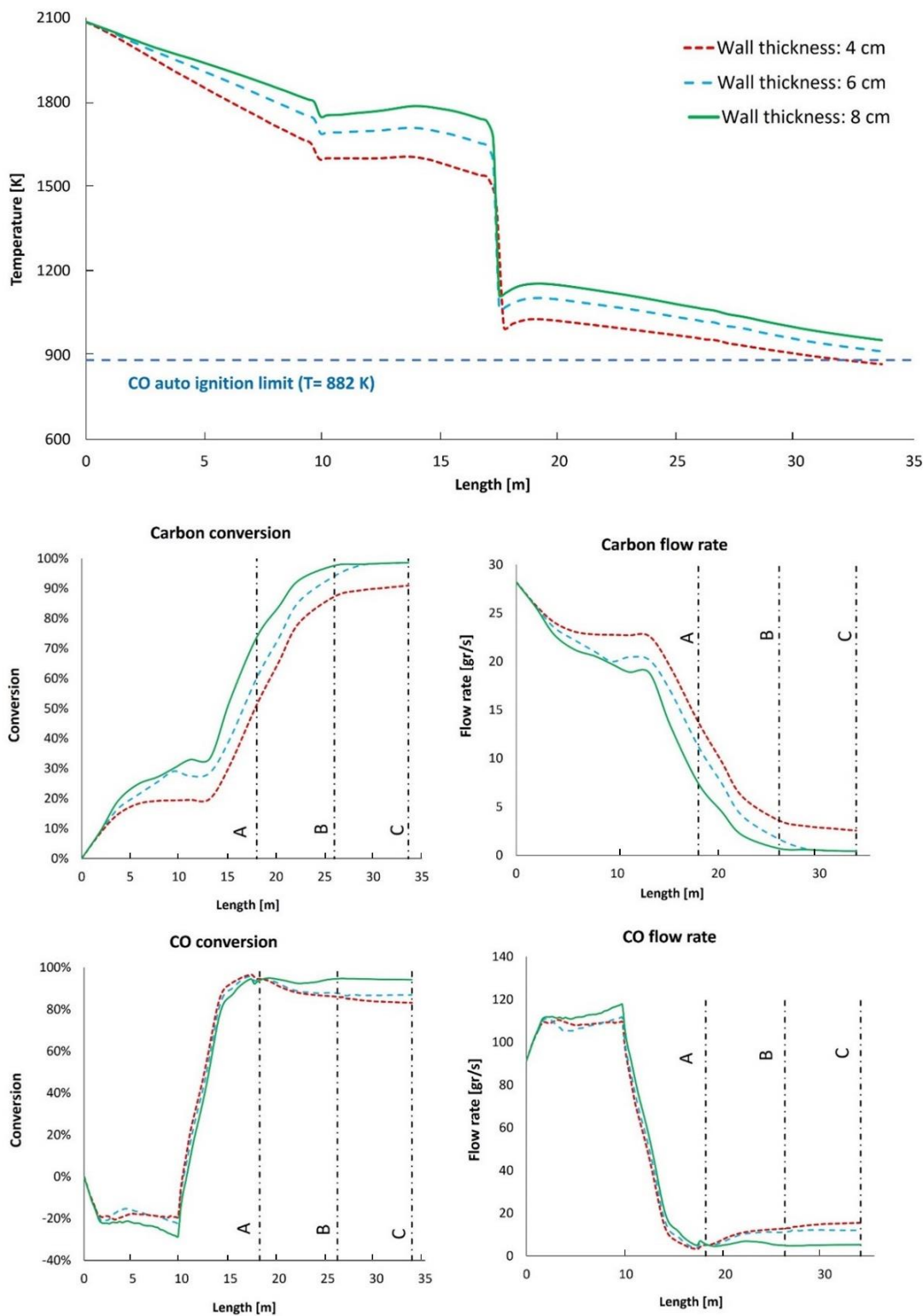


Figure 6-11. Effect of wall thickness on temperature and composition profile for frog-leg geometry with upper oxygen injection

Particles in solid-state bounce off the wall with a much lower chance of being captured. The physical state of individual particles can be liquid, semi-liquid, or solid, depending on the composition. The injected particles to CCF are mainly composed of  $\text{Fe}_2\text{O}_3$ , which is reduced to  $\text{Fe}_3\text{O}_4$  and  $\text{FeO}$ . The predicted temperature of 1723 K to 1872 K (the melting temperature of pure  $\text{Fe}_3\text{O}_4$ ) is needed for the semi-liquid or liquid-state of iron ore.

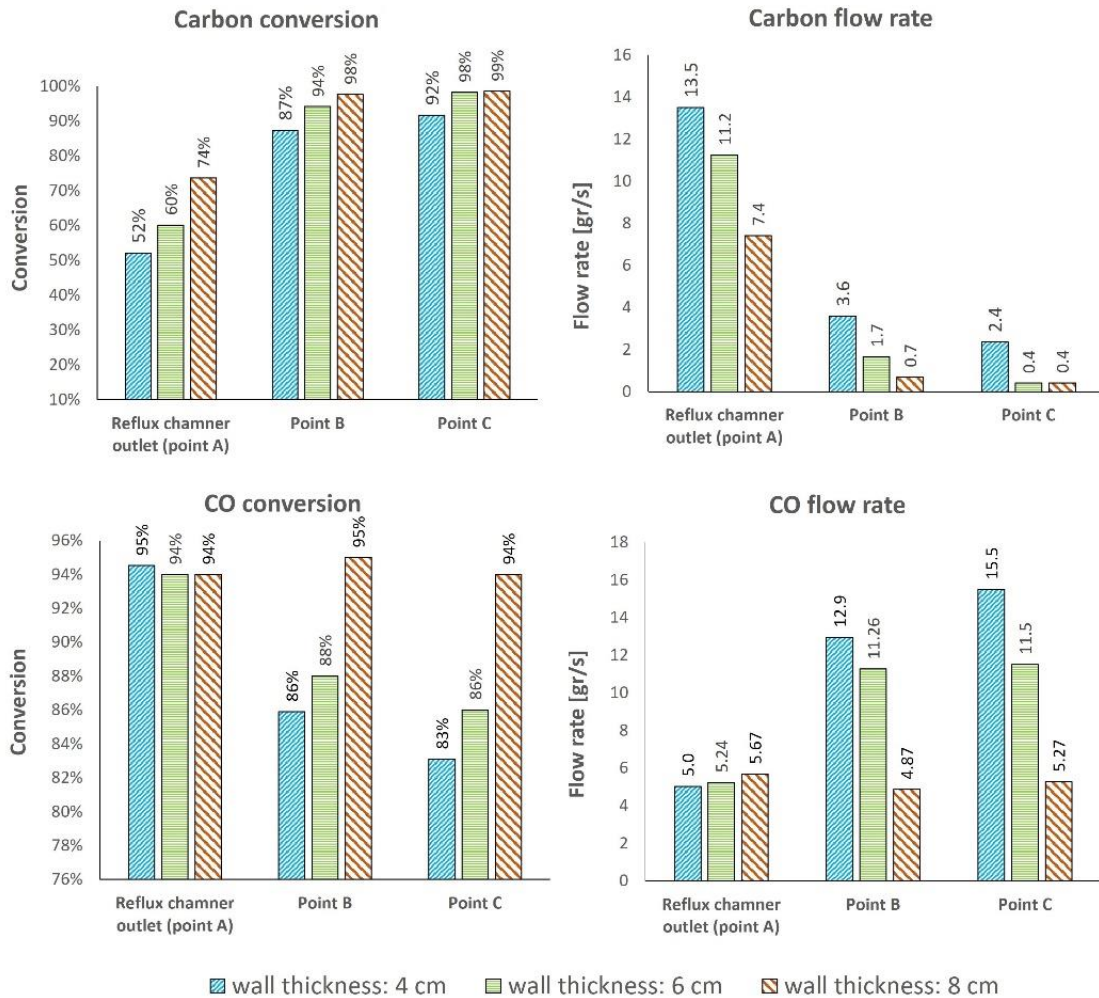


Figure 6-12. CO and carbon, conversion, and flow rate at different measurement points for different wall thicknesses.

If the maximum temperature is considered here, with the original design of the dog-leg (with a wall thickness of 4 cm), the temperature falls under 1872 K halfway through the reflux chamber length (around 5.9 meters). This length is 4.8 and 5.8 meters for frog-leg design with upper and lower oxygen injection, respectively. Considering the longer length of the reflux chamber for frog-leg design and based on the predicted temperature profiles, most of the wall length will not capture any

particles. Therefore, increasing wall thickness will put more of the reflux chamber volume above the maximum melting temperature of particles to increase the capturing efficiency of the walls.

## 6.5. Conclusion

A CFD model is developed to study the HIsarna off-gas system. The model is validated and used for further modification of the reflux chamber. The geometry of the reflux chamber is changed from “dog-leg” to “frog-leg” geometry by adding another bent at the upper section of the chamber before the air quench section. The modification offers great potential for increasing the capturing efficiency of the pre-reduced iron ore particles escaping from the CCF. In this chapter, the effect of this modification on CO and carbon conversion and the general impact on the temperature and gas composition profiles is investigated without focusing on the particle capturing effect. It is possible to inject oxygen at different positions in the reflux chamber (frog-leg geometry). The frog-leg geometry can noticeably affect the parameters and profiles depending on the oxygen injection position. Injecting oxygen at a lower level leads to the best performance with the highest carbon and CO conversion inside the reflux chamber and upstream compared to the dog-leg geometry. However, once the oxygen is injected at the upper level, a low conversion of unwanted species is predicted in the whole off-gas system. This is mainly due to a lower local temperature inside the reflux chamber, leading to a lower CO-carbon mixture conversion rate. The unreacted portion enters the low-temperature regions and ultimately reaches sections where the temperature falls under the auto-ignition point of CO with no further conversion. By observing this result, it can be concluded that reflux chamber performance plays an important role in the whole off-gas system performance.

The mentioned issue with the upper injection design could be addressed by increasing the wall thickness inside the reflux chamber. This simple modification will reduce the heat loss through the walls and increase the local temperature across the reflux chamber. Higher temperature leads to an increased rate of CO and carbon conversion inside the reflux chamber and, consequently, lower emission of these species into those regions with low temperatures.



# Chapter 7

## ZINC FERRITE FORMATION IN HISARNA OFF-GAS SYSTEM

**This chapter is based on the following paper:**

Ashkan Hosseini, Elmira Moosavi-Khoonsari, Koen Meijer, Johannes Hage, Tim Peeters, Erik Offerman & Yongxiang Yang (2022) **Thermodynamic analysis of zinc ferrite ( $ZnFe_2O_4$ ) formation inside the HISarna off-gas system**, Ironmaking & Steelmaking, DOI: 10.1080/03019233.2022.2124491

Pilot plant operation has shown that a high raw materials versatility characterizes the HISarna reactor and is therefore attractive for processing secondary ferrous sources. Zinc-bearing material has drawn particular attention among the materials that can be recycled through HISarna. During the fourth HISarna campaign in 2014, a test was performed where ferrous dust containing zinc (Zn) was injected into the HISarna together with iron ore, and it was demonstrated that it was possible to enrich Zn up to 16% into the HISarna off-gas dust. The objective is to achieve an enrichment level of Zn in the HISarna dust to make it suitable for direct reuse in Zn smelting as a secondary source complementing Zn ore (the primary source). In this context, Zn oxide (ZnO) is a favorable product of zinc element reaction with other components. Due to the presence of molten slag in the dust (containing iron oxide), Zn vapor can go through another route to form zinc ferrite ( $ZnFe_2O_4$ ), which is an undesired product for zinc smelters. It is important to understand how the process conditions and parameters should be controlled to minimize the ferrite formation and maximize the free ZnO formation. Hence, the main focus of this study is to identify the spots in the HISarna off-gas system where there is a high potential for  $ZnFe_2O_4$  formation using thermodynamic analysis (FactSage) and computational fluid dynamic (CFD) tools. It was concluded that favorable spots for  $ZnFe_2O_4$  formation are locations with low temperature, high partial pressure of oxygen, and high concentration of iron oxide particles. These spots are detected, and proper geometrical modification of the off-gas system is proposed to minimize or delay the formation of unwanted zinc ferrite.

## 7.1. Introduction

**Z**inc (Zn) industry demands Zn ore at an acceptable price but is also very interested in secondary resources to offset the need for prime ores. The availability of prime Zn ore and concentrates is declining and, therefore, driving up the prices. Thus, there is an increasing interest in suitable secondary resources of Zn concentrates. One feasible way is to extract Zn from by-products and waste streams and reuse it for Zn production. This can reduce the need for landfilling or even open the possibility of processing the contents of existing landfills and tailings, ultimately reducing their environmental impacts and contributing to the circular economy.

The steel industry produces large volumes of zinc-coated (galvanized) products, which can be easily recycled via the electric arc furnace (EAF) route. In this route, scrap is charged into the furnace and heated using an electric arc. The charged material is melted to form slag and metal layers while Zn is vaporized and, along with slag particles, forms a fume (also known as dust) that escapes from the top space [1]. The EAF dust is rich in Zn, generally in the order of 7% to 40%, depending on the zinc content of the utilized scrap [2–6]. Havlik et al. [7] have reported an average of 22% Zn content based on a review of 19 different experimental resources with minimum and maximum of 13% and 39%, respectively.

During the EAF process, the Zn element can speciate into either zinc oxide (ZnO) or zinc ferrite ( $\text{ZnFe}_2\text{O}_4$ ) compound. If the amount of ZnO in the dust is high enough, it can be directly used in the zinc smelting process to produce pure metallic Zn. However, the presence of  $\text{ZnFe}_2\text{O}_4$  and iron oxide compounds (on average 31% [7]) in the dust does require an additional processing step (pyro and hydrometallurgical routes) to enrich ZnO content before it is suitable for smelting application [1, 2, 8]. The most common routes are pyrometallurgical routes such as the Waelz kiln process, which are characterized by high Zn recovery efficiency but high energy consumption and pollutant emission. On the other hand, hydrometallurgical routes are less energy intensive and more eco-friendly, but complete recovery of Zn has proved to be very difficult due to the stability of  $\text{ZnFe}_2\text{O}_4$  [7, 9]. If Zn content in the initial dust is mainly in the form of ZnO, high recovery efficiency is expected for any recovery routes [9].



Based on the plant data and analysis, which will be discussed in the coming sections, the HIsarna process is characterized by high raw material versatility. It is, therefore, attractive for processing secondary iron sources similar to the EAF process. Among the materials that can be recycled through HIsarna, galvanized steel scrap, basic oxygen furnace dust, and zinc-bearing briquettes are worth mentioning.

Based on the laboratory analysis of the collected dust upstream of the HIsarna plant, a considerable amount of Zn in the form of  $\text{ZnFe}_2\text{O}_4$  and ZnO was detected once zinc-bearing material was injected into the main reactor. This finding led HIsarna technologists and researchers to believe that by injecting zinc-bearing material into the process, the Zn content can be concentrated in the off-gas dust (similar to the EAF process). However, it is desired to obtain a dust with a minimum content of  $\text{ZnFe}_2\text{O}_4$  (rich in ZnO) from which it is more convenient to recover the Zn element.

In the HIsarna process, the evaporated Zn can end up in two main zinc-bearing compounds. It could react directly with oxidants such as  $\text{O}_2$ ,  $\text{CO}_2$ , or  $\text{H}_2\text{O}$  to form zinc oxide (ZnO) or react with oxygen and pre-reduced ore (mainly  $\text{Fe}_3\text{O}_4$ ) to form zinc ferrite ( $\text{ZnFe}_2\text{O}_4$ ) [10–13]. In this context, ZnO is a favorable by-product since zinc recovery from  $\text{ZnFe}_2\text{O}_4$  requires further treatment due to its high stability [2]. There have been numerous studies on  $\text{ZnFe}_2\text{O}_4$  and ZnO formation in iron and steelmaking processes, especially in the EAF process.

Pickles [14, 15] have investigated the effect of different parameters on the formation of zinc–manganese ferrite in electric arc furnace dust using thermodynamic analysis for the Zn–Fe–Mn–O–H–C system. He has reported that gas composition and mainly the high ratio of  $\text{CO}/\text{CO}_2$  and  $\text{H}_2/\text{H}_2\text{O}$  had a significant impact on limiting the formation of both ZnO and  $\text{ZnFe}_2\text{O}_4$ . Temperature reduction is reported to be a favorable condition for the formation of ferrite. Increasing the amount of zinc and manganese content in the gas can reduce the formation of ferrite; however, an increase in the formation is reported at higher concentrations of iron oxide.

Sureerat et al. [16] have investigated the reduction properties of reducing gases ( $\text{H}_2$ -CO mixture) to eliminate and decompose the  $\text{ZnFe}_2\text{O}_4$  compound in the EAF off-gas over the 400 to 1600 °C range. Both experimental and thermodynamic analysis were performed. They have reported that ferrite reduction occurs at relatively high temperatures depending on the reducing gas component. For example,  $\text{ZnFe}_2\text{O}_4$

reduction by hydrogen is feasible at temperatures above 1100 °C. But, temperatures above 1500 °C are required for reduction by carbon monoxide.

Suetens et al. [10] have performed a detailed experimental study on the formation of ZnFe<sub>2</sub>O<sub>4</sub> in EAF dust to investigate the possibility of in-process separation (IPS) of Zn from the dust. They have concluded that the ferrite formation is thermodynamically favourable in an atmosphere with high oxygen content (or air intake) and low temperature, like in previous studies.

Nedar [13] has proposed a gas-solid reaction mechanism for ferrite formation where the oxygen reacts with zinc vapour in the presence of liquid iron. The liquid iron is oxidized to form FeO and Fe<sub>3</sub>O<sub>4</sub>, and depending on the oxidized form, two different routes are possible, as illustrated and elaborated in other studies [10–12]. This mechanism is confirmed by experimental analysis and again points out the importance of oxygen and temperature for ferrite formation.

Learning from the above studies, one can find many similarities between the dust formation in the EAF process and occurring phenomena inside the HIsarna reactor when zinc-bearing material is injected. As will be discussed in the coming sections, the off-gas system provides the most favourable environment for ZnFe<sub>2</sub>O<sub>4</sub> formation. This is attributed to the high concentration of iron oxide particles, low temperature, and a high partial pressure of O<sub>2</sub>, or equivalently, the absence of carbon monoxide (resulting in a low partial pressure of CO) [10–17]. From the literature and considering the conditions inside the HIsarna off-gas system, several key reactions for ZnFe<sub>2</sub>O<sub>4</sub> and ZnO formation and reduction are identified, as presented below:

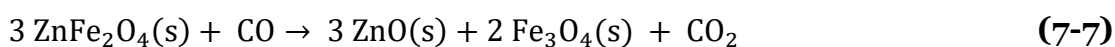
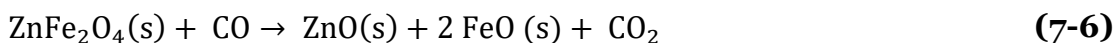
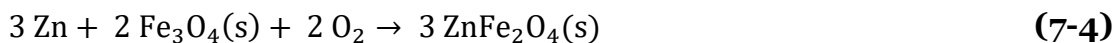


Figure 7-1 shows the Gibbs energy change versus the temperature of the mentioned reactions.

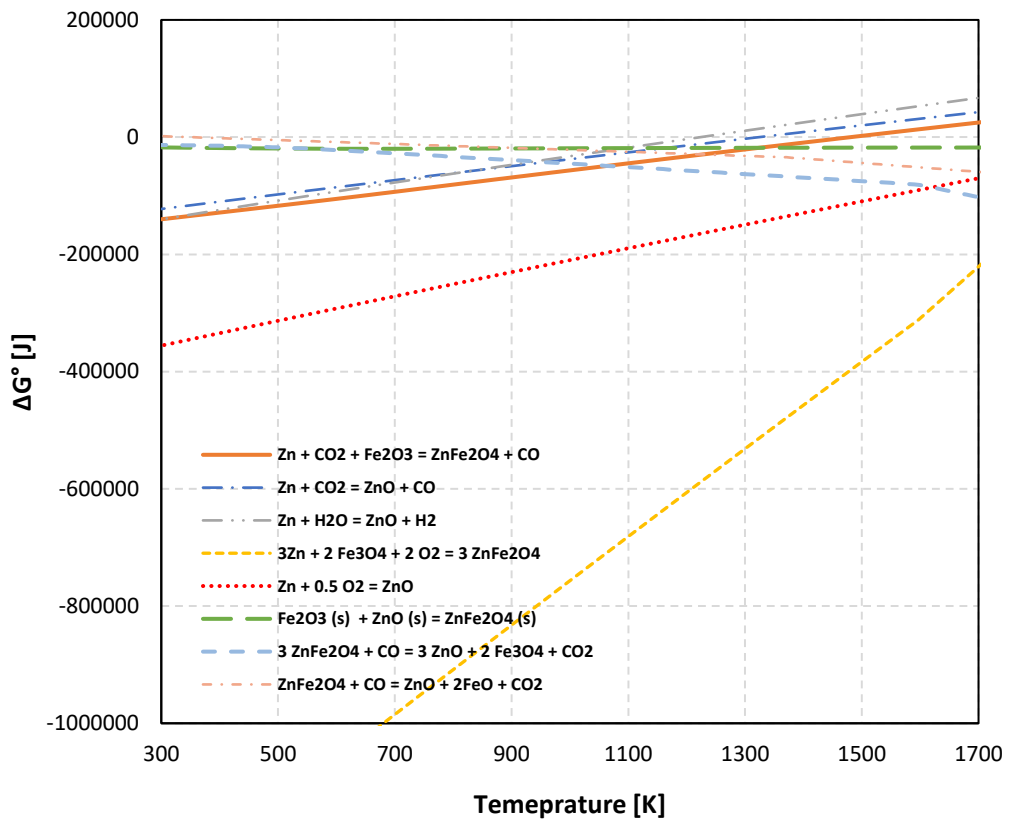


Figure 7-1. Gibbs energy change versus temperature for possible reactions involving Zn.

Reaction (7-4), which is the main ferrite-forming reaction based on the references [8, 9], exhibits high thermodynamic favorability (with a negative  $\Delta G^\circ$ ) within the specified temperature range, particularly at lower temperatures. The same analysis reveals that the reactions leading to  $\text{ZnFe}_2\text{O}_4$  formation are even more thermodynamically favorable compared to both  $\text{ZnFe}_2\text{O}_4$  reduction and  $\text{ZnO}$  formation. This makes the task of preventing ferrite formation a significant challenge within the HIsarna process.

## 7.2. Zinc recovery through the HIsarna process

As discussed before, the HIsarna plant operation has shown that the furnace is characterized by a high versatility of raw materials, making it attractive for zinc recovery. Zinc-bearing materials can be introduced into the process at different reactor sections. For instance, dust-form material is injected through nozzles into the CCF, while granular material is fed into the SRV via an inclined chute, as

illustrated in Chapter 1, Figure 1-29. The zinc content of the injected material rapidly evaporates, ascends, and ultimately accumulates in the off-gas dust, which is collected by cyclones and baghouses.

During the fourth HIsarna campaign in 2014, a test was conducted in which dust containing Zn was injected into the HIsarna CCF along with iron ore. The dust primarily consisted of iron oxides but contained up to 5 wt% Zn. The tests demonstrated the possibility of enriching Zn up to 16% in the HIsarna dust, as depicted in Figure 7-2. However, during this test, injecting only a small amount of dust for a short period was possible. Consequently, the achieved Zn enrichment was limited. Nevertheless, it opened up the potential for attaining significantly higher levels of Zn in the HIsarna off-gas dust without establishing a zinc cycle, as seen in blast furnaces, and without detrimental zinc accumulation within the process. These promising results led to further investigation of the potential for enriching Zn content in the dust, making it suitable for direct reuse in Zn smelting as a secondary source and an alternative to Zn ore, the primary source.

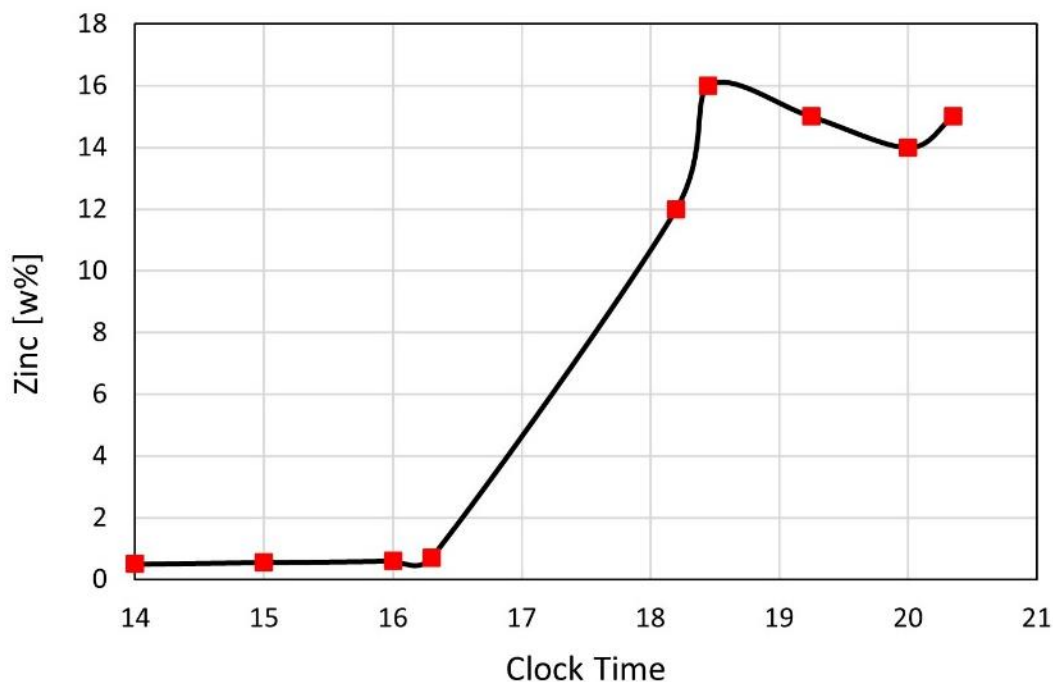


Figure 7-2. Result of Zn enrichment of the HIsarna flue dust after injection of Zn-containing dust into CCF (data taken from HIsarna plant)

In this chapter, using thermodynamic (FactSage) and computational fluid dynamic (CFD) tools, the regions with a high risk of ferrite formation are detected inside the main reactor and off-gas system. According to findings, with current operation and

configuration, the formation of  $\text{ZnFe}_2\text{O}_4$  is inevitable and can only be minimized through proper geometrical and operational modification. The study is mainly based on thermodynamic equilibrium calculations, and the kinetics effect is not considered.

### 7.3. Tools and Methods

To have a detailed analysis of the formation of  $\text{ZnFe}_2\text{O}_4$  inside the off-gas system, profiles of temperature, gas composition, and molten pre-reduced ore flow rate inside the reflux chamber and the rest of the off-gas system are needed. The temperature and composition measurements are only available at limited points, which is depicted in Chapter 2, Figure 2-4 (points A, B, and D for temperature and at points A and D for flue gas compositions). Measuring the flow rate of molten particles is a nearly impossible task due to the extremely high temperatures and the molten state of the particles inside the reflux chamber. The limited measurement points available do not offer sufficient local information for a thorough analysis of the off-gas system. Given this limitation, the calculated profiles from the discussed and validated CFD model can be reliably employed to address this challenge.

FactSage thermochemical software [18] is a valuable tool for equilibrium calculations by varying parameters such as temperature, pressure, and compositions to predict the formed phases in an initial mixture. The equilibrium diagram for an identical mixture, similar to the HIsarna off-gas system environment, is plotted by varying the temperature and partial pressure of oxygen. Using the calculated temperature and composition profiles from the validated CFD model, discrete operating points are mapped on the equilibrium graphs to see possible formed phases and compounds inside the off-gas system.

#### 7.3.1. CFD results

The results from CFD calculations to obtain temperature, composition, and particle flow rate profiles are discussed in detail in previous chapters. For convenience, the results are summarized and depicted in Figure 7-3. The reduction of the molten ore flow rate along the reflux chamber is important, as the formation of zinc ferrite heavily depends on the presence of iron oxide. This gradual reduction has the potential to limit the formation of zinc ferrite.

### 7.3.2. FactSage calculation

The atmosphere inside the HIsarna reactor is predominantly reducing, characterized by high CO and H<sub>2</sub> content, as illustrated in Figure 7-4.A. As discussed earlier, these reducing gases and elevated gas temperatures significantly limit the formation of both ZnO and ZnFe<sub>2</sub>O<sub>4</sub> [10,14,15].

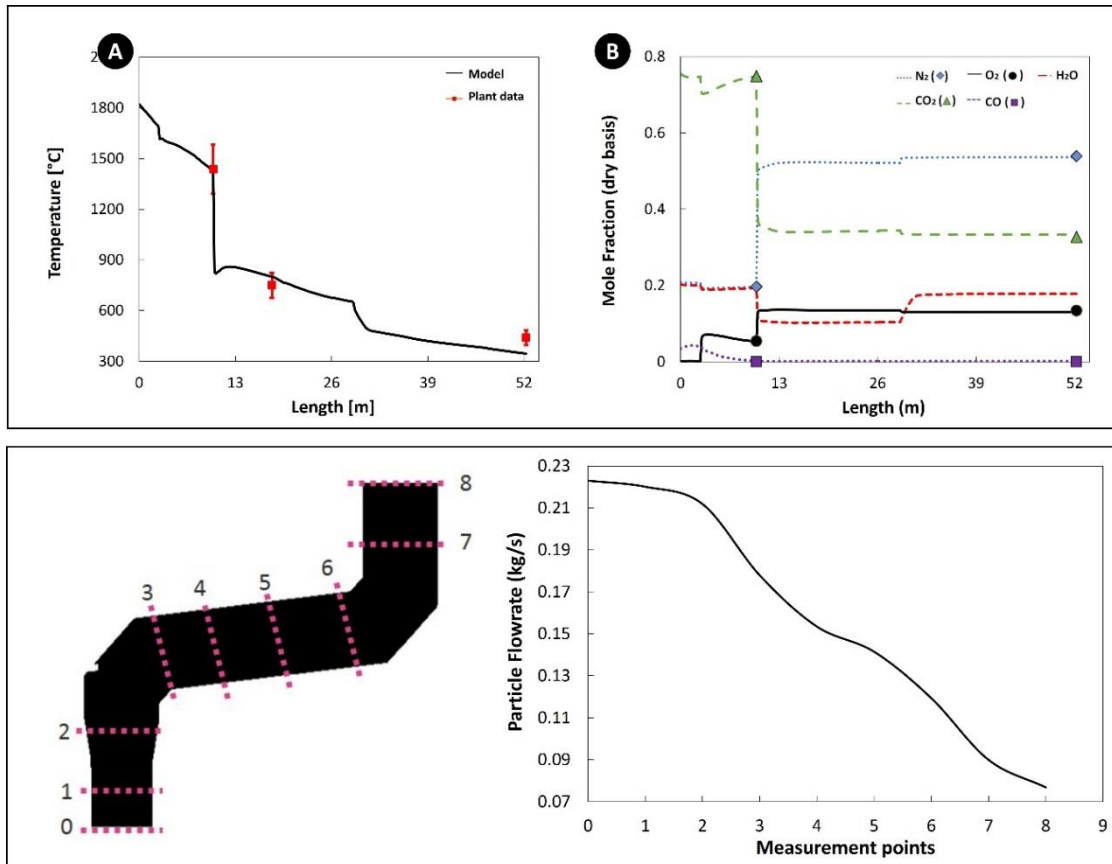


Figure 7-3. **A:** calculated gaseous composition and temperature: model predictions (solid lines) plant measured (symbols); **B:** flow rate of particles across the reflux chamber (dog-leg geometry) along off-gas system.

Figure 7-4.B shows the effect of temperature on the formation of ZnFe<sub>2</sub>O<sub>4</sub> in a mixture of CO, CO<sub>2</sub>, H<sub>2</sub>O, O<sub>2</sub>, Zn, and Fe<sub>3</sub>O<sub>4</sub>(s) for different CO/CO<sub>2</sub> ratios. The ratios of other gaseous and solid compounds are fixed with respect to CO<sub>2</sub>. Zn content that ends up in the spinel phase takes the form of ZnFe<sub>2</sub>O<sub>4</sub>. It is evident that increasing the ratio of CO/CO<sub>2</sub> can significantly diminish the formation of ZnFe<sub>2</sub>O<sub>4</sub>, particularly at higher temperatures. According to this thermodynamic analysis, the formation of ZnFe<sub>2</sub>O<sub>4</sub> at temperature and CO/CO<sub>2</sub> range of the SRV and CCF is thermodynamically unfavourable. However, at a lower ratio of CO/CO<sub>2</sub>, which

occurs inside the off-gas system, ferrite formation at any temperature range is highly favorable.

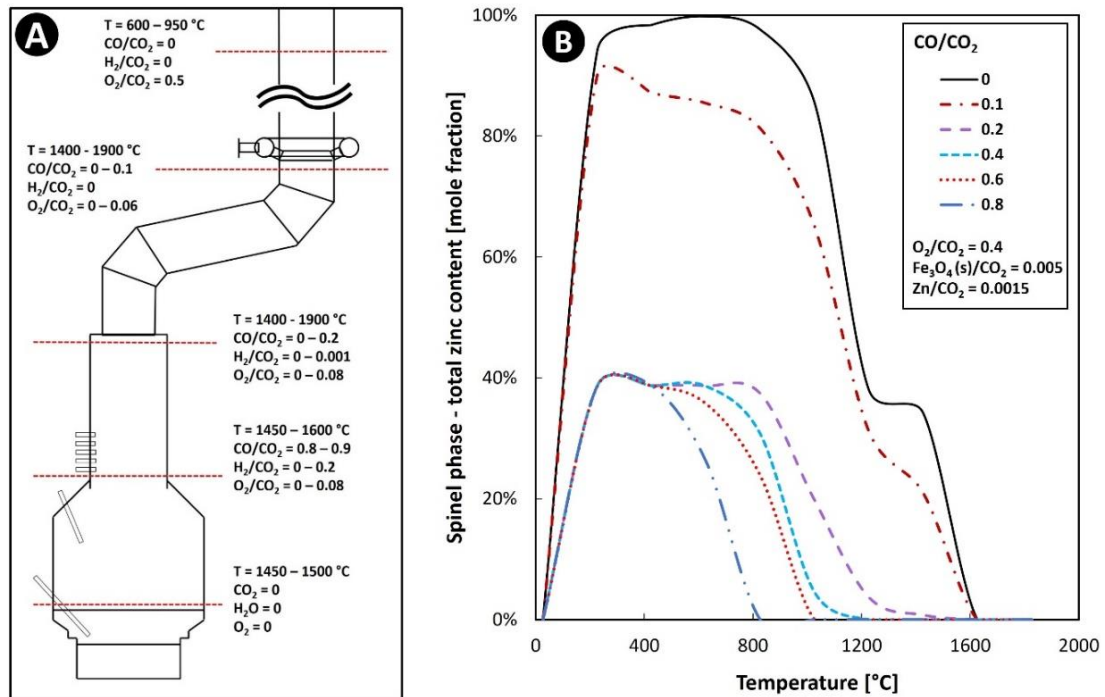


Figure 7-4. A: gaseous composition and temperature at different outlet sections; B: total zinc prediction in spinel phase

Table 7-1. Components used to plot equilibrium graphs in FactSage software

Component	Mole fraction/Partial pressure [atm]
$\text{CO}_2$	0.547
$\text{H}_2\text{O}$	0.173
$\text{N}_2$	0.158
$\text{O}_2$	Variable from 0 to 0.12
Zn	Variable – arbitrary values
$\text{Fe}_3\text{O}_4$	Variable – arbitrary values

From Figure 7-4.B, it can be concluded that most of the Zn content remains in vapor form at the inlet of the off-gas system. The “phase diagram” module of the FactSage software is used to plot the equilibrium graphs using the listed components in Table 7-1. Figure 7-5 shows an example of the plotted equilibrium graph. Equilibrium graphs are based on the temperature and  $\log_{10} P_{\text{O}_2}$  as  $y$  and  $x$  axis respectively. Temperature is varied from 500 to 2000  $^{\circ}\text{C}$  and  $P_{\text{O}_2}$  is varied from 0 to 0.12 atm with a maximum value existing above the air quench. For all calculations, the molar ratio of  $\left(\frac{\text{Zn}_{(\text{g})}}{\text{Fe}_3\text{O}_4 + \text{Zn}_{(\text{g})}}\right)$  is varied from 0.01 to 0.9 and is fixed for each plot. For

simplicity, this ratio will be called “ $R$ ” from now on, which is the ratio of zinc vapor to the sum of iron oxide and zinc vapor. The variation of  $R$  depends on the zinc content of the injected zinc-bearing material and the amount of zinc vapour reaching the off-gas system inlet.

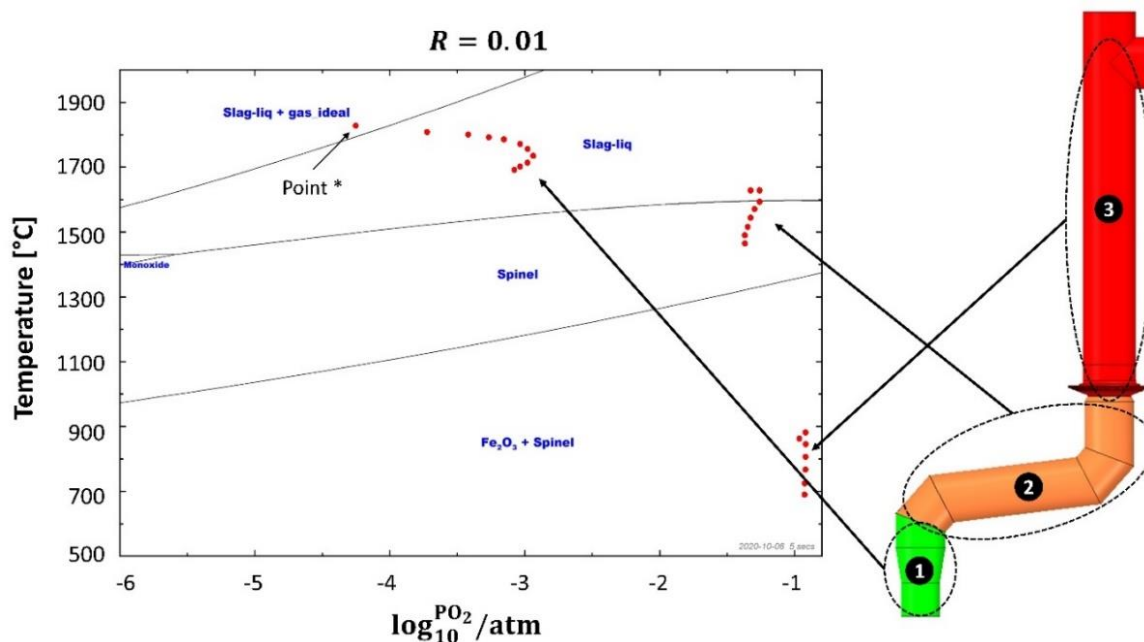


Figure 7-5. Equilibrium graph with mapped operating points for  $R = 0.01$

The equilibrium graphs are divided into different regions separated by solid lines. Each region might contain one or a combination of phases. Possible formed phases are “Ideal gas”, “Liquid slag” (slag-liq), “Spinel”, “Monoxide” (slag in solid form), and “Fe<sub>2</sub>O<sub>3</sub>”. Another possible phase is “Zincite”, which is formed at a very high  $R$  ratio (when zinc vapour content is high in the flue gas), as shown in later figures.

Each phase contains specific components with calculated values. The potential components of interest for this study in each phase are listed in Table 7-2. Factsage software enables the evaluation of the composition at each point on the equilibrium graph, although this detailed analysis is not presented in this study for brevity.

Figure 7-5 also includes operating points (red dots) for different sections of the off-gas system. These operating points represent discrete locations along the reflux chamber and up-leg (up to point B in Figure 2-4) with calculated temperature and partial pressure values obtained from the discussed validated CFD model. For example, point \* designates the reflux chamber inlet with a temperature of 1812 °C and an almost zero oxygen partial pressure ( $P_{O_2} \approx 10^{-4}$  atm). The same convention



applies to all of the plotted operating points. The equilibrium graphs with mapped points make it possible to observe where these operating points fall and which phases might form for a specific ratio of zinc vapor and iron oxide.

Table 7-2. possible phases and components inside each phase

Phase	Possible component
Slag-liq	Iron oxide (major FeO, Fe <sub>2</sub> O <sub>3</sub> ) and ZnO (minor)
Spinel	Fe <sub>3</sub> O <sub>4</sub> and ZnFe <sub>2</sub> O <sub>4</sub>
Ideal Gas	CO, CO <sub>2</sub> , Zn, O <sub>2</sub> , H <sub>2</sub> O, H <sub>2</sub>
Zincite	ZnO (major), iron oxide (minor)
Fe <sub>2</sub> O <sub>3</sub>	Iron oxide

For example, in Figure 7-5, the operating points in section 1 of the reflux chamber (before oxygen injection) fall into the “Slag-liq + ideal gas” region where zinc element speciate into the slag in the form of ZnO or remains in gaseous form due to high temperature and absence or existence of minor oxygen. In section 2, there is a sharp increase in the amount of oxygen, leading to a local temperature drop. This creates a favorable condition for ZnFe<sub>2</sub>O<sub>4</sub> formation. As observed, most of the operating points fall into the spinel phase, where the major component is Fe<sub>3</sub>O<sub>4</sub>, and all of the zinc elements speciate into ZnFe<sub>2</sub>O<sub>4</sub>. A similar scenario is observed in section 3, where the major phases are Fe<sub>2</sub>O<sub>3</sub> and spinel.

## 7.4. Results and discussion

### 7.4.1. Current pilot scale – Dog-leg geometry

Figure 7-6 depicts an equilibrium graph with mapped operating points for different  $R$  ratios for the current operating condition of the reflux chamber. As it can be seen, at the lowest investigated ratio where  $R = 0.01$ , the operating points before oxygen injection points fall in “Slag-liq” and move to the “Spinel” containing region after oxygen injection. As the ratio increases (indicating higher zinc vapor content in the flue gas), the operating points in section 1 shift into the “Slag-liq + gas” region, where most of the zinc vapor remains in the gaseous phase. The “Zincite” phase, characterized by nearly pure ZnO content, is observed within the  $R$  range of 0.4 to 0.5 and expands as the zinc to iron oxide ratio increases. At  $R$  ratios of 0.8 and 0.9, most operating points are situated within the “Slag” and “Slag + zincite” regions, signifying that the zinc element is present in the form of ZnO.

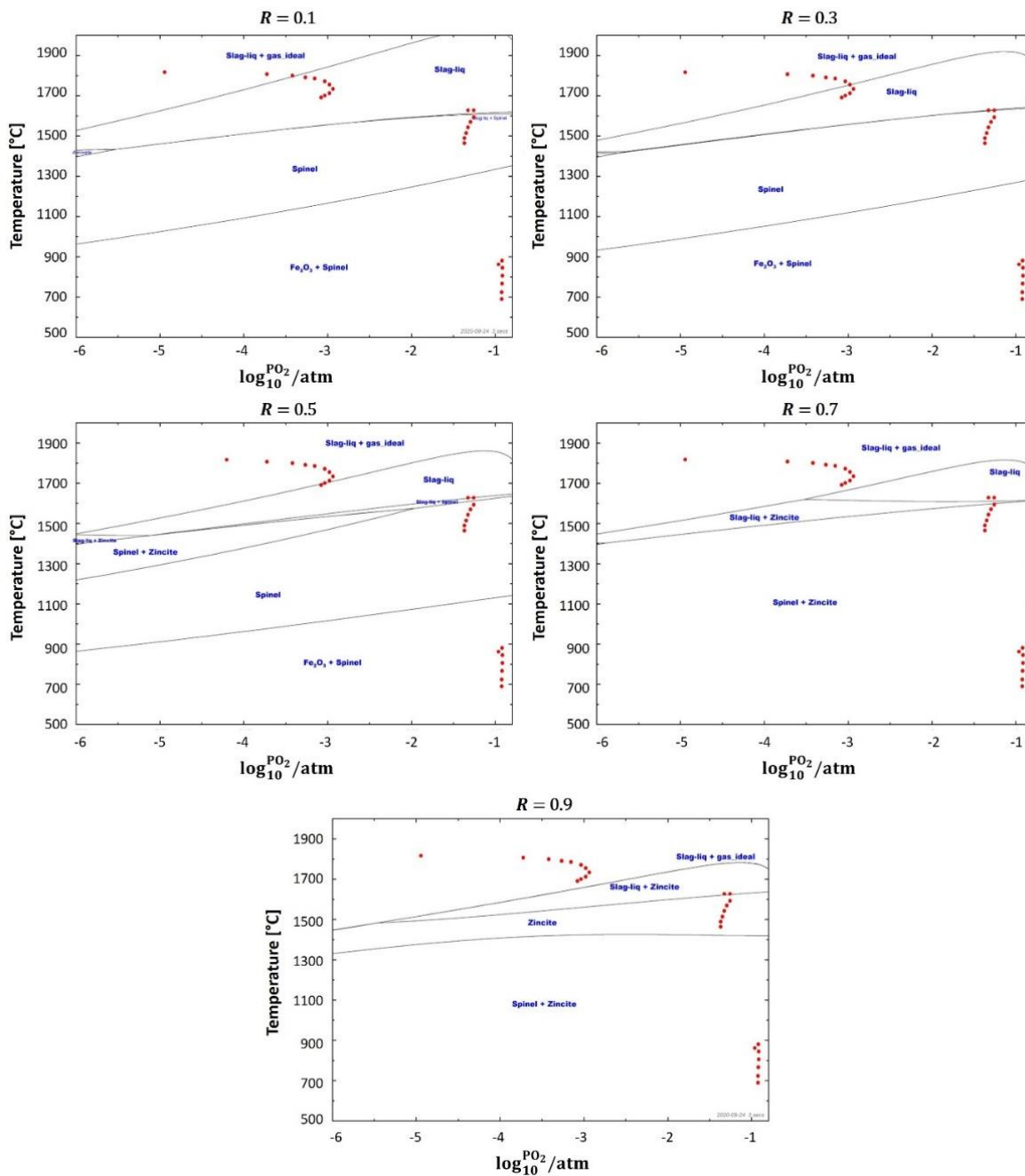


Figure 7-6. Equilibrium graph with mapped operating points for “dog-leg” geometry and for different “R” values

Nevertheless, at all ratios, the formation of spinel and ZnFe<sub>2</sub>O<sub>4</sub> remains inevitable, particularly in sections 2 and 3. These sections experience a rapid local and global temperature drop and a sharp increase in oxygen partial pressure, as illustrated in Figure 7-3.A. According to the calculations, an increase in Zn vapor content in flue gas, even at low temperatures, will facilitate the formation of ZnO, aligning with findings from other researchers [2],[11],[12],[14]. However, achieving such a high R ratio poses a significant challenge. For instance, in previous plant operations, 2

tons/hr of scrap material containing 2%w Zn coating was injected into the SRV bath, resulting in an average 0.011 kg/s of zinc vapor. If the entire vapor from the bath, along with 0.223 kg/s of pre-reduced ore escaping CCF (which contains 85%  $\text{Fe}_3\text{O}_4$ ), reaches the CCF outlet, a maximum ratio of  $R = 0.15$  at the inlet and 0.35 at the outlet of the reflux chamber can be anticipated.

At these ratios, as indicated by the calculated equilibrium graphs, the majority of the Zn element is expected to speciate into the  $\text{ZnFe}_2\text{O}_4$  component within the "Spinel" phase. This agrees with laboratory analysis of collected dust in the baghouse (at the current pilot plant) shown in Figure 7-7. As it can be seen, on average, around 2.5% of the total weight of the sampled dust contains zinc-bearing compounds, and of that percentage, 92% is in the form of  $\text{ZnFe}_2\text{O}_4$ , and only 8% of injected Zn ended up in the form of ZnO.

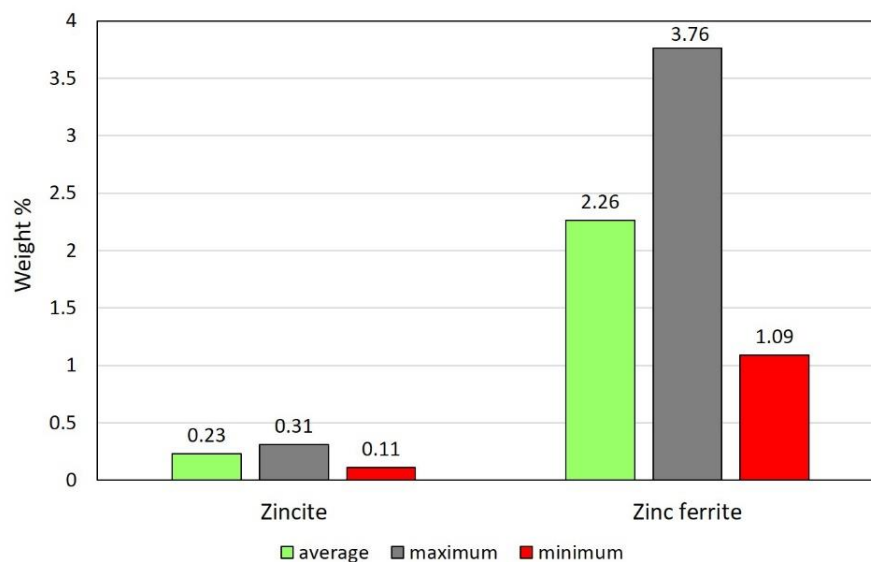


Figure 7-7. laboratory analysis of HIsarna baghouse dust for Zincite ( $\text{ZnO}$ ) and Zinc ferrite ( $\text{ZnFe}_2\text{O}_4$ ) fraction (Tata Steel R&D).

Therefore, it can be concluded that  $\text{ZnFe}_2\text{O}_4$  formation is thermodynamically inevitable at current operating conditions and setup. Even in the absence of oxygen, prevention of  $\text{ZnFe}_2\text{O}_4$  formation is not a straightforward task, mainly due to the high stability of the spinel at lower temperatures [10].

#### 7.4.2. Modified reflux chamber – Frog-leg geometry

From previous discussions and calculations, the impact of temperature and oxygen partial pressure on the formation of ZnO and  $\text{ZnFe}_2\text{O}_4$  became evident. In this

section, the primary focus will be on the geometrical and operational modifications of the reflux chamber. According to equilibrium graphs, this segment of the off-gas system still presents opportunities to minimize the formation of  $\text{ZnFe}_2\text{O}_4$ . To maximize the formation of ZnO-containing phases, high temperatures and lower partial pressures of oxygen (or high partial pressure of CO) are required inside the reflux chamber. Considering a fixed condition at the inlet of the chamber, the following solutions are available to practice:

- a) One solution is to increase the  $R$  ratio, as discussed in the study of Pickles [14, 15] and based on the thermodynamic calculations in section 7.4.1. This can be achieved by increasing zinc content inside the off-gas system by injecting more zinc-bearing material into the process. However, with this solution, increasing the  $R$  ratio to a certain extent is possible since injecting a very high amount of zinc-bearing material is complex and might cause technical issues. For example, injecting galvanized scrap particles in large quantities into the SRV molten liquid could cause local liquid freezing, which is detrimental to the steady operation of the plant.
- b) It is also possible to increase the  $R$  ratio by increasing particle capturing inside the reflux chamber or CCF to limit the availability of  $\text{Fe}_3\text{O}_4$ , especially in those regions with high oxygen partial pressure and low temperature.
- c) Another feasible solution would be to modify the geometry of the reflux chamber to provide a larger region with high temperature and low partial pressure of  $\text{O}_2$  or to keep CO partial pressure as high as possible before the post-combustion (creating a reducing environment). The presence of CO in the flue gas will limit the formation reaction of  $\text{ZnFe}_2\text{O}_4$ .

In Chapters 5 and 6, a modified geometry to increase particle capturing was offered and discussed in detail for particle and gaseous flow analysis. The geometry was called frog-leg, which is the same as dog-leg geometry with a second bend added. As discussed, it is possible to inject oxygen at two different levels. The system's behavior for the formation of zinc ferrite will be the same for the lower injection; therefore, in this chapter, the focus will be on the frog-leg geometry with upper oxygen injection. As will be discussed, by injecting oxygen from the upper injector, the post-combustion is delayed, which is beneficial for zinc ferrite formation prevention.

The temperature, composition, and particle flow rate profiles using the developed CFD model for frog-leg geometry have been discussed in detail in Chapter 6. To recap, Figure 7-8 summarizes the obtained results.

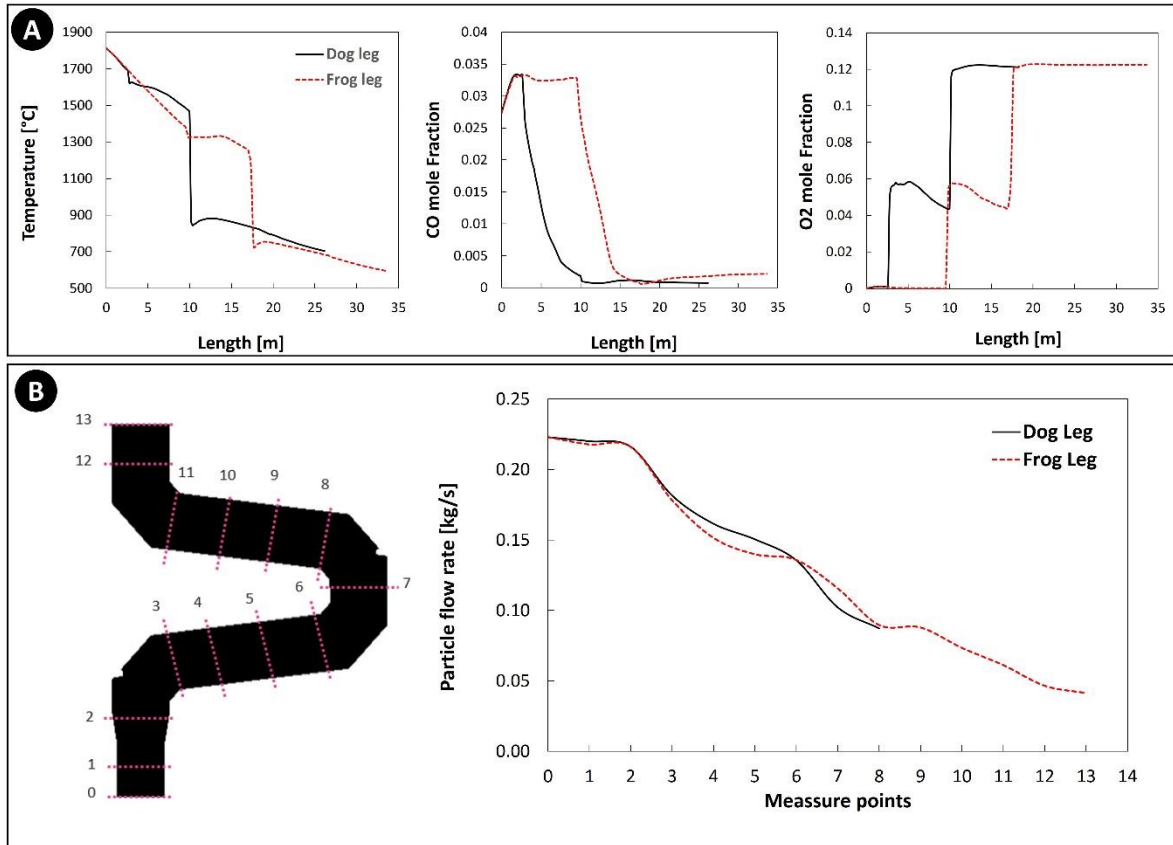


Figure 7-8. Predicted gaseous composition and temperature profile along frog-leg and air quench (A) (obtained from CFD calculations up to point C in Figure 2.4); Predicted flow rate of particles across the frog-leg geometry (B).

In dog-leg geometry, the temperature falls drastically at the length of 10 m, whereas for frog-leg, this drastic reduction happens at the length of 18 m, providing an extra 8 meters length for the flue gas to stay at high temperature. Also, the same figure shows that oxygen injection and CO combustion are delayed for 8 m, which is again beneficial to preventing  $\text{ZnFe}_2\text{O}_4$  formation and promoting ZnO formation.

Once ZnO is formed inside the slag, it will be stable and in the form of small distinguished particles. This is confirmed by the study of Suetens et al. [10], which reported the presence of ZnO particles inside the collected dust from EAF via EDS mapping (Energy Dispersive Spectroscopy). Gaseous reduction or solid-state reactions represent the sole mechanisms for destabilizing and reducing the formed ZnO. Solid-state reactions, governed by kinetics, are slow and are challenging to occur within the brief resident time available inside the off-gas system. The

likelihood of ZnO reduction through reducing gases is also restricted. In a gas-solid reaction, the gaseous compound must diffuse into the solid surface, which is improbable given the very low partial pressure of the CO-H<sub>2</sub> mixture within the off-gas system.

It is also worth mentioning that, according to the thermodynamic calculations (Gibbs free energy) and study of Sureerat et al. [16], the reduction of both ZnO and ZnFe<sub>2</sub>O<sub>4</sub> can proceed only at high temperatures and a highly reducing environment. Thus, a stable ZnO content inside the reflux chamber and above can be expected. The other benefit of this modification is that the content of molten pre-reduced particles is constantly decreased, as depicted in Figure 7-8.B. In dog-leg geometry, the flow rate of particles entering the oxygen injection area is around 0.182 kg/s; however, for the frog-leg geometry, the flow near oxygen injection is 0.089 kg/s. This means an increase in the *R* ratio in the oxygen-rich region, which can limit the formation of ZnFe<sub>2</sub>O<sub>4</sub> inside the reflux chamber.

These conclusions can be quantified using the same FactSage analysis to explore potential ZnFe<sub>2</sub>O<sub>4</sub> forming locations within the frog-leg configuration. The results are depicted in Figure 7-9, and, as observed, in comparison to the dog-leg geometry, a higher number of operating points in section 1 of the frog-leg falls within the liquid "Slag" phase. However, spinel formation remains inevitable due to temperature reduction in the oxygen and air injection regions. The operating points shift upward with an increase in the *R* ratio, and the formation of spinel (and ZnFe<sub>2</sub>O<sub>4</sub>) will be limited in a manner similar to that discussed for the dog-leg geometry. The geometrical modification can also positively contribute to the combustion and removal of other undesired compounds, such as carbon particles and CO-H<sub>2</sub> mixture inside the off-gas, which has been investigated in Chapter 6 [19].

In conclusion, based on the analysis so far, for any reflux chamber configuration (dog-leg or frog-leg), the most efficient way to increase the ZnO content of the collected dust would be increasing the *R* ratio by injecting a higher amount of zinc-bearing material. Steel scrap injection into the molten slag would be an interesting option as it is a very efficient way to recover the scrap's iron content and reduce iron ore consumption. However, when it comes to zinc recovery, it has shortcomings. Achieving a high "*R*" ratio requires a considerable amount of steel scrap injection, which can reduce the slag temperature and might cause a disturbance in

temperature control and local freezing. Therefore, it is suggested to inject zinc-bearing material not only in the form of steel scrap injection into the molten slag but also through other forms and other sections of the process, such as zinc-bearing dust injection into the CCF or SRV upper section. This way, the Zn content along the off-gas system is evenly distributed, and local disturbances are recovered faster.

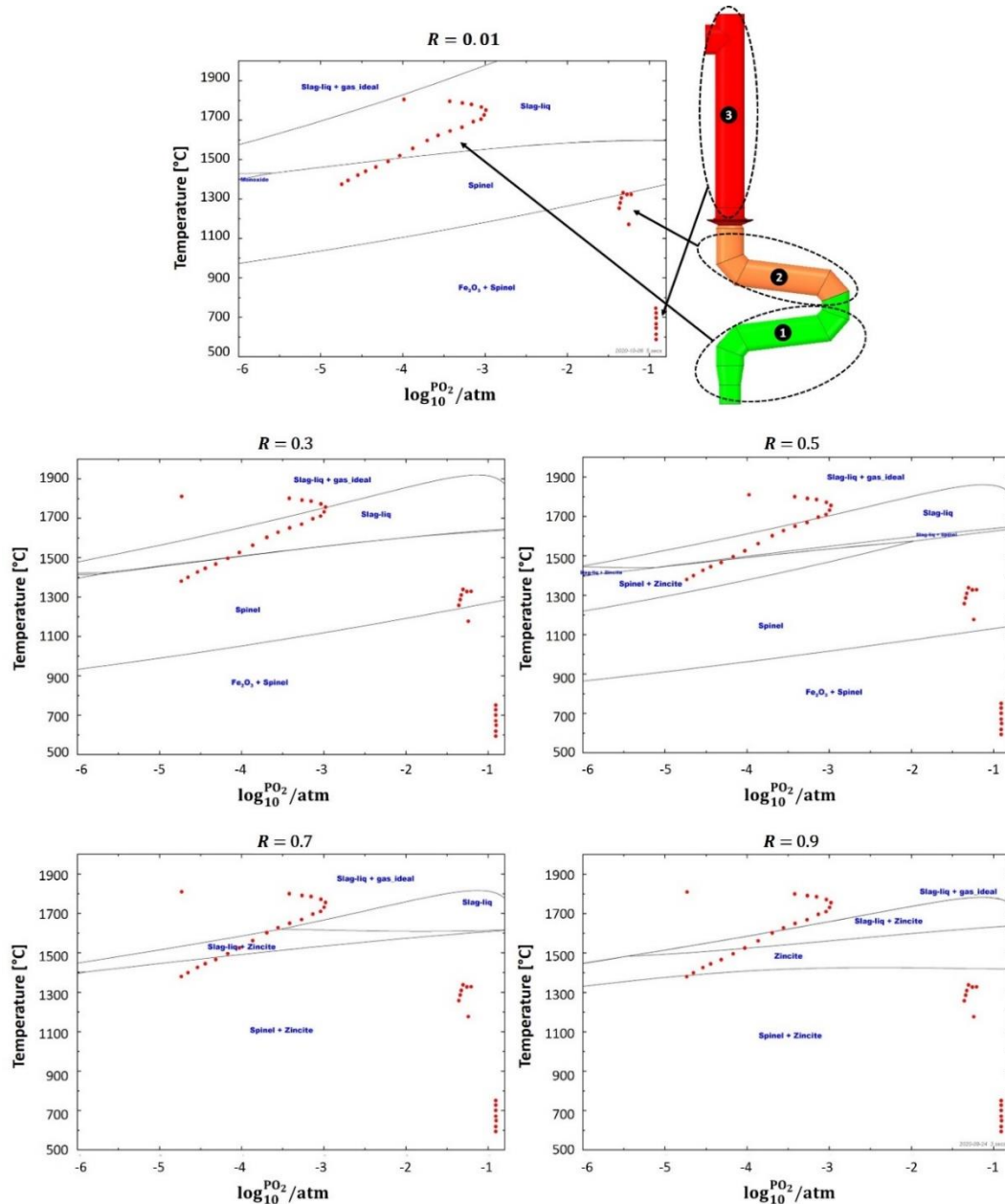


Figure 7-9. Equilibrium graph with mapped operating points for “frog-leg” geometry and for different  $R$  values

### 7.4.3. Reflux chamber wall modification

A further modification might be required to ensure that the operating points inside section 1 of the frog-leg geometry stay away from the “Spinel” region for minimum

and maximum  $R$  ratio. Considering the modified geometry, the only feasible way is to keep the temperature as high as possible inside the chamber. This can be achieved by either increasing refractory wall thickness to reduce the heat losses through the walls or increasing CO content at the inlet of the off-gas system to provide more fuel for post-combustion. The validated CFD model is used to investigate both solutions. Figure 7-10.A shows the temperature profile for different refractory wall thicknesses of the reflux chamber.

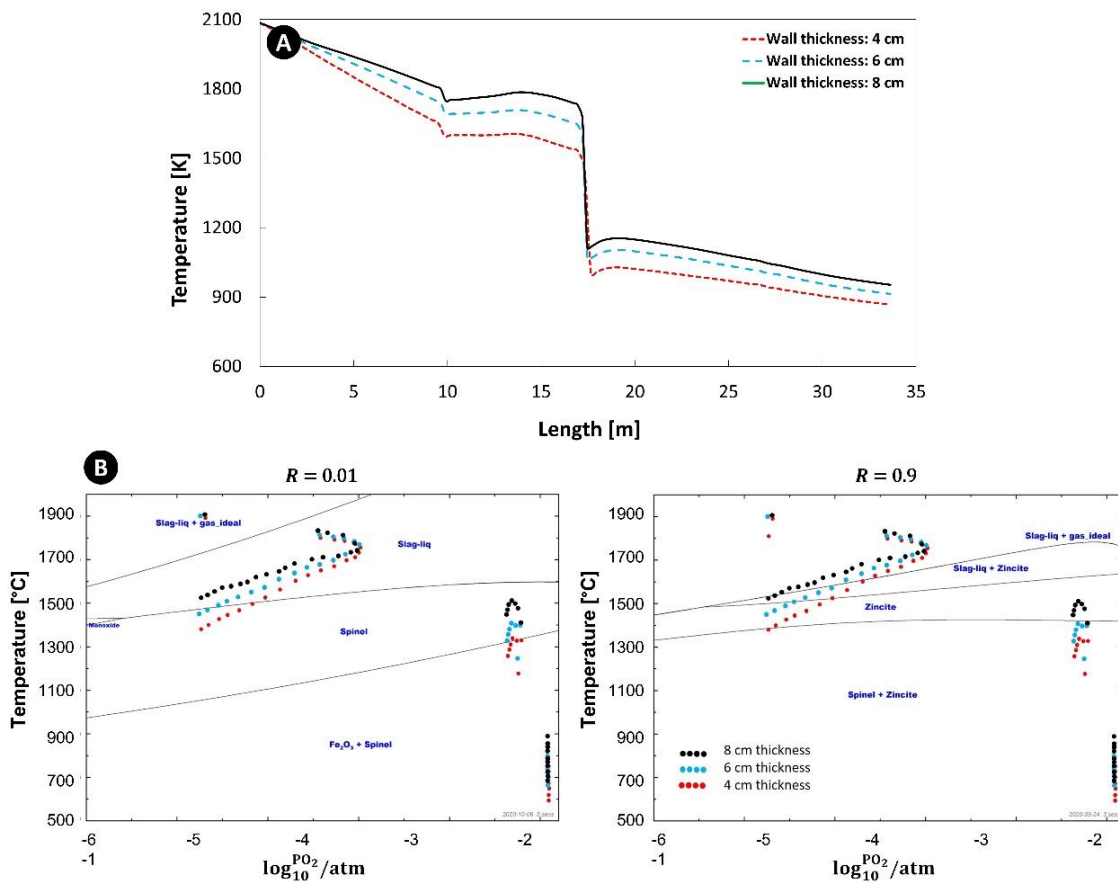


Figure 7-10. Calculated temperature profile for off-gas system (A) with frog-leg geometry for different wall thickness (up to point C); Equilibrium graph with mapped operating points for frog-leg geometry (B)

For a fixed equilibrium graph, the operating points shift upward by increasing the flue gas temperature as depicted in Figure 7-10.B for maximum and minimum considered  $R$  ratio. This shift will locate the operating points of section 1 in a more favorable equilibrium region where the zinc element remains either in gaseous form or speciates into the slag in the form of ZnO. It is worth noting that even at high temperatures, the “Spinel” and  $ZnFe_2O_4$  formation is still inevitable once the oxygen becomes available (upper region of frog-leg). So, practically, this geometrical



modification could minimize the  $\text{ZnFe}_2\text{O}_4$  to a certain extent and may not entirely prevent the undesired product formation.

#### 7.4.4. Increasing CO content inside the reflux chamber

As discussed before, due to the harsh conditions inside the reflux chamber, the refractory wall is exposed to thermo-chemical stresses, which can cause wall material loss and thickness reduction. It is required to refresh the refractory wall regularly, which might not be feasible during long runs. Therefore, using wall thickness and material to reduce ferrite formation might not be feasible during long runs. A more viable solution would be increasing the CO content of the flue gas at the inlet of the reflux chamber by reducing the CCF post-combustion ratio. Since the HIsarna process has a transient nature, in real plant operation, the amount of CO at the inlet of the off-gas system can reach up to 10% (molar fraction). Figure 7-11 shows the effect of CO content on flue gas temperature and oxygen composition, along with the operating point position on the equilibrium graph for both dog and frog-leg geometry. Noticeably, with an increase in CO content at the inlet, the majority of operating points shift upward and into regions where Zn vapor speciates into ZnO, even in section 2, where post-combustion oxygen is injected in substantial amounts. Keeping CO partial pressure high inside the reflux chamber offers several benefits. Higher CO content means higher fuel for the post-combustion process, which in turn signifies higher heat release and temperature profile to limit the evolution of  $\text{ZnFe}_2\text{O}_4$ , similar to the effect of wall thickness. As mentioned earlier, with higher temperatures, the operating points on the equilibrium graph are shifted upward to the regions with favorable forms of the Zn element. Moreover, high CO content consumes oxygen across the reflux chamber and lowers its partial pressure to create a reducing environment where the CO/CO<sub>2</sub> ratio is high. The higher the CO/CO<sub>2</sub> ratio, the lower the risk of  $\text{ZnFe}_2\text{O}_4$  formation (see Figure 7-4). Nevertheless, a high CO content at the inlet of the reflux chamber may cause its incomplete post-combustion and, therefore, possibly emissions

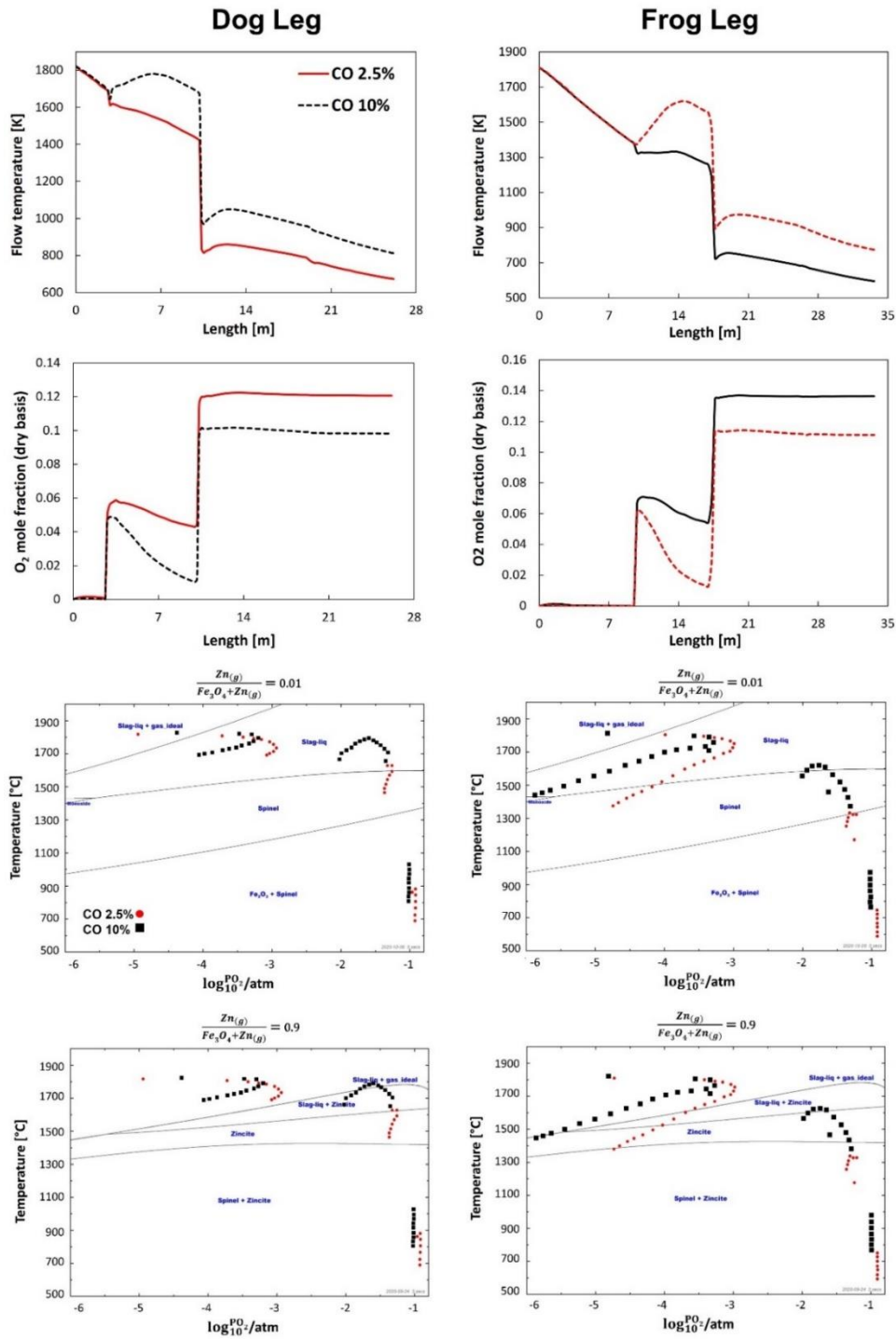


Figure 7-11. Effect of CO content on temperature, oxygen profile, and operating point for dog-leg and frog-leg geometry and for lowest and highest “R” ratio.

### 7.5. Conclusions

A thermodynamic analysis of  $ZnFe_2O_4$  and  $ZnO$  formation within the off-gas system of the HIsarna process has been conducted. The objective is to prevent or minimize the formation of the  $ZnFe_2O_4$  compound, as it is an undesired by-product of the Zn vapor reaction with iron oxide.

Since limited measure points from the real plant data are available, a CFD model was developed and validated to describe the composition and temperature profile variation inside the off-gas system.

The analysis was performed using equilibrium graphs and mapped operating points obtained from CFD calculations. It was found that the most favorable conditions for  $\text{ZnFe}_2\text{O}_4$  formation are high oxygen partial pressure, high content of pre-reduce iron ore (high  $\text{Fe}_3\text{O}_4$  content), and low temperature, which are in agreement with other experimental and numerical studies.

These conditions are met at the current state of the plant operation. According to the thermodynamic analysis, the off-gas system has a higher  $\text{ZnFe}_2\text{O}_4$  formation potential than the SRV and CCF sections. Inside the SRV and CCF, the formation of  $\text{ZnFe}_2\text{O}_4$  is limited due to the highly reducing environment. On the other hand, in the off-gas system, the atmosphere is highly oxidizing owing to the injection of post-combustion oxygen and air. Since the oxidizer is injected at a very low temperature (20-30 °C), it causes a rapid temperature drop across the off-gas system, significantly contributing to the formation of  $\text{ZnFe}_2\text{O}_4$ .

Among the proposed solutions, the simplest approach is to increase the zinc to iron oxide molar ratio ( $R$  ratio), thereby shifting the mapped operating points into the phasic regions with the ZnO compound as the final product of Zn vapor reactions. However, attaining high  $R$  ratios poses challenges, and the formation of  $\text{ZnFe}_2\text{O}_4$  is still anticipated within the off-gas system, even at the highest  $R$  ratio.

To further minimize the  $\text{ZnFe}_2\text{O}_4$  formation, a geometrical modification of the reflux chamber is proposed by adding another turn to the current design. The same analysis is conducted for the modified geometry, demonstrating an expanded area with low oxygen content and high temperature. This expansion allows for increased residence time, enabling the Zn element to speciate into the desired phases with ZnO content.

Furthermore, the proposed modification can lead to a higher capturing efficiency of the molten pre-reduced particles by the walls. This inherently can reduce the  $\text{Fe}_3\text{O}_4$  content of the flue gas and increase the  $R$  ratio, which limits the formation of  $\text{ZnFe}_2\text{O}_4$ .

Maintaining high CO partial pressure inside the reflux chamber would be another feasible solution; however, an excessive increase in CO partial pressure could result in incomplete CO post-combustion and, ultimately, emissions.

Nevertheless, the proposed modifications can reduce ferrite formation to a certain extent but may not entirely eliminate it. The inevitability of  $\text{ZnFe}_2\text{O}_4$  formation persists, especially for operating points near the oxygen and air injection, where some points still fall into spinel-containing zones. Zn vapor is expected to speciate into the  $\text{ZnFe}_2\text{O}_4$  compound in these areas through reactions with oxygen and iron oxide at low temperatures.

## References

- [1] T. Suetens, Recovery of Zinc and Iron from Electric Arc Furnace Dusts: The Feasibility of In-Process Separation, (2015).
- [2] C.C. Wu, F.C. Chang, W.S. Chen, M.S. Tsai, Y.N. Wang, Reduction behavior of zinc ferrite in EAF-dust recycling with CO gas as a reducing agent, *J Environ Manage.* 143 (2014) 208–213. <https://doi.org/10.1016/J.JENVMAN.2014.04.005>.
- [3] M. Omran, T. Fabritius, E.-P. Heikkinen, Selective Zinc Removal from Electric Arc Furnace (EAF) Dust by Using Microwave Heating, *Journal of Sustainable Metallurgy.* 5 (2019) 331–340. <https://doi.org/10.1007/s40831-019-00222-0>.
- [4] G. Orhan, Leaching and cementation of heavy metals from electric arc furnace dust in alkaline medium, *Hydrometallurgy.* 78 (2005) 236–245. <https://doi.org/https://doi.org/10.1016/j.hydromet.2005.03.002>.
- [5] G. Salihoglu, V. Pinarli, Steel foundry electric arc furnace dust management: Stabilization by using lime and Portland cement, *J Hazard Mater.* 153 (2008) 1110–1116. <https://doi.org/https://doi.org/10.1016/j.jhazmat.2007.09.066>.
- [6] C.F. Pereira, Y.L. Galiano, M.A. Rodríguez-Piñero, J.V. Parapar, Long and short-term performance of a stabilized/solidified electric arc furnace dust, *J Hazard Mater.* 148 (2007) 701–707. <https://doi.org/https://doi.org/10.1016/j.jhazmat.2007.03.034>.
- [7] T. Havlík, B.V. e Souza, A.M. Bernardes, I.A.H. Schneider, A. Miškufová, Hydrometallurgical processing of carbon steel EAF dust, *J Hazard Mater.* 135 (2006) 311–318. <https://doi.org/https://doi.org/10.1016/j.jhazmat.2005.11.067>.
- [8] B. Janković, S. Stopić, A. Güven, B. Friedrich, Kinetic modeling of thermal decomposition of zinc ferrite from neutral leach residues based on stochastic geometric model, *J Magn Magn Mater.* 358–359 (2014) 105–118. <https://doi.org/10.1016/J.JMMM.2014.01.046>.
- [9] P. Palimaka, S. Pietrzyk, M. Stępień, K. Ciećko, I. Nejman, Zinc Recovery from Steelmaking Dust by Hydrometallurgical Methods, *Metals* . 8 (2018). <https://doi.org/10.3390/met8070547>.
- [10] T. Suetens, M. Guo, K. Van Acker, B. Blanpain, Formation of the ZnFe<sub>2</sub>O<sub>4</sub> phase in an electric arc furnace off-gas treatment system, *J Hazard Mater.* 287 (2015) 180–187. <https://doi.org/https://doi.org/10.1016/j.jhazmat.2015.01.050>.
- [11] C.-L. Li, M.-S. Tsai, Mechanism of Spinel Ferrite Dust Formation in Electric Arc Furnace Steelmaking, *ISIJ International.* 33 (1993) 284–290. <https://doi.org/10.2355/isijinternational.33.284>.
- [12] T. Suetens, M. Guo, K. Van Acker, B. Blanpain, Zn Loss into ZnFe<sub>2</sub>O<sub>4</sub> in an Open Type Electric Arc Furnace: An In-Process Separation Performance Model, *Journal of Sustainable Metallurgy.* 1 (2015) 297–303. <https://doi.org/10.1007/s40831-015-0033-5>.
- [13] L. Nedar, Dust formation in a BOF converter, *Steel Research.* 67 (1996) 320–327. <https://doi.org/https://doi.org/10.1002/srin.199605497>.
- [14] C.A. Pickles, Thermodynamic Modeling of Zinc Speciation in Electric Arc Furnace Dust, 30 (2011) 3–15. <https://doi.org/doi:10.1515/htmp.2011.001>.
- [15] C.A. Pickles, Thermodynamic modelling of the formation of zinc–manganese ferrite spinel in electric arc furnace dust, *J Hazard Mater.* 179 (2010) 309–317. <https://doi.org/10.1016/J.JHAZMAT.2010.03.005>.

- [16] Sureerat Polsilapa, David R. Sadedin, Panyawat Wangyao, Thermodynamics Analysis for the Zinc Ferrite Reduction by Hydrogen, *High Temperature Materials and Processes*. 30 (2011) 587–592. <https://doi.org/doi:10.1515/htmp.2011.119>.
- [17] A.G. Ryazanov, A. V. Senin, N.A. Kornilov, The Effect of Temperature and Roasting Time on the Conversion of Zinc Ferrite to Zinc Oxide in the Electric Arc Furnace Dust, *IOP Conf Ser Mater Sci Eng*. 969 (2020) 12040. <https://doi.org/10.1088/1757-899x/969/1/012040>.
- [18] P.S. and M.-A.V.E. C. W. Bale, E. Bélisle, P. Chartrand, S. A. Deckerov, G. Eriksson, A.E. Gheribi, K. Hack, I. H. Jung, Y. B. Kang, J. Melançon, A. D. Pelton, S. Petersen, C. Robelin. J. Sangster, *FactSage Thermochemical Software and Databases, Calphad*. 54 (2016) 35–53.
- [19] A. Hosseini, V. Dhiman, K. Meijer, C. Zeilstra, J. Hage, T. Peeters, E. Offerman, Y. Yang, CFD Modelling of Off-gas System HIsarna Iron Making Process Part 2: Reflux Chamber Geometry Modification and Effects on Flow Behaviour, *Ironmaking & Steelmaking*. (2022). <https://doi.org/10.1080/03019233.2022.2060457>.

# Chapter 8

## FLUIDIC OSCILLATOR FOR POST-COMBUSTION

This chapter explores the utilization of a fluidic oscillator for introducing oxidant into the reflux chamber. The fluidic oscillator is a stationary device that converts steady pressurized inlet flow into oscillatory flow at the exit without requiring external power. It can enhance turbulence intensity and the dispersion of oxygen in the injection zone, thereby improving the mixing of fuel and oxidant. Additionally, it contributes to achieving better residence time distribution within the combustion zone.

A CFD analysis of the fluidic oscillator is conducted, and a specific geometry is proposed. The oscillator is then integrated into the main body of the reflux chamber, and a reactive flow analysis is performed to assess its impact on combustion efficiency and the removal of the CO-H<sub>2</sub> mixture.

The findings indicate that the oscillator can achieve the removal of undesired species in a shorter length of the reflux chamber while using a lower flow rate for injected oxygen.



## 8.1. Introduction

The effect of turbulence on the combustion process has been the subject of many researches. The importance of turbulent flow becomes more evident for the lean combustion process where the availability of fuel is limited.

In such cases, combustion efficiency is influenced not only by the overall quality of the lean mixture and the residence time within the combustion chamber but also by the mixing process itself. To achieve a higher mixing rate, turbulent flow is created inside the combustion chamber. In general, increased turbulence leads to better mixing capabilities within the flow. Turbulence in combustion chambers is primarily generated by introducing swirl flow into the combustor and breaking down large fuel injectors into several smaller ones. Augmenting turbulence intensity within the combustion chamber effectively accelerates flame propagation speed and enhances the combustion performance [1].

Fubai Li et al. [1] have shown that increasing the turbulence intensity inside pistol engines (by geometrical modifications) can significantly improve the combustion of a flue lean mixture of natural gas.

In another study, Fru et al. [2] performed direct numerical simulation (DNS) of a premixed methane-air fuel in a laminar and turbulent regime. They observed a linear increase in flame propagation speed with turbulence intensity. However, local quenching events were reported for highly turbulent conditions and leaner mixtures beyond a certain turbulence intensity threshold. Despite these quenching events, they concluded that turbulence intensity positively affects flame propagation speed.

Rose et al. [3] conducted a CFD analysis of turbulent jet combustion, focusing on the impact of turbulence intensity on temperature and CO mass fraction in a turbulent reacting gas-particle mixture. They observed that turbulence intensity significantly influenced the evolution of the temperature field. In scenarios with higher turbulence, enhanced transport led to improved mixing of CO with fresh air further downstream, resulting in a lower concentration of unburnt CO. In contrast, lower turbulence intensity resulted in incomplete CO combustion, causing concentrated CO to exit the combustion domain. The situation inside the HIsarna post-combustion chamber is not similar to a regular combustion chamber; however, learning from other studies, it can be concluded that inducing highly turbulent zones



(recirculation) will result in better mixing and, therefore, much more effective combustion. In the HIsarna off-gas system, the fuel is lean (CO-H<sub>2</sub> mixture) and comes from the lower part of the furnace. Oxygen is injected directly into the flue gas path. This injection is designed to penetrate the flue gas and promote mixing. The objective is to enhance turbulence intensity in the vicinity of the oxygen injection zone. Several solutions have been proposed to address this challenge. For instance, one approach involves modifying the injector to induce a swirling motion in the oxidant flow. However, this method still has limitations in terms of achieving efficient mixing, and oxygen distribution near the injection zone remains uneven. The most promising solution to date is the implementation of a fluidic oscillator as an oxidant injector. The use of this equipment makes it possible to generate higher turbulence and achieve better oxygen dispersion near the oxygen injection zone. This will lead to better combustion of the CO-H<sub>2</sub> mixture with lower oxygen injection in a shorter length of the reflux chamber. Fluidic oscillators are a kind of non-moving devices that convert steady pressurized inlet flows to an oscillatory flow or pulsatile flows at the exit without any need for external power [4]. Fluidic oscillators, also known as sweeping jets, are interesting equipment in mechanical science due to their unique properties and applications. The jet's unsteady nature and momentum addition's distributed nature make it very attractive to the engineering community [5]. Figure 8-1 shows a common geometry of a fluidic oscillator with related terminologies. The general working principle of such a device is quite simple and shown in sequence in Figure 8-2.

It is best described by Hossain et al. [5] as follows:

*“A jet enters into the cavity from a pressurized inlet via the **power nozzle**. Then, the power jet expands to fill the throat and the feedback channels. Two opposite vortices begin to form on both sides of the power jet. As the intensity of the vortices increases, one vortex becomes dominant. This causes the power stream to deflect against the opposite wall. When the power stream deflects to the side wall, it attaches to it due to the “Coanda effect.” This allows a portion of the fluid to enter into the same side **feedback channel**, which flows back to the **control port** and causes the power stream to detach from the side wall. The power stream then switches to the opposite wall, and the same process repeats, resulting in an oscillatory fluid motion at the exit of the throat [5]”.*

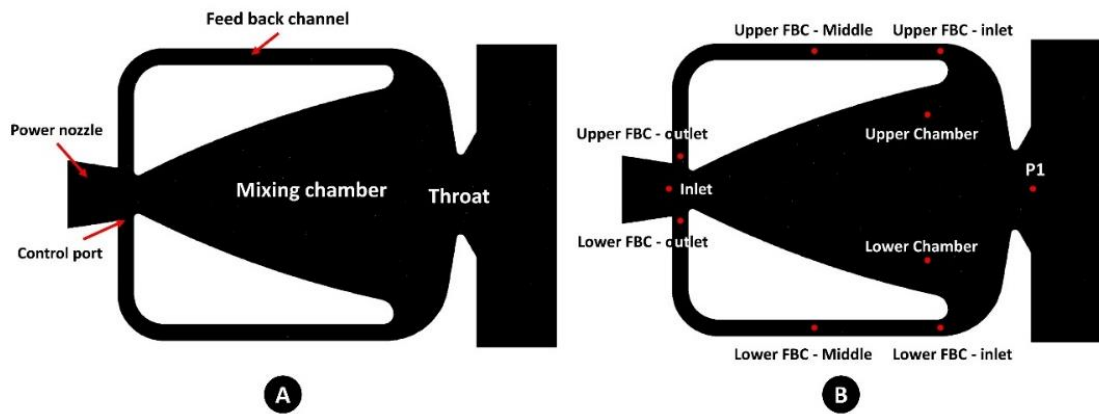


Figure 8-1. Illustration of the fluidic oscillator (A) and possible monitoring point for CFD calculations (B)

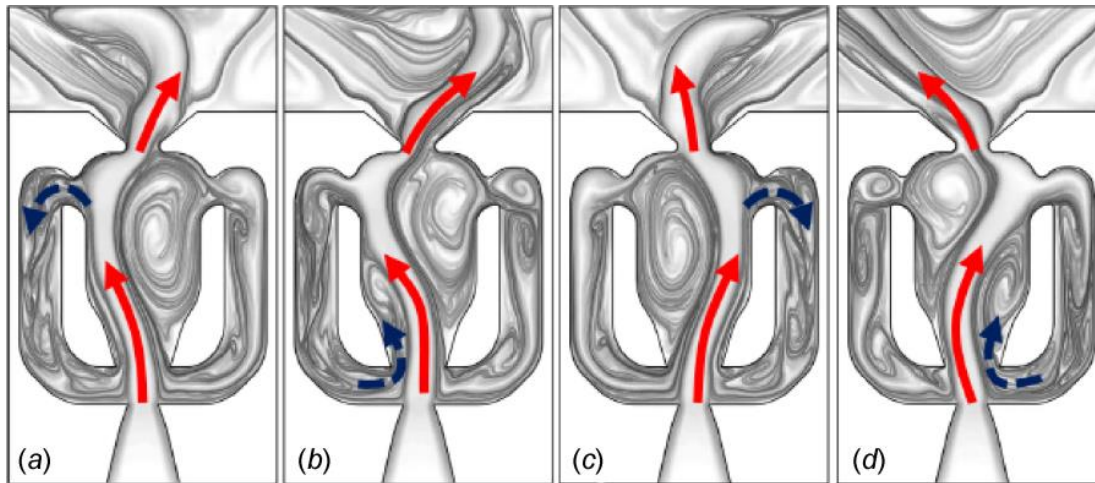


Figure 8-2. Fluidic oscillator schematic and sequence of switching mechanism [5]

Fluidic oscillators have great potential in the fields of mixing enhancement, intensification of turbulence levels, skin friction reduction, wide spreading of fluid jets instead of impinging spots, stimulation of special vibration modes, creation of various sweeping flow patterns, periodic disturbing of boundary layers and heat transfer enhancement [4,5]. Its application has been verified in many industries, including controllers, chemicals and processes, medicals, instrumentations, HVAC, and heat transfer [4]. A short review of some of the performed research on oscillator applications is listed in Table 8-1.

To discuss a few, Joulaei et al. [6] investigated the effect of the sweeping motion of the fluidic oscillator on heat transfer over a hot plate, as shown in Figure 8-3. They have reported a better heat transfer using the fluidic oscillators and have modified the geometry for further enhancement of Nusselt number. The same finding is confirmed by other studies on heat transfer improvement [5–7,17–19].

Table 8-1. Summary of few performed reaches on fluidic oscillator application in fluid flow

Mechanism	Application – studied parameters	Fluid	Reference
Heat transfer	Hot plate impinged by a sweeping jet	Gas (Air)	[6][7][5]
Heat transfer	Impingement cooling flow and the heat transfer processes over a concave and a convex surface	Gas (Air)	[7]
Heat transfer	Slot-air-jet	Gas (Air)	[7]
Heat transfer	Film cooling	Gas (Air)	[5]
Heat transfer	Microchannel heat exchanger	liquid (Water)	[8]
Flow control	Impinging jet flow and heat transfer on a semi-circular concave surface	Gas (Air)	[9]
Flow control	Jet impingement cooling on a concave surface	Gas (Air)	[10]
Flow control	Fluidic amplifier in the liquid-jet hammer	liquid	[11]
Flow control	Actuator	Gas (Air)	[12]
Erosion behaviour	Fluidic DTH hammer	Gas-particles	[13]
Erosion behaviour	Downhole cleaning device	Gas (Air)	[14]
Drilling and erosion	Bi-stable fluidic amplifier in the liquid-jet hammer	liquid	[11]
Active controlling boundary layer separation	Low-pressure turbine	Gas (Air)	[15]
Active combustion control	Gas turbine	Gas (Natural gas)	[16]

In another interesting study, Qu et al. [15] performed a CFD analysis to investigate the control mechanism of a fluidic oscillator in the suppression of non-reattachment separation of a boundary layer from an ultra-high-lift low-pressure turbine under a low Reynolds number.

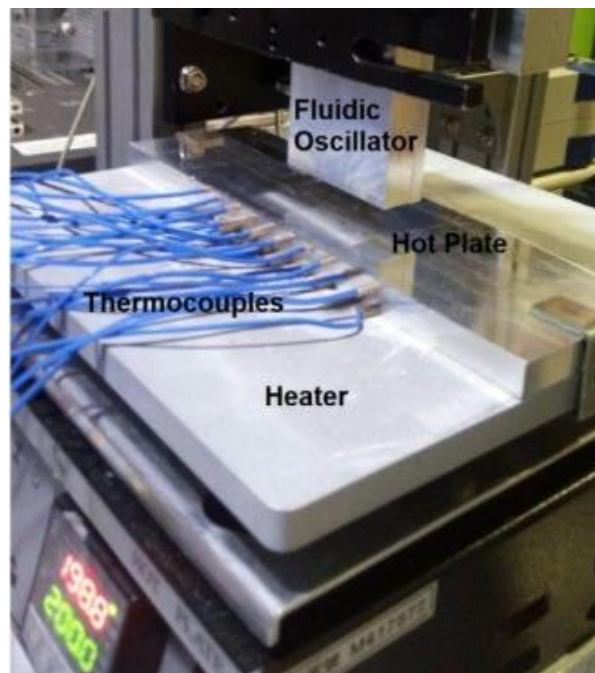


Figure 8-3. Experimental set up of Joulaei et al. [6]

It was found that the pulse jet of the fluidic oscillator generated a stream-wise vortex pair above the surface of the blade suction, which promoted an exchange of momentum between the boundary layer for the blade suction surface and the main flow and suppressed boundary layer separation as shown in Figure 8-4.

The stream-wise vortex pair at  $\theta=30^\circ$  showed the characteristics of higher strength, smaller size, slower decay, and longer penetration distance than the results at  $\theta=90^\circ$ , such that the momentum exchange between the low-energy fluid inside the boundary layer and the main flow is sustainable, which promoted the laminar boundary layer to produce bypass transition and significantly improved the aerodynamic performance of the turbine.

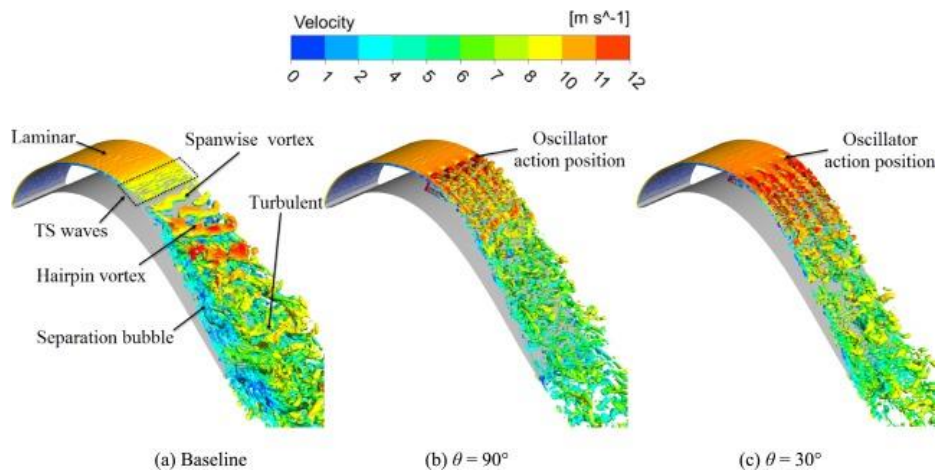


Figure 8-4. Velocity iso-surface contour of the obtained result for fluidic oscillator application in the study of Qu et al. [15]

Guyot et al. [16] have studied the application of a fluidic oscillator in fuel flow modulation and optimization for two different burner configurations: a bluff body burner and a generic swirl-stabilized burner. Based on their observations, the fluidics' fuel flow modulation caused a significant reduction of the pressure oscillations. The results obtained in this work show that the fluidic oscillator allows for fuel modulation and, hence, combustion control without the need for complex and fast-moving parts, thus ensuring a long actuator lifetime. This makes the fluidic oscillator highly appropriate for application in industrial gas turbines.

Ming et al. [8] have conducted an interesting research on applying fluidic oscillators in the microchannel heat exchanger. They have reported that the sweeping jets, generated by the fluidic oscillator array, created higher averaged Nusselt numbers and more uniform temperatures on the target surface than the direct jets. Micro-

channel heat exchangers integrated with the fluidic oscillator arrays were promising for cooling electronics with large surfaces.

In this chapter, the application of a fluidic oscillator for oxygen injection into the HIsarna post-combustion chamber (reflux chamber) is proposed and investigated in detail. Based on the literature review, and as discussed before, there is only the study by Guyot et al. [16] on the application of the fluidic oscillator for the combustion process. However, they have utilized it for injecting fuel, not the oxidizer. To the author's knowledge, this is the first large-scale application of this equipment in a post-combustion application for CO-H<sub>2</sub> mixture.

## 8.2. Transient simulation of fluidic oscillator

### 8.2.1. Governing equation

In this section, the fluidic oscillator is simulated as a standalone equipment with a turbulent non-reactive model. k- $\epsilon$  model is unable to capture the fluctuating nature of the flow. Therefore, the utilized turbulence model has to be either k- $\omega$  or large eddy simulation (LES) approach. Here k- $\omega$  is used for turbulence modelling since the LES model requires a much finer mesh grid and higher computing power. The governing equations are the same as explained in detail in Chapter 2.

### 8.2.2. Geometry, mesh, and boundary conditions

Figure 8-5 shows the proposed oscillator geometry with related dimensions. The mesh is generated by embedding uniform 1 mm polyhedral cells and five uniform inflation layers (prism cells), leading to a grid with approximately 800,000 cells. For k- $\omega$  turbulence model ( $y^+$  is kept around unity).

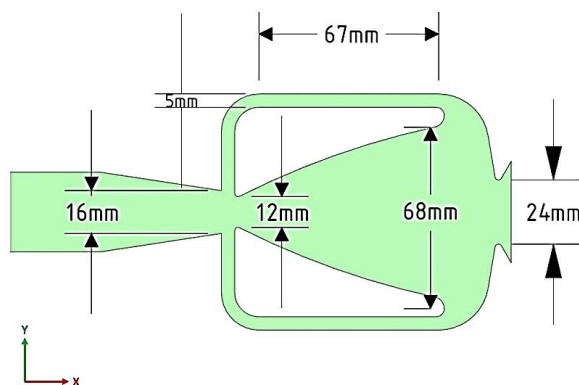


Figure 8-5. Proposed fluidic oscillator geometry and dimensions

Table 8-2 shows the inlet boundary condition imposed during the calculations. Pure oxygen is injected at the inlet of the oscillator at 293 K and initially with a flow rate of 0.27 kg/s. The flow rate is reduced by 50% (0.135 kg/s) to ensure the proposed design creates oscillation with proper frequencies for different flow rates.

Table 8-2. Inlet condition for oscillator CFD modelling

Parameter	value
Flow rate [kg/s]	0.27 to 0.135
Temperature [K]	293
Operating Pressure [bar]	1
Density [Kg/m <sup>3</sup> ]	Ideal gas relation

### 8.2.3. CFD results

The oscillation is monitored at the outlet and “throat” of the oscillator (Point P1 in Figure 8-1.B) as a vortex average of  $\alpha = \tan^{-1}\left(\frac{V_y}{V_x}\right)$  which will be called “Amplitude” from now on. Figure 8-6 shows the transient calculated amplitude.

After acquiring a steady oscillation, the flow rate is reduced to 0.135 kg/s at 0.154 seconds of the simulation. As can be seen, there is a slight difference in the generated oscillation. Figure 8-6 shows the Fast Fourier Transform (FFT) analysis of the obtained oscillation, which better reveals this slight difference.

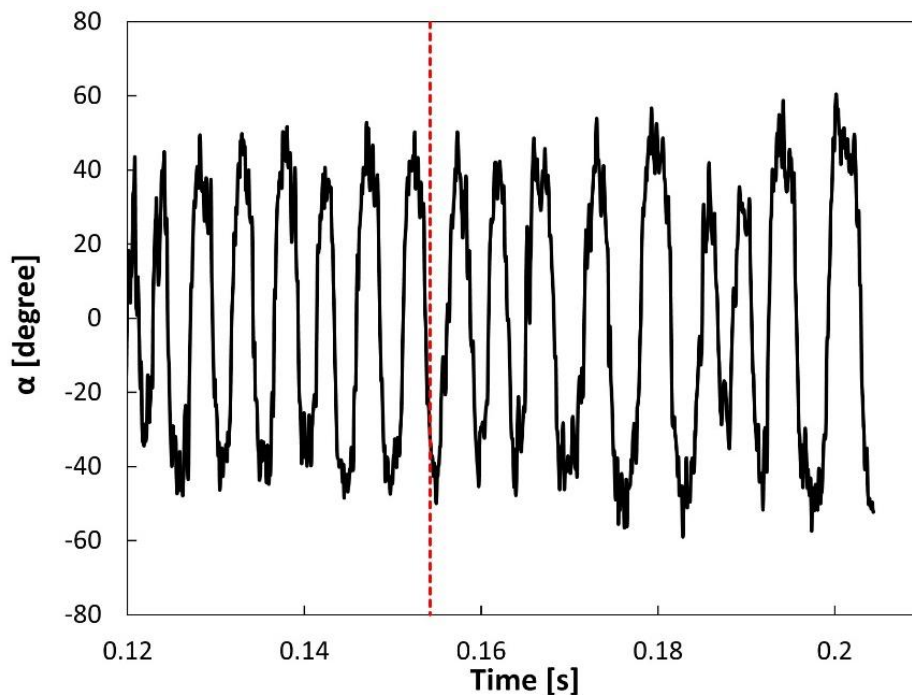


Figure 8-6. Predicted oscillation amplitude for flow rate of 0.27 and 0.135 kg/s



After achieving a steady oscillation, the flow rate is reduced to 0.135 kg/s at 0.154 seconds into the simulation. There is a slight difference in the generated oscillation. The Fast Fourier Transform (FFT) analysis of the obtained oscillation in Figure 8-7 better reveals this slight difference. From the analysis, reducing inlet flow generates an oscillation with slightly higher amplitude and lower frequency. Nevertheless, in both cases, the oscillation is stable.

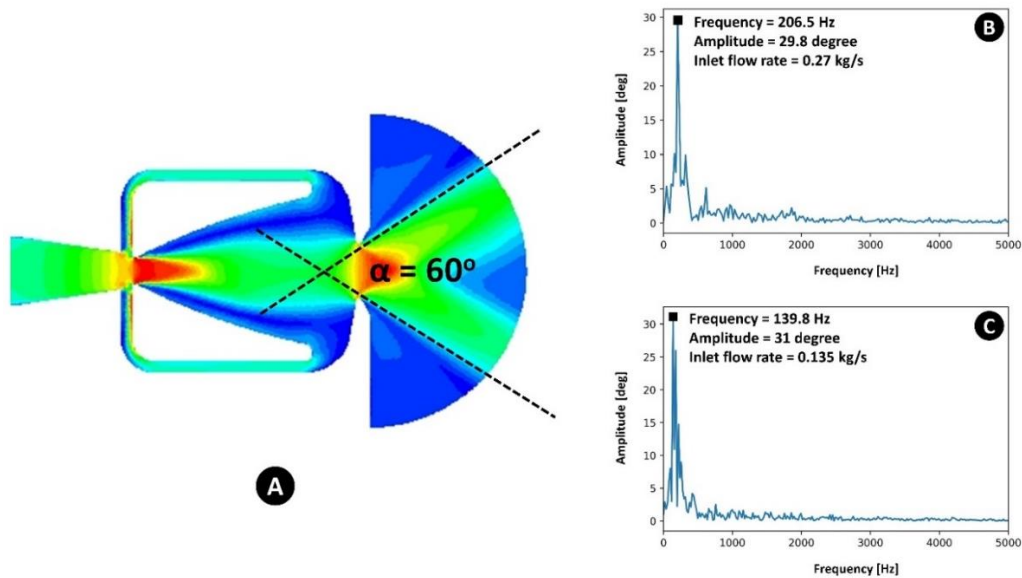


Figure 8-7. Transient average velocity contour (A) and FFT analysis of the oscillation amplitude for 0.27 kg/s (B) and 0.135 kg/s (C)

The fluidic oscillator can significantly increase the outlet velocity compared to the velocity at the inlet. This is mainly due to the converging-diverging geometry of both inlet and outlet. The Mach number can reach a value close to unity, as illustrated in Figure 8-8. Therefore, in cases where subsonic flow is of interest, care must be taken in the geometrical design and assigned inlet condition.

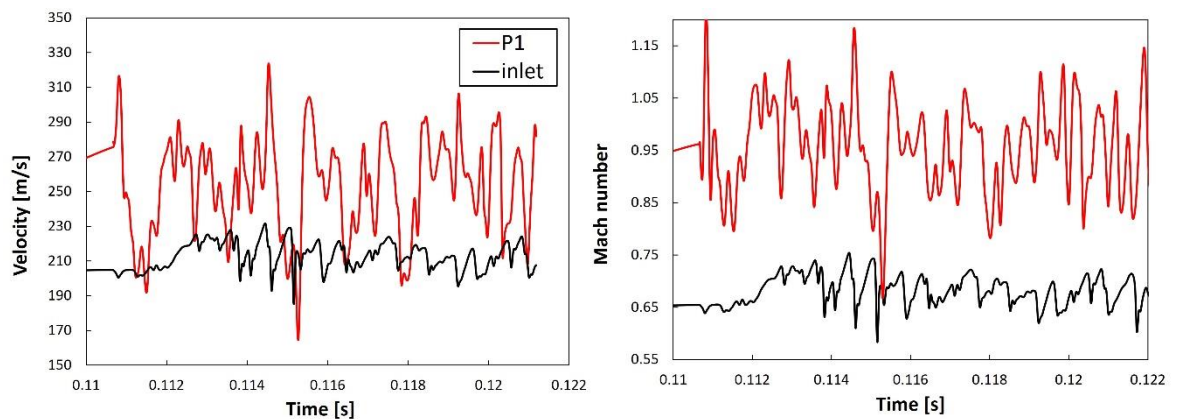


Figure 8-8. Predicted velocity and Mach number at inlet and outlet of the oscillator (see Figure 8-1 .B)

### 8.3. Fluidic oscillator for post-combustion

Now that a proper oscillator design is obtained, it is time to investigate the effect of the oscillator once it is used as an injector. The oscillator injector will be called osci-injector from now on.

#### 8.3.1. Geometry, mesh, and boundary conditions

For this study, the boundary conditions differ slightly from those in previous chapters. Previously, the incompressible ideal gas law was used for density calculations, which is a valid assumption for flow velocities below the speed of sound (subsonic flow). However, when using the oscillator, the local Mach number can reach 1.5, making it necessary to account for the compressibility of the flow by using the compressible ideal gas law for density calculations. Table 8-3 shows the boundary conditions for both static and oscillator injection cases. A relatively high amount of CO (10%) is introduced at the reflux chamber inlet to better observe the oscillator's effect in a fuel-rich flow. Composition profiles, swirl motion, and carbon particles at the inlet are omitted in all simulations for simplicity.

Table 8-3. Boundary condition for the simulations

<b>Flue gas inlet</b>	<b>Value</b>
Mass flow [kg/s]	4.33
Composition mole fraction	
CO	0.1
H <sub>2</sub>	0.002
H <sub>2</sub> O	0.20
N <sub>2</sub>	0.166
CO <sub>2</sub>	0.532
<b>Oxygen injection</b>	
Mass flow [kg/s]	0.27
Composition mole fraction	
O <sub>2</sub>	0.995
N <sub>2</sub>	0.005

For both cases, coupled solver is used with a time step of  $10^{-4}$ . Since the oscillator case has a fluctuating nature, data sampling for steady statistics is activated to acquire a steady average solution.

#### 8.3.2. CFD results

Figure 8-9 compares CO, O<sub>2</sub>, and turbulent intensity contour for both static and osci-injectors. The impact of the osci-injector is immediately apparent. The osci-injector



significantly enhances the oxygen dispersion near the injection zone compared to the static injector, primarily due to the sweeping motion it induces. This sweeping motion promotes turbulent flow over a broader area and elevates turbulence intensity in the injection zone, as depicted in the same figure.

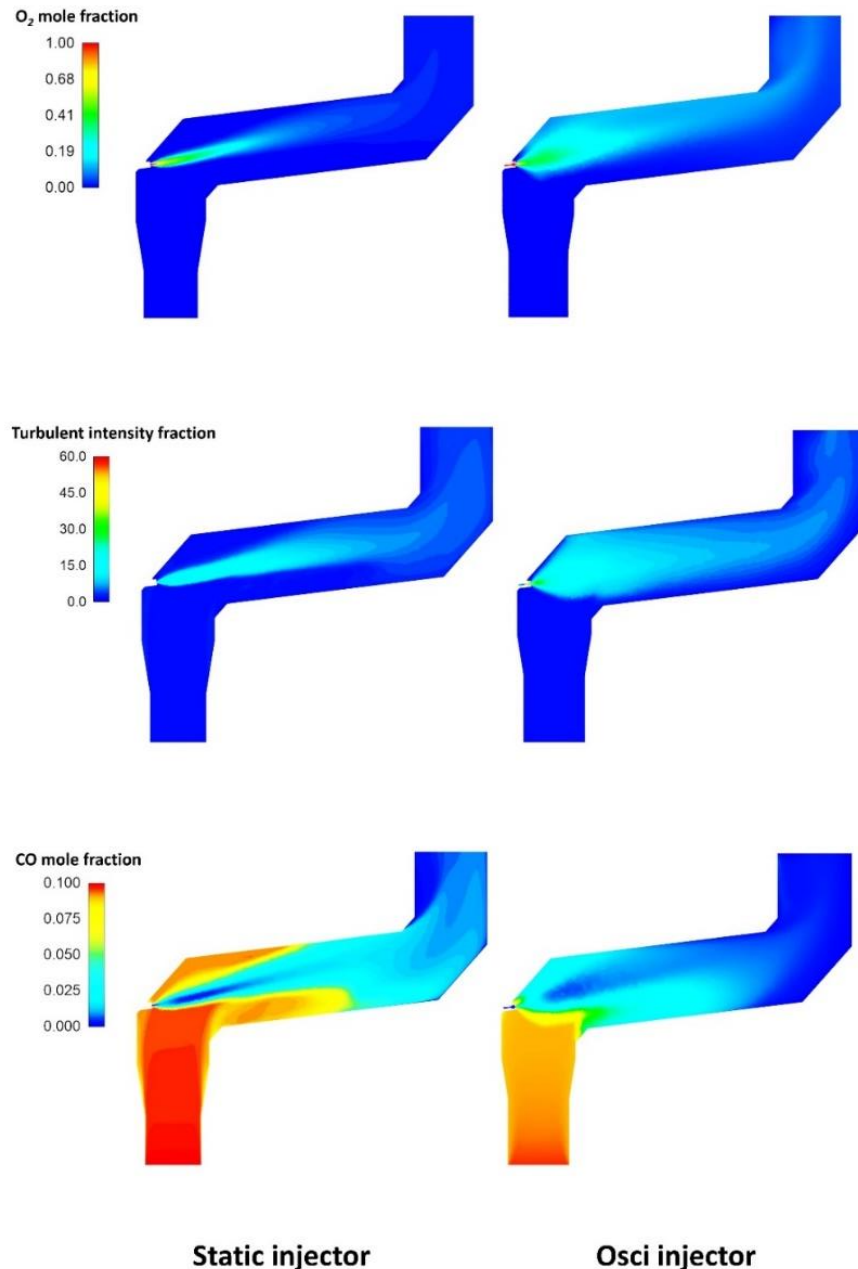


Figure 8-9. Turbulent intensity, CO and O<sub>2</sub> mole fraction contour for both static and osci-injector. Improved oxygen distribution and increased turbulence intensity can result in higher CO combustion efficiency. Figure 8-10 quantitatively compares the two different injectors regarding various combustion parameters. It is evident that the

osci-jet can achieve more efficient CO combustion within a shorter section of the reflux chamber, exhibiting a higher consumption rate and lower emissions at the outlet. The other important effect of the osci-jet is the local reduction of the flow temperature in the injection zone due to better mixing of the cold-injected oxygen. This can also potentially lead to a higher CO combustion efficiency as a very high temperature is detrimental to the CO consumption reactions since it will trigger the reverse reactions (see Chapter 3, section 3.8).

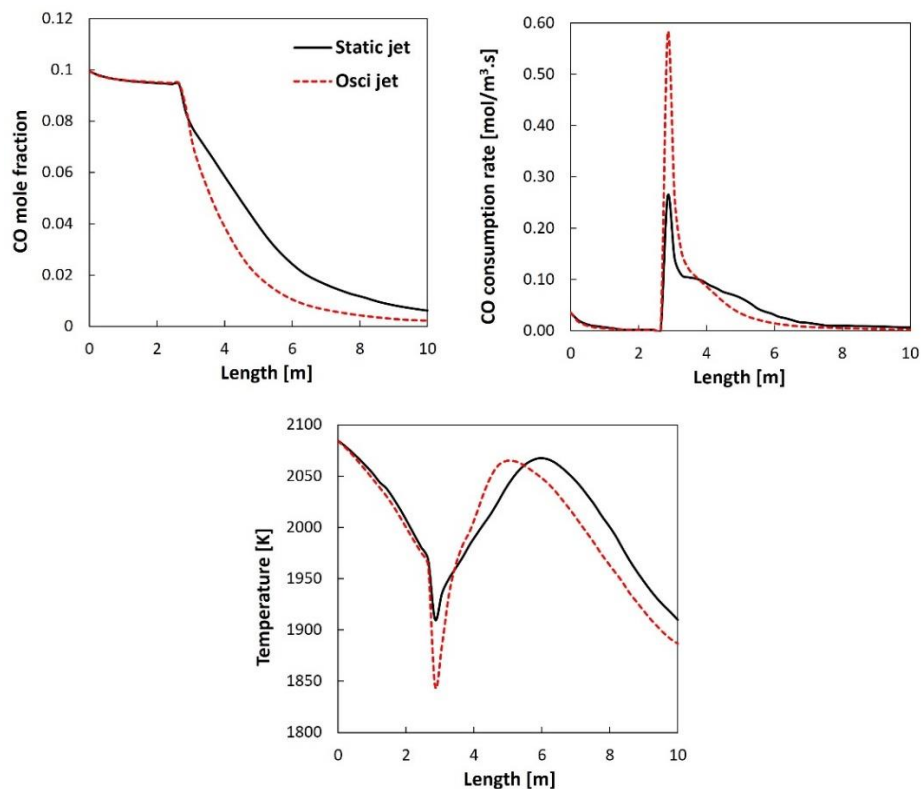


Figure 8-10. Calculated profiles for static and osci-jet injectors

Due to these promising results, the proposed geometry is already built and will be tested in the coming HIsarna trials.

## 8.4. Conclusion

This chapter investigates the application of the fluidic oscillator for large-scale CO-H<sub>2</sub> removal in the reflux chamber. Currently, the oxygen is injected through a static injection using a straight nozzle. The preferred approach is to eliminate all undesired compounds within the reflux chamber, where temperatures are at their highest. While the CO-H<sub>2</sub> mixture emitted from the reflux chamber can still be removed above the air quench, the transient nature of the process may result in CO

concentrations exceeding 10% at the reflux chamber inlet. These elevated levels cannot be effectively removed within the off-gas system. Therefore, the goal is to enhance the removal efficiency of the CO-H<sub>2</sub> mixture within the reflux chamber.

Simulation results demonstrate that the utilization of the oscillator can enhance the dispersion of oxygen and increase turbulence intensity within the reflux chamber, leading to a higher removal efficiency of the CO-H<sub>2</sub> mixture. However, additional parametric studies are necessary to optimize the fluidic oscillator's application. For example, the injection angle is currently set at 7°, similar to the static injector. A sensitivity analysis is required to determine the ideal angle for the osci-jet geometry. Another vital parameter is the injected flow rate, which can be further reduced and fine-tuned based on the CO content of the flue gas. This flexibility is attributed to the oscillator's ability to distribute oxygen more effectively within the reflux chamber.

It is worth noting that the application of the oscillator for CO-H<sub>2</sub> mixture post-combustion is at the initial stage, and more detailed studies for better designs are required. Moreover, the effect of carbon particles in this study is omitted, which could affect the outcome of the model.

## References

- [1] F. Li, C. Liu, H. Song, Z. Wang, Improving Combustion and Emission Characteristics in Heavy-Duty Natural-Gas Engine by Using Pistons Enhancing Turbulence, (2018). <https://doi.org/https://doi.org/10.4271/2018-01-1685> UI - 2018-01-1685.
- [2] G. Fru, D. Thévenin, G. Janiga, Impact of Turbulence Intensity and Equivalence Ratio on the Burning Rate of Premixed Methane–Air Flames, *Energies* . 4 (2011). <https://doi.org/10.3390/en4060878>.
- [3] M. Rose, S.M. Frolov, P. Roth, M.G. Neuhaus, Application of a lagrangian PDF Method to Turbulent Gas/Particle Combustion, in: W. Rodi, D.B.T.-E.T.M. and E. 4 Laurence (Eds.), Elsevier Science Ltd, Oxford, 1999: pp. 851–860. <https://doi.org/https://doi.org/10.1016/B978-008043328-8/50082-5>.
- [4] S. Ghanami, M. Farhadi, Fluidic Oscillators' Applications, Structures and Mechanisms-A review, 7 (2019) 9–27. <https://doi.org/10.22111/tpnms.2018.25051.1153>.
- [5] M.A. Hossain, R. Prenter, R.K. Lundgreen, A. Ameri, J.W. Gregory, J.P. Bons, Experimental and Numerical Investigation of Sweeping Jet Film Cooling, *J Turbomach.* 140 (2017). <https://doi.org/10.1115/1.4038690>.
- [6] A. Joulaei, M. Nili-Ahmadabadi, K. Chun Kim, Parametric study of a fluidic oscillator for heat transfer enhancement of a hot plate impinged by a sweeping jet, *Appl Therm Eng.* 205 (2022) 118051. <https://doi.org/https://doi.org/10.1016/j.applthermaleng.2022.118051>.
- [7] C. Gau, C.M. Chung, Surface Curvature Effect on Slot-Air-Jet Impingement Cooling Flow and Heat Transfer Process, *J Heat Transfer.* 113 (1991) 858–864. <https://doi.org/10.1115/1.2911214>.
- [8] T. Ming, Z. Wang, X. Liao, T. Shi, G. Tan, Y. Wu, Unsteady RANS simulation of fluid dynamic and heat transfer in an oblique self-oscillating fluidic oscillator array, *Int J Heat Mass Transf.* 177 (2021) 121515. <https://doi.org/https://doi.org/10.1016/j.ijheatmasstransfer.2021.121515>.
- [9] M. Choi, H.S. Yoo, G. Yang, J.S. Lee, D.K. Sohn, Measurements of impinging jet flow and heat transfer on a semi-circular concave surface, *Int J Heat Mass Transf.* 43 (2000) 1811–1822. [https://doi.org/https://doi.org/10.1016/S0017-9310\(99\)00257-4](https://doi.org/https://doi.org/10.1016/S0017-9310(99)00257-4).
- [10] G. Yang, M. Choi, J.S. Lee, An experimental study of slot jet impingement cooling on a concave surface: effects of nozzle configuration and curvature, *Int J Heat Mass Transf.* 42 (1999) 2199–2209. [https://doi.org/https://doi.org/10.1016/S0017-9310\(98\)00337-8](https://doi.org/https://doi.org/10.1016/S0017-9310(98)00337-8).
- [11] J.-M. Peng, Q. Zhang, G. Li, J.-W. Chen, X. Gan, J. He, Effect of geometric parameters of the bistable fluidic amplifier in the liquid-jet hammer on its threshold flow velocity, *Comput Fluids.* 82 (2013) 38–49. <https://doi.org/https://doi.org/10.1016/j.compfluid.2013.05.002>.
- [12] J.W. Gregory, E.P. Gnanamanickam, J.P. Sullivan, S. Raghu, Variable-Frequency Fluidic Oscillator Driven by a Piezoelectric Bender, *AIAA Journal.* 47 (2009) 2717–2725. <https://doi.org/10.2514/1.44078>.
- [13] L. Tang, S. Zhang, X. Zhang, J. Peng, U. Shabir, Numerical investigation of the dynamic erosion behavior in fluidic oscillators with a periodic oscillating jet, *Powder Technol.* 395 (2022) 634–644. <https://doi.org/https://doi.org/10.1016/j.powtec.2021.10.011>.
- [14] E.D. Webb, R.L. Schultz, R.G. Howard, J.C. Tucker, Next Generation Fluidic Oscillator, SPE/ICoTA Coiled Tubing Conference & Exhibition. (2006) SPE-99855-MS. <https://doi.org/10.2118/99855-MS>.

- [15] X. Qu, Y. Zhang, X. Lu, J. Zhu, Y. Zhang, Unsteady fluidic oscillators for active controlling boundary layer separation in an ultra-high-lift low-pressure turbine, *Aerosp Sci Technol.* 119 (2021) 107130. <https://doi.org/https://doi.org/10.1016/j.ast.2021.107130>.
- [16] D. Guyot, B. Bobusch, C.O. Paschereit, S. Raghu, Active Combustion Control Using a Fluidic Oscillator for Asymmetric Fuel Flow Modulation, in 44th AIAA/ASME/SAE/ASEE Joint Propulsion Conference & Exhibit, American Institute of Aeronautics and Astronautics, 2008. <https://doi.org/doi:10.2514/6.2008-4956>.
- [17] C.M. Khalde, A. V Pandit, J.S. Sangwai, V. V Ranade, Flow, mixing, and heat transfer in fluidic oscillators, *Can J Chem Eng.* 97 (2019) 542–559. <https://doi.org/https://doi.org/10.1002/cjce.23377>.
- [18] V. Tesar̃, Flow pulsation in the near-wall layer of impinging jets, *EPJ Web Conf.* 45 (2013).
- [19] G. Saliba, V. Raimbault, S. Colin, A. Batikh, S. Orioux, R. Gilblas, L. Baldas, Jet impingement cooling using fluidic oscillators: an experimental study, *J Phys Conf Ser.* 2116 (2021) 12028. <https://doi.org/10.1088/1742-6596/2116/1/012028>.

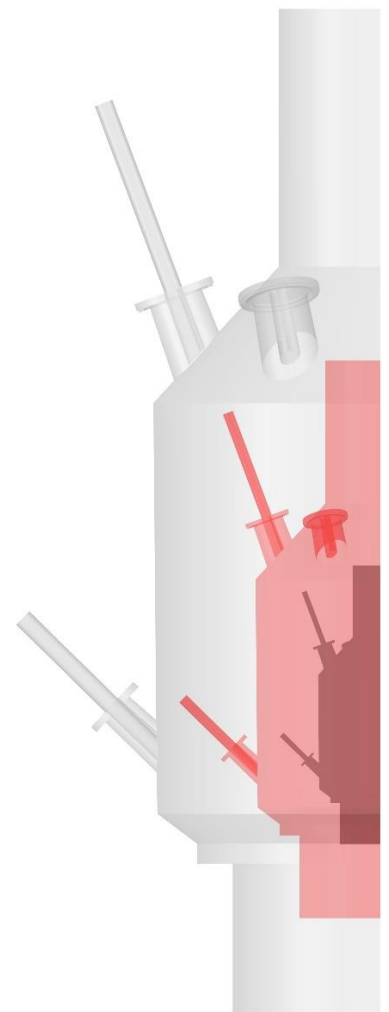
# Chapter 9

## SCALE UP FROM PILOT TO INDUSTRIAL SCALE

**This chapter is based on the following paper:**

Hosseini, A., Hage, J.L.T., Duiker, A. et al. Off-Gas System Scale-Up of HIsarna IronMaking Process: A CFD-Based Approach. *Metall Mater Trans B* 53, 3557–3574 (2022). <https://doi.org/10.1007/s11663-022-02620-4>

For all industrial applications, predicting system characteristics and behaviour plays a vital role before constructing costly and complex multi-physics systems. Correct and reliable predictions become even more important once the aim is to go from small to large-scale processes to establish an industrial demonstration. In this chapter, a CFD-based scale-up of the HIsarna off-gas system is performed, and detailed steps in the scale-up procedure are discussed. A three-dimensional CFD model is developed and validated based on the available pilot scale data and used to design and scale up the off-gas system. Only one part of the off-gas system, the reflux chamber, is studied. Detailed kinetics for volumetric and gas-solid reactions are incorporated in the validated model with special attention to the wall boundary condition and modelling. The effects of reflux chamber geometry, oxygen injection ports, oxygen injection flow rate, isolation wall thickness, and inlet flue gas composition on different system characteristics, such as heat loss through the wall, CO-H<sub>2</sub>-Carbon mixture conversion, flue gas, and wall temperature are investigated. The aim of the scaled-up geometry, like the pilot scale, is to achieve complete combustion of the unwanted species inside the reflux chamber to ensure zero emissions from the off-gas system. Compared to the pilot scale, the scaled-up reflux chamber can handle and remove a higher fraction of unwanted species coming from the main reactor, leading to lower CO-H<sub>2</sub> and carbon particle emissions. This improvement is mainly due to a higher volume, which provides longer residence time for the volumetric and gas-solid reaction to proceed.



## 9.1. Introduction

One of the most challenging engineering tasks is the scale-up of a device, a reactor, or a process. Scale-up aims to successfully reproduce a desired product when manufactured commercially [1]. To successfully move from small to large scale, one must understand how the size variation impacts physical and chemical phenomena. The information transfer between the different scales is crucial because similar yields and conversions should be achieved in both large and small scales. The construction and operating parameters are often changed during the scale-up procedures to maintain the same performance.

The scale-up procedure usually starts from the “laboratory scale” (lab scale), in which fundamental questions about the process, such as different interphase interactions, flow properties, production efficiency, etc., are investigated, and the feasibility of a process is determined. The process then is scaled up to a “pilot scale” to study operational parameters and avoid the risk of direct scaling to a full scale. In some cases, before going to full commercial scale, scale-up from pilot to “demonstration scale” (demo scale) might be necessary. Demo scale is sometimes the final technology hurdle in the decision to go commercial. Demonstration plants differ from pilot plants in that the equipment and process flowsheet resemble commercial scale much more closely. Utilizing the demonstration scale, large quantities of the final product can be produced for market testing, and its success will determine the viability of the new product's development under the quality criteria required by the client. Finally, the commercial (industrial) scale is constructed using research findings and operational experience from previous scales.

The current HIsarna plant is built on a pilot scale, capable of producing 60,000 tons of hot metal per year (thm/yr). This pilot plant's demo and industrial scale will be built in Jamshedpur, India, with a capacity of 400,000 thm/yr and 1 million thm/yr, respectively. Figure 9-1 shows a schematic view of the main reactor for different scales.

Traditionally, dimensionless numbers and experimental correlations have been used to calculate a scaled-up unit's proper operating parameters and sizes. However,

extrapolating such correlations beyond the experimental dataset is untenable due to the possibly existing non-linearities and neglecting geometric differences and complexities in correlations [2]. Furthermore, using dimensionless numbers and correlations can make the scale-up process complex and does not always yield the expected results [1].

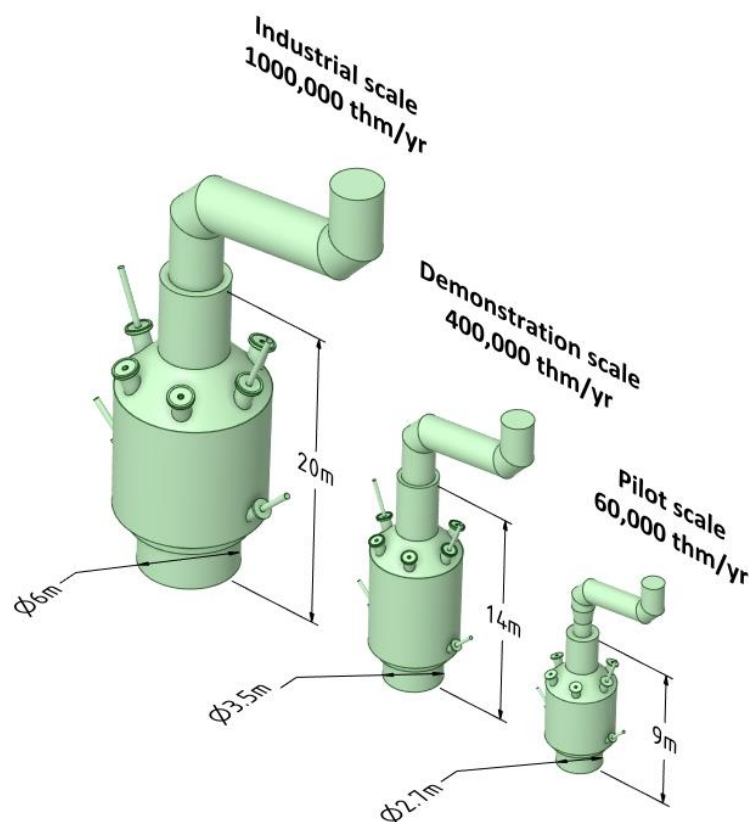


Figure 9-1. Scaled-up scheme of main reactor and reflux chamber for the pilot, demo, and industrial scale

CFD tools have become an excellent alternative to dimensionless number-based methods with the development of computational capacity. Detailed phenomena can be implemented in CFD models with which the scale-up calculation can be much easier and more effective than traditional methods [1, 2]. There are many CFD-assisted scale-up studies in literature for different processes such as fermentation [3–5], coal combustion, gasification, burners [6–9], bioreactors and bubble columns [1,2,10–13], gas cleaning and upgrading [14,15], spouted and fluidized beds [11,19,20] and crystallization [18].

To mention a few, Azuhata et al. [6] have performed a CFD-based scale-up of a laboratory scale coal burner to a scale with a 25 times higher coal feed rate. They



have developed and validated a base model using laboratory data and modelled the scaled-up cases to evaluate the performance and the gaseous composition profiles in the flame of the large-scale furnace. According to the derived results, mixing times of oxidant with fuel is a major problem in scale-up for coal combustors.

In another study, Singh et al. [7] used laboratory data from a gas-solid vortex reactor to develop a CFD model for scale-up purposes. A geometrical optimization was performed by investigating the effect of length to diameter ratio on solid loading capacity and particle loss in the reactor.

Biglari et al. [9] have performed the scale-up of a small-scale fluidized bed gasifier using both CFD and dimensionless numbers and reported accurate hydrodynamics and pressure drop predictions using CFD models. Important design and operation parameters such as minimum fluidization velocity and solid velocity are accurately predicted. They have reported higher efficiency and robustness of CFD models compared to the dimensionless numbers for scale-up procedures.

Cui et al. [8] performed CFD modelling of a circulating fluidized bed (CFB) for laboratory, pilot, and industrial scales. Their main focus was on flow dynamics, angles of the furnace, gas-solid flow interaction, combustion, heat transfer characteristics, and, more importantly, the effect of the scale on gas emission and boiler efficiency. As the boiler scale is increased, lower CO, NO<sub>x</sub>, and SO<sub>2</sub> emissions are predicted. On the other hand, carbon conversion and combustion efficiency are reduced for the industrial scale boiler with lower thermal input. Ali et al. [10] have investigated the role of CFD modelling for a photobioreactor sparger scale-up. To develop their initial CFD model, they have incorporated detailed algal growth kinetic at the pilot scale to study and optimize the sparger parameters, such as the number and diameter of holes and gas flow rate. The final design and scale-up correlations are proposed based on the effect of studied parameters on generated bubble volume fraction, average light intensity, friction velocity, power input, and biomass concentration.

## 9.2. Scale-up procedure

The scale-up process in this study is schematically shown in Figure 9-2.

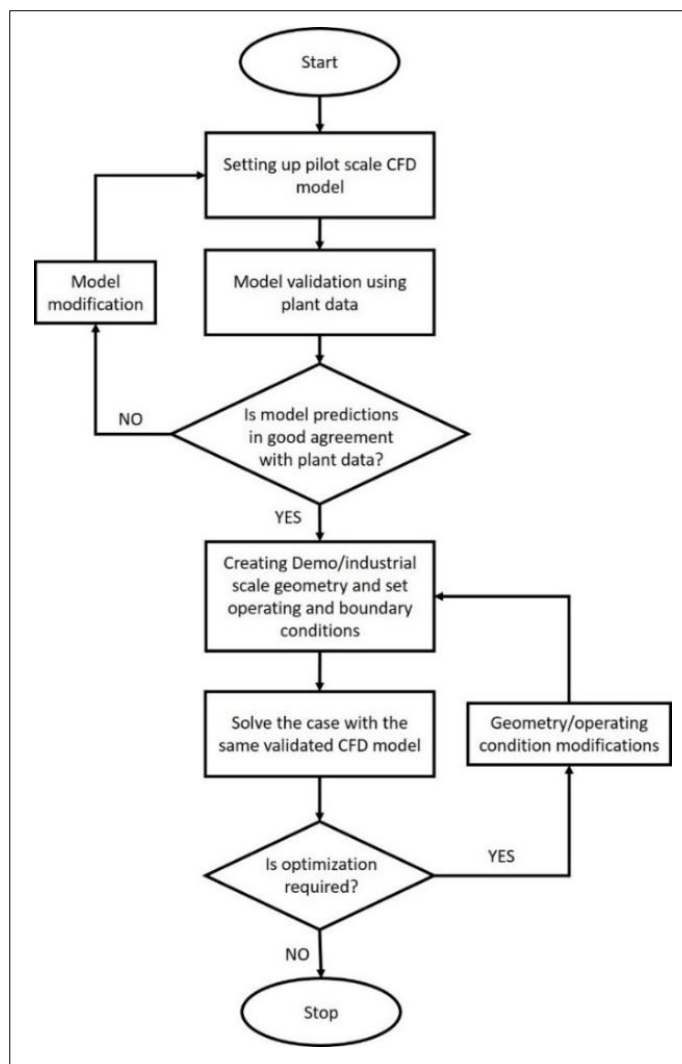


Figure 9-2. Scale-up procedure flowchart for CFD-based scale-up (based on reference [1])

To better elaborate the above chart, the following steps are considered:

- A CFD model is developed for pilot scale by considering the entire off-gas geometry and implementing all possible phenomena and detailed wall modelling.
- The model is validated using measured temperature, heat loss, and gas composition at different points.
- Inlet condition for industrial scale is available from the scaled-up CCF model. The oxygen required for coal and CO-H<sub>2</sub> mixture combustion is calculated using the inlet condition.
- The wall properties, such as thermal conductivity, density, heat capacity, and thickness, are determined via FEM analysis by considering proper cooling pipe diameter, anchor length, and refractory thickness.

- The initial geometry is proposed using the defined boundary conditions and the validated CFD model. The geometry is then modified to meet the hydrodynamic requirements.
- The final geometry is proposed, and oxygen injection is optimized.
- The refractory wall thickness is then reduced on the final optimized design to investigate the effect of gradual wall thinning on the performance of the reflux chamber.

## 9.3. Industrial scale modelling

### 9.3.1. Inlet boundary conditions

Table 9-1 shows the inlet conditions for pilot and industrial scale. The industrial inlet conditions are, in fact, predicted outlet conditions of the CCF using available scaled-up CFD and process models developed by Tata Steel R&D and are not mentioned in this thesis. The operating pressure for industrial cases is higher to design smaller pieces of equipment in the construction stage.

Table 9-1. inlet condition for pilot and industrial scale

	Pilot	Industrial
<b>Operating Condition</b>		
Temperature [K]	2086	1891
Flue gas mass flow [kg/s]	4.326	65.63
Carbon mass flow [kg/s]	0.0283	0.082
Carbon particle diameter [ $\mu\text{m}$ ]	120	120
Inlet diameter [m]	1.15	3.15
Operating pressure [Pa]	100925	181297
<b>Gas composition (vol. %)</b>		
CO	0.0261	0.16
CO <sub>2</sub>	0.61	0.50
H <sub>2</sub>	0.002	0.0165
O <sub>2</sub>	0	0
N <sub>2</sub>	0.166	0.103
H <sub>2</sub> O	0.20	0.22
Sum	1.0001	0.9995
PCR	96.63%	80.65%

### 9.3.2. Oxygen injection calculations

Using the available inlet conditions, the necessary stoichiometric oxygen to fully burn the unwanted species (the CO-H<sub>2</sub>-Carbon mixture) can be calculated by considering the following global reactions:



An excess ratio of 4 is used for the final oxygen injection flow rate, as reported in Table 9-2 for both pilot and industrial scales.

### 9.3.3. Wall design

Heat loss and gain can play a major role in chemical reactions. For example, some reactions discharge heat, increasing system temperature and further speeding up the reaction, letting off even more heat and causing temperatures to rise further and vice versa. Controlling reaction temperature is important to a successful pilot plant scale-up.

Table 9-2. Calculated stoichiometric and excess oxygen required for full combustion of the CO-H<sub>2</sub>-Carbon mixture

<b>Pilot scale</b>		
<b>Component</b>	<b>Inlet flow rate [kg/s]</b>	<b>Stoichiometric oxygen [kg/s]</b>
<b>CO</b>	0.088	0.050
<b>H<sub>2</sub></b>	0.00048	0.004
<b>Carbon</b>	0.021	0.055
	Total Stoichiometric oxygen	0.110
	Excess ratio	4.0
	Injected Oxygen flow rate	0.27
<b>Industrial scale</b>		
<b>CO</b>	8.66	5.0
<b>H<sub>2</sub></b>	0.066	0.53
<b>Carbon</b>	0.085	0.23
	Total Stoichiometric oxygen	5.70
	Excess ratio	3.98
	Injected Oxygen flow rate	28.5

For the industrial scale, the cooling pipes that make up the cooling jacket have an inner diameter (ID) of 80 mm and pipe wall thickness of 6 mm, which is larger than the pilot scale (ID: 28 mm, thickness 5 mm). In the pilot scale, the cooling water is at atmospheric pressure with an average temperature of 313 K (40 °C). In contrast, pressurized water will be used on the industrial scale due to much higher heat losses to the cooling circuit. The cooling water pressure is kept at 18 bar with an average temperature of 473 K (200 °C). This will change the properties of water and the convective heat transfer coefficient, which determines the heat pickup load by the water. The thermophysical properties of water are obtained based on the equation of state and relations proposed by Wagner et al. [19] and Huber et al. [20,21], which can be easily accessed and calculated through the NIST online calculator [22] for different temperature and pressure. The heat transfer coefficient ( $h$ ) of cooling water is calculated according to the Pak and Cho relation [7] based on the Reynolds ( $Re$ ), Prandtl ( $Pr$ ), and Nusselt ( $Nu$ ) numbers and reported in Table 9-3 for both scales.

The other important parameter is the determination of the effective properties of the equivalent wall. As mentioned before, from the study of several parameters and conditions, thermal conductivity is the driving physical parameter in thermal exchanges [23].

Table 9-3. Cooling water operating condition for both scales

<b>Parameter</b>	<b>Pilot</b>	<b>Industrial</b>
<b>Temperature [K]</b>	313 (40 °C)	473 (200 °C)
<b>Pressure [bar]</b>	1	18
<b>Density [kg/m<sup>3</sup>]</b>	992	860
<b>Viscosity [Pa. s]</b>	$6.53 \times 10^{-4}$	$1.37 \times 10^{-4}$
<b>Heat capacity [J/kg. K]</b>	4183	4500
<b>Thermal conductivity [W/m. K]</b>	0.629	0.657
<b>Velocity [m/s]</b>	1	1
<b>Pipe diameter [m]</b>	0.028	0.08
<b>Re</b>	42,562	502,189
<b>Pr</b>	4.34	0.938
<b>Nu</b>	232	836
<b>h [W/m<sup>2</sup>. K]</b>	5,000	6,800

Therefore, it is crucial to obtain a proper value for the thermal conductivity of the equivalent wall. Figure 9-3 shows the schematic view of the pipe, anchors, and refractory wall with their respective dimensions for pilot and industrial scale.

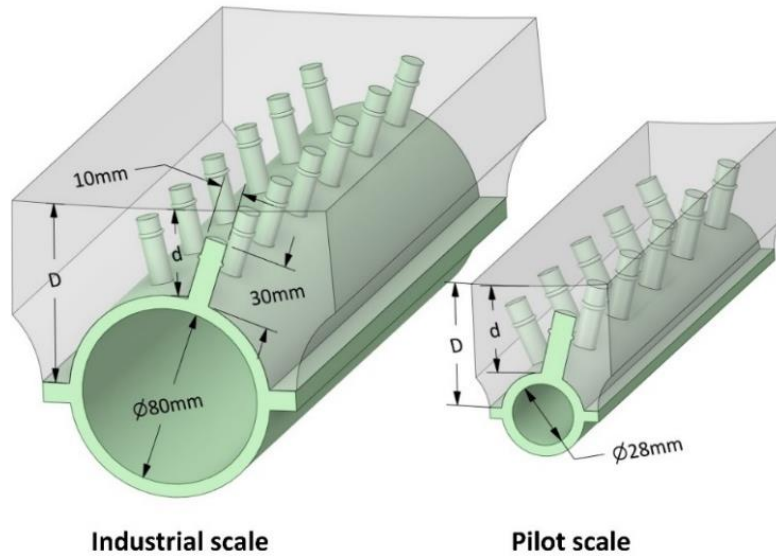


Figure 9-3. Cooling pipe, anchors, and refractory wall depiction for pilot and industrial scale

The anchor size is considered to be the same for both scales. The same FEM analysis discussed in Chapter 2 is utilized to obtain the thermal conductivity of the industrial scale wall for different thicknesses. Just as a reminder, the wall thickness is represented by two variables. The tip thickness “ $d$ ” refers to the wall thickness from the anchor base, and the base thickness “ $D$ ” is the thickness from the middle of the cooling pipe. The tip thickness is the same for both pilot and industrial cases. The refractory is applied up to 10 mm above the anchor tips for both scales. However, the base thickness is thicker for the industrial case, and more refractory material is required to cover the cooling pipes.

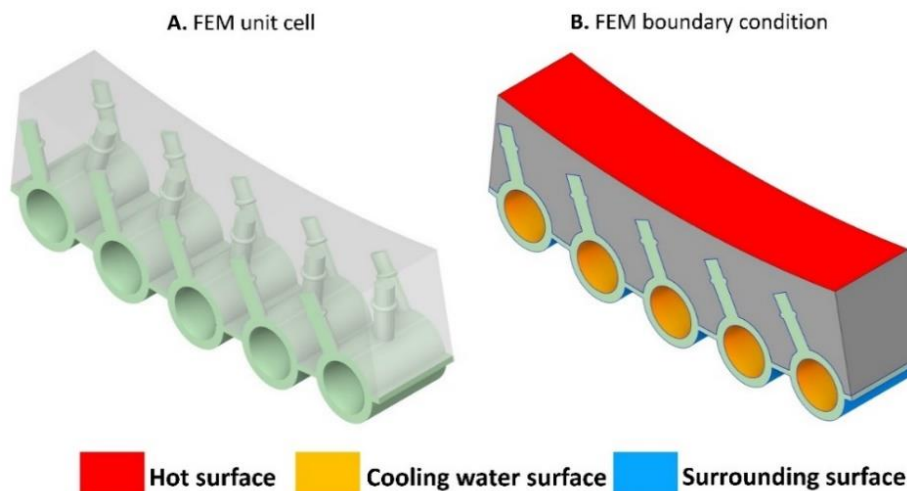


Figure 9-4. Unit cell geometry and Thermal boundary conditions for FEM analysis of unit cell for pilot scale

For FEM analysis, a symmetrical unit cell with surface thermal boundary conditions depicted in Figure 9-4 is used (similar to the discussion in Chapter 2). The boundary conditions for both scales are reported in Table 9-4.

Table 9-4. Boundary conditions for FEM analysis of industrial and pilot scale wall

	Pilot	Industrial
<b>Hot surface</b>	T:1673 K, h: 200 W/m <sup>2</sup> . K	T:1673 K, h: 200 W/ m <sup>2</sup> . K
<b>Cooling water surface</b>	T:314 K, h: 5000 W/ m <sup>2</sup> . K	T:473 K, h: 6800 W/ m <sup>2</sup> . K
<b>Surrounding surface</b>	T:293 K, h: 50 W/ m <sup>2</sup> . K	T:293 K, h: 50 W/ m <sup>2</sup> . K

From the FEM analysis, it is possible to determine heat flux and the average temperature of the surfaces to ultimately determine the effective thermal conductivity of the equivalent wall, as mentioned in Chapter 2, Equation 2-67.

Effective densities and heat capacities of the equivalent walls are calculated using mixing law and based on the anchor and refractory mass fractions from Equations 2-55 and 2-56 in Chapter 2. The obtained values from FEM analysis and effective properties for different tip thicknesses are reported in Table 9-5, and the effective thermal conductivity is depicted in Figure 9-5 for both scales.

Table 9-5. FEM results for pilot and industrial scale

d [mm]	25	30	35	40	45	50
<b>Industrial scale</b>						
HF (kW/m <sup>2</sup> )	66.3	45.7	38.4	34.1	30	26.9
T <sub>c</sub> [K]	482.5	480.78	479.62	479	478	477.5
T <sub>h</sub> [K]	1402.2	1449.8	1481.6	1503	1523.2	1543
d <sub>eff</sub> [mm]	46	51	56	61	66	71
k <sub>eff</sub> [W/m. K]	3.31	2.4	2.15	2.1	1.9	1.79
ρ <sub>eff</sub> [kg/m <sup>3</sup> ]	2648	2600	2562	2533	2503	2471
cp <sub>eff</sub> [J/kg. K]	865	869	872	874	876	879
<b>Pilot scale</b>						
HF (kW/m <sup>2</sup> )	115	72.5	57.3	48.3	42	37.1
T <sub>c</sub> [K]	332.6	328.66	325.5	323.5	322	321
T <sub>h</sub> [K]	1257.64	1322.6	1386.5	1430.4	1462.5	1487
d <sub>eff</sub> [mm]	34.5	39.5	44.5	49.5	54.5	59.5
k <sub>eff</sub> [W/m. K]	4.29	2.88	2.4	2.16	2	1.89
ρ <sub>eff</sub> [kg/m <sup>3</sup> ]	3251	3136	3044	2970	2907	2855
cp <sub>eff</sub> [J/kg. K]	818	827	834	840	845	849

As it can be seen, the effective thermal conductivity for the equivalent wall of the industrial scale is lower than the pilot case for the same tip thickness. The reason is

the smaller anchor size with respect to the pipe diameter and also the higher volume fraction of refractory material, which has a very low thermal conductivity.

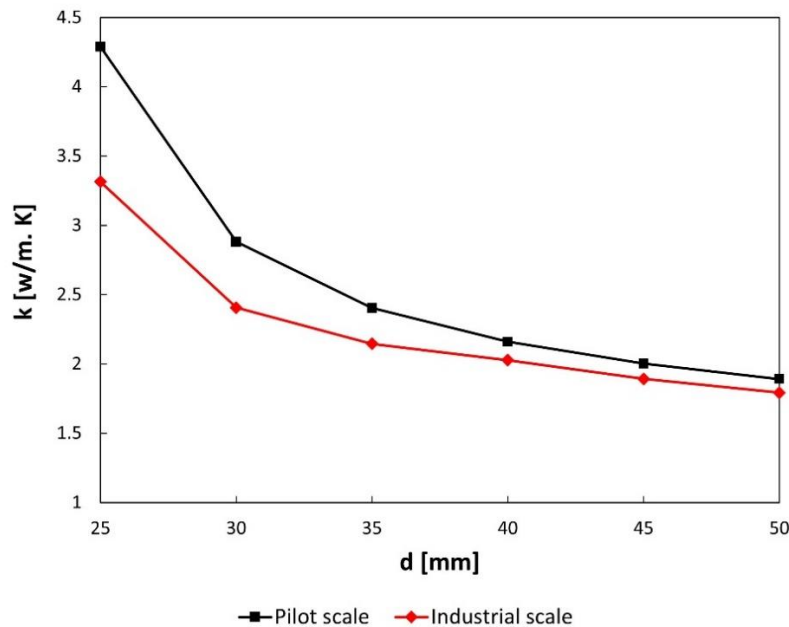


Figure 9-5. Effective thermal conductivity of equivalent wall with respect to the refractory layer thickness for pilot and industrial scale

### 9.3.4. Industrial scale model summary

The summary of boundary conditions for the industrial scale “base model” is reported in Table 9-6. The same mesh size (as in pilot scale geometry) is applied to create a computational grid for a scaled-up reflux chamber, generating a computational grid with 2.2 million cells.

Table 9-6. Summary of boundary conditions for industrial scale

Inlet conditions	Reported in Table 9-2
Oxygen injection [kg/s]	28.5
<b>Wall layer properties</b>	
<b>First layer (Equivalent wall)</b>	
Effective wall thickness [mm]	61 (d = 40)
Effective thermal conductivity [W/m. K]	2.1
Effective density [kg/m <sup>3</sup> ]	2533
Effective heat capacity [J/kg. K]	874
<b>Second layer (steel pipe wall)</b>	
wall thickness [mm]	6
Thermal conductivity [W/m. K]	$k = \begin{cases} 0.00025 \times T[\text{K}] + 0.80175 & 1073 \leq T \leq 1273 \\ 0.0007 \times T[\text{K}] + 0.2289 & 1273 < T \leq 2273 \end{cases}$
Density [kg/m <sup>3</sup> ]	7850
Heat capacity [J/kg. K]	461
<b>Cooling water properties</b>	
Heat transfer coefficient [W/m <sup>2</sup> . K]	6800
Average temperature [K]	473



All included sub-models, such as radiation, turbulence, chemistry and kinetics, are the same as discussed for the pilot model development. Pressure-velocity coupling is done through coupled algorithm, and the same discretization scheme and convergence criterion discussed in Chapter 2 is used for the industrial scale modelling.

## 9.4. Results and discussion

### 9.4.1. Geometry and oxygen injectors

In the pilot scale, the oxygen is injected through a single injector with a diameter of 3 cm. This diameter is suitable for injecting the oxygen flow rate of 0.27 kg/s, resulting in a tip velocity of 200 m/s. It is desired to keep the injection Mach number low and in the subsonic flow range for two main reasons.

Firstly, Subsonic flows are generally easier to control than supersonic flows due to their greater stability, lower sensitivity to disturbances, and the simplicity of control mechanisms. Supersonic flows involve complexities such as shock waves and compressibility effects, making them more challenging to predict and manage. Secondly, higher injection speed delays the oxygen dispersion inside the reflux chamber and might locally delay the gaseous mixing and initiation of the combustion. Therefore, a Mach number = 0.5 is chosen for the initial design.

To respect this value, a single injector with a diameter = 27.5 cm is considered for the industrial case. However, a single injector with this diameter is quite large and might be challenging to install and maintain during the operation. Therefore, for the industrial scale, the same oxygen amount is injected by a higher number of smaller injectors. Based on the hydrodynamic analysis, four injectors with an individual diameter of 14 cm are considered for the final design. Using the same hydrodynamic analysis, the initial horizontal length ( $L_2$ ) of the reflux chamber is varied to determine the best length.

The value of  $L_2$  is determined based on the oxygen and flue gas streamlines to have minimum recirculation inside the reflux chamber and avoid the oxygen jet hitting the walls. The final dimension for the industrial scale is reported in Table 9-7, with labels shown in Figure 9-6.

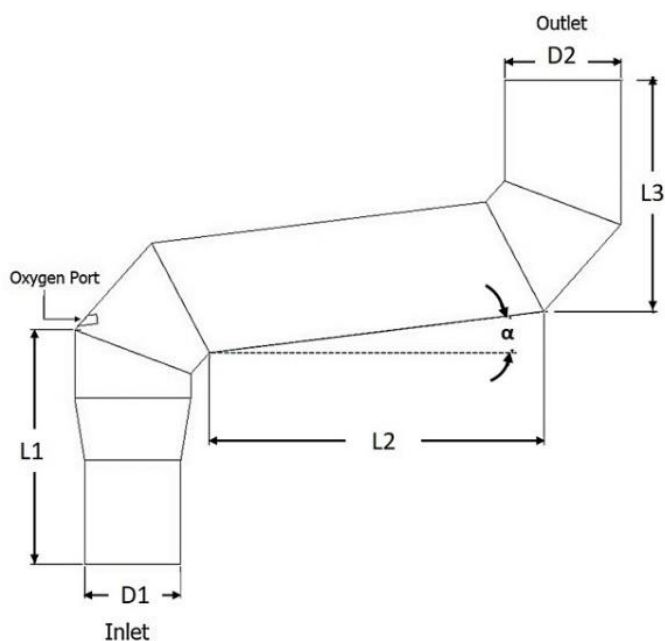


Figure 9-6. Reflux chamber dimension for the scale-up

Table 9-7. Pilot and final industrial scale dimension

Dimension parameters [m]	Pilot	Industrial	Scaling-up factor
D1	1.15	3.15	2.74
D2	1.39	3.15	2.27
L1	2.82	4	1.42
L2	4	9.5	2.38
L3	2.8	6.85	2.45
$\alpha$	7°	7°	-
Oxygen port diameter	0.03	0.14	4.66
Number of Oxygen injectors	1	4	-
Inner wall surface area [m <sup>2</sup> ]	42	208.5	4.96

### 9.4.2. Base model

Figure 9-7 shows the temperature, composition contour, and profile along the reflux chamber length. The profiles are plotted as average values over a cross section swept along the centreline of the system (length).

The amount of CO and H<sub>2</sub> is slightly increasing before the oxygen injection point (length: 4.4 m). This is mainly due to the CO production from the carbon reaction with the H<sub>2</sub>O-CO<sub>2</sub> mixture and CO<sub>2</sub>-H<sub>2</sub>O dissociation into CO and H<sub>2</sub>. Over the same length, the temperature decreases constantly, mainly due to heat losses through the wall, endothermic dissociation of CO<sub>2</sub> and H<sub>2</sub>O, and the endothermic reaction of

carbon with  $\text{H}_2\text{O}-\text{CO}_2$  mixture. Then, there is a sharp increase in oxygen concentration where the oxygen is injected into the reflux chamber with a severe drop in local temperature. Due to the combustion of the  $\text{CO}$  and  $\text{H}_2$ , oxygen is reduced, and the temperature is sharply increased and becomes constant after the second bend.

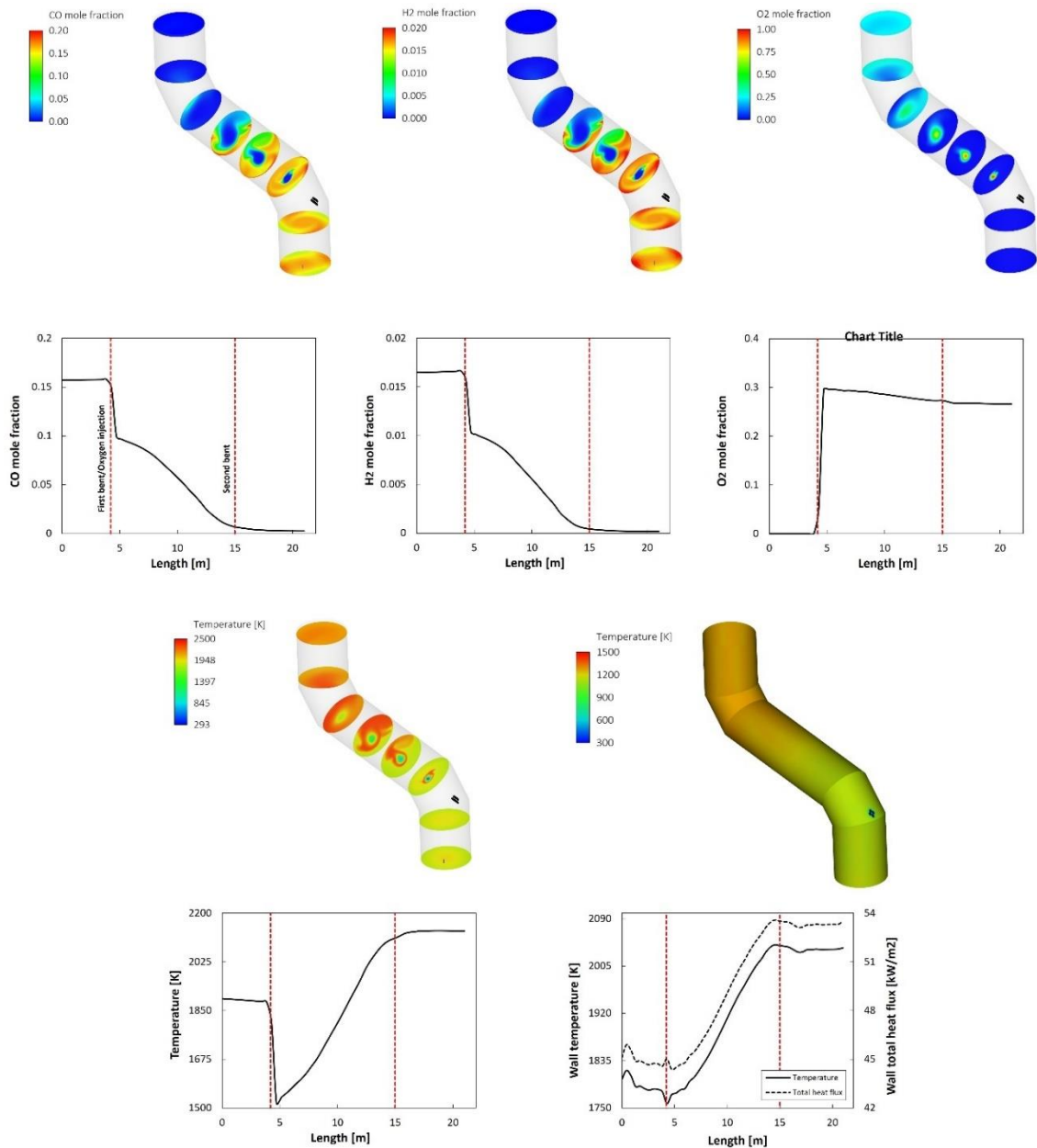


Figure 9-7. Temperature and composition contours (A) and profiles (B)

The wall temperature is almost constant up to the oxygen injection and is increased without a noticeable drop in the oxygen injection region. This is because the oxygen is injected in the centreline of the reflux chamber and is not uniformly spread in the cross sections, leading to a higher wall temperature and flue gas temperature near

the wall. The total heat flux follows the same trend as wall temperature and sharply increases at the combustion region. With the current design and operating condition, complete combustion of the CO-H<sub>2</sub>-Carbon mixture is achieved in a short length of the reflux chamber.

### 9.4.3. Effect of oxygen injection and optimization of post-combustion

The calculated oxygen flow rate of 28.5 kg/s is based on an access ratio = 4, similar to the pilot case, to remove all unwanted species. A set of simulations is performed to investigate the impact of reducing the oxygen injection flow rate in 20% intervals on the combustion of a CO-H<sub>2</sub>-Carbon mixture in the base case. Figure 9-8 shows the impact of this reduction on CO conversion and temperature profile inside the reflux chamber. Conversion of unwanted species is calculated as:

$$\text{conversion} = \frac{m_{in} - m_L}{m_{in}} \quad (9-6)$$

where  $m_{in}$  and  $m_L$  are species mass flow rates at the inlet and random location of the reflux chamber, respectively.

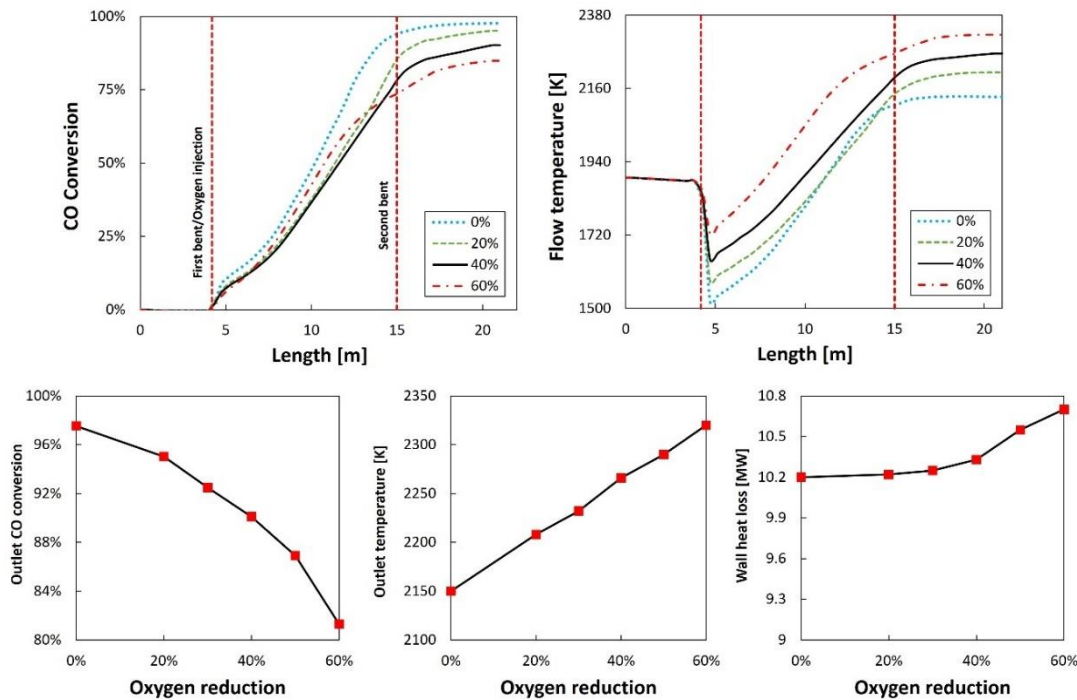


Figure 9-8. Effect of oxygen reduction on CO conversion and temperature profile along and at the outlet of the reflux chamber

As it can be seen, the profiles follow a similar trend as discussed before. Oxygen reduction has a negative effect on CO conversion for two main reasons. Firstly, reducing oxygen will reduce the amount and penetration of the oxygen inside the flue gas flow, reducing the conversion of unwanted species. Secondly, reducing the oxygen increases the flue gas temperature as oxygen is injected at room temperature and has a considerable local cooling effect. The temperature at the injected point is considerably reduced at higher oxygen injection flow rates, and the same is true for the rest of the reflux chamber length. Increasing temperature has a negative effect on CO-H<sub>2</sub> combustion. A Chemkin® analysis using the same kinetic data of the CFD models is performed to investigate this effect in more detail. A mixture with the same composition of the reflux chamber inlet is considered for a batch reactor model analysis at different initial mixture temperatures. Figure 9-9 shows the CO conversion and the final temperature of the mixture for different initial temperatures.

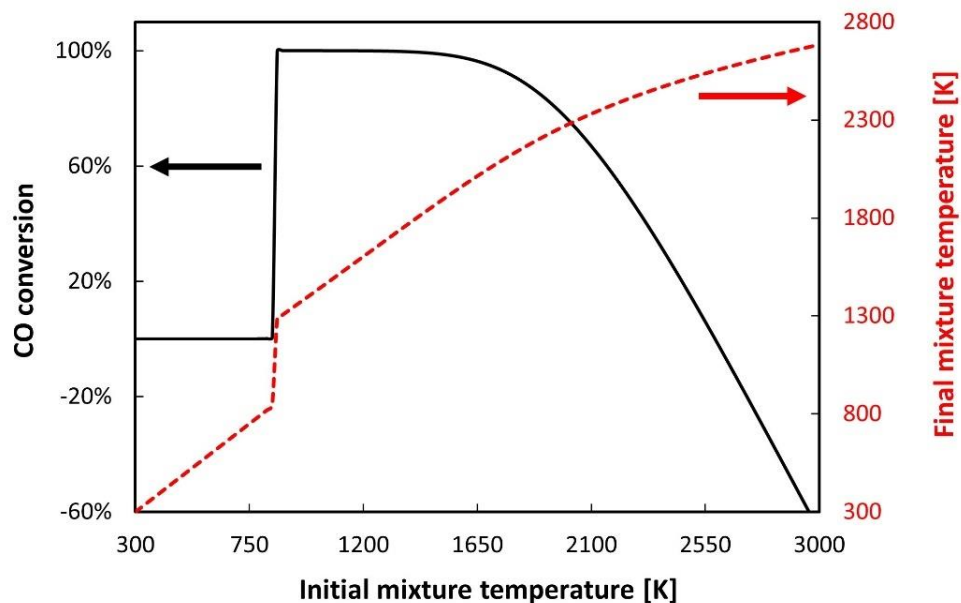


Figure 9-9. Effect of temperature on CO conversion of a batch model analysis

As it can be seen from the graphs, the conversion is zero before 850 K, which is the auto-ignition point of the specified mixture. Increasing the initial temperature increases both conversion and final temperature; however, a further increase in initial and final temperature will lead to a lower conversion as CO<sub>2</sub> starts to dissociate into CO mainly through thermal dissociation and reverse water gas shift reaction. The detail of individual reactions leading to this backward conversion is not mentioned here for brevity; however, it is worth mentioning that a negative

conversion is predicted after a certain temperature, which means a net production of CO. With this analysis, it is clear that reducing the oxygen increases the flue gas temperature, which reduces the CO conversion. Therefore, an increase in temperature is not always beneficial for CO-H<sub>2</sub> removal, and there is an optimum temperature range for the complete removal of these species.

Figure 9-10 shows the carbon particle tracks coloured by particle diameter for various reductions in oxygen injection. The decrease in oxygen injection can significantly impact the combustion of carbon particles, reducing carbon conversion within the reflux chamber. However, for the current design, even for the highest considered oxygen reduction, a negligible amount of carbon emission is predicted from the reflux chamber outlet. However, compared to the industrial scale, the complete carbon conversion inside the reflux chamber for the pilot scale could not be achieved (maximum: 50 to 70%) even for the highest oxygen injection excess ratio. The reason is less available length and volume for the pilot case, which provides less residence time for carbon particles inside the reflux chamber. In the end, oxygen reduction has a negligible effect on heat losses through the wall, though it is slightly increased by reducing the oxygen injection, which is linked to the flue gas temperature increase.

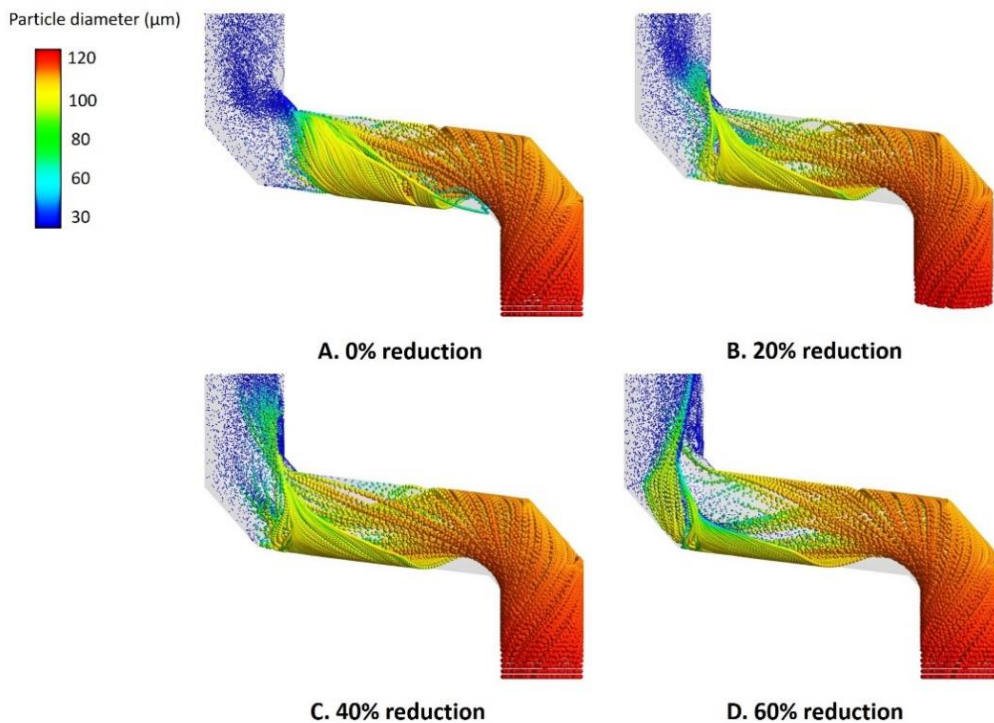


Figure 9-10. Carbon particle track for different oxygen reduction cases

According to pilot plant data, the emissions from the reflux chamber can still be removed in the air quench section of the off-gas (above the reflux chamber), where the temperature is still high. However, the aim is to achieve as high conversion as possible inside the reflux chamber, as there is a risk of temperature reduction below the auto-ignition point of the gaseous mixture above the air quench section.

Therefore, reducing oxygen injection is possible, but it should be in a quantity that the unwanted species (CO and carbon) are still combusted at a higher temperature than the auto-ignition point and avoiding a large amount of CO into the off-gas sections where the temperature is low. In conclusion, the feasibility of reducing oxygen injection depends on compliance with environmental regulations and the permissible level of CO emissions. A fully scaled-up off-gas system modelling, including all sections, is required for a better analysis.

#### **9.4.4. Effect of wall thickness**

The base model considers a fresh refractory base thickness ( $d=40$  mm). As discussed before, the refractory layer is thinning due to the harsh conditions inside the reflux chamber. From pilot plant measured data and modelling, the wall condition inside the reflux chamber determines temperature and composition profiles throughout the whole off-gas system. It also directly affects the off-gas system heat recovery and downstream equipment performance.

A set of simulations is performed to study the effect of gradual reduction in refractory layer thickness. Along with thickness reduction, the thermal and physical properties of the equivalent wall used in the models are also changed, as reported in Table 9-5 for the industrial case. Figure 9-11 shows the temperature and composition profile for different refractory base thicknesses. As illustrated in Figure 9-11.D, the increase in heat loss is more pronounced for  $d=25$ mm, where the tip of anchors becomes visible, and more heat is conducted through the tips into the cooling wall. The averaged flue gas temperature (Figure 9-11.A) is almost constant for all studied wall thicknesses but decreases at the outlet for thinner walls.

However, a noticeable reduction in temperature is observed for the film (flue gas flow temperature in the vicinity of the wall) and wall temperature once the wall

thickness is reduced, which is related to the higher thermal conductivity and heat losses through thinner walls.

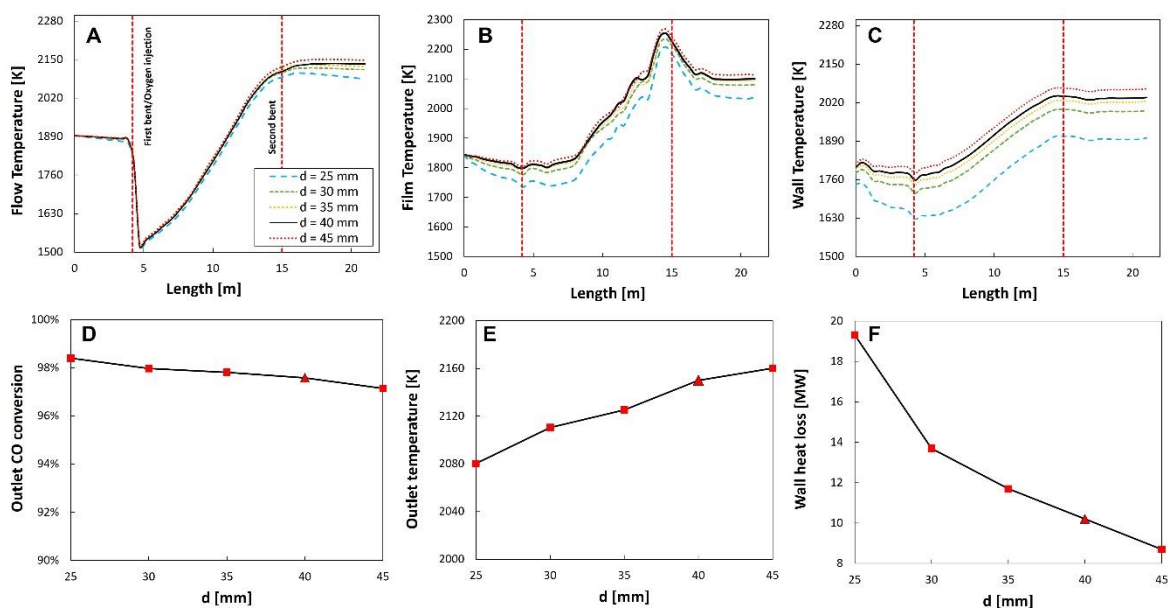


Figure 9-11. Effect of wall thickness reduction on CO conversion and temperature profile along and at the outlet of the reflux chamber

Since the wall thickness has a minor effect on the mean flue gas temperature (especially in the middle of the flow), no major difference in CO conversion is predicted. However, the conversion is slightly higher for thinner walls, which can be related to a lower temperature after the second bend. As discussed in section 9.4.3 and illustrated in Figure 9-9, lowering the flue gas temperature can increase CO conversion.

#### 9.4.5. Effect of CO at the inlet

The CO content in the flue gas at the pilot scale can range from 0 to 12% at its peak, with a similar trend predicted for the industrial scale. Based on measurements and the CFD model of the pilot scale, the fluctuation in CO content significantly influences the behavior of the flue gas, consequently impacting the performance of components within the off-gas system. A set of simulations is performed to determine the effect of the CO content on the performance of the reflux chamber. Figure 9-12 shows the effect of CO content of flue gas entering the reflux chamber. As it can be seen, depending on the content of CO, the trends of the previously discussed results are drastically changed as CO is the primary heat-generating



source. The amount of CO increases in the flue gas before reaching the oxygen injection zone. This increase is more pronounced for lower inlet CO content. The reason is the lower partial pressure of CO in the flue gas, which is favourable for reverse reactions leading to CO production. Increasing the inlet CO content increases the partial pressure of CO, and forward reactions proceed.

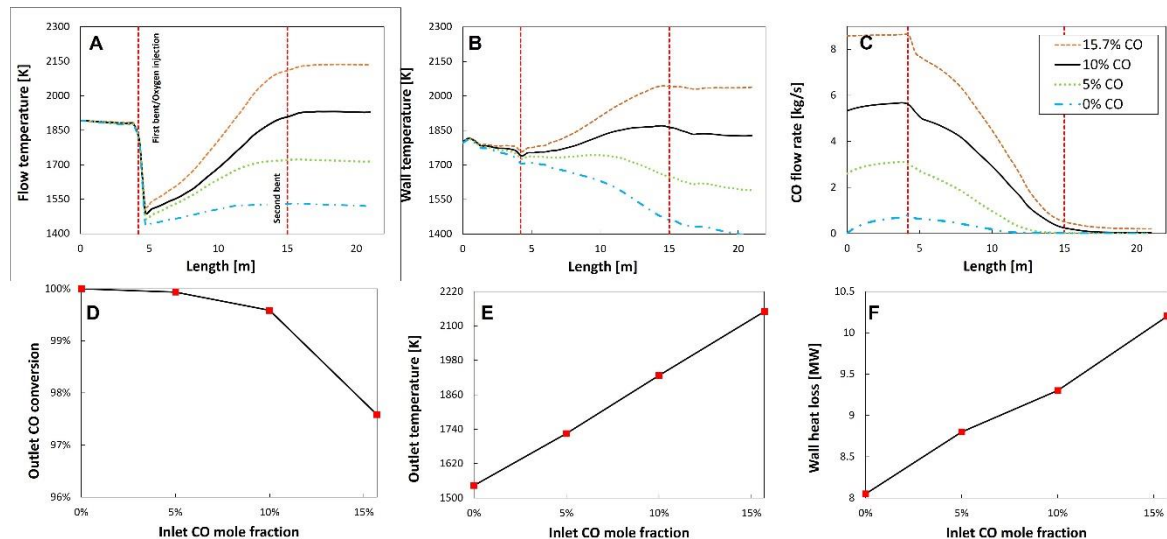


Figure 9-12. Effect of the inlet CO content on CO conversion and temperature profile along and at the outlet of the reflux chamber

For 0% CO content, the flue gas temperature is relatively constant during and after oxygen injection, and the wall temperature is constantly reducing. Higher CO content means higher fuel for combustion, higher flue gas and wall temperature, and higher heat losses through the wall.

Based on measured data from the pilot plant, it is unlikely for the CO content inside the off-gas system to be 0% at the inlet of the reflux chamber. The only condition that makes this scenario possible is the presence of oxygen in the inlet flue gas, which is not the case here. Nevertheless, it is still worth considering this possibility to understand better the effect of gaseous composition on reflux chamber performance and flue gas flow behaviour.

## 9.5. Conclusions

A CFD-assisted scale-up design for the reflux chamber of the HIsarna off-gas system was performed from a pilot to an industrial scale. Complementary to the traditional methods, CFD analysis is an valuable tool for incorporating even the most intricate details into system geometry and calculations.

Initially, a CFD model is developed and validated for the pilot scale using the measured plant data and incorporating entire geometry and detailed kinetic data for volumetric and gas-solid reactions. During the model development, special attention is paid to the walls since the wall modelling plays a major role in determining heat loss and temperature profile inside the reflux chamber and the rest of the off-gas system (according to the pilot scale measured data). The same CFD model is used for the hydrodynamic analysis of scaled-up cases to determine the optimized geometry and oxygen injection flow rate. The dimensions and operating conditions are based on achieving full combustion of the CO-H<sub>2</sub>-Carbon mixture entering the reflux chamber. With a fixed geometry, the effects of oxygen injection, refractory wall thickness, and inlet flue gas CO content on temperature and composition profile and heat loss through the wall are studied and discussed in detail.

From the analysis, the oxygen injection could be further decreased; however, this optimization should be considered only when the emission limitations are met.

Since post-combustion oxygen is injected at ambient temperature, it substantially cools the flue gas temperature, and the local temperature can drastically drop. This cooling effect is less pronounced for lower oxygen injection, and therefore, the mean and outlet temperature of the flue gas is increased. A lower oxygen injection is associated with reduced CO conversion, attributed to lower oxygen availability, limited mixing, and higher local temperatures, which are detrimental to CO combustion. A minor increase in the wall heat loss is predicted for lower oxygen injection.

The wall of the reflux chamber is made of cooling pipes and is isolated using a layer of refractory coating with embedded anchors to hold them firm on the pipes. According to the pilot scale inspections and measurements, the original thickness of the refractory coating is reduced drastically due to chemical and thermal stresses inside the reflux chamber, and the wall thickness is no longer constant throughout the chamber length. The same phenomenon is expected for the scaled-up cases where the wall material is similar to the pilot case.

Among the studied parameters, CO concentration in the flue gas considerably affects the flue gas behaviour and the overall reflux chamber performance. Increasing CO

concentration drastically changes the flue gas temperature, wall temperature, composition profile, and heat loss through the wall since CO is indeed a fuel and the primary heat-generating source. Higher inlet CO content will generate more heat, and for a fixed wall thickness, a higher heat loss and possibly higher CO emission from the reflux chamber is predicted.

Altogether, the proposed geometry and operating conditions can combust all unwanted species in a short length of the reflux chamber for all investigated variations of parameters.

## References

- [1] A. Egedy, S. Fogarasi, T. Varga, Á. Imre-Lucaci, T. Chován, CFD-based scale-up and environmental assessment of a rotating drum leaching reactor for WEEE recycling, *Clean Technologies and Environmental Policy*. 17 (2015) 1373–1380. <https://doi.org/10.1007/s10098-015-0974-1>.
- [2] J. Scully, L.B. Considine, M.T. Smith, E. McAlea, N. Jones, E. O’Connell, E. Madsen, M. Power, P. Mellors, J. Crowley, N. O’Leary, S. Carver, D. Van Plew, Beyond heuristics: CFD-based novel multiparameter scale-up for geometrically disparate bioreactors demonstrated at industrial 2kL–10kL scales, *Biotechnology and Bioengineering*. 117 (2020) 1710–1723. <https://doi.org/https://doi.org/10.1002/bit.27323>.
- [3] V. Cappello, C. Plais, C. Vial, F. Augier, Scale-up of aerated bioreactors: CFD validation and application to the enzyme production by *Trichoderma reesei*, *Chemical Engineering Science*. 229 (2021) 116033. <https://doi.org/https://doi.org/10.1016/j.ces.2020.116033>.
- [4] J.-M. González-Sáiz, D. Garrido-Vidal, C. Pizarro, Scale up and design of processes in aerated-stirred fermenters for the industrial production of vinegar, *Journal of Food Engineering*. 93 (2009) 89–100. <https://doi.org/https://doi.org/10.1016/j.jfoodeng.2009.01.002>.
- [5] J. Morchain, J.-C. Gabelle, A. Cockx, A coupled population balance model and CFD approach for the simulation of mixing issues in lab-scale and industrial bioreactors, *AIChE Journal*. 60 (2014) 27–40. <https://doi.org/https://doi.org/10.1002/aic.14238>.
- [6] S. Azuhata, K. Narato, H. Kobayashi, N. Arashi, S. Morita, T. Masai, A study of gas composition profiles for low NO<sub>x</sub> pulverized coal combustion and burner scale-up, *Symposium (International) on Combustion*. 21 (1988) 1199–1206. [https://doi.org/https://doi.org/10.1016/S0082-0784\(88\)80351-5](https://doi.org/https://doi.org/10.1016/S0082-0784(88)80351-5).
- [7] P. Singh, P. Mahanta, P. Kalita, Numerical investigation of fluid flow and heat transfer in a gas-solid vortex reactor without slit: Scale-up and optimization, *International Communications in Heat and Mass Transfer*. 128 (2021) 105590. <https://doi.org/https://doi.org/10.1016/j.icheatmasstransfer.2021.105590>.
- [8] Y. Cui, W. Zhong, X. Liu, J. Xiang, Study on scale-up characteristics in supercritical CO<sub>2</sub> circulating fluidized bed boiler by 3D CFD simulation, *Powder Technology*. 394 (2021) 103–119. <https://doi.org/https://doi.org/10.1016/j.powtec.2021.08.028>.
- [9] M. Biglari, H. Liu, A. Elkamel, A. Lohi, Application of Scaling-Law and CFD Modeling to Hydrodynamics of Circulating Biomass Fluidized Bed Gasifier, *Energies*. 9 (2016). <https://doi.org/10.3390/en9070504>.
- [10] H. Ali, J. Solsvik, J.L. Wagner, D. Zhang, K. Hellgardt, C.W. Park, CFD and kinetic-based modeling to optimize the sparger design of a large-scale photobioreactor for scaling up of biofuel production, *Biotechnology and Bioengineering*. 116 (2019) 2200–2211. <https://doi.org/https://doi.org/10.1002/bit.27010>.
- [11] L. Böhm, L. Hohl, C. Bliatsiou, M. Kraume, Multiphase Stirred Tank Bioreactors – New Geometrical Concepts and Scale-up Approaches, *Chemie Ingenieur Technik*. 91 (2019) 1724–1746. <https://doi.org/https://doi.org/10.1002/cite.201900165>.
- [12] E. Gavi, D.L. Marchisio, A.A. Barresi, CFD modelling and scale-up of Confined Impinging Jet Reactors, *Chemical Engineering Science*. 62 (2007) 2228–2241. <https://doi.org/https://doi.org/10.1016/j.ces.2006.12.077>.
- [13] J. Gimbut, C.D. Rielly, Z.K. Nagy, Modelling of mass transfer in gas–liquid stirred tanks agitated by Rushton turbine and CD-6 impeller: A scale-up study, *Chemical Engineering*

- Research and Design. 87 (2009) 437–451. <https://doi.org/https://doi.org/10.1016/j.cherd.2008.12.017>.
- [14] W.C. Wilfong, B.W. Kail, Q. Wang, T. Ji, V.A. Kusuma, P. Shah, N. Fusco, S. Yi, F. Shi, M.L. Gray, Scale-up of immobilized amine sorbent pellets for landfill gas upgrading, using benchtop and pilot equipment, Powder Technology. 395 (2022) 243–254. <https://doi.org/https://doi.org/10.1016/j.powtec.2021.09.056>.
- [15] Y. Liu, V. Raman, R.O. Fox, A.D. Harvey, Scale up of gas-phase chlorination reactors using CFD, Chemical Engineering Science. 59 (2004) 5167–5176. <https://doi.org/https://doi.org/10.1016/j.ces.2004.09.018>.
- [16] Q. Wang, K. Zhang, S. Brandani, J. Jiang, Scale-up strategy for the jetting fluidized bed using a CFD model based on two-fluid theory, The Canadian Journal of Chemical Engineering. 87 (2009) 204–210. <https://doi.org/https://doi.org/10.1002/cjce.20148>.
- [17] J. Parker, K. LaMarche, W. Chen, K. Williams, H. Stamato, S. Thibault, CFD simulations for prediction of scaling effects in pharmaceutical fluidized bed processors at three scales, Powder Technology. 235 (2013) 115–120. <https://doi.org/https://doi.org/10.1016/j.powtec.2012.09.021>.
- [18] X. Liu, D. Hatzivramidis, H. Arastoopour, A.S. Myerson, CFD simulations for analysis and scale-up of anti-solvent crystallization, AIChE Journal. 52 (2006) 3621–3625. <https://doi.org/https://doi.org/10.1002/aic.10962>.
- [19] W. Wagner, A. Pruß, The IAPWS Formulation 1995 for the Thermodynamic Properties of Ordinary Water Substance for General and Scientific Use, Journal of Physical and Chemical Reference Data. 31 (2002) 387–535. <https://doi.org/10.1063/1.1461829>.
- [20] M.L. Huber, R.A. Perkins, A. Laesecke, D.G. Friend, J. V Sengers, M.J. Assael, I.N. Metaxa, E. Vogel, R. Mareš, K. Miyagawa, New International Formulation for the Viscosity of H<sub>2</sub>O, Journal of Physical and Chemical Reference Data. 38 (2009) 101–125. <https://doi.org/10.1063/1.3088050>.
- [21] M.L. Huber, R.A. Perkins, D.G. Friend, J. V Sengers, M.J. Assael, I.N. Metaxa, K. Miyagawa, R. Hellmann, E. Vogel, New International Formulation for the Thermal Conductivity of H<sub>2</sub>O, Journal of Physical and Chemical Reference Data. 41 (2012) 33102. <https://doi.org/10.1063/1.4738955>.
- [22] Thermophysical Properties of Water, (n.d.). <https://webbook.nist.gov/cgi/fluid.cgi?ID=C7732185&Action=Page> (accessed November 10, 2021).
- [23] J. Joliff, Y. , Belec, L. and Chailan, Finite Element Analysis of the Material's Area Affected during a Micro Thermal Analysis Applied to Homogeneous Materials, Journal of Surface Engineered Materials and Advanced Technology. 1 (2011) 1–8. <https://doi.org/10.4236/jsemat.2011.11001>.

# Chapter 10

## CONCLUSIONS AND RECOMMENDATIONS

**The individual conclusions are already included in each chapter. This chapter summarizes all derived conclusions for each topic (not chapter-based). Furthermore, recommendations are made regarding the developed models and possible HISarna process improvement.**

## 10.1. Conclusions

### 10.1.1. CFD modelling of the HIsarna off-gas system

- According to the model predictions of the off-gas system, the reflux chamber emerged as the most critical and intricate component to model. Despite its seemingly simple exterior, it contains complex phenomena within.
- The developed model is comprehensive, encompassing all major phenomena occurring within the off-gas system, including turbulence, reactions, mass transfer, convective and radiative heat transfer, conductive heat transfer through the walls, detailed modeling of the solid walls, and gas-solid interaction. Various sub-models are available for each phenomenon. It has been observed that the selection of models for describing these phenomena influences model stability, convergence, accuracy, and solution time costs.
- Selecting radiation, turbulence, and turbulence chemistry interaction (TCI) is of utmost importance among the sub-models. A comprehensive analysis was performed to compare different models, and the best combination was selected. It was concluded that the discrete ordinate model (for radiation), k- $\epsilon$  model (for turbulence), and eddy dissipation concept (for TCI), along with polyhedral mesh, lead to the best solution stability and accuracy of the produced results.
- The inclusion of carbon combustion impacts the predicted profiles owing to its highly exothermic nature. While the carbon particle volume fraction remains relatively low (<1%), a visible difference in predicted profiles is observed between the two scenarios with and without carbon reactions. This discrepancy becomes more pronounced with higher concentrations. The conclusion is that carbon combustion cannot be overlooked for any flow rate and volume fractions in the flue gas.
- For the current off-gas system case, wall modelling is the most important part of the CFD model setup. The reflux chamber walls are composite walls with varying thermos-physical properties, which can noticeably affect the heat loss through the walls. This, in turn, can affect the temperature profiles of the off-gas system and temperature distribution on the inner and outer wall surfaces.

- Due to the importance of wall modelling, a methodology using the FEM and CFD analysis is proposed for designing the reflux chamber walls to be as physically sound as possible. This approach allows for the redesign of walls for any scenario or scale.
- Changing the reflux chamber's geometry from a dog-leg to a frog-leg configuration can enhance the removal of undesired species. The frog-leg configuration includes an additional bend, allowing for a longer residence time for pollutants to combust with the injected oxygen. Moreover, including this extra bend effectively enhances the capture of escaped molten ore particles.
- The developed CFD model for pilot scale geometry is utilized to design the up-scaled reflux chamber. The proposed scaled-up geometry can remove the unwanted species via oxygen injection.
- An extensive sensitivity analysis has concluded that oxygen injection inside the reflux chamber can be reduced by up to 50%. It has been noted that the flue gas temperature is sufficiently high to ignite the CO-H<sub>2</sub>-Carbon mixture above the reflux chamber and in the air quench section. This observation and the proposed reduction in oxygen injection have been validated for flue gas with low CO content entering the reflux chamber (up to 4%). However, the reduction in oxygen injection will be less than 50% for higher CO content. Additional sensitivity studies are needed to determine the optimal oxygen reduction point for varying inlet CO contents.

### **10.1.2. Thermodynamic analysis of zinc ferrite formation**

- Thermodynamic analysis revealed that the most critical location for zinc ferrite formation is within the off-gas system, given the presence of oxygen and local low temperatures. In contrast, SRV and CCF are not conducive environments for ferrite formation, as they offer highly reducing conditions with uniformly distributed high temperatures.
- From a thermodynamic perspective, the formation of zinc ferrite under the current conditions of the off-gas system appears quite favorable. However, altering the configuration to a frog-leg design with upper oxygen injection has demonstrated the potential to reduce ferrite formation. The frog-leg



configuration, combined with upper oxygen injection, creates a larger area characterized by low partial pressure of oxygen and higher temperatures. This extended exposure allows more time for Zn to speciate into the slag phase in the form of zinc oxide, thereby reducing the likelihood of ferrite formation. Nevertheless, it should be noted that under any geometry and operational conditions, the formation of zinc ferrite remains inevitable and can only be decreased.

### **10.1.3. Fluidic oscillator application**

- A post-combustion modification has been made to the existing oxygen injector, introducing a fluidic oscillator. This new design enables the enhancement of turbulence intensity while ensuring the uniform distribution of the oxidant inside the reflux chamber through a sweeping motion.
- Enhanced oxygen separation resulted in removing the CO and H<sub>2</sub> at a shorter distance from the reflux chamber inlet, with virtually no pollutants escaping the oxygen-rich zone.
- Spreading the oxygen over a wider range led to a decrease in local temperature, providing an additional advantage in achieving complete combustion of the CO-H<sub>2</sub> mixture.

## **10.2. Recommendations**

### **10.2.1. CFD modelling**

Despite efforts to develop a comprehensive CFD model for the HIsarna off-gas system, there is still potential for further improvement.

- The first improvement involves developing a transient model for the off-gas system. However, this would require a significantly higher computational resource investment to conduct successful transient simulations. This approach holds particular significance as the HIsarna process inherently exhibits transient behavior. Implementing a time-dependent model would enable the study of various other process aspects, including dynamic responses to abrupt changes in boundary conditions. For example, it would allow the investigation of CO emissions at the outlet by increasing the inlet

CO composition and determining the time required to mitigate emissions (by increasing the oxygen flow rate). A transient model would be essential and valuable for constructing a digital twin of the off-gas system.

- To create a more comprehensive model, including other gas-solid reactions such as iron oxide reduction and oxidation is imperative.
- In the context of capturing molten ore particles inside the reflux chamber and modeling particle-wall interactions, an approach based on particle velocity (e.g., Weber number) and particle angle of attack on the walls could yield more accurate and reliable predictions. However, it is worth noting that experimental data in this area is currently only available for liquid particles, such as water. The absence of experimental data for the interaction between molten ore particles and walls poses a considerable challenge for this kind of modeling.

### **10.2.2. Thermodynamic modelling**

The thermodynamic calculations presented in this thesis offer a qualitative understanding of zinc ferrite formation in the off-gas system, which is undeniably valuable. However, alternative approaches can be employed to predict the behavior of zinc vapor throughout the entire process. One of these approaches is the effective equilibrium reaction zone (EERZ). With the EERZ approach, it becomes feasible to construct a one-dimensional dynamic model encompassing the entire process, from SRV and CCF to the off-gas system. This approach holds great promise in providing robust, precise, and dynamic predictions integrated with real-time measurements. In particular, the EERZ approach can be utilized to develop a digital twin for the entire HIsarna process.

### **10.2.3. Plant measurements**

Any mathematical model must be validated against measured values to be reliable for further applications.

Limited measurements are available for the current HIsarna process modelling, which limits the possibility of new model developments and validations. For example, for CFD modelling of the HIsarna off-gas system, the temperature is measured only at three points, and the off-gas composition is measured only at two

points. In a particular study, attempts were made to model NO<sub>x</sub> formation in the off-gas system. Despite the development of models, the reliability of the results was limited by the availability of only one measurement point for NO<sub>x</sub> (above the air quench section). Consequently, validating the model solely based on one measurement point was deemed unreliable, making it challenging to confidently utilize or publish the findings in a scientific paper or include them in this thesis.

This is also true for particle flow modelling. Moreover, almost no measurements related to zinc vapor behaviour are available inside the off-gas system except for the zinc content measurements in the collected dust in the cyclone and filter bags. This will make the development of new models challenging.

#### **10.2.4. Experimental studies**

As previously mentioned, there is currently a lack of experimental data pertaining to the kinetic information required for the development of a dependable CFD model concerning the behavior of zinc vapor and the formation of zinc-containing compounds. To bridge this gap, a comprehensive experimental campaign is essential to replicate conditions within the HIsarna environment, covering both the off-gas system and the main reactor. This effort could provide the requisite kinetic data (similar to that available for carbon gasification and CO-H<sub>2</sub> mixture combustion). The acquired data can then be utilized to construct a CFD model for the formation of zinc oxide and zinc ferrite within the process.

# Nomenclature

Parameter	Description and units
$A_r$	Pre-exponential factor [consistent units]
$A_p$	Particle surface area [ $m^2$ ]
$a$	Absorption coefficient
$C$	Constant coefficients
$C_{j,r}$	Molar concentration of species $j$ in reaction $r$ [ $kmol/m^3$ ]
$C_\zeta$	Volume fraction constant equal to 2.1377
$C_\zeta$	Volume fraction constant
$C_\tau$	Time scale constant equal to 0.4082
$D_\omega$	Cross diffusion term [ $1/s^2$ ]
$d_{char}$	Unreacted core diameter [remaining carbon] [ $m$ ]
$d_p$	Particle diameter including product [ash] layer [ $m$ ]
$E$	Total energy [ $J/kg$ ]
$E_r$	Activation energy for the reaction [ $J/kmol$ ]
$\vec{F}$	Force [ $N$ ]
$f_i$	Molar fraction of species in the reactions
$\vec{g}$	Gravity constant [ $m/s^2$ ]
$G$	Incident radiation [ $W/m^2$ ]
$G_k$	Generation of turbulence kinetic energy [ $W/m^3$ ]
$G_\varepsilon$	Generation of turbulence dissipation energy [ $W/m^3$ ]
$G_b$	Generation of turbulence kinetic energy due to buoyancy [ $W/m^3$ ]
$h_j$	Enthalpy of species [ $kJ/kg$ ]
$h$	Heat transfer coefficient [ $W/m^2\cdot K$ ]
$I$	Spectral radiation intensity $W/(m^2\cdot sr\cdot m)$
$IM$	Unity matrix
$\vec{J}_j$ and $\vec{J}_i$	Diffusion flux of species $kg/(m^2\cdot s)$
$K_r$	Equilibrium constant for the $r^{th}$ reaction
$k$	Turbulent kinetic energy [ $m^2/s^2$ ],
$k_{eff}$	Effective conductivity [ $W/(m\cdot K)$ ]
$k_{f,r}$	Forward rate constant for $r^{th}$ reaction
$k_{b,r}$	Backward rate constant for $r^{th}$ reaction
$k_c$	Mass transfer coefficient [ $m/s$ ]
$k_s$	Kinetic rate constant [ $g/(cm^2\cdot s\cdot atm)$ ]
$k_{diff}$	Diffusion rate constant [ $g/(cm^2\cdot s\cdot atm)$ ]
$k_{dash}$	Ash diffusion rate constant [ $g/(cm^2\cdot s\cdot atm)$ ]
$k_x, k_y, k_z$	Thermal conductivities along their respective axis [ $W/(m\cdot K)$ ]
$M_{w,i}$	Molecular weight of species $i$ [ $kg/kmol$ ]
$m_p$	Particle mass [ $kg$ ]
$m_p \frac{\vec{u} - \vec{u}_p}{\tau_r}$	Drag force [ $N$ ]
$\frac{dm_c}{dt}$	Rate of char depletion [ $kg/s$ ]
NTs	Number of tries
$n$	Spectral index of refraction of the medium
Nu	Nusselt number
$p$	Pressure [ $Pa$ ]
$P_i - P_i^*$	Effective pressure [ $atm$ ]
Pr	Prandtl number
$Q$	Heat generation per unit volume [ $j/m^3$ ]

$q_r$	Radiative flux [W/m <sup>2</sup> ]
$\widehat{R}_{i,r}$	Arrhenius molar rate of creation/destruction of species $i$ in reaction $r$ [mol/s]
$R$	Universal gas constant [J/(kmol. K)]
$R_i$	Net rate of production/consumption of species by chemical reaction [mol/s]
$R_{char,i}$	Overall rate of solid reaction per unit particle surface area [kg/(m <sup>2</sup> . S)]
$Re$	Reynolds number
$S_k$ and $S_\epsilon$	User-defined source terms in turbulence equation
$S_r$	Strain rate magnitude [1/s]
$S_i$	Source term in species transport [kg/(m <sup>3</sup> ·s)]
$S_h$	Source term for the reaction heat and other volumetric heat sources
$\vec{r}$	Position vector [m]
$\vec{s}$	Direction vector
$\vec{s}'$	Scattering direction vector
$s$	Path length [m]
$T_p$	Particle temperature [K]
$T$	Fluid temperature [K]
$t$	Time [s]
$u'$	Fluid fluctuating velocity [m/s]
$\bar{u}$	Fluid mean velocity [m/s]
$\vec{u}$	Fluid phase velocity [m/s]
$\vec{u}_p$	Particle velocity [m/s]
$We$	Webber number
$Y_M$	Contribution of the fluctuating dilatation in compressible turbulence to the overall dissipation rate
$Y_k$	Dissipation of kinetic energy [m <sup>2</sup> /s <sup>3</sup> ]
$Y_\omega$	Dissipation of eddy dissipation frequency [m <sup>2</sup> /s <sup>3</sup> ]
$y_{dis}$	Distance to the next surface [m]
$Y_i$	Local mass fraction of each species
$Y_i^*$	Mass fraction of fine-scale species after reacting over the time $\tau^*$
$Y^{eq}$	Chemical equilibrium mass fraction
$Y_{i,s}$	Vapor mass fraction at the surface
$Y_{i,\infty}$	Vapor mass fraction in the bulk gas
$y_j$	Mass fraction of reactive surface species

### Greek letters

$\sigma$	Stefan-Boltzmann constant
$\sigma_s$	Scattering coefficient
$\Omega'$	Solid angle
$\Gamma$	Effective diffusivities [kg/m-s]
$\epsilon$	Energy dissipation rate [m <sup>2</sup> /s <sup>3</sup> ]
$\mu_t$	Turbulent viscosity [m <sup>2</sup> /s]
$\mu$	Molecular viscosity [kg/m-s]
$\rho$	Density of fluid [kg/m <sup>3</sup> ]
$\rho_p$	Density of the particle [kg/m <sup>3</sup> ]
$\rho_s$	Density of solid [kg/m <sup>3</sup> ]
$\tau_r$	Particle relaxation time
$\tau_{char}$	Characteristic time-scale
$\tau^*$	Time scale in EDC
$\tau_{eff}$	Effective shear stress [Pa]
$\omega$	Eddy dissipation frequency [1/s]
$\sigma_k$ and $\sigma_\omega$	Turbulent Prandtl numbers
$v_i$	Corresponding stoichiometric coefficient
$\eta'_{j,r}$	Rate exponent for reactant species $j$ in reaction $r$
$\eta''_{j,r}$	Rate exponent for reactant species $j$ in reaction $r$
$v'_{i,r}$	Stoichiometric coefficient for reactant $i$ in reaction $r$

$v_{i,r}''$	Stoichiometric coefficient for product $i$ in reaction $r$
$\theta$	Net effect of third bodies on the reaction rate
$\gamma_{j,r}$	Third-body efficiency of the $j^{th}$ species in the $r^{th}$ reaction
$\beta_r$	Temperature exponent
$\zeta^*$	Length fraction of the fine scales
$\delta$	Porosity of the ash layer
$\nu$	kinematic viscosity [ $\text{m}^2/\text{s}$ ]

### Abbreviations

CCF	Cyclone converter furnace
CFD	Computational fluid dynamics
DEM	Discrete element method
DOM	Discrete ordinate method
DPM	Discrete phase method
DRW	Discrete random walk
EAF	Electric arc furnace
EDC	Eddy dissipation concept
EDM	Eddy dissipation
EMA	Effective medium approximations
FCO	Field char oxidation
FCO	Field Char Oxidation
FEM	Finite element method
FR-EDM	Finite rate eddy dissipation
HBS	Hot blast stove
ODE	Ordinary differential equation
PCR	Post combustion ratio
RTE	Radiative transport equation
RVE	Representative volume element
SRV	Smelting reduction vessel
UDF	User defined function
USCM	unreacted shrinking core model
WSGGM	Weighted-sum-of-gray-gases model

# Summary

HI sarna is a new and breakthrough smelting reduction technology for producing liquid hot metal for steelmaking directly from iron ores. Compared to the conventional blast furnace route, HI sarna achieves a 20% reduction in CO<sub>2</sub> emissions by eliminating coking and the need for iron ore agglomeration processes such as sintering and pelletizing and directly receiving fine coal and iron ore. The process is built on a pilot scale capable of producing 8 tons/hour of hot metal. The technology combines the Cyclone Converter Furnace (CCF) technology (developed by Hoogovens/Corus/Tata Steel) with the Smelting Reduction Vessel (SRV) from the HIsmelt technology (developed by RioTinto). Operational since 2010 at the IJmuiden Works of Tata Steel Nederland, it has been continually developed towards industrial demonstration.

Fine iron ore and pure oxygen are injected into the CCF. The oxygen is needed as an oxidizer to partially combust the CO-H<sub>2</sub> mixture of the off-gas from the SRV. The combustion process supplies heat to pre-reduced ore particles, melting them during their fly time in the CCF. Eventually, the molten ore particles accumulate on the furnace wall, forming a liquid film that drips along the wall and falls into the molten bath of the SRV. Coal is introduced into the slag layer of the bath via a carrier gas to fully reduce pre-reduced iron oxide (FeO<sub>x</sub>) droplets falling from the CCF above. CO gas is generated in the form of bubbles, rising to the top space of the SRV, where it undergoes partial combustion with oxygen injected through oxygen lances (OL), providing the necessary heat in the SRV.

Through operational analysis of the pilot plant, it has been determined that replacing half of the primary raw material with galvanized steel scrap as a secondary source in the HI sarna process is feasible. This substitution would result in a significant reduction in the injection of fine iron ore. Another advantage is the continuous evaporation of zinc from the scrap surface, accumulating in the off-gas dust, which can later be separated and recovered. In contrast to the blast furnace route, the zinc element does not form a circulating loop inside the reactor but is

converted to the oxidized/ferrite form, ultimately ending up in the dust bag and filters.

However, plant measurements and laboratory analysis of the HIsarna dust reveal that the evaporated zinc primarily reacts with available oxygen and iron oxides to form zinc ferrite. This necessitates additional pre-processing steps before feeding into the zinc smelting unit, incurring extra costs. Consequently, the formation of ferrite is deemed undesirable.

In a nutshell, this thesis focuses on developing a precise computational fluid dynamic (CFD) model to predict the behaviour of the HIsarna off-gas system. This model is crucial for predicting temperature and composition profiles within the off-gas system, particularly in zones where data are not measured at the pilot plant. The possibility of zinc ferrite formation reduction and off-gas system is investigated using plant measurements, CFD data analysis, and thermodynamic calculations. Furthermore, the developed CFD model is utilized to propose modification/optimization of the process, reducing iron ore dust escaping the system, reducing post-combustion oxygen consumption, optimizing post-combustion lance, and off-gas system scale-up.

**Chapter 1** of the thesis is dedicated to a brief history of ironmaking and introduces the HIsarna process in detail, as well as the research focus and thesis structure. **Chapter 2** focuses on establishing and validating a CFD model and offers a detailed description. **Chapter 3** provides an extensive discussion of the model selection and sensitivity analysis. This chapter primarily delves into critical insights regarding the reasons behind the choice of sub-models within the CFD model. Flow analysis of the off-gas system is presented in **Chapter 4**, and in **Chapter 5**, the behaviour of the escaped ore entering the off-gas system is investigated, and potential solutions to mitigate injected ore losses from the off-gas system are discussed. The modified geometry introduced in Chapter 5 is subjected to analysis using the same validated CFD model, ensuring its effective operation within the entire off-gas system. These findings are discussed in **Chapter 6** of the thesis.

In **Chapter 7**, the formation of zinc oxide and zinc ferrite are investigated in the original and modified geometry of the off-gas system, and possible solutions to reduce the ferrite formation are proposed. In **Chapter 8**, a modification to the



oxygen lance is proposed to enhance the combustion of the CO-H<sub>2</sub> mixture. This modification involves using a fluidic oscillator instead of injecting oxygen through a conventional nozzle. The results demonstrate an improvement in CO-H<sub>2</sub> combustion in the reflux chamber. The proposed geometry is constructed and implemented in the reflux chamber for further evaluation and is discussed in detail.

In **Chapter 9** (Part 3), the CFD model developed for the pilot plant is employed to conduct a CFD-based scale-up of the off-gas system to the industrial scale. Within this chapter, the optimized geometry and recommended operating conditions are presented.

Conclusions, remarks, and recommendations are presented in the final chapter of the thesis (**Chapter 10**).

# Samenvatting

Hisarna is een nieuwe en baanbrekende smeltreductietechnologie waarbij vloeibaar ruwijzer rechtstreeks wordt geproduceerd uit ijzererts voor gebruik in de staalproductie. In vergelijking met de conventionele hoogovenroute leidt Hisarna tot een vermindering van de CO<sub>2</sub>-uitstoot met 20% door het elimineren van de productiestappen waarin cokes wordt gevormd uit steenkool en waarin ijzeroxidepellets worden gemaakt. Steenkool en fijn ijzererts worden namelijk rechtstreeks toegevoegd aan de Hisarna-reactor.

Het Hisarna-proces is een combinatie van de 'Cyclone Converter Furnace' (CCF)-technologie (ontwikkeld door Hoogovens/Corus/Tata Steel) en het 'Smelting Reduction Vessel' (SRV) van de HIs melt-technologie (ontwikkeld door RioTinto). Tata Steel Nederland in IJmuiden heeft een proeffabriek gebouwd die is gebaseerd op Hisarna-technologie. De proeffabriek produceert 8 ton ruwijzer per uur. De proeffabriek, die sinds 2010 operationeel is, wordt doorontwikkeld naar het niveau waarop de industriële relevantie kan worden gedemonstreerd.

De hoofdreactor kan in twee secties worden verdeeld. Fijn ijzererts wordt samen met zuivere zuurstof in de CCF geïnjecteerd. Het zuurstof is nodig als oxidator om het CO-H<sub>2</sub>-mengsel, dat als afgas afkomstig is van het SRV, gedeeltelijk te verbranden. Het verbrandingsproces levert warmte aan de voor-gereduceerde ertsdeeltjes en smelt deze tijdens de vlucht in de CCF. De gesmolten ertsdeeltjes worden uiteindelijk afgezet tegen de wand van de reactor. De opeenhoping van de ertsdeeltjes op de wand creëert een vloeistoffilm die langs de wand druppelt en in het smelt-bad van de SRV valt. Steenkool wordt in de slaklaag van het bad geïnjecteerd met behulp van een draaggas om de druppeltjes van voor-gereduceerd ijzeroxide (FeOx), die vanuit de CCF erboven in het bad vallen, volledig te reduceren. CO-gas wordt gegenereerd in de vorm van bellen en bereikt de bovenste ruimte van de SRV waar het CO-gas gedeeltelijk wordt verbrand met zuurstof die wordt geïnjecteerd via zuurstoflansen (OL), waardoor de benodigde warmte in de SRV wordt geleverd.

Op basis van de operationele analyse van de proeffabriek is het mogelijk om de helft van de primaire grondstof te vervangen door gegalvaniseerd staalschroot als secundaire bron voor het HIsarna-proces. Als hieraan wordt voldaan, zal dit leiden tot een aanzienlijke vermindering van de injectie van fijn ijzererts. Een ander voordeel van het HIsarna-proces is dat het zink kan worden teruggewonnen uit het schroot. Dit werkt als volgt. Door de constante verdamping van het zink vanaf het schrootoppervlak wordt het zink uiteindelijk geconcentreerd in het afgasstof, waaruit het zink kan worden teruggewonnen. In tegenstelling tot de hoogovenroute, circuleert het zink niet rond in de reactor, maar komt het zink voornamelijk in geoxideerde/ferrietvorm terecht in de stofzakken en filters. Echter, volgens de fabrieksmetingen en laboratoriumanalyse van het HIsarna-stof, zal het verdampte zink meestal eindigen in de vorm van vast zinkferriet, hetgeen een verdere verbewerkingsstap vereist alvorens het in de zinksmelter verwerkt kan worden. De vorming van ferriet is ongewenst, want de verbewerkingsstap zal extra kosten met zich meebrengen.

Samengevat gaat deze studie over het ontwikkelen van een nauwkeurig CFD-model om het gedrag van het HIsarna-afgassysteem te voorspellen. Dit model is nodig voor het voorspellen van de temperatuur en de samenstelling van het afgassysteem, met name in zones waar niet wordt gemeten in de proeffabriek. Het ontwikkelde CFD-model wordt vervolgens gebruikt om: 1) wijziging/optimalisatie van het proces voor te stellen, 2) het ontsnappen van ijzerertsstof uit het systeem te verminderen, 3) het zuurstofverbruik na verbranding te verminderen, 4) de naverbrandingslans te optimaliseren, 5) de mogelijkheid te onderzoeken van de vermindering van de vorming van zinkferriet en 6) het opschalen van het afgassysteem te onderzoeken.

Hoofdstuk 1 van het proefschrift is gewijd aan een korte geschiedenis van de ijzerproductie en introduceert het HIsarna-proces in detail, evenals de focus van het onderzoek en de structuur van het proefschrift. Hoofdstuk 2 richt zich op het opzetten en valideren van een CFD-model en biedt hiervan een gedetailleerde beschrijving. Hoofdstuk 3 biedt een uitgebreide discussie over de selectie van het model en de gevoeligheidsanalyse. Dit hoofdstuk gaat vooral in op kritische inzichten met betrekking tot de redenen achter de keuze voor sub-modellen binnen het CFD-model. De stroomanalyse van het afgassysteem wordt gepresenteerd in hoofdstuk 4. In hoofdstuk 5 wordt het gedrag van het ontsnapte erts dat het

afgassysteem binnenkomt onderzocht, en worden mogelijke oplossingen besproken om geïnjecteerde ertsverliezen uit het afgassysteem te beperken. De gewijzigde geometrie, geïntroduceerd in hoofdstuk 5, wordt onderworpen aan analyse met behulp van hetzelfde gevalideerde CFD-model, waardoor de effectieve werking ervan binnen het gehele afgassysteem wordt gegarandeerd. Deze bevindingen worden besproken in Hoofdstuk 6 van het proefschrift.

In Hoofdstuk 7 wordt de vorming van zinkoxide en zinkferriet onderzocht in de originele en gewijzigde geometrie van het afgassysteem en worden mogelijke oplossingen voorgesteld om de ferrietvorming te verminderen. In Hoofdstuk 8 wordt een aanpassing aan de zuurstoflans voorgesteld om de verbranding van het CO-H<sub>2</sub> mengsel te verbeteren. Deze wijziging omvat het gebruik van een fluïde oscillator in plaats van het injecteren van zuurstof door een conventioneel mondstuk. De resultaten tonen een verbetering aan van de CO-H<sub>2</sub>-verbranding in de refluxkamer. De voorgestelde geometrie wordt geconstrueerd en geïmplementeerd in de refluxkamer voor verdere evaluatie en wordt in detail besproken.

In Hoofdstuk 9 (Deel 3) wordt het CFD-model, dat voor de proeffabriek is ontwikkeld, gebruikt om een op CFD gebaseerde opschaling van het afgassysteem naar industriële schaal uit te voeren. In dit hoofdstuk worden de geoptimaliseerde geometrie en aanbevolen bedrijfsomstandigheden gepresenteerd.

Conclusies, opmerkingen en aanbevelingen worden gepresenteerd in het laatste hoofdstuk van het proefschrift (hoofdstuk 10).

# Publications

- 1 Hosseini, R. Calis, D. van der Plas, P. Put, J. Agema, K. Meijer, J.L.T. Hage, E. Offerman, Y. Yang, **Computational Fluid Dynamics Modelling of HISarna Off-Gas System—Wall Modelling and Heat Loss Prediction**. *Processes* (2023), 11, 3082, DOI: <https://doi.org/10.3390/pr11113082>. → [\(Chapter 2\)](#)
- 2 Hosseini, V. Dhiman, K. Meijer, C. Zeilstra, J. Hage, T. Peeters, E. Offerman & Y. Yang, **CFD modelling of the off-gas system of HISarna iron making process. Part 1: model development using detailed reaction mechanism for post-combustion of CO–H<sub>2</sub> mixture and carbon particles**, *Ironmaking & Steelmaking* (2022), 49:8, 828-844, DOI: 10.1080/03019233.2022.2062929. → [\(Chapter 2 and Chapter 4\)](#)
- 3 Hosseini, J. Hage, K. Meijer, E. Offerman & Y. Yang. **On the Importance of Model Selection for CFD Analysis of High Temperature Gas-Solid Reactive Flow; Case Study: Post Combustion Chamber of HISarna Off-Gas System**. *Processes* (2023), 11, 839, DOI: <https://doi.org/10.3390/pr11030839>. → [\(Chapter 3\)](#)
- 4 Hosseini, V. Dhiman, K. Meijer, C. Zeilstra, J. Hage, T. Peeters, E. Offerman & Y. Yang, **CFD modelling of the off-gas system HISarna iron making process part 2: reflux chamber geometry modification and effects on flow behaviour**, *Ironmaking & Steelmaking* (2022), 49:8, 783-794, DOI: 10.1080/03019233.2022.2060457. → [\(Chapter 6\)](#)
- 5 Hosseini, E. Moosavi-Khoonsari, K. Meijer, J. Hage, T. Peeters, E. Offerman & Y. Yang **Thermodynamic analysis of zinc ferrite (ZnFe<sub>2</sub>O<sub>4</sub>) formation inside the HISarna off-gas system**, *Ironmaking & Steelmaking* (2022), 50:5, 485-499, DOI: 10.1080/03019233.2022.2124491. → [\(Chapter 7\)](#)
- 6 Hosseini, J. Hage, A. Duiker, K. Meijer, T. Peeters, E. Offerman & Y. Yang, **Off-Gas System Scale-Up of HISarna Iron-Making Process: A CFD-Based Approach**, *Metall Mater Trans B* (2022), 53, 3557–3574, DOI: <https://doi.org/10.1007/s11663-022-02620-4>. → [\(Chapter 9\)](#)
- 7 Hosseini, E. Georgopoulos, V. Dhiman, J. Hage, K. Meijer, C. Zeilstra, E. Offerman & Y. Yang, **Granular Flow Modelling of Galvanized Steel Scrap Injection into the HISarna Iron-Making Reactor**. *Steel research int.* (2022), 93: 2200193, DOI: <https://doi.org/10.1002/srin.202200193>.
- 8 E. Georgopoulos, A. Hosseini, T. Kerry, J. Hage, K. Meijer, E. Offerman & Y. Yang, **Experimental and Discrete Element Method Analysis of Galvanized Steel Scrap Particles Along and After an Inclined Chute**. *Steel research int.* (2022), 93: 2200075, DOI: <https://doi.org/10.1002/srin.202200075>.

# Acknowledgments

First and foremost, I extend my heartfelt appreciation to my supervisors and promoters at TU Delft. I am sincerely grateful to Professor **Yongxiang Yang** for his unwavering support and trust; working in his team was devoid of any pressure. I also want to express my gratitude to Professor **Erik Offerman**, whose guidance taught me the importance of being humble.

My sincere regards to the TATA experts. Many thanks to Dr. **Hans Hage** and **Koen Meijer** for their support and for providing a safe environment for me to work at TATA offices and arranging things in a way for me to be in direct contact with the HIsarna team. Special thanks to **Hans**, whose invaluable assistance made the completion of this thesis much smoother.

I wish to convey my appreciation to **Vinod Dhiman**, Dr. **Sripriya Rajendran**, **Jelle Agema**, Dr. **Tim Peeters**, and Dr. **Christiaan Zeilstra** for generously sharing their data and offering valuable insights on my research. Special thanks to my teammates, **Tim Kerry** and **Evangelos Georgakopoulos** for their valuable supports.

My sincere appreciation to **EIT RawMaterials** for funding “**ReclaMet project**” of which this Ph.D. research formed an integral part.

I want to thank the invisible staff of TU Delft, caretakers, and custodians. Their diligent work keeps our surroundings safe and clean, often without us even realizing. These individuals, who are not always in the spotlight, are not only dedicated professionals but also enjoyable companions to be around.

I want to express my heartfelt thanks to my friends for their support and companion during the pandemic. A special mention to **Elvira**, my constant companion during the challenging times of Covid.

I extend my deep appreciation to my parents for their love and for shaping me into the person I am today.

This thesis is dedicated to my parents, my siblings, and the love of my life.

# Curriculum vitae

Ashkan was born on the 18th of September 1989 and raised in the Kurdistan region of Iran in a city called Bookan. After high school in 2007, he entered the University of Tehran and obtained his B.Sc. degree in chemical engineering. After graduation, he worked as a quality control engineer for a while, then gained admission to Politecnico di Milano in 2015. He received admission to study Energy Engineering, and it was there that he became passionate about mathematical modeling and computational fluid dynamics. His enthusiasm for CFD modeling was such that he invested half of his scholarship funds in acquiring a dedicated workstation PC solely for his simulations. Using that computer, he mastered CFD and developed a nice portfolio through various random simulations. The same portfolio later earned him the PhD position at TU Delft. In 2017, he started an internship at HZDR research center in Germany, which gave him a great opportunity to work on his CFD and modeling skills. He started his PhD on the 15th of September 2018 under the supervision of Prof. Yongxiang Yang and Prof. Erik Offerman. His expertise mostly lies in mathematical, thermodynamic, and CFD-DEM modeling of chemical and metallurgical processes, industrial equipment design, and scale-up. In parallel, he is also quite interested in renewable energies and occasionally works on small related projects.